UNIVERSITÀ DEGLI STUDI DI MILANO

DOTTORATO DI RICERCA IN SCIENZE DELLA TERRA

Ciclo XXXII

DIPARTIMENTO DI SCIENZE DELLA TERRA

Quantitative analysis of fabric evolution and metamorphic transformation in crystalline basements

Ph.D. Thesis

GEO/03

Luca Corti

Matricola R11512

Tutors

Prof. Michele Zucali

Dr. Davide Zanoni

Coordinator

Prof. Fernando Camara Aritigas

“Passion is
in all great researches
and it is necessary to
all creative endeavors”
W.E. Smith

CHAPTER 1 - INTRODUCTION **1**

CHAPTER 2 - GEOLOGICAL SETTING **9**
2.1 The Alpine orogen and its domains 9
2.1.1 Austroalpine domain 11
2.1.2 Penninic domain 12
2.1.3 Helvetic domain 12
2.1.4 Southern Alps 13
2.3 The Sesia-Lanzo Zone 13
2.4 The Argentera Massif 17

CHAPTER 3 – METHOD AND TECHNIQUES **21**
3.1 Multiscale structural analysis 21
3.2 3D geological modelling 21
3.3 Chemical imaging and fabric analysis 25
3.4 X-ray computed microtomography 26

CHAPTER 4 - FIRST CASE STUDY: LAGO DELLA VECCHIA AREA **29**
4.1 Analysis of fabric evolution and metamorphic reaction progress 29
4.1.1 Introduction 29
4.1.2 Geological setting 33
4.1.3 Mapping method and analytical techniques 33
4.1.4 Field data 37
4.1.4.1 Rock type 37
4.1.4.2 Structural Analysis 40
4.1.5 Conclusion 44
4.1.6 Acknowledgements 45

4.2 Tectonometamorphic evolution of the Lago della Vecchia metaintrusive and its country rocks, Sesia-Lanzo Zone, Western Alps 45
4.2.1 Introduction 46
4.2.2 Geological setting 46
4.2.2.1 Lithostratigraphic-metamorphic outline 46
4.2.2.2 Structural-metamorphic outline 50
4.2.2.3 Geochronological outline 51
4.2.3 Method 53
4.2.4 Mesostructural analysis 53
4.2.4.1 Rock types 53
4.2.4.2 Mesostructural evolution 55

4.2.5 Microstructural evolution 58
4.2.5.1 Pre-Alpine evolution 58
4.2.5.2 Alpine evolution 59
4.2.6 Mineral chemistry 63
4.2.7 Metamorphic conditions 69
4.2.8 Discussion 73
4.2.8.1 Tectonometamorphic and geodynamic evolution 73
4.2.8.2 Contrasting histories vs. Contrasting memories along EMC 74
4.2.9 Conclusion 75
4.2.10 Acknowledgements 76

4.3 LREE distribution in allanite during subduction controlled by strain partitioning in rock matrix. 76
4.3.1 Introduction 77
4.3.2 Material and methods 79
4.3.2.1 Geological outline 79
4.3.2.2 Allanite sampling 80
4.3.2.3 Methods 81
4.3.3 Results 82
4.3.3.1 Microstructures 82
4.3.3.2 Chemical imaging 84
4.3.3.3 Mineral Chemistry 88
4.3.3.4 Single crystal X-ray diffraction 89
4.3.4 Discussion 92
4.3.4.1 Crystallography constrains 92
4.3.4.2 LREE released vs. rock matrix total strain 94
4.3.5 Conclusion 96
4.3.6 Acknowledgment 96

CHAPTER 5 - SECOND CASE STUDY: MT. MUCRONE AREA 97
5.1 3D reconstruction of fabric and metamorphic domains in a slice of continental crust involved in the Alpine subduction system: the example of Mt. Mucrone (Sesia-Lanzo Zone, Western Alps) 98
5.1.1 Introduction 98
5.1.2 Geological outline 100
5.1.3 Lithostratigraphy and mesostructures 102
5.1.3.1 Metaintrusives 104
5.1.3.2 Micaschists 104
5.1.3.3 Gneisses 105
5.1.3.4 Metabasites (eclogites and glaucophanites) 106
5.1.3.5 Marble and “quartzites” 106

5.1.4 Structural and metamorphic evolution 106
5.1.5 3D reconstruction method 107
5.1.5.1 2D interpolation 108
5.1.5.2 3D modelling 110
5.1.6 Results 111
5.1.7 Discussion 115
5.1.8 Conclusions 117
5.1.9 Acknowledgment 119

5.2 Integrating X-ray computed tomography with chemical imaging to quantify mineral re-crystallization from granulite to eclogite metamorphism in the Western Italian Alps (Sesia-Lanzo Zone) 119
5.2.1 Introduction 120
5.2.2 Material and Methods 122
5.2.2.1 Geological Outline 122
5.2.2.2 Sample Description 124
5.2.3 Method 126
5.2.3.1 Chemical imaging and fabric analysis 126
5.2.3.2 X-ray computed tomography 129
5.2.3 Results 131
5.2.3.1 2D chemical and fabric results 131
5.2.3.2 3D fabric and metamorphic results 142
5.2.4 Discussion and Conclusion 146
5.2.4.1 Micro-scale and kinetics implications 146
5.2.4.2 General implications 147
5.2.5 Acknowledgments 148

CHAPTER 6 - THIRD CASE STUDY: MT. FRISSON AREA 149
6.1 Introduction 149
6.2 Mesostructural analysis 154
6.2.1 Rock types 155
6.2.1.1 Variscan metamorphic basement 155
6.2.1.2 Permo-Triassic metamorphic cover rocks 157
6.2.2 Mesostructural evolution 158
6.2.2.1 Variscan 158
6.2.2.1 Alpine 158
6.3 Microstuctural evolution 159
6.3.1 Variscan 159
6.3.2 Alpine 162
6.4 Mineral chemistry 164
6.4.1 Variscan metamorphic basements 164

6.4.2 Permo-Triassic metamorphic cover rocks 165
6.5 Bulk rock chemical analysis 168
6.6 Rutile U-Pb geochronology 170
6.7 Metamorphic conditions 172
6.8 Discussion 177
6.8.1 Eclogite protoliths 177
6.8.2 Tectonometamorphic evolution and geodynamic implications 177

CHAPTER 7 – DISCUSSION 179
7.1 Pre-Alpine and Alpine geodynamics in paleo-European and -African continental crust 179
7.2 Correlation between fabric and metamorphic heterogeneities 180

CHAPTER 8 - CONCLUSION 185

CHAPTER 8 - REFERENCES 187

APPENDIX A
Interactive map. A petrostructural map of the Lago della Vecchia - Valle d'Irogna area (Sesia-Lanzo Zone, Western Alps): 4.1 section

APPENDIX B
Mineral chemical analysis and qualitative estimate of the whole rock chemistry: 4.2 section

APPENDIX C
Mineral chemical analysis of allanite crystals: 4.3 section

APPENDIX D
Allanite CIF file. Suppemental material of 4.3 section

APPENDIX E
Gatta G.D., Milani S., Corti L., Comboni D., Lotti P., Merlini M., and Liermann H.P. (2019): Allanite at high pressure: effect of REE on the elastic behaviour of epidote-group minerals. Physics and Chemistry of Minerals, doi: 10.1007/s00269-019-01039-9

APPENDIX F
Supplemental material of 5.2 section

APPENDIX G
Analytical conditions and results of whole rock analysis (6.5 section)

List of abbrevations

A	fold Axis
AP	fold Axial Plane
AsR	Aspect Ratio
ASZ	Autier Shear Zone
BA-FA	Back-Arc to ForeArc ophiolite
BG	Banded Gneiss
BSE	Back-Scattered Electron
BSZ	Bersezio Shear Zone
C	Coronite
CS	Case Study
CSZ	Casterino Shear Zone
CT	Computed Tomography
D	Depth
DBS	Dent-Blanche System
DEM	Digital Elevation Model
DFE	Degree of Fabric Evolution
DRP	Degree of Reaction Progress
E-; N-MORB	Enriched-; Normal-Mid Ocean Ridge Basalt
ECM	External Crystalline Massifs
EDS	Energy Dispersive Spectroscopy
EMC	Eclogitic Micaschists Complex
EMPA	Electron MicroProbe Analyzer
FE	Fabric Evolution
FMSZ	Ferriere-Mollieres Shear Zone
FSZ	Fremamorta Shear Zone
FWHM	Full-Width-at-Half-Maximum
GIS	Geographic Information System
GMC	Gneiss Minuti Complex
GSV	Gesso-Stura-Vésubie Complex
H-; L-REE	Heavy-; Light-Rare Earth Elements
ICM	Internal Crystalline Massifs
IIDK	II Zona Dioritico-Kinzigitica
IMA	International Mineralogical Association
K	bulk moduli
L	Lineation
LA-ICP-MS	Laser Ablation-Inductively Coupled Plasma-Mass Spectrometry
LILE	Large Ion Lithophile Element
Lp	Lorentz-polarization
LPO	Lattice Preferred Orientation
M	Mylonite
MB	Metabasite
MBW	Marked-Watershed segmentation

MI	Metaintrusive
Min-GSD	Mineral-Grain Size Detector
MLC	Maximum Likelihood Classification
MP	Metapelite
MT	Metamorphic Transformation
NSZ	Neiglier Shear Zone
OBA	Back-Arc Ophiolites
OIB	Ocean Island Basalt
P	Pressure
PCA	Principal Components Analysis
PF	Penninic Frontal thrust
PL	Periadric lineament
Q-XRMA	Quantitative-X Ray Map Analyzer
RCTS	Rocca Canavese Thrust Sheet
S	Foliation
SLZ	Sesia-Lanzo Zone
SPO	Shape Preferred Orientation
SZ	Shear Zone
T	Tectonite
T	Temperature
TAS	Total Alkali versus Silica
TMC	Tinée Metamorphic Complex
TMUs	Tectono-Metamorphic Units
V	Vein
VOI	Volume of Interest
WDS	Wave-length Dispersive Spectroscopy

Chapter 1
Introduction

The aim of this work is the study of the relationships between the degree of fabric evolution and metamorphic reaction progress in crystalline basements through a multiscale structural analysis and multidisciplinary approach. The knowledge of crust and mantle dynamics is mostly based on the study of fabric elements, metamorphic assemblages, and their relationships within the rock-volume, now exposed after the subduction- and collision-related processes. Within convergent margins, the coupling and uncoupling of lithospheric slices are responsible for the tectonic architecture of metamorphic belts (*e.g.*, Polino et al., 1990; Royden, 1996; Bousquet, 2008; Willingshofer and Sokoutis, 2009; Beltrando et al., 2010; Spalla et al., 2010; Roda et al., 2012; Duretz and Gerya, 2013; Willingshofer et al., 2013; Ruh et al., 2015). The lithospheric slices can be recognized as tectono-metamorphic units once their tectonic and metamorphic history is proved to be homogeneous over a defined time interval (Schwartz et al., 2000, Engi et al., 2001; Gerya and Stockhert, 2005; Spalla et al., 2005; Ernst and Liou, 2008; Guillot et al., 2009; Blanco-Quintero et al., 2011). Petro-structural mapping and multiscale structural analysis are crucial to characterize the tectono-metamorphic evolution of lithospheric slices and the relationships between degree of fabric evolution and metamorphic transformation. In particular, the relationship between fabric evolution and metamorphic reaction progress with the development of dominant (*i.e.* pervasive) fabric can be used to investigate the complexity of convergent dynamics (*e.g.* Passchier et al. 1981; England and Thompson 1984; Spear and Peacock 1989; Johnson and Duncan 1992; Dewey et al., 1993; Cuthbert et al., 2000; Parrish, 2001; Štípská et al., 2008; Hoobs et al., 2010; Salvi et al., 2010; Gosso et al., 2015). Adjacent rock volumes characterized by the same dominant fabric may record different tectono-metamorphic histories. On the contrary, adjacent rock volumes showing dominant fabrics developed under different metamorphic conditions may record the same tectono-metamorphic history due to heterogeneous registration of the superposed deformation and metamorphic stages (Park, 1969; Myers 1978; Bell, 1981, Bell and Rubenach 1983; Williams, 1985; Passchier et al. 1990; Johnson and Vernon 1995; Marquer et al. 1996; Spalla et al., 2005). In order to evaluate whether rock volumes record the same tectono-metamorphic history, mapping petro-structural heterogeneities in adjacent rock volumes is crucial (*e.g.* Turner and Weiss 1963; Park 1969; Hobbs et al. 1976; Williams 1985; Lardeaux & Spalla 1990, 1991; Passchier et al. 1990, Johnson, 1995; Spalla et al. 2000; Ernst and Liou, 2008; Gosso et al., 2015).

The relationship between deformation and metamorphism in basements have long been studied (Turner and Weiss 1963; Park 1969; Hobbs et al. 1976) and it is currently generally accepted that the

single use of geometric criteria during structural correlation turns out to be poorly reliable (Spalla et al. 2000), mainly due to heterogeneity of deformation partitioning that commonly affects crystalline basements (*e.g.* Myers 1970; Ramsay and Huber 1983; Mørk 1985; Austrheim 1987; Austrheim 1990; Ramsay & Lisle 2000). Similarly, the metamorphic correlation without any structural constrains it is not sufficient again because strain partitioning may influence the heterogeneous distribution of metamorphic assemblages or, even worst, it can result into gaps in the metamorphic memory of rocks (Spalla et al. 2005; Pearce and Wheeler 2010). These vacancies in metamorphic evolution are referenced to be due to the catalysing effect of deformation on the metamorphic reaction progress (*e.g.* Spalla et al. 2000; Spalla et al. 2005; Hobbs et al. 2010; Chapman et al. 2019) or local instabilities due to diffusion processes (*e.g.* Pearce and Wheeler 2010) or stress-driven reaction heterogeneities (Schmalholz and Podladchikov 2014; Tajcmanova et al. 2014; Zhong et al. 2017).

Syn-metamorphic finite strain gradients, from domains that completely escaped deformation (coronite) or that partially (tectonite) or pervasively (mylonite) recorded deformation, are common in adjacent rock volumes (*e.g.* Bell and Rubenach 1983; Lardeaux and Spalla 1990; Bell and Hayward 1991; Spalla and Zucali 2004; Spalla et al. 2005; Salvi et al. 2010; Gosso et al. 2015).

More in details, in coronitic (low strain) domains, metamorphic reactions take place without development of a new oriented fabric. In contrast, where the strain is accumulated, tectonitic and mylonitic fabric develop in intermediate and high strain domains, respectively. In the last two cases metamorphic assemblages define normal planar/linear tectonites or mylonites (Spalla et al., 2010; Zucali et al., 2002; Salvi et al., 2010; Gosso et al., 2015). Therefore, structural correlation in metamorphic basements has to be based on a coherent sequence of tectono-metamorphic stages. Indeed, the combined use of *P-T* estimates and deformation histories (d-t) over large areas has become the basis for the individuation of tectonometamorphic units (TMUs of Spalla et al., 2000; Spalla et al., 2005). Heterogeneities, accompanying fabric evolution, also characterize metamorphic reaction progress facilitating the reconstruction of structural and metamorphic evolution back in time. The resulting distribution of the superposed fabrics elements and metamorphic assemblages allows the evaluation of the percentage of the mechanically and chemically reacting volumes during the successive tectono-metamorphic stages. The correlation between degree of fabric evolution and degree of metamorphic reaction progress of superposed tectono-metamorphic imprints can be used for quantifying the size of rock volumes affected by such structural and metamorphic heterogeneities in crustal portions implicated in convergent dynamics (*e.g.* Salvi et al. 2010; Gosso et al. 2015). Estimates of the degree of fabric evolution and metamorphic reaction progress relationships made on rock-volumes reworked during various thermo-mechanical evolutions shows that the dominant tectono-metamorphic imprint is related to the high degree of fabric evolution and metamorphic

reaction progress (*e.g.* Southalpine domain: Spalla et al. 2000; Sesia-Lanzo Zone: Zucali et al. 2002; Delleani et al. 2012, 2013; Corti et al. 2017; Dent Blanche nappe: Roda and Zucali 2008; Baletti et al. 2012; Languard-Tonale unit: Salvi et al. 2010).

Detailed multiscale correlation between deformation and metamorphism has been shown to be of primary importance to constrain the relationships between fabric and metamorphism (*e.g.* Turner and Weiss 1963; Park 1969; Hobbs et al. 1976; Williams 1985; Stünitz 1989; Lardeaux and Spalla 1990; Passchier et al. 1990; Johnson and Vernon 1995; Spalla et al. 2000; Zucali et al. 2002; Spalla and Zucali 2004; Gosso et al. 2010; Salvi et al. 2010; Hobbs et al. 2011; Delleani et al. 2012; Gosso et al. 2015; Rebay et al. 2015; Cantù et al. 2016; Corti et al. 2017, 2018; Delleani et al. 2018). Combining this approach with petrologic investigations allows the individuation of the rock volumes sharing the same *P*-*T*-d-t evolutions (Rebay and Spalla, 2001; Zucali et al., 2002; Spalla and Zucali, 2004; Zucali et al., 2004; Gosso et al., 2010; Salvi et al., 2010; Zucali and Spalla, 2011; Delleani et al., 2012; Cantù et al., 2016; Delleani et al., 2018; Corti et al., 2018) and, combined with numerical models, it has been used to test the reliability of geodynamic models of subduction-collision processes (Meda et al., 2010; Roda et al., 2012; Roda et al., 2019).

Classical structural geology studies have been progressively reinforced by a collection of quantitative data through texture analysis (*e.g.* Frassi et al. 2017; Zucali et al 2014), synchrotron X-ray computed microtomography (*e.g.* Zucali et al 2014b) and chemical mapping of superimposed structures in metamorphic rocks (Lanari et al. 2014; Ortolano et al. 2014; Visalli, 2017). In this view, the quantitative analysis of the relationships between deformation and metamorphism related to the superimposed fabrics allows the evaluation of the mechanically and chemically reacting volume percentage, during successive tectono-metamorphic stages.

In this work, the multiscale (atomic- to km-scale) structural analysis and multidisciplinary approach (high-grade terrains fieldwork, GIS database, Python-based software, optical and electron microscopy, thermobarometric estimates, thermodynamic modelling, absolute age, SPO analysis, high-resolution optical scan, quantitative X-Ray Map Analysis, micro-CT, 3D geology modelling, and X-ray single crystal diffraction) are used to quantitatively investigate the textural and chemical heterogeneities developing during deformation and metamorphism partitioning (Fig. 1.1).

This quantitative petrological and structural analysis is a powerful method to:

(i) better constrain the tectono-metamorphic evolutions;

(ii) providing rheological constraints for numerical modeling on subduction dynamics;

(iii) defining the physical and chemical parameters controlling the fabric evolution, the metamorphic transformation, and their interplay within subduction-collision systems.

In this perspective, this quantitative approach is applied in three different portions of the Alpine metamorphic basements (mainly metagranitoids, metapelites, metabasites, and granulites) in different thermal environments and structural levels: HP-LT (Sesia-Lanzo Zone) and IP-HT (Argentera Massif). In this view, the parameters controlling the degree of fabric evolution and metamorphic reaction progress are explored in the following chapters. The analysis of the parameters that control the relationships between degree of fabric evolution and metamorphic transformation can be done once the deformation-metamorphism PT conditions for the succesive tectonometamorphic stage are estimated. Detail geological and structural mapping, multiscale structural analysis, mineral chemical analysis, and *P-T* estimates for succesive fabric and metamorphic re-equilbration are useful to reconstruct the tectono-metamorphic evolution of polydeformed and polymetamorphosed crystalline basements. This method is applied to infer the tectonometamorphic evolution of two continental crust rock volume forged in different metamorphic conditions: i) the Lago della Vecchia continental crust rocks surfacing within the Seisa-Lanzo Zone and characterized by dominant Alpine H*P*-L*T* blueschist-facies conditions (4.2 section) and ii) the Frisson mylonitic granulites surrounded by migmatities outcropping within the Argentera Massif and characterized by a dominant H*P*-H*T* amphibolite-facies metamorphic imprint (6.1 section).

The contouring of domains that show homogeneous fabric and metamorphic development is facilitated by integrating meso- with micro-scale structural analysis to estimate the degree of fabric evolution and metamorphic reaction progress for each deformational stage. The approach allows to define the km-scale pervasiveness of a single deformation-metamorphic stage in 2D-dimension (4.1 section) and 3D-dimension (5.1 section).

The quantitative estimation of deformation and chemical variation at grain-scale during vary *PT* conditions and different degree of fabric evolution and metamorphic transformation can be done through the integration of microstructural analysis, mineral chemical analysis, quantitative chemical imaging, and single-crystal X-ray diffraction. This approach is used to explore structural parameters, chemical compositions, and texture patterns of natural allanite crystals from the Lago della Vecchia metagranitoids in the Sesia-Lanzo Zone (4.3 section). In this light, the crystal-chemical features of the allanite are constrained in response to the different conditions of the surrounding plastically deformed rock matrix and the LREE fraction released from allanite as function of the accumulated strain in the host rocks is estimated.

The modal percentage, the mineral chemical variation, the grain-size distribution, the grains orientation, and the grain boundary geometries of the mineral phases marking superposed fabrics in metamorphic rocks are the first order parametes for recognizing homogeneous metamorphic domains for each re-equilibration stage and to constraint the chemistry of the mineral phases linked to the

development of metamorphic-related static and dynamic fabrics. In the 5.2 section, these parameters are quantified through a multidisciplinary approach combining detail microstructural analysis, X-ray computed microtomography, and X-ray chemical mapping obtained from an Electron MicroProbe Analyzer (EMPA). The combined use of EMPA X-ray chemical mapping with the X-ray µ-CT technique permit to constrain the chemistry and deformation of the mineral phases linked to the metamorphic transformation and strain partitioning.

Fabric and metamorphism correlation

1: ***Multiscale structural analysis and tectonometamorphic evolution***

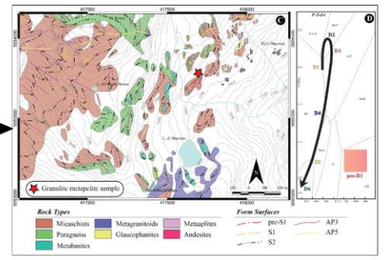

2: ***Quantative analysis of fabric and metamorphic heterogeneities***

Microstructures

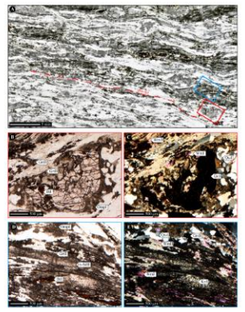

DFE - DRP punctual estimation

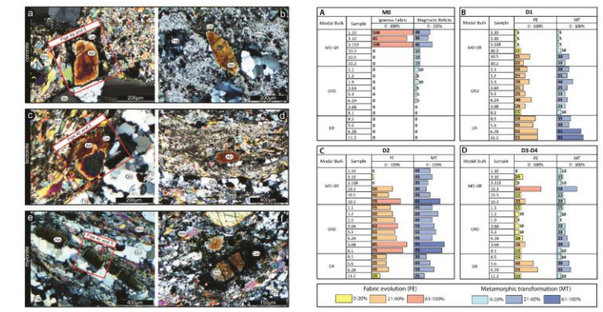

2D-3D modelling

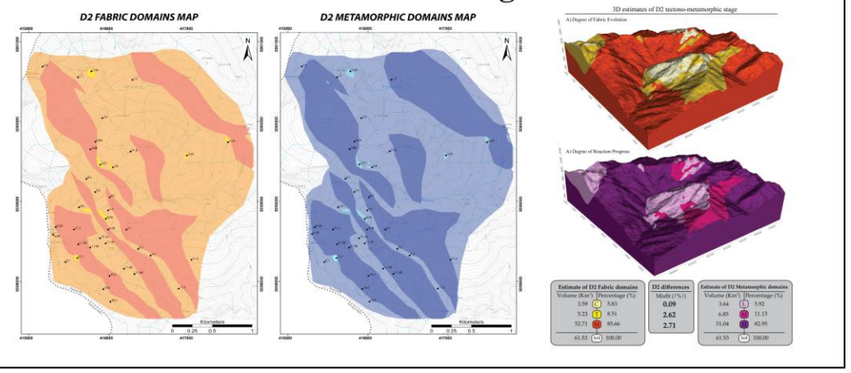

Chemistry

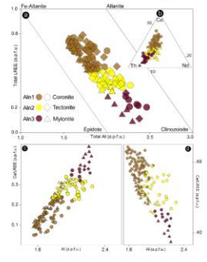

Chemical imaging

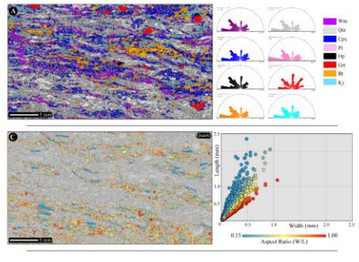

X-CT analysis

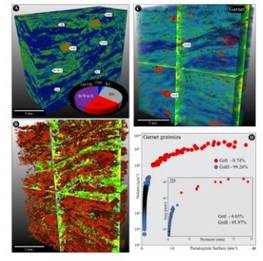

3: ***Tectonics and Geodynamic implications***

Improve the numerical modelling

Numerical model

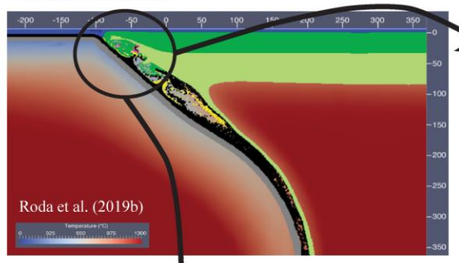

Model vs. field data

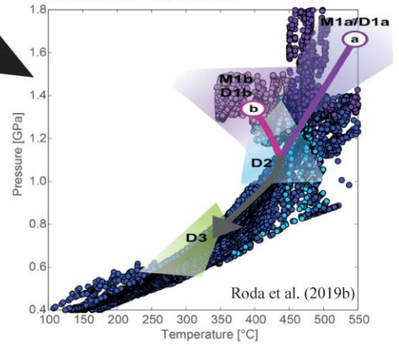

Stress

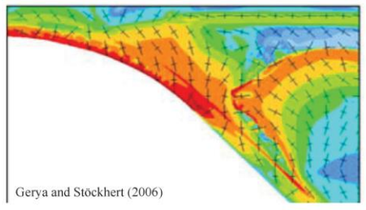

Strain rate

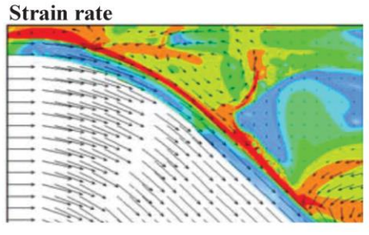

Regional DFE-DRP heterogeneities

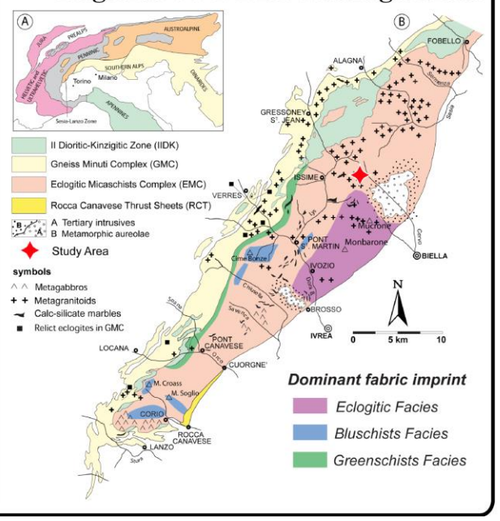

Quantification of parameters controlling the fabric and metamorphic heterogeneities:
rock-type; thermal regime; mineral chemical diffusion; modal mineral percentage; grain-size distribution; grains orientation; grain boundary geometries; role of fluids; crystallographic structures deformation

Figure 1.1. Fabric and metamorphic correlation workflow. The multiscale structural analyis and tectonometamorphic evolution are the first-order classification for a quantitative analysis of fabric and metamorphic heterogeneities. Microstrural analysis of DFE-DRP punctual estimation allow the 2D and 3D modelling of volume characterized by homogeneou degree of fabric evolution and metamorphism reaction progress. These km-scale models are used as a guide for deeper quantitative analyis at cm- to atomic-scale in order to quantify the parameters controlling the fabric and metamorphic heterogeneities. These parameters allows more accurate 2D-3D models. The DFE-DRP results are useful as input data for numerical modeling of geodynamics processes.

Chapter 2

Geological setting

2.1 The Alpine orogen and its domains

The Alps extend from the Vienna Basin to the Gulf of Genova, south of which the chain is interrupted by the Ligurian-Provençal-Algerian and Tyrrhenian basins during Neogene time (*e.g.* Dewey et al., 1973; Doglioni, 1991; Spadini et al., 1995; Doglioni et al., 1997; Rosenbaum and Lister, 2004; Schettino and Turco, 2006; Doglioni et al., 2007; Malusà et al., 2011; Carminati et al., 2012; Turco et al., 2012). Since the Late Cretaceous onwards, the Alpine orogeny results from the convergence between the European and Adriatic plates that led to the closure of the oceanic domain of the Alpine Tethys and the collision between the continental margins of Adria and Europe (*e.g.* Lardeaux, 2014; Dal Piaz et al., 2003). This chain is subdivided in four main tectonic domains individuated at the lithospheric scale after the seismic-integrated geophysical exploration of the whole belt by the ECROS-CROP-NFP20-TRANSALP projects (*e.g.*, Schmid et al. 2004; Cassinis, 2006). From the internal to the external part of the Alps the principal tectonic domains are: Southern Alps; Austroalpine domain; Penninic domain; Helvetic domain (Fig. 2.1). The Southern Alps are a south verging thrust system involving, since Cretaceous time, continental basement and cover units, both recording a scattered very low-grade Alpine metamorphism only close to Periadriatic lineament (Spalla et al. 2014 and refs. therein). The Austroalpine and Penninic domains were deformed at deep structural levels during Alpine subduction and collision, as accounted by predominant high-pressure metamorphic evolution (*e.g.* Spalla et al. 2014 and refs. therein). The external margin of the Austroalpine domain is infolded within Mesozoic sedimentary sequences of the Penninic domain, which were deformed and metamorphosed during the Alpine convergence (Polino et al. 1990; Handy and Oberhansli, 2004; Bousquet et al. 2004; Gerya & Stockhert, 2006; Thoni et al., 2008; Handy et al. 2010; Roda et al. 2012; Spalla et al. 2014). The Penninic domain consists of a system of metamorphic nappes formed by continental and oceanic material derived from the subducting European plate. The Helvetic domain consists of a Europe-verging thick- to thin-skin thrust system, involving basement and cover slices, structured during the continental collision since the Cenozoic (Bigi et al., 1990). Cretaceous-Paleogene Alpine high-pressure rocks are confined within the axial part of the chain in a rootless crustal prism that consists of tectonic units belonging to the Penninic and Austroalpine domains and bounded by the Penninic frontal thrust (PF) towards the European foreland, and the Periadric lineament (PL) towards the Adriatic hinterland (*e.g.* Bousquet et al. 2008; Roda et al. 2012).

The wide span of time for the formation of high-pressure rocks in both continental and oceanic slices (Bousquet et al. 2004; Babist et al. 2006) suggests that most units were buried and exhumed during ongoing subduction of the European oceanic lithosphere (lower plate) accompanied by tectonic erosion of the Adria active margin before the onset of the continental collision (Spalla et al. 1996; Roda et al. 2012). On the outer side of PF and PL, in the Helvetic and Southalpine domains units do not record Alpine high-pressure imprints; this indicates that these domains have never been involved in the Alpine subduction system, being exclusively forged during the Alpine evolution at shallow crustal levels (*e.g.* Spalla et al. 2014; Zanchetta et al., 2015).

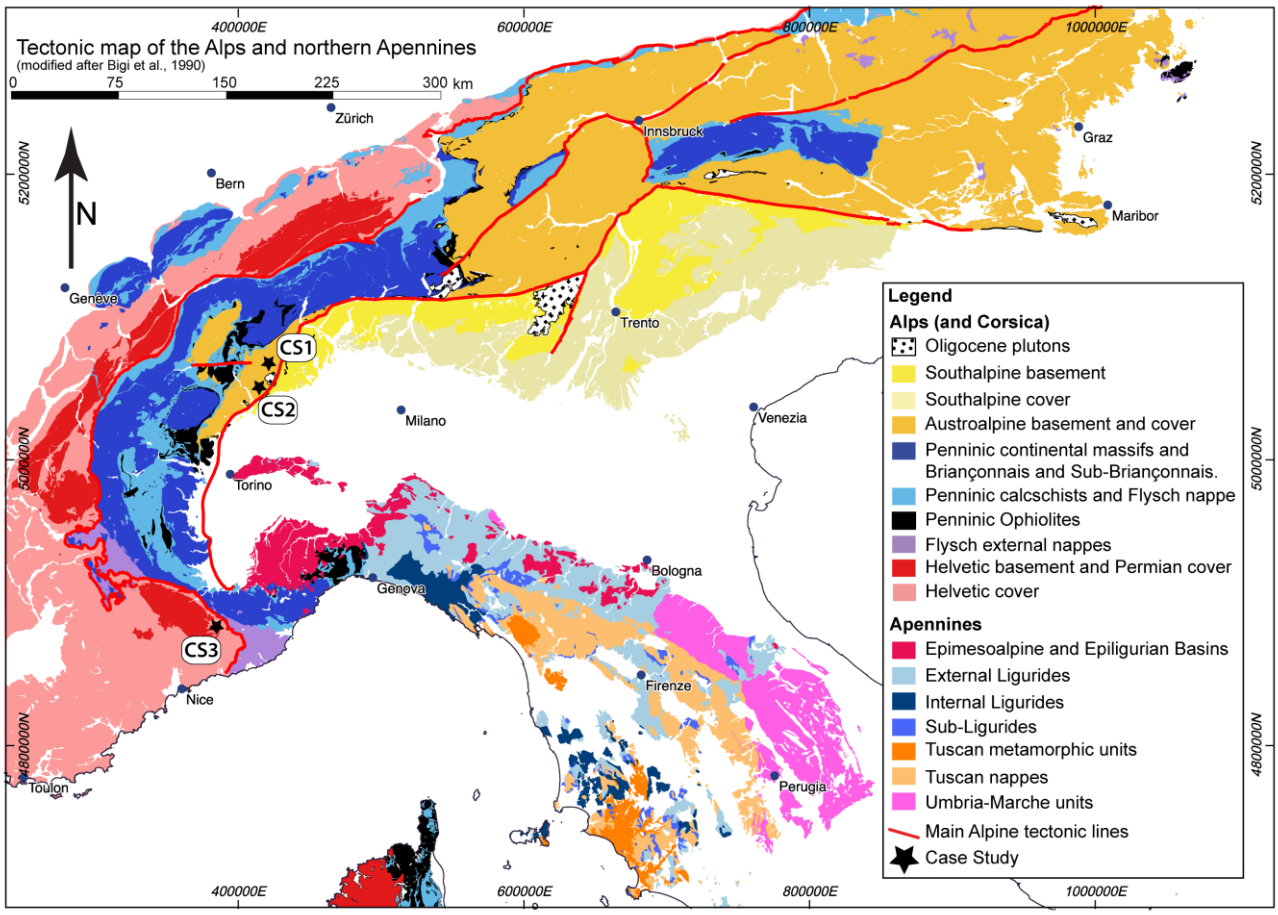

Figure 2.1. Tectonic map of the Alps, northern Corsica, and Northern Apennines with lengend modified after Bigi et al. (1990) and Gosso et al. (2019). Reference system: WGS 84 / UTM zone 32N. The case studies (CS) are located (black stars).

2.1.1 Austroalpine domain

The Austroalpine domain is subdivided into two sectors (Western and Eastern), based on contrasting size, structural position, metamorphism and the deformation ages (Tricart, 1984; Avigad et al., 1993; Stampfli et al. 2002; Dal Piaz et al. 2003; Bousquet et al., 2004; Rosenbaum and Lister, 2005). These mainly continental crustal nappes represent the former southern passive margin of the Alpine Tethys.

The Western Austroalpine domain consists of the Sesia-Lanzo Zone (SLZ) and numerous external klippen traditionally grouped in the Dent-Blanche System (DBS) (Berthelsen, 1992; Ballevre et al., 1986; Cortiana et al., 1998; Dal Piaz et al., 2003). These continental units override or are tectonically interleaved with the ophiolitic Piedmont zone, the major remnant of the Mesozoic ocean (Tricart and Schwartz, 2006; Dal Piaz et al. 2003; Beltrando et al. 2014). SLZ and DBS, which they preserve structural and metamorphic pre-Alpine relicts, record Late Cretaceous alpine metamorphism in eclogite to lower blueschist facies conditions and have been juxtaposed together with Penninic units during the subduction-exhumation processes (Dal Piaz et al. 2003; Manzotti et al. 2014). Eclogite facies metamorphism in the SLZ is dated at ca. 85-65 Ma (Duchêne et al. 1997; Rubatto et al. 1999; Cenki-Tok et al. 2011) and followed by blueschist facies overprint dated at 60 Ma (Babist et al. 2006). The contact metamorphic aureoles around 31 Ma and shallow depth intrusives (Biella and Traversella plutons) indicates that the SLZ was cooled, under greenschist facies condition, before 31 Ma (Zanoni et al. 2010; Berger et al 2012). The age of eclogite facies metamorphism in the DBS is contrasting at 75 Ma in the Pillonet klippe (Cortiana et al., 1998); in the Emilius, Etirol-Levaz and Glacier-Refray klippen is dated at ca. 55-40 Ma (Dal Piaz et al. 2003). The age of metamorphic peak, under blueschist facies condition, is dated ca. 36-48 Ma (Cosca et al., 1994).

The Eastern Austroalpine is a gigantic pile of cover and basement nappes, which extends from the Swiss/Austrian border to the Pannonian basin (Dal Piaz et al. 2003; Janak et al., 2004). The Engadine, Tauren, and Rechnitz tectonic windows expose the ophiolitic units of the Penninic domain and attest the allocthony of the surrounding Austroalpine units. To the north, the Austroalpine overrides the outer-Penninic Rheno-Danubian flysch belt; to the south, it is juxtaposed to the Southern Alps along the Periadriatic lineament (Schmid et al., 1989; Dal Piaz et al. 2003). The Eastern Austrpalpine displays an eclogitic to Barrovian metamorphism dated as early-mid Cretaceous (Ratschbacher 1989; Miller et al., 2005) and the principal tectono-metamorphic history of the Eastern Austroalpine is older (pre-Late Cretaceous) than that of the Western Austroalpine (Late Cretaceous-Eocene) (Janak et al., 2004).

2.1.2 Penninic domain

The Penninic domain groups the oceanic and continental units, which issued from the proximal European continental margin and the Mesozoic ocean (Dal Piaz et al. 2003). In the Western Alps, the Penninic domain includes, from top to bottom: i) the ophiolitic Piedmont zone; ii) the continental Internal Crystalline Massifs (ICM): Dora-Maira, Grand Paradiso, and Monte Rosa; iii) the Grand St. Bernard (Brianconnais) multinappe system; iv) the Ossola-Tessin window, and the Valais zone, including ophiolitic units and/or flysh decollement nappes, bounded by the Penninic frontal thrust (Polino et al., 1990; Handy et al., 2010).

In the Central Alps, the Ossola Tessin window is overlain, to the east, by the Tambò and Suretta continental units, and capped by the Malenco-Avers ophiolite, Margna nappe, and Platta ophiolite (Mancel and Merle, 1987; Marquer et al., 1996; Dal Piaz et al. 2003). In the Eastern Alps, the Penninic domain is mainly exposed in the Engadine, Tauren, and Rechnitz windows. In Central-Eastern Alps, the Penninic domain is represented by the nappe system of San Bernardino, exposed in the tectonic windows of Ossola-Ticino, Engadine, Tauren, and Rechnitz; they consist of metasedimentary cover derived from Triassic carbonate to evaporitic sequences; Jurassic limestones and clastic deposits of debated age (Permian vs Cretaceous) and crystalline basement representing monocyclic units (mainly from Permian intrusives) and polycyclic units with Variscan and older tectono-metamorphic reworking (von Raumer et al., 2003).

These ophiolitic complexes are characterized by eclogitic to blueschist facies metamorphism. An intense Alpine metamorphic imprint characterizes the entire domain: the Penninic basement in Western Alps display eclogitic metamorphism of Eocene age (Lardeaux 2014; Dal Piaz et al. 2003). In contrast, the continental units exposed in the Tauren window are dominated by a greenschist to amphibolite facies Barrovian overprint that obliterated most of the previous high-*P* paragenesis (Dal Piaz et al. 2003).

2.1.3 Helvetic domain

The Helvetic domain consists of Hercynian crystalline basement and related cover units. The Variscan basement is exposed in the External Crystalline Massifs (ECM) such as the Argentera-Mercantour, Pelvoux-Belledonne, Aiguilles Rouges-Mont Blanc, and Aar-Gotthard Massifs.

These massifs consist of polymetamorphic basement with ages even older than Variscan ages, covered by a thick sedimentary sequence of Late Carboniferous to Oligocene ages (Marotta and Spalla 2007).

The Helvetic domain was strongly deformed from the Late Oligocene, when the orogeny propagated to the distal European margin (Dal Piaz et al. 2003). The pattern of rifting faults was largely reactivated

and inverted (Stampfli et al. 2002). Basement and cover units were accreted in front of the exhumed Austroalpine-Penninic collisional wedge, below the Pennininc frontal thrust, and partly recrystallized in anchizone (sedimentary cover) to greenschist, locally amphibolite facies conditions (southern Gotthard), without traces of subduction metamorphism (Lardeaux 2014; Dal Piaz et al. 2003).
In Eastern Alps, the Helvetic domain is reduced to some decollement cover sheets discontinuously exposed in front and below the Rheno-Danubian flysch belt (Dal Piaz et al. 2003).

2.1.4 Southern Alps

The Southern Alps are the typical example of a deformed passive continental margin well exposed and represents the south-verging portion of the Alpine chain. Starting from the Cretaceaous and until the Oligocene, the Adriatic domain was the gently deformed retro-wedge of the Alps (Zanchetta et al., 2015), intensively reworked only at its eastern edge by the Paleogene SW-vergent Dinaric belt. From the Neogene, the Southalpine thrust-and-fold belt developed and progressively propagated towards the Padane-Adriatic foreland, reactivating rifting faults (Castellarin et al. 2006; Carminati et al. 2010). Its front is mainly buried beneath the alluvial deposits of the Po Plain and sealed by Late Pliocene or Quaternary deposits. To the north, the Southern Alps are bounded by the Periadriatic lineament (Dal Piaz et al. 2003).
The Alpine exhumation exposed a plutonic complex of rocks from intermediate to mafic compositions, which have intruded into the deep pre-Alpine continental crust during the Permian (Zingg et al. 1990). This magmatic complex derived from partial melting of the sub-continental mantle and can be found at the base of the crust as a result of a density and viscosity contrast with the lithospheric mantle below (Peressini et al. 2007). The Alpine metamorphic imprint is not pervasive and is characterized by localized metamorphism under greenschist facies conditions, testifying the shallow tectonic evolution of this domain (Dal Piaz et al. 2003).

2.3 The Sesia-Lanzo Zone

The Sesia-Lanzo Zone (SLZ) belongs to the Austroalpine domain of the Western Alps that recorded a pervasive Alpine HP metamorphism (Compagnoni 1977) and thus it is interpreted as a subducted slice of the Adria continental margin (Polino et al., 1990). The SLZ is now bounded by relicts of the Ligurian-Piemontese Tethys to the north and by the Periadriatic lineament to the south, which separates the SLZ form the Southern Alps (Delleani et al. 2013).
During the Alpine subduction, the SLZ has been tectonically eroded from the continental margin of the upper plate Adria and then subducted up to 60 km depth. During the Cretaceous the SLZ registered a

pervasive metamorphic imprint under eclogite facies conditions (Lardeaux, 2014), followed by a re-equilibration under blueschist conditions compatible with an exhumation during the subduction of oceanic lithosphere (Spalla et al. 1996; Gosso et al. 2010). Afterwards, it was partially affected by a greenschist facises event, associated with the exhumation to the uppermost part of the Cenozoic nappe stack (Duchêne et al. 1997; Zucali et al. 2002).

On the basis of its lithological composition and dominant metamorphic imprint, the SLZ has been classically subdivided into two tectonic units named upper and lower unit. The upper unit or the "II Zona Dioritico-Kinzigitica" (IIDK) was not re-equilibrated in eclogite-facies conditions during the Alpine convergence and widely preserves the pre-Alpine high temperature-low pressure (HT-LP) metamorphic imprints. The IIDK is principally composed of metapelites and metabasites characterized by a dominant pre-Alpine metamorphic imprint under amphibolite/granulite-facies condition (the so-called kinzigitic complex (Compagnoni 1977) with minor metagranitoids and few slices of mantle peridotite (Compagnoni 1977; Delleani et al. 2013). The Alpine metamorphic evolution is polyphasic and displays a pervasive re-equilibration under greenschist-facies conditions that partly obliterates the bluschist-facies mineral assemblages (Delleani et al. 2013). The lower unit is subdivided into three metamorphic complexes that record a pervasive Alpine metamorphic imprint (Zucali 2011 and refs. therein): the Eclogitic Micaschists Complex (EMC); the Gneiss Minuti Complex (GMC) and the Rocca Canavese Thrust Sheet (RCTS) (Pognante 1989) where a lawsonite blueschist-facies metamorphic imprint characterizes the peak stage (Zucali & Spalla 2011).

The EMC and the GMC complexes have been eclogitized during the Alpine subduction, but only the first preserves the eclogitic imprint as dominant, whereas the second shows a pervasive Alpine retrogression under greenschist-facies conditions (Spalla et al. 1983; Delleani et al. 2013). The EMC and GMC rocks include metapelites, paragneisses, metagranitoids, metabasites, and impure marbles with an Alpine polyphasic deformation under eclogite-facies conditions, followed by retrogression under blueschist- to greenschist-facies conditions (Compagnoni 1977; Lardeaux et al. 1982; Pognante & Spencer 1991; Zucali & Spalla 2011; Delleani et al. 2013). The exhumation of this portion of SLZ to shallow structural levels (low-pressure, greenschist-facies conditions) was accomplished before the emplacement of the Cenozoic intrusive bodies of Biella and Traversella, as evidenced by the development of HT-LP contact mineral assemblages that overprint the greenschist-facies and late-Alpine parageneses (Zanoni et al. 2010).

The upper unit (IIDK) consists of an association of high grade metapelites, silicate marbles, amphibolites, and granulites displaying evidence of partial melting (kinzigite) and in which pre-alpine high temperature assemblages are preserved (Lardeaux & Spalla 1991; Dal Piaz 2010; Manzotti et al. 2014), showing an upper amphibolite to granulite facies conditions metamorphism. *P*-*T* estimates

indicates pressures of 6-8kbar and temperature of 700-850°C (Lardeaux et al. 1982; Lardeaux & Spalla 1991). The lower unit consists of high-grade gneisses, amphibolites, granulites, marbles, and intrusive rocks. Relicts of pre-Alpine HT metamorphism are found in the EMC such as HT assemblages in amphibolites of central EMC (Lardeaux et al. 1982; Gosso et al. 2010), in metapelites of the Monte Mucrone area (Compagnoni 1977), and whitin the Biella pluton aureole (Zanoni 2016). Metapelites, outcropping in IIDK, are characterized by the development of a penetrative foliation under amphibolite facies conditions, followed by a granulitic overprinting (Lardeaux & Spalla 1991). In these rocks *P-T* estimates indicate an early metamorphic imprint at 7-9 kbar and 700-800°C (Lardeaux & Spalla 1991) and dated at ca. 280Ma (Pin & Sills 1986), followed by a re-equilibration stage at ca. 240-230 Ma (Schmidt et al. 1987) at 4-5 kbar and 560-630°C (Lardeaux & Spalla 1991).

The intrusive rocks, costituted by gabbros and granitic to granodioritic bodies intruded in the HT basement, are diffuse in the SLZ but are most common in the north of Aosta valley, between Monte Mucrone, Lago della Vecchia, Gaby-Gressoney Valley, and the Sesia Valley (Compagnoni 1977).

In the SLZ, geochronological data for Monte Mucrone granite indicate 286±2 Ma (Braun et al. 2007), 293±3 Ma (Bussy et al. 1998), 297±18 Ma (Rubatto et al. 1999), and 287±7 Ma (Cenki-Tok et al. 2011). The Cima di Bronze gabbro is dated 352±8 Ma (Rubatto et al. 1999), Ivozio gabbro display ages of 355±9 Ma (Rubatto et al. 1998), and Sermenza gabbro is dated 288±4 Ma (Bussy et al. 1998). Older metaintrusive rocks have been found in the Tavagnasco and Montestrutto areas and display monzogranitic silica-poor compositions. U/Pb radiometric method indicates ages of 435±8 Ma and 396±21 Ma (Liermann et al. 2002).

Therefore, the Alpine metamorphism and deformation are recorded heterogeneously between the different units, but even within them heterogeneity can be mapped (Zucali et al. 2002). In IIDK large volumes of rock preserves pre-Alpine structures. In EMC rock volumes are undeformed during the Alpine evolution: the Monte Mucrone and Lago della Vecchia metagranitoids preserve a magmatic texture and igneous minerals (Zucali et al. 2002; Zucali 2011; Delleani et al. 2013; Corti et al., 2017). In GMC only HP relicts survived the pervasive greenschist fabric (Zucali et al. 2002). The amount and duration of strain related to the *P-T* evolution of the different units can therefore vary considerably (Zucali et al. 2002; Zucali & Spalla 2011).

In the EMC an early prograde Alpine blueschist facies metamorphic imprint under *P-T* conditions of P>1.8GPa and T>600°C (Zucali et al. 2002; Zucali & Spalla 2011) and $P \geq 2$ GPa at about 480-580 °C (Delleani et al. 2013) is recorded. Alpine HP eclogitic metamorphic imprint in EMC superimposed at *P-T* conditions of 13-15 kbar and 500-550°C (Compagnoni 1977; Lardeaux & Spalla 1991); 15-20 kbar and 500-600°C (Pognante 1989); P>1.5GPa and T = 500-600°C (Zucali & Spalla 2011). The peak of Alpine metamorphism is followed by a retrogression under blueschist facies conditions at *P-T*

conditions of *P*<1.6 GPa and *T*<450°C (Pognante 1989); *P*<1.5 GPa and *T*<600°C (Zucali et al. 2002); 12.5kbar and 450-550°C (Zucali 2011). The exhumation under greenschist conditions occurred at *P*-*T* of <13 kbar and 450-500°C (Pognante et al. 1987); *P*<0.7 GPa and *T*<350°C (Zucali et al. 2002); 0.15-0.25 GPa and 320-360°C (Regis et al. 2014).

An alternative subdivision for the SLZ has been proposed by several authors: Venturini et al. (1994) identified a Monometamorphic Cover Complex (MCC) located between the EMC and GMC; this complex consists of terrigenous and carbonatic metasediments (Scalaro Unit) associated with mafic rocks and minor Qz-rich metasediments (Bonze Unit). Babist et al. (2006) proposed a subdivision based on the correlation of the structures at regional scale. Rubatto et al. (1999) and Babist et al. (2006) recognized a polymetamorphic evolution in the Bonze unit. Indeed, in the Bonze unit new geochronological data on H*P* assemblages, permitted to identify two distinct H*P* metamorphism episodes (dated respectively ≈79-75Ma and ≈70-65Ma; Rubatto et al. 2011). An innovative subdivision of the inner part of SLZ considers two tectono-metamorphic slices: the Druer and the Fondo slices (Regis et al. 2014). The different *P*-*T*-t paths reconstructed for the Fondo and Druer slices suggest that the two units have followed different trajectories within the subdution channel. In particular, the rocks of the Fondo slice recorded two distinct H*P* events under eclogite facies conditions (see Rubatto et al., 2011), and the Druer slice recorded only one H*P* event (Regis et al. 2014). Fondo and Druer slices show coherent exhumation paths starting from 65Ma, so as to say at the onset of exhumation (Regis et al. 2014).

Comparing the Fondo and Druer slice *P*-*T*-t paths with those reconstructed in other parts of SLZ (see review in Manzotti et al., 2014), it is evident that the structuration of the SLZ is more complex than that proposed in the classical models; this is because several crustal slices showing independent *P*-*T*-t evolutions and may have juxtaposed at different stages of the exhumation.

Recent numerical models (Gerya et al. 2002; Stöckhert and Gerya, 2005; Meda et al. 2010; Roda et al. 2010; Roda et al. 2012) show complex exhumation trajectories of rock volumes that are consistent with natural data suggesting evolutions such as those recording two HP events. Furthermore, the numerical predictions indicate that also contrasting *P*-*T*-t paths result from the flow dynamics into the hydrated mantle channel in which small crustal slices are coupled and decoupled during the subduction and exhumation process. Therefore, the EMC may represent a composite object formed by several sub-units coupled within the mantle wedge; in this view a detailed mapping of the contact of adjacent slices (different tectono-metamorphic units) may suggest shape and dimension of the EMC objects involved in the Alpine subduction systems. Thus, reconstructing the *P*-*T*-t paths of further areas could provide a more accurate interpretation about the movements of the crustal slices involved in the Alpine subduction channel.

Moreover, this finding is in contrast with the general definition of the EMC that according to the classical literature is characterized by a dominant eclogitic tectono-metamorphic imprint. Indeed, the more recent literature shows a dominant retrograde metamorphic imprint under blueschist facies conditions linearly distributed along EMC-strike, such as Cima Bonze, Scalaro village (Babist et al. 2006, Regis et al. 2014), M. Soglio (Pognante, 1989; Spalla and Zulbati, 2003), Val Chiusella (Babist et al. 2006) and M. Croass (Pognante, 1989). All these heterogeneities in the dominant tectono-metamorphic imprint open a question about the actual distribution of the eclogitic tectono-metamorphic imprint and on the complexity of the *P*-*T*-d-t evolution in the EMC. Indeed, the same rock volume preserving the same pervasive metamorphic imprint may record different *P*-*T*-d-t evolution and on the other hand, rock volumes recording different metamorphic imprints may record the same *P*-*T*-d-t evolution (Gosso et al., 2015 and references therein).

2.4 The Argentera Massif

The Argentera-Mercantour External Crystalline Massif is the southernmost of the External Crystalline Massif (Bigi et al., 1990) and it extends in the territories of Cuneo, Nice, and Provence across the Italy-France border. Its highest peak is the Monte Argentera (3297 m). The Argentera Massif consists of migmatized paragneisses, amphibolites, diatexites, and granitoids that registered a polyphasic Variscan metamorphism and are crosscut by the post metamorphic Argentera Massif granite (Corsini, Ruffet, & Caby, 2004; G. V. Dal Piaz, 1993; Latouche & Bogdanoff, 1987). The Alpine history locally affected the Massif whose present structure is the result of the Variscan and Alpine evolutions.

The Argentera Massif consists of two main metamorphic complexes: the south-west Tinée Metamorphic Complex (TMC) and the Gesso-Stura-Vésubie Complex (GSV) (Faure-Muret, 1955; Malaroda et al., 1970; Bogdanoff et al., 1991; Rubatto et al., 2001; Compagnoni et al., 2010; Carosi et al., 2016), which are separated by steeply dipping, NW-SE direction, regional-scale Ferriere-Mollieres Shear Zone (FMSZ) (Faure-Muret, 1955; Compagnoni et al., 2010; Carosi et al., 2016). The FMSZ is inferred as a dextral transpressive shear zone, during Late Carboniferous (*i.e.* 330-310 Ma, Musumeci and Colombo, 2002; Corsini et al., 2004; Simonetti et al., 2018) and successively re-activated during the Alpine cycle (*i.e.* 27-21 Ma, Corsini et al., 2004).

Both complexes experienced eclogite and H*P*-granulite facies metamorphisms followed by a L*P*-granulite/amphibolite-facies re-equilibration, accompanied by migmatite formation, and followed by late tilting of nappe-stack and horizontal shearing (Latouche & Bogdanoff, 1987).

The Tineé Complex has been subdivided into three series (Faure-Muret, 1955): the Varélios-Fougieret metasediments, the Anelle-Valabres-Iglière Formation, comprising mafic granulites, coronitic gabbros

and marbles, and the gneissic Rabouns series. Granitoids are represented by the Igliére metagranodiorites intruded in the Anelle-Valabres-Iglière Formation and by small dykes in the Rabouns Series (Bogdanoff & Ploquin, 1980; Latouche & Bogdanoff, 1987; Malaroda, 1999).

The GSV Complex is constituted by migmatitic Ordovician granitoids banded by paragneisses with boudins of mafic, ultramafic and carbonatic rocks as amphibolites, eclogites, granulites, peridotites, and serpentinites, and marbles (Compagnoni et al., 2010 and references therein). The migmatitic leucosome contains amphibolite facies assemblages due to the dominant metamorphic imprint registered by the GSV constrained at 650-700°C and 0.4-0.6 GPa; anatexites can contain sillimanite and cordierite. The best-preserved mafic bodies outcrop in the localities of Laghi del Frisson, Valle della Meris, and Lago di Nasta. Paquette et al. (1989) proposed two eclogitic metamorphic events at 424 Ma and 351 Ma, whereas Rubatto et al. (2001) described a single H*P*-H*T* metamorphic event (443-332 Ma) or two subsequent eclogitic Ordovician and Devonian H*P*-H*T* events, followed by Variscan amphibolite facies metamorphism, culminated in a widespread anatectic event. In the eastern complex, coarse-grained undeformed cordierite-bearing melts clearly crosscut (Blasi and Schiavinato, 1968; Blasi, 1971) and progressively obliterate the main foliation in biotite and sillimanite-bearing migmatites. The first syn-tectonic partial melting settled in equilibrium with biotite, garnet, and sillimanite and the second post-kinematic, at lower pressure, is in equilibrium with cordierite; this latter event is dated at 323 ± 12 Ma by U/Pb method on zircons (Rubatto et al., 2001). In the GSV complex, a huge granitic body intersects the dominant foliation (Boucarut, 1967; Ferrara & Malaroda, 1969) dated at 292-299 Ma (Malaroda, 1969; Corsini et al., 2004).

The granulitic rocks of Laghi del Frisson and Valle della Meris suggest a granulitic H*P* event at 750-720 °C and 1.5-1.4 GPa followed by re-equilibration during decompression at 710 °C and 1.10 GPa and mylonitic deformation in amphibolite facies conditions at 665 ±15 °C and 0.85 GPa (Compagnoni et al., 2010; Ferrando et al. 2008; Rubatto et al. 2010). The GSV is intruded by Carboniferous-Permian granitoids as the Granito Centrale dell'Argentera and other intrusive bodies of Visean and Stefanian ages. Corsini et al. (2004) dated the Granito Centrale at 296-299 Ma. The crystalline basement is in tectonitic contact with Carboniferous-Triassic sedimentary cover represented by Stefanian black shales and sandstones, and Triassic quartzites, conglomerates, sandstones, and siltstones. The Giurassic sediments comprise dolomites and limestones (Malaroda & Carraro, 1970).

From Carbonifeorus to Lower Triassic time, up to 4000m of siliciclastic sedimentary sequences characterized by wide lateral variations of thickness, were deposed on the basement rocks, followed by evaporites and finally by shallow water limestones of Middle to Upper Triassic ages (Faure-Muret, 1955). Extensional faults have ruled the deposition of both Permian and Triassic beds (Aicard, 1968; Delteil et al. 2003). Although not yet constrained in basement rocks, magmatic activity in the

Argentera Massif area is likely to have been lasting also through the Permian, as testified by riolitic and dacitic volcanoclastics within the sedimentary record (Malaroda et al., 1970; Romain & Vernet, 1978). The following Mesozoic sedimentation was characterized by pelagic and hemipelagic limestones, which occupied a transition zone between the reduced succession, characterizing the Helvetic-Provencal Domain, and the Douphinois (Faure-Muret, 1955). Lower Jurassic deepening successions are witness of the European passive margin development in the southwestern part of the Helvetic-Provencal Domain (Lemoine et al., 1986).

Tectono-sedimentary relationships in the external domains of the southwestern Alps constrain the different stages of the Alpine continental collision, which started concurrently with the deposition of "Priabonian trilogy" in the foreland basin (Ford et al., 1999; Ford & Lickorish 2004). The frontal flexure in the southwestern Alps ceased in the early Oligocene, when internally derived Embrunais-Ubaye nappes were thrusted westward, overcoming the Priabonian sequence (Kerckhove, 1969; Merle and Brun, 1984). Consequently, narrow thrust-sheet-top basins – Dévoluy, Esclangon, Barrême, Saint Antonin basins – formed ahead of the Embrunais-Ubaye nappes (Evans and Elliott, 1999). From this moment forward, the Alpine deformation was localized along the Digne Thrust, a reactivated Lower Jurassic normal fault that intersect regional scale strata of Middle Triassic evaporites, far west of the Argentera Massif (Ford et al., 1999).

The structural setting of the Argentera is the result of the Variscan and Alpine convergences. The regional migmatitic foliation developed during the high grade Variscan metamorphism is NW-SE trending and NW to SE plunging at medium to high angles. The massif is crosscut by different Variscan and Alpine shear zones. In the central part of the massif, the Valletta and the Bersezio Shear Zones (Carosi et al., 2016; Simonetti et al., 2018) are both N150-N160 trending and display a quite vertical pervasive foliation and a dextral strike-slip kinematic (Corsini et al., 2004). The Fremamorta Shear Zone crosscut the entire eastern part of the Argentera massif, affecting the Granito Centrale and up to Triassic metasediments. The Ferriere-Mollières Shear Zone, dated at 327 ±3 Ma, displays dextral strike-slip kinematic. The Alpine deformation caused the reactivation of NW-SE trending shear zones, as the Ferriere-Mollières Shear Zone, while the WNW-ESE lineaments are reactivated as thrust.

The dating of the Alpine-late Alpine tectonic reactivation and new faulting (Corsini et al., 2004; Sanchez et al., 2011 and references therein), suggests that the Argentera Massif exhumation happened between 22 and 8 Ma through strike-slip dextral faults and thrusting. The reactivation of the Pennine Front is younger and dated at 9-4 Ma (Labaume et al. 2008; Sanchez et al., 2011 and references therein).

Chapter 3

Method and techniques

The integration of multiscale structural analysis, 2D estimation of fabric and metamorphism heterogeneities, 3D geological modelling, mineral chemical analysis, X-ray chemical mapping, and X-ray tomography is an innovative approach to quantify the correlation between deformation and metamorphism. In particular, the combined use of the microstructural analysis with EMPA-derived chemical imaging and 3D reconstruction of grains shape distribution through X-ray microtomography allow a quantitative estimation of fabric and metamorphic heterogeneities. Using the mesoscale structural analysis as a reference, the quantitative micro-scale chemical and fabric information obtained from several samples can be extended at km-scale. This is because the multiscale structural analysis allows linking the meso-scopic fabrics with metamorphic assemblages that materializes them. The results obtained are useful to the (1) construction of more reliable 2D/3D km-scale models of structural and metamorphic gradients; (2) define the physical and chemical parameters controlling the fabric evolution, the metamorphic transformation, and their interplay; (3) to improve knowledge on the tectono-metamorphic evolution of active margins.

The following sections show the methodological approach of the multiscale structural analysis to infer the tectonometamorphic evolution of crustal volumes involved in subduction-collision systems and the modern techniques used to quantify the heterogeneous fabric reworking and metamorphic transformation and their relationships in the polydeformed basement.

3.1 Multiscale structural analysis

An effective working method to individuate the volumes recording the same structural and metamorphic evolution is the combined use of structural correlation of mesoscopic deformation features and microstructural analysis to decipher equilibrium metamorphic assemblages supporting transient mapped fabrics that represent the finite doformation accumulated by rocks.

Therefore, an analytical approach able to obtain a more confident tectonic correlation is provided by:

i. Structural maps that display a grid of the foliation trajectories overprinting the lithostratigraphy;
ii. Kinematic compatibilities of all superposed structures at the regional scale, to separate successive deformation stages;

iii. A sampling strategy based on the selection of sites critical to identify the mineralogical support of superposed fabrics in different lithologies and to recognize compatibilities between parageneses formed in different chemical systems;

iv. Cross control of fabric sequences and metamorphic assemblages in adjacent rock volumes that recorded heterogeneously the deformation;

v. Evaluation of mineral chemical variations in microstructural sites located along fabric gradients, from the low- to the high-strain zones;

vi. vi. Thermobarometric estimates on assemblages marking successive fabrics of known relative chronology;

vii. Reconstruction of *P*-*T*-d-t paths.

The contouring of homogeneous fabric domains (coronitic, tectonic, and mylonitic) is facilitated by integrating meso-structural information with microstructural analysis to estimate the degree of fabric evolution and metamorphic transformation in volume percentage.

The low degree of fabric evolution (*i.e.*, coronitic) corresponds to the incipient development of the new fabric and the metamorphic reactions take place without the formation of a new oriented fabric. The medium degree of fabric evolution (*i.e.* tectonitic) corresponds to the differentiation of a new foliation, which can be either a differentiated crenulation cleavage or a pervasive foliation. The high degree of fabric evolution (*i.e.* mylonitic) coincides with the progressive obliteration of the earlier fabrics by complete grain-scale reworking and development of new continuous foliations (Bell & Rubenach, 1983).

Microstructural analysis performed on thin sections strategically distributed throughout the study area allows to a punctual estimation of degree of fabric evolution and metamorphic reation progress for each deformational stage. The fabric evolution is estimated on the basis of the amount of newly formed fabric compared to relic fabrics. The degree of fabric evolution is cathegorized into three groups: Coronite (C) 0-20%; Tectonite (*T*) 21-60%; Mylonite (M) > 60%. The degree of reaction progress reflects the modal proportion of mineral phases, related to a specific deformation phase, as inferred using graphical comparison at optical microscope. Three class have been individuated: Low (L) 0-20%; Medium (M) 21-60%; High (H) > 60%.

Furthermore, microstructural analysis is used to define the relationships between deformation (different strain domains) and mineral growth for each deformation stage to identify equilibrium mineral assemblages in different rock types and strain domains. These constrains are the guide to select mineral compositions and perform *P*-*T* estimates for each superposed fabric and the reconstruction of *P*-*T*-t-d paths.

3.2 3D geological modelling

The integration of data from geological mapping, multiscale structural analysis, and estimations of the degree of fabric evolution and metamorphic reaction progress allow constructuing a 3D quantitative model of structural and metamorphic heterogeneities.

Geomodeller® software allowed a quantitative 3D estimation of domains characterized by homogeneous fabric evolution and metamorphic reaction progress. This software is based on the surface potential-field method to build 3D geological models from geological map, DEM, and structural orientations as data input (Chilès et al. 2004). Each geological interface is treated as an iso-potential surface of a potential-field defined in 3D space. The potential-field interpolation is based on a co-kriging statistical analysis defining the correlation between geological and structural data values as a function of the distances between data points. These distances are calculated using a system of parametric coordinates defined internally to the potential-field (Lajaunie et al. 1997). The software takes into account the iso-potential surfaces (*i.e.* geological interfaces) to compute those distances through an implicit method based on a system of potential-field functions (Calcagno et al. 2008). In details, it is able to model geological bodies integrating the location of geological interfaces (iso-potential data) used as spatial distribution parameters and their structural data orientation (potential gradients) used as anisotropy shape parameters. The combination of these functions allows a full spatial and volumetric description of shapes of geological bodies (Guillen et al. 2011).

The 3D quantification of the relationships between the degree of fabric evolution and metamorphic reaction progress during polyphasic tectono-metamorphic evolution are feasible trough the reconstruction of the boundaries between homogeneous domains using the foliation trajectories map and several cross-sections as structural guide. The location precision of these boundaries varies between 5 and 50 m, depending on the density of the input petro-structural data.

The consistency of the 3D results has been verified by visual inspection, to check the geologically coherent geometries and intersection relationships, plotting the modelled surfaces on the 2D maps and cross-sections in order to verify the model reliability with respect to the input data. The model allows defining the size, shape, and spatial relations of rock volumes showing homogeneous fabric and metamorphic transformation degree. Comparing these models, it is possible to calculate the volumetric misfit between the corresponding homogeneous fabric and metamorphic volumes.

3.3 Chemical imaging and fabric analysis

Three different image processing tools (*i.e.* GSD, Q-XRMA and Min-GSD) have been applied both at the scale of the entire thin section and of the microdomain one. These tools are based on various scripts and functions adopted for images analysis, implemented within the most common GIS software, which have been increasingly used in solving various geoscientific issues (*e.g.*, Li et al., 2008; DeVasto et al., 2012; Pradhan, 2013; Ortolano et al., 2014a, 2014b; Belfiore et al., 2016; Fiannacca et al., 2017; Berrezueta et al., 2019).

The first tool adopted is the Grain Size Detector (GSD - Visalli, 2017). Such tool permits the users to trace a map of polygonal features representative of the grains composing the rock, by processing high-resolution thin section optical scans. In such a way, a database containing several data of grain sizes and shapes (*e.g.* area, axial ratio, orientation with respect the foliation and others) is obtained. With this aim, a 24 bit-depth optical scan has been acquired with a resolution of 4800 dpi via an Epson V750 dual lens system scanner. According to Visalli (2017), the above scan resolution was selected as the best setting for acquiring an image at high quality, reducing, at the same time, the required hard drive space storage and image processing time.

The analytical procedure of the tool is based on the sequential application of four image-processing steps, within the GIS environment: (i) the filtering step, to improve the quality of the input scan, by emphasizing grains boundaries and reducing noise; (ii) the image segmentation step, required to distinguish, select and extract boundaries of different grains; (iii) the vectorization step, needed to create polygon features that trace the original grains of the thin section; and, finally, (iv) the quantification step, useful to calculate grains sizes and shapes parameters.

The second tool applied is the Quantitative X-Ray Map Analyzer (Q-XRMA - Ortolano et al., 2018). In this case, users are able to classify rock-forming minerals starting from an array of X-ray maps as well as to calibrate these maps for deriving pixel-based chemical data and end-member fraction maps, by using a sufficient number of spot chemical analyses as internal standards (De Andrade et al., 2006). With this aims, major element X-ray maps (*i.e.*, Al, Ca, Cr, Fe, K, Mg, Mn, Na, Si, Ti) of the entire thin section (c. 38∗20 mm) have been acquired using a JEOL 8200 electron microprobe equipped with five WDS spectrometers located at the Department of Earth Science, University of Milan. Operating conditions were 160 ms dwell time, 15 kV accelerating voltage and a probe current of 100 nA. A spatial resolution of about 60 μm in both x and y directions was used for acquiring an image with a resolution of 360x610 pixels. Spot chemical analyses used as internal standards to calibrate X-ray maps were performed using the JEOL 8200 EMPA. Operating conditions were: ~1 μm beam spot, 15 kV accelerating voltage, and 5 nA beam current. Natural minerals and synthetic oxides were used as

standards. The analytical procedure of the Q-XRMA tool is subdivided into three different cycles: i) the first cycle consists of various stages implying a multivariate statistical data handling of the X-ray maps, based on the sequential application of the Principal Components Analysis (PCA) and the supervised Maximum Likelihood Classification (MLC) (Ortolano et al., 2014b). As a result, users can distinguish mineral phases constituting the analyzed thin section/microdomain as well as extrapolate the associated modal percentages; ii) the second cycle comprises two sub-procedure allowing to perform, on one hand, an in-depth analysis of a selected phase identified during the first cycle for detecting occurrences of sub-phases (*e.g.* mineral zoning) and, on the other hand, to calibrate native X-ray maps through a multiple linear regression algorithm. In this last case, the element concentrations values (expressed as atoms per formula unit, a.p.f.u) can be predicted for each pixel representative of a specific investigated mineral phase; iii) the third cycle permits users to manage the calibrated X-ray maps obtained during the second cycle, for constructing maps of end-member proportions as well as quantifying chemical variations within the investigated phases.

The third tool adopted is the Mineral Grain Size Detector (Min-GSD - Visalli, 2017). This tool allows users to merge together the outputs of the GSD and Q-XRMA in order to label each grain polygon feature with the appropriate mineral name, as the GSD tool alone is not capable to make any division between grains of the same/different minerals, unless the user manually renames each polygon. The analytical procedure requires the sequential application of three different steps: (i) a preliminary manual georeferencing stage, in ArcGIS® environment, between the GSD and Q-XRMA outputs. This is in order to ensure a valid overlap between the two images; (ii) a raster to point conversion of the Q-XRMA output, with the aim to convert each classified pixel in point feature storing the datum of the mineral name; and finally, (iii) a spatial join operation between the GSD output and the Q-XRMA point converted image in order to attach the correct mineral name to each polygon feature. In this view, the tool calculates the highest frequency of the pixels having the same label enclosed within a polygon.

3.4 X-ray computed microtomography

X-ray computed microtomography (µ-CT) is a nondestructive technique based on the 3D mapping of the X-ray attenuation coefficient across the investigated sample (Baruchel et al., 2000). Using X-ray µ-CT based on a cone-beam geometry it is possible to achieve a maximum spatial resolution close to the focal spot size of the microfocus X-ray source. Moreover, it has been demonstrated (Wilkins et al., 1996) that by using a tomographic instrument based on a microfocus source, it is possible to take advantage of phase-contrast effects at the edges of the different features present within the sample volume. This could allow to improve the contrast and spatial resolution in the images, obtaining sharper borders of the sample features and detecting details smaller than the pixel size of the detector (Mancini, 1998). Phase-contrast X-ray µ-CT measurements based on synchrotron and microfocus X-ray sources applied in the Earth science domain represent a powerful tool for the non-destructive characterization of the internal microstructures and the mineral phases separation thanks to their different density and/or chemical composition (Ketcham and Carlson, 2001; Ketcham, 2005; Zandomeneghi et al., 2010; Polacci et al., 2010; Baker et al., 2012; Cnudde and Boone, 2013). Through virtual slicing of the sample volume and applying image processing and analysis 3D tools, it is possible to achieve a quantitative shape preferred orientation (SPO) analysis by means of the geometrical, morphological, and orientation parameters extraction (Voltolini et al., 2011; Zucali et al., 2014).

Phase-contrast X-ray µ-CT data have been acquired on centimeter-sized samples at the TomoLab station at the Elettra synchrotron facility in Basovizza (Trieste, Italy). This station is equipped with a sealed microfocus source (Hamamatsu, Japan), which guarantees a minimum focal spot size of 5 µm. For each sample, a set of 2400 projections was acquired over a total scan angle of 360°. A water-cooled, 12-bit, 4008 x 2672 pixels CCD camera (Photonic Science, UK) was used as detector applying a 2x2 binning to the pixels. Scanning acquisition conditions were: Voltage = 130 kV, current = 61 nA, filter = 1.5 mm of Al, exposure time per projection = 6.5 sec, source-to-sample distance = 220 mm and source-to-detector distance = 311 mm. The reconstruction of the tomographic slices was done using the commercial software COBRA (Exxim, USA) with an isotropic voxel size of 17.7 µm. The reconstructed slices were visualized by using the freeware ImageJ (Schneider et al., 2012), while the 3D visualization, through volume rendering procedure, was obtained by the Pergeos software. PerGeos software allows the mineral quantification through user-friendly 3D visual imaging and mineral phases segmentation by mapping gray value to specific colors. To reduce imaging noise, the reconstructed µ-CT data was pre-filtered using variance weighted mean filter (noise variance = 400, radius = 2 pixels; Gonzalez & Woods, 2002). Prior to the volume data processing, we crop out a sub-volume (VOI:

Volume of Interest) suitable for the analysis to avoid the dark background masking the slices with respect to the outer region of the sample. The mineral phases are separated from each other using 3D Marked-Watershed segmentation (MBW; Meyer & Beucher, 1990). The algorithm is based on semi-automatic thresholding, where the boundary between minerals is defined by using the gradient function (*i.e.*, the local deviation) as the grey-values delimiters. The material to be segmented is marked using the manual Interactive Overlay Thresholding function seeded with local maxima of distance map. During the procedure it is possible to have areas with multiple adjacent local maxima. This issue can be minimized taking only the largest local maxima (Sayab et al., 2017). The MBW algorithm then expand the seeded markers over the related mineral phases using a landscape function which is defined by the gradient volume (*i.e.*, active contours algorithm). Once the segmentation is achieved post-segmentation filtering was needed to improve the edge preservation and to remove the background voxels. The filtering was retained to a minimum level to preserve the shape of the objects. In this view, we used the closing procedure for avoid dark "unclassified" voxels (Sayab et al., 2015). Thanks to this imaging analysis it is possible to separate different mineral classes refletting different X-ray attenuation. The 3D grain size distribution and the shape preferred orientation (SPO) analysis for each mineral phase have been calculated along with the entire rock volume and for each XY plane thanks to the Separate Object procedure using the Skeleton algorithm. Through the labeling tool it is possible to extract the useful parameters, *i.e.* length, width, volume, orientation angles, eigenvalue, and eigenvector, for each object.

Chapter 4

First case study: Lago della Vecchia area

4.1 Analysis of fabric evolution and metamorphic reaction progress

The following sections refer to the published paper: Corti L., Alberelli G., Zanoni D. and Zucali M. (2017): Analysis of fabric evolution and metamorphic reaction progress at Lago della Vecchia-Valle d'Irogna, Sesia-Lanzo Zone, Western Alps. Journal of Maps, v. 13, p. 521-533, doi: 10.1080/17445647.2017.1331177.

Abstract

The Lago della Vecchia-Valle d'Irogna rocks are part of the Eclogitic Micaschists Complex (EMC) of the Sesia-Lanzo Zone, western Austroalpine domain. The 1:10,000 scale map includes metaintrusive, minor micaschist, banded gneiss, and metabasic boudins. The multiscale structural analysis reveals successive magmatic and tectono-metamorphic stages: during M0 the metaintrusive protoliths emplaced; D1 took place under eclogite-facies conditions; during D2 stage, a pervasive foliation developed under retrograde blueschist-facies conditions; D3-D4 and D5 structures developed under greenschist-facies conditions; during M6 andesitic dykes intruded. The mapped degree of fabric evolution (FE) and metamorphic transformation (MT) related to D2-foliation shows that the metamorphic transformation was not controlled only by bulk rock and mineral compositions, but also by fabric evolution. The development of a pervasive blueschist-facies D2-foliation is in contrast with the eclogitic dominant fabric generally recorded in the EMC. This difference suggests that FE and MT are potentially responsible for km-scale heterogeneities in the tectono-metamorphic record.

Keywords: multiscale structural analysis; fabric evolution; metamorphic transformation progress; petro-structural mapping; blueschist-facies condition; Austroalpine.

4.1.1 Introduction

Within convergent margins, the coupling and uncoupling of lithospheric slices are responsible for the tectonic architecture of metamorphic belts (*e.g.* Spalla, Gosso, Marotta, Zucali, & Salvi, 2010). The lithospheric slices can be recognized as tectono-metamorphic units once their tectonic and metamorphic history is proved homogeneous over a defined time interval (Spalla, Zucali, di Paola, &

Gosso, 2005). Petro-structural mapping and multiscale structural analysis are crucial to characterize the tectono-metamorphic evolution of lithospheric slices and the relationships between degree of fabric evolution (FE) and metamorphic transformation (MT). In particular, the relationship between fabric evolution and metamorphic reaction progress with the development of dominant (*i.e.* pervasive) fabric can be used to investigate the complexity of convergent dynamics (*e.g.* Salvi, Spalla, Zucali, & Gosso, 2010; Gosso et al., 2015). Adjacent rock volumes characterized by the same dominant fabric may record different tectono-metamorphic histories. On the contrary, adjacent rock volumes showing dominant fabrics developed under different metamorphic conditions may record the same tectono-metamorphic history due to heterogeneous registration of the superposed deformation and metamorphic stages (Spalla et al., 2005). In order to evaluate whether rock volumes record the same tectono-metamorphic history, mapping petro-structural heterogeneities in adjacent rock volumes is crucial (*e.g.* Zucali, Spalla, & Gosso, 2002; Salvi et al., 2010; Delleani, Spalla, Castelli, & Gosso, 2012; Delleani, Spalla, Castelli, & Gosso, 2013; Gosso et al., 2015). Since deformation heterogeneity commonly affects crystalline basements (*e.g.* Myers, 1970; Mørk, 1985), the field structural correlation exclusively grounded on geometric criteria is poorly reliable, because of spatial variations in deformation style (Spalla et al., 2010). During incremental deformation related to a specific stage, rock volumes may escape deformation (coronite) or may be partially (tectonite) or pervasively (mylonite) deformed (Lardeaux & Spalla, 1990). In coronitic (low strain) domains, metamorphic reactions take place without formation of a new oriented fabric. Where the strain is accumulated, tectonitic and mylonitic fabric develop in intermediate and high strain domains, respectively. In the last two cases metamorphic assemblages define normal planar/linear tectonites or mylonites (Spalla et al., 2010; Zucali et al., 2002; Salvi et al., 2010; Gosso et al., 2015). Therefore structural correlation in metamorphic basements has to be based on a coherent sequence of tectono-metamorphic stages. Heterogeneous partitioning of deformation makes this correlation difficult, but allows the preservation of structures and related metamorphic assemblages that can be used to trace back the tectono-metamorphic history (Spalla et al., 2010).

In this work, we combined geological mapping and multiscale structural analysis to produce a petro-structural 1:10,000 scale map of FE and MT and investigate the tectono-metamorphic history of the EMC at Lago della Vecchia-Valle d'Irogna (upper Cervo valley, Biella, Sesia-Lanzo Zone). The study area consists of metaintrusive, minor micaschist, banded gneiss, cataclastic-mylonitic gneiss, and numerous decimeter-sized metabasic boudins and lenses. These rocks preserve Alpine superimposed fabrics that developed under metamorphic conditions varying between eclogite to greenschist facies. The map covers an area of 7.5 km^2 where strain partitioning in metaintrusive led to the preservation of igneous texture and magmatic minerals in coronitic domains wrapped by tectonitic and mylonitic

foliations. The presented interactive map shows the Alpine superimposed structures and the associated metamorphic assemblages by means of foliation trajectories indicated with different colors (panel 1 and panel 2 of interactive map) and the relationships between degree of fabric evolution (panel 3 of interactive map) and degree of metamorphic transformation (panel 4 of interactive map) for the dominant deformational stage. Mineral abbreviations are as in Kretz (1983) with the exception of Wm (white mica), Amp (amphibole), and Op (opaque minerals).

4.1.2 Geological setting

The Sesia-Lanzo Zone (SLZ) represents the largest portion (~90 x 20 km) of Austroalpine continental crust that has been eclogized during the Alpine subduction and now exposed in the axial zone of the Western Alps (Dal Piaz, Hunziker, Martinotti, 1972; Compagnoni et al., 1977; Venturini, Martinotti, Armando, Barbero, & Hunziker, 1994; Zucali et al., 2002; Babist, Handy, Konrad-Schmolke, & Hammerschmidt, 2006; Delleani et al., 2013; Lardeaux, 2014; Manzotti, Ballèvre, Zucali, Robyr, & Engi, 2014; Regis et al., 2014). The SLZ is bounded by rocks of the Penninic domain to the northwest, and the Canavese Line (Periadriatic Line) to the southeast, which separates the SLZ from the Southern Alps (Fig. 4.1.2A).

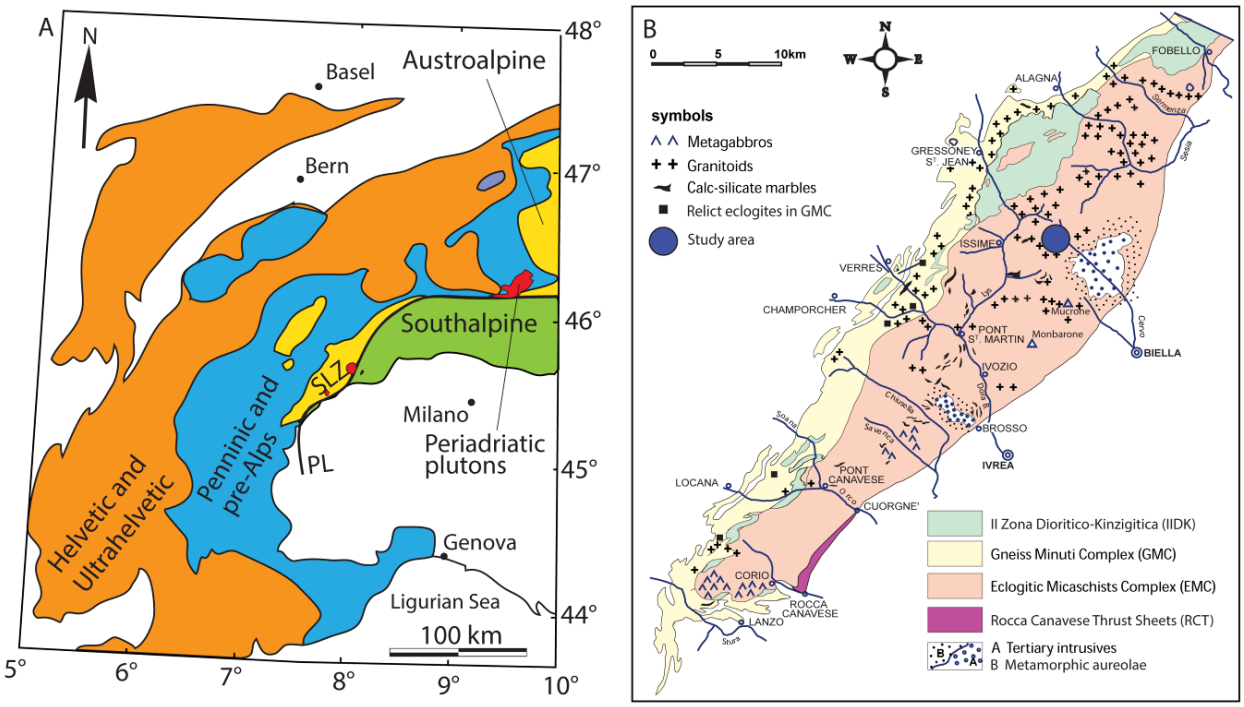

Figure 4.1.2. Geological outline of the Sesia-Lanzo Zone. (A) Simplified tectonic map of the Western Alps. SLZ: Sesia-Lanzo Zone. PL: Periadriatic Line (modified from Handy et al., 2005). (B) Tectonic map of the Sesia-Lanzo Zone with the location of the study area (modified from Compagnoni et al., 1977; Passchier et al., 1981; Spalla & Zulbati, 2003).

The SLZ is classically divided into four main complexes (Fig. 4.1.2B; Compagnoni et al., 1977; Gosso, 1977): (1) the II Dioritic-Kinzigitic Zone (IIDK) preserves a pervasive pre-Alpine H*T* metamorphic imprint; (2) the Gneiss Minuti Complex (GMC) and (3) the Eclogitic Micaschists Complex (EMC) display a dominant Alpine metamorphic imprint and locally preserve pre-Alpine H*T* relicts (Compagnoni et al., 1977; Lardeaux, Gosso, Kiénast, & Lombardo, 1982; Gosso, Messiga, Rebay, & Spalla, 2010; Manzotti et al., 2014; Zanoni, 2016); (4) the Rocca Canavese Thrust Sheets is characterized by a blueschist Alpine imprint with no eclogite facies relicts (Pognante, 1989; Spalla & Zulbati, 2003; Cantù, Spaggiari, Zucali, Zanoni, & Spalla, 2016). The EMC and GMC consist of metapelite, paragneiss, metagranitoid, metabasite, and impure marble recording Alpine polyphasic deformation and eclogite facies peak conditions. The peak conditions are represented by the dominant fabric in EMC and by relict domains in GMC (Pognante, Compagnoni, & Gosso, 1980; Stünitz, 1991; Spalla, Lardeaux, Dal Piaz, Gosso, & Messiga, 1996; Tropper & Essene, 2002; Zucali et al., 2002; Spalla & Zulbiati 2003; Spalla et al., 2005). Eclogite facies metamorphism is dated around 85-65 Ma (Cenki-Tok et al., 2011; Rubatto et al., 2011; Regis et al., 2014) and occurred at conditions of 13-20 kbar and 500-600°C (Compagnoni et al., 1977; Pognante, Talarico, Rastelli, & Ferrati, 1987; Lardeaux & Spalla, 1991; Zucali et al., 2002). Peak conditions were followed by retrogression under blueschist facies conditions (Spalla, De Maria, Gosso, Miletto, & Pognante, 1983; Pognante, 1991; Spalla, Lardeaux, Dal Piaz, & Gosso, 1991; Babist et al., 2006; Zucali & Spalla, 2011; Delleani et al., 2013; Giuntoli & Engi, 2016) dated ~60Ma and occurred at $P < 15$ kbar and $T = 450$-550°C (Zucali et al., 2002; Zucali, 2011; Regis et al., 2014). Finally, the greenschist re-equilibration occurred at $P < 8$ kbar and $T < 350$°C before 30Ma (Zucali et al., 2002; Babist et al., 2006; Zanoni, Spalla, & Gosso, 2010). The exhumation was accomplished during subduction of the Alpine Tethys lithosphere (Polino, Dal Piaz, & Gosso, 1990; Spalla et al., 1996; Gosso et al., 2010; Roda, Spalla, & Marotta, 2012). Some authors (Pognante, 1989; Ramsbotham, Inger, Cliff, Rex, & Barnicoat, 1994; Venturini, 1995; Babist et al., 2006; Regis et al., 2014; Giuntoli & Engi, 2016) found evidence of a strong blueschist to greenschist facies retrogression within EMC, thus testifying a heterogeneous record of the tectono-metamorphic stages. On this ground, Regis et al. (2014) interpreted the SLZ as represented by a composite unit that can be divided into several slices with different pre-Mesozoic lithologies and Alpine tectono-metamorphic evolutions: (1) the Druer slice represents the southeastern portion of SLZ and mainly consists of micaschist and minor metabasite and metagranitoid with a pervasive Alpine eclogite-facies metamorphic imprint; (2) the Intermediate Unit and GMC, in the northwestern portion of SLZ, mainly consist of fine-grained gneiss with dominant retrograde blueschist to greenschist facies assemblages; (3) the Fondo slice is a thin and discontinuous layer of Mesozoic metasediment with subordinate metabasite interposed between Druer slice and GMC-Intermediate Unit. This slice

registered two successive Alpine metamorphic imprints under eclogite to blueschist facies conditions followed by a greenschist facies overprint; (4) the IIDK has the characteristics classically described.
The Lago della Vecchia-Valle d'Irogna area is located within the EMC (Figure 4.1.2B), in the Intermediate Unit according to the classification of Regis et al. (2014), just to the north of the Oligocene Biella pluton, far from its contact aureole (Romer, Schärer, & Steck, 1996; Zanoni, Bado, Spalla, Zucali, & Gosso, 2008; Berger, Thomsen, Ovtcharova, Kapferer, & Mercolli, 2012; Zanoni, 2016).

4.1.3 Mapping method and analytical techniques

The mapping strategy used here required mesoscale and microscale structural analysis to constrain metamorphic assemblages marking different fabrics and crystallized at different times (Passchier, Myers, & Kroner, 1990; Spalla, Siletto, di Paola, & Gosso, 2000; Zucali et al., 2002). Mesoscale structural analysis aims recognizing strain gradients, continuously followed in the field, that are classified in terms of coronitic, tectonitic, and mylonitic domains (Figure 4.1.3A).

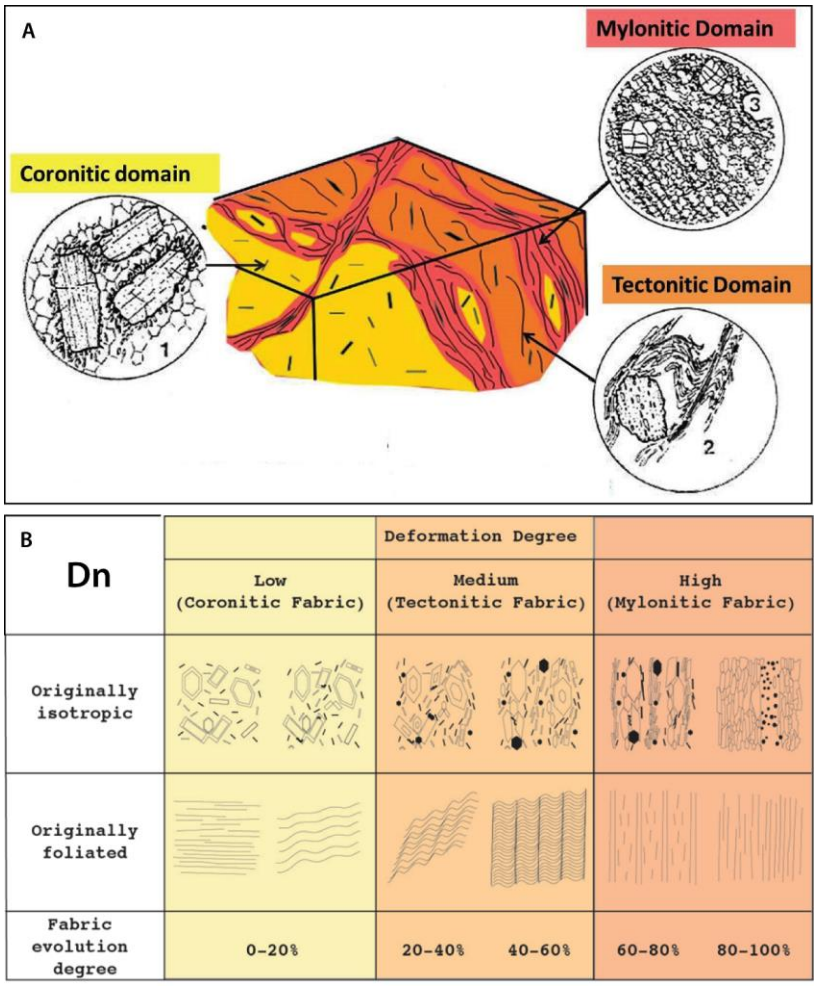

Figure 4.1.3. (A) Idealized block diagram showing the coexistence of contrasted metamorphic texture due to the deformation partitioning at meso- and micro-scales (modified after Lardeaux & Spalla, 1990). (B) Semi-quantitative estimate of fabric evolution during progressive foliation development, starting from originally foliated or isotropic rocks (Bell & Rubenach 1983; Salvi et al., 2010; Gosso et al., 2015). Dn: successive deformation stage.

This analysis is crucial to understand the superposition of tectonic structures that are represented on a structural map by means of form surface trajectories. According to this method, rock types have been represented on a “outcrop” map (panel 1 of interactive map) in which surfacing rocks are separated by cover drift and for any outcrop the syn-D2 degree of fabric evolution is represented. In the “interpretative” map, (panel 2 of interactive map) cover drift is not reported and lithological boundaries are interpreted on the basis of structural data. The two maps, derived from an original mapping at 1:5,000 scale, are presented at 1:10,000 scale and show the outcrop contours, lithology, and structural elements that were georeferenced and stored into a GIS (Geographic Information System) geo-database. The topography shape file was acquired from the Geo-Portal of the Piemonte Region (http://www.geoportale.piemonte.it/cms). The orientations of structural elements, such as axial plane foliations, fold axial planes and axes, are reported on the outcrop map with different symbols to indicate their relative chronology. Two cross-sections and the interpretative map overlay on a DEM (panel 5 of interactive map), which is available from the SINAnet (Isprambiente) website (http://www.sinanet.isprambiente.it/it/sia-ispra/download-mais/dem20/view), have been performed to show the 3D-geometry of the mapped area. The orientation data are represented on equal area lower hemisphere Schmidt diagrams and grouped according to their relative chronology. The contouring of domains that show homogeneous fabric development is facilitated by integrating meso- with micro-scale structural analysis to estimate the FE and MT in volume percentage (Figure 4.1.3B; Salvi et al., 2010; Gosso et al., 2015). The estimate of the FE is based on the degree of grain-scale reorganization of the dominant fabrics. The successive stages of crenulation cleavage development up to complete transposition (Bell & Rubenach, 1983; Salvi et al., 2010) were used as a guide. Multiscale deformation partitioning in metaintrusive for D2 deformational stage is reported as example in Figure 4.1.4. The degree of fabric evolution and degree of metamorphic reaction progress are estimated for each deformational stage and rock type. Therefore, for each deformational stage the results are presented in Table 4.1.1 and consist of:

- Modal bulk: rock-types distinguished based on modal mineral composition and CIPW normative analysis;
- Sample: sample label of analyzed thin section;
- Fabric evolution: estimation of the area occupied by the orientated planar fabric referred to the deformational stage considered (0-20% coronitic; 21-60% tectonitic; 61-100% mylonitic).
- Metamorphic transformation: modal amount of mineral assemblage produced by new mineral growth and recrystallization related to the metamorphic re-equilibration considered (0-100%).

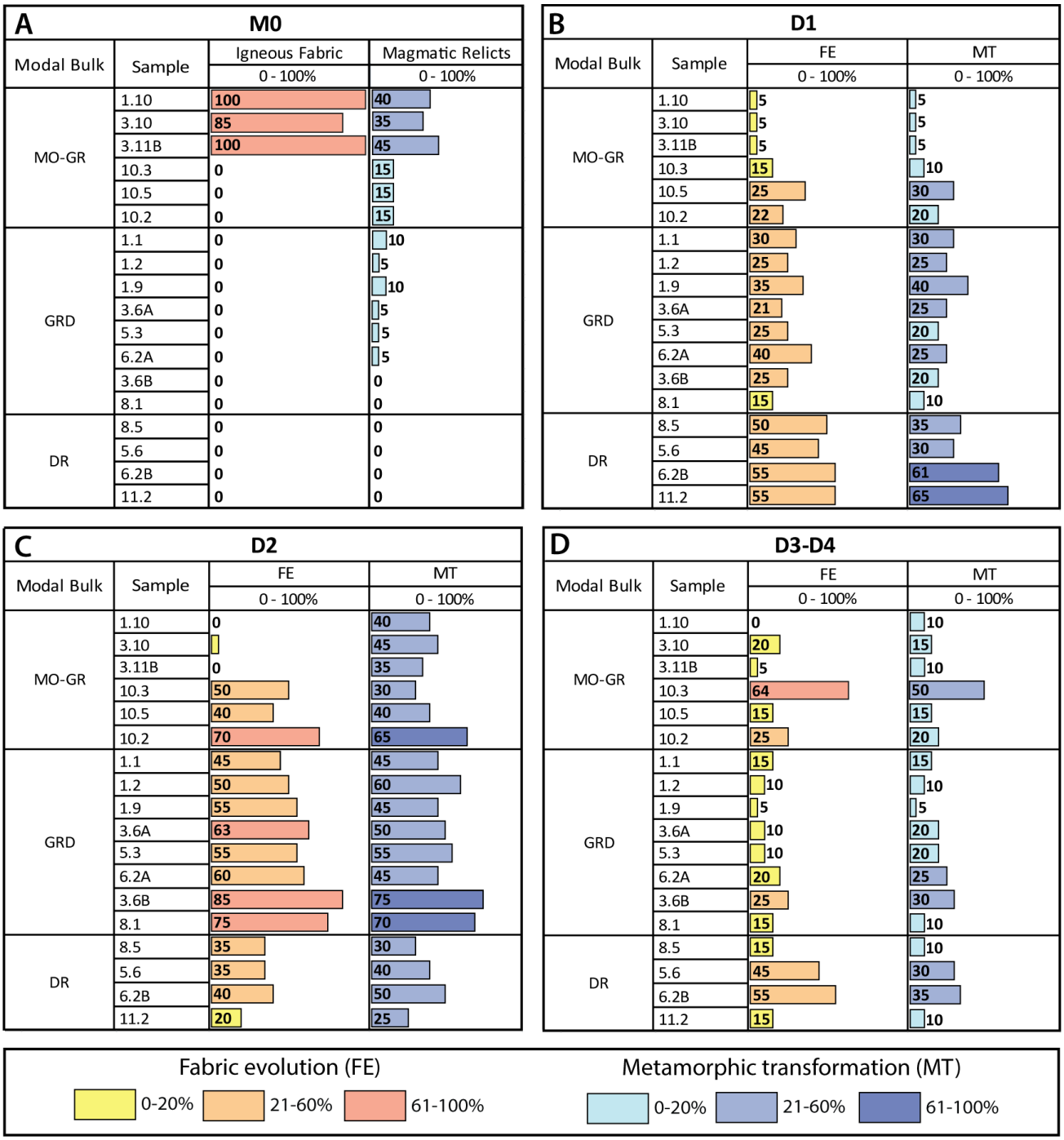

Table 4.1.1. Evaluation of the degree of fabric evolution (FE) and degree of metamorphic reaction progress (MT) in metaintrusive for: (A) M0 magmatic stage; (B) D1 deformation stage; (C) D2 deformation stage; (D) D3-D4 deformation stage. Rock-types distinguished based on modal mineral composition and CIPW normative analysis are MO-GR (monzogranite), GRD (granodiorite), DR (diorite).

The approach used in this study permitted to define the pervasiveness of a single deformation-metamorphic stage. Two 1:10,000 thematic maps represent the correlation of fabric evolution and metamorphic transformation for D2 stage (panel 3 and panel 4 of interactive map).

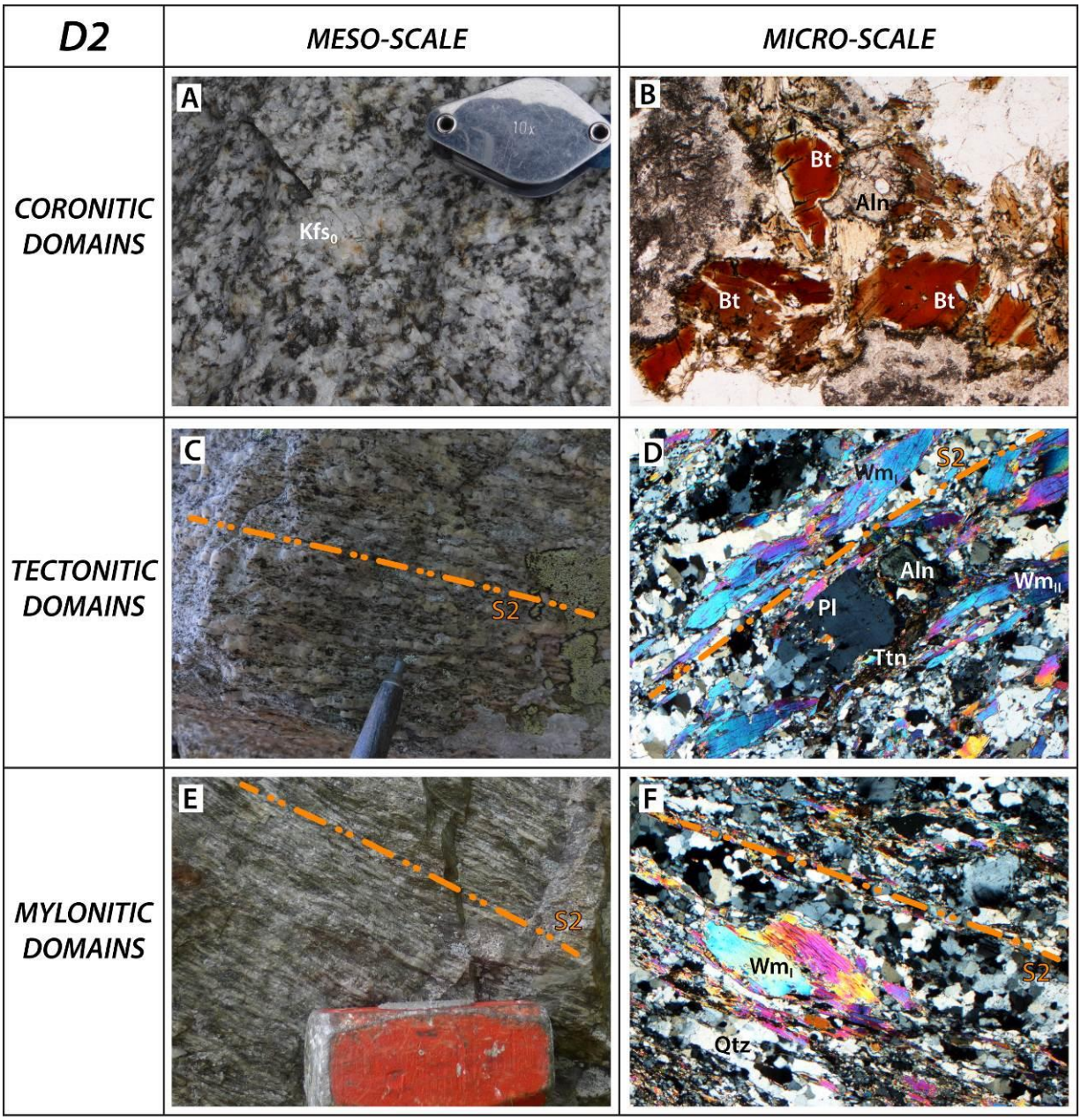

Figure 4.1.4. Multiscale deformation partitioning (coronitic, tectonitic, and mylonitic domains) in metaintrusive for D2 deformational stage. Detailed microstructural descriptions are reported in Table 4.1.3. (A) Preserved magmatic fabric and igneous Kfs in low-strain domains (UTM: 415987-5059526). (B) Aggregates of igneous Bt with a brown to reddish brown pleochroism in tabular and pseudo-hexagonal habits and single grains of Aln characterized by high birefringence; plane polarized light (UTM: 417479-5059237). (C) Tectonitic domains consist of fine- to medium-grained rocks characterized by the pervasive S2 foliation (UTM: 415394-5058667). (D) S2 is a spaced foliation marked by SPO and LPO of WmII associated with aggregates of Ttn and porphyroblasts of Pl. S2 wraps syn-D1 Wm_I and magmatic Aln relicts; crossed polars (UTM: 417479-5059237). (E) Mylonitic domains consist of fine-grained rocks with pervasive S2 foliation (UTM: 416299-5059103). (F) S2 is a spaced and discontinuous foliation marked by SPO and LPO of Wm_{II} that wraps Wm_I porphyroclasts; crossed polars (UTM: 415127-5060649).

4.1.4 Field data

The mapped area consists of metaintrusive and their country rocks (Zucali, 2011), both characterized by a penetrative foliation marked by Qtz, Wm, Ep, and Grt that wraps metabasite boudins and lenses and micaschist lenses. Based on microstructural analysis, metamorphic assemblages were reconstructed (Table 4.1.2). The microstructural and petrographic observation indicate that the pervasive fabric developed at retrograde blueschist-facies conditions and structural relicts of eclogite-facies assemblages are preserved only in the metabasite. Greenschist-facies mineral assemblages are restricted to the main shear zones. Detailed microstructural features of these rock types for each successive deformational stage are displayed in Table 4.1.2.

4.1.4.1 Rock type

Metaintrusive is subdivided based on mesoscopic fabric recognized during the fieldwork in: 1) coronitic metaintrusive; 2) tectonitic metaintrusive; 3) mylonitic metaintrusive. The country rocks consist of: 1) tectonitic metapelite, with minor eclogitic metabasite boudins; 2) mylonitic- to tectonitic-banded gneiss.

Metaintrusive

The intrusive protoliths consist principally of monzogranite that occurs as meter- to decameter-sized outcrops and minor meter-sized granodioritic lenses within the monzogranite. The partitioning of the Alpine deformation is responsible for the preservation of igneous textures and minerals in meter-sized coronitic lenses and the development of tectonitic and mylonitic fabrics in metaintrusive. Tectonitic and mylonitic fabrics wrap coronitic domains, which were found in several localities (Rifugio Lago della Vecchia and to the west of P.ta Canaggio) as meter- to decameter-long bodies. Coronitic metaintrusive is medium- to coarse-grained rocks showing a well-preserved isotropic and hypidiomorphic igneous texture with igneous relics such as Bt, Kfs, Pl, Grt, Wm, and Aln, partially replaced by Alpine Grt, Wm, Ep, and Amp (see details in Table 4.1.2). Coronitic metaintrusive is constituted by Qtz (30-40%) + Wm (15-20%) + Pl (10-15%) + Grt (10-15%) + Bt (7-10%) + Kfs (5-10%) + Ep (5-10%) + Aln (5%) + Amp (2%). Tectonitic metaintrusive constitutes the most common lithotype in the area and consists of fine- to medium-grained rocks that contain Qtz (30-50%) + Wm (20-30%) + Ep (15-20%) + Grt (5%) + Amp (5%) + magmatic mineral relicts such as Kfs (5%) and Aln (5%). These rocks mostly show a well-developed foliation marked by shape- preferred orientation (SPO) of Qtz and aggregates of Wm, Ep, and Grt.

Stage	Rock type			
	Metaintrusive	*Metabasite*	*Banded Gneiss*	*Metapelite*
M0	Preserved M0 fabrics only in coronitic rocks. Igneous mineral relicts are Bt_0, Kfs_0, Wm_0, Aln_0, Grt_0, Ttn_0, Bt_0 occurs in single crystals with a continuous corona of Grt_1 at the contact with Pl_0. Between single crystals of Wm_0 and Grt_0, fine-grained corona of Wm_1, Ep_1, and Grt_1 developed. Corona of Amp_1, Grt_1, and Bt_1 developed between Ttn_0 and Plg_0. Aln_0 occurs in well-preserved single crystals and different coronitic mineral assemblages developed as a function of the mineral phase Aln_0 is in contact with.	Not found	Pre-D1 fabrics are not preserved . Igneous mineral relicts are found and mainly consist of Kfs_0 crystals partially replaced by Pl_0 within microlithons, sub-millimetre sized Aln_0 crystals are rimmed by coronae of Zo_1, Czo_1, and Ep_1.	Not found
D1	Mineral assemblage: Wm_1, Czo_1, Grt_1, Zo_1, Qtz_1, Mnz_1, and Rt_1. D1 mineral relicts are preserved as porphyroblasts wrapped by S2-foliation. Grt_1 porphyroblasts show an internal foliation marked by fine-grained crystals of Wm_1, Zo_1/Czo_1, and Rt_1 smaller than in matrix minerals; this suggests that Grt_1 growth started during an earlier stage of S1 development.	Mineral assemblage: Cpx_1, Wm_1, Grt_1, Czo_1. These minerals are arranged in SPO of Cpx_1 in equilibrium with Grt_1, Wm_1, and minor Czo_1. Cpx_1 occurs as large porphyroblasts with rational grain boundaries with Wm_1 and Grt_1.	Relicts of D1 fabrics are constituted by Wm_1, Grt_1, Ep_1, Zo/Czo_1, and Rt_1. This mineral assemblage consists of large and deformed Wm_1 porphyroblasts, Grt_1 cores with inclusions of Rt_1, and Zo/Czo_1 boudinated crystals.	Mineral assemblage: Wm_1, Grt_1, Zo/Czo_1, Rt_1. Relicts of S1 foliation, constituted by SPO of Wm_1 and Zo/Czo_1, are preserved within microlithons. Grt_1 porphyroblasts show an internal foliation marked by fine-grained crystals of Wm_1, Zo_1, and Rt_1 smaller than in the matrix; this suggests that Grt_1 growth started during an earlier stage of S1 development.
D2	Mineral assemblage: Wm_{II}, Qtz_{II}, Czo_{II}, Zo_{II}, Grt_{II}, Pl_{II}, Ttn_{II}, Op_{II}. These minerals are arranged in S2 spaced and discontinuous foliation marked by SPO of Wm_{II}, Czo_{II}, Zo_{II}, Pl_{II} associated with Grt_{II} and Ttn_{II}. Rational grain boundaries between Grt_{II} and S2 marking minerals are preserved in portions where successive fabric overprints are not pervasive. Ttn_1 occurs in small sub-euhedral and euhedral crystals in contact with Wm_{II}. S2 is locally associated with boudinage of Zo_1 and gentle folding of Wm_1.	Mineral assemblage: Cpx_{II}, Amp_{II}, Wm_{II}, Grt_{II}, Zo_{II}, Pl_{II}, Op_{II}. S2 is mainly a discontinuous and spaced foliation that is continuous in high-strain domains. SPO and LPO of Cpx_{II}, Amp_{II}, Wm_{II}, Zo_{II}, Czo_{II} mark S2 in equilibrium with Grt_{II}. D2 phases are also associated with boudinage of Cpx_I. In low-strain domains the same minerals replace D1 assemblage in coronitic fabrics.	Mineral assemblage: Wm_{II}, Grt_{II}, Zo/Czo_{II}, Ep_{II}, Ttn_{II}, Qtz_{II}. These phases are arranged into a S2 spaced foliation marked by SPO and LPO of Wm_{II}, SPO of Zo/Czo_{II} and Ep_{II} associated with Grt_{II} and Ttn_{II}. Grains boundaries between Grt_{II} and S2 marking minerals are rational in portions where successive fabric overprints are not pervasive. Ttn_1 occurs in small sub-euhedral and euhedral crystals in equilibrium with Wm_{II}; in low-strain domains Ttn_1 defined coronae around Wm_1 and Rt_1. S2 overprints S1 foliation and is locally associated with boudinage of Zo_1 and Wm_1.	Mineral assemblage: Wm_{II}, Grt_{II}, Zo/Czo_{II}, Ep_{II}, Ttn_{II}, Qtz_{II}. S2 foliation is a zonal and continuous foliation marked by SPO and LPO of Wm_{II}, SPO of Zo/Czo_{II} associated with Grt_{II} and Ttn_{II}.
D3-D4	Mineral assemblage: Wm_{III}, Qtz_{III}, Ep_{III}, Pl_{II}, Ttn_{II}, Chl_I, Amp_{II}, Op_{II}. D3-D4 are characterized by local development, at low angle with S2 foliation, of S3 foliation marked by fine-grained SPO of Wm_{III}, Ep_{III}, Amp_{III}, and Chl_{II}. In low-strain domains, the same minerals replace previous assemblages.	Mineral assemblage: Wm_{III}, Amp_{II}, Ep_{III}, Pl_{II}, Ttn_{II}, Qtz_{III}, Op_{II}. D3-D4 are constituted by fine-grained aggregate of Amp_{II}, Ep_{III}, Wm_{III}, Ttn_{II} showing SPO between boudinated Cpx and along grain boundary of porphyroblasts.	Mineral assemblage: Wm_{III}, Ep_{III}, Chl_I, Amp_{III}, Pl_{II}, Qtz_{III}. D3-D4 are characterized by local development of S3 foliation at low angle with S2 foliation. S3 is marked by fine-grained aggregates of Wm_{III}, Ep_{III}, Chl_I, Amp_I. In low-strain domains, the same minerals replace previous assemblages. Wm_{III} and Chl_I developed along [001] planes of kinked $Wm_{I/II}$, Chl_I partially replaces Grt_{III} along grain boundaries and micro-fractures. Zo/Czo_{II} and Ep_{II} are overgrown by a fine-grained aggregate of Wm_{III} and Ep_{III}.	Mineral assemblage: Wm_{III}, Ep_{III}, Chl_I, Amp_{III}, Pl_{II}, Qtz_{III}. D3-D4 are characterized by micro-folding associated with an axial plane S3-foliation marked by fine-grained aggregates of Wm_{III}, Ep_{III}, Chl_I, and Amp_{III}. In low-strain domains, the same minerals replace previous assemblages. Wm_{III} and Chl_I developed along [001] planes of kinked $Wm_{I/II}$, Chl_I partially replaces $Grt_{I/II}$ along grain boundaries and micro-fractures.
D5	Mineral assemblage: Ch_{III}, Amp_{III}, Qtz_{III}, Op_{III}. D5 is characterized by the development of coronitic mineral assemblage marked by Chl_{III} and Amp_{II} and it is related to an extremely localized overprint along D5 shear zones.	Not found	Mineral assemblage: Chl_{II}, Amp_{III}, Qtz_{III}, Op_{III}. D5 is related to an extremely localized overprint constituted by the development of S5 foliation marked by SPO and LPO of Chl_{III} and Amp_{III}.	Not found

Table 4.1.2. Microstructural features of each deformational stage recorded in the mapped rock types.

Mylonitic metaintrusive consists of fine-grained rocks showing a millimeter-spaced foliation defined by SPO of Wm, Ep, and Amp that wraps porphyroblasts of Grt and locally magmatic porphyroclasts of Kfs. Mylonitic metaintrusive forms decameter- to kilometer-long shear zones mostly trending NW-SE (see the panel 2 and panel 5 within the interactive map) that locally mark the contact between metaintrusive and country rocks. Mylonitic metaintrusive is constituted by Qtz (40-50%) + Wm (15-20%) + Ep (15-20%) + Grt (5-10%) + Amp (5-10%) + Chl (5%). Within metaintrusive, centimeter- to meter-scale meta-aplitic dykes (type locality: close to Rosei, to the east of Olmo, located along the Torrente Irogna, and at Colle della Vecchia) and numerous boudins occur.

Banded gneiss

Banded gneiss has intermediate composition between metaintrusive and metapelite and consists of fine-grained rocks. These rocks show a centimeter- to meter-thick layering of leucocratic Wm-poor and mafic Wm-Ep rich layers. The layering seems to be related to the degree of fabric evolution; the layering thickness decreases with the increase of the finite strain, as it occurs near Irogna Inferiore. Banded gneiss mostly outcrops between mylonitic and tectonitic metaintrusive and metapelitic lenses (see the interactive map).

In banded gneiss, the pervasive millimeter-spaced foliation is mostly mylonitic and marked by compositional layering. The mafic layers are constituted by Wm (30-45%) + Qtz (10-20%) + Ep (5-15%) + Grt (10-25%) + Amp (5-10%). The content of Wm, Ep, and Grt highly vary in volume percent as a function of the bulk composition. The leucocratic layers are characterized by a less-develop foliation and are constituted by Qtz (50-60%) + Grt (10-15%) + Pl (10-15%) + Ep (5%) + Wm (5%) + Amp (5%) + probably magmatic relicts of Kfs (< 5%).

Metapelite

The metapelite consists mostly of tectonitic micaschist with minor gneiss and occurs as decameter- to meter-sized lenses within the metaintrusive. Metapelite is wrapped and elongated within the pervasive D2-foliation and enclosed in mylonitic metaintrusive and banded gneiss. These rocks mostly outcrop on the west shore of Lago della Vecchia, at Lago del Giaspret, and around C.le d'Irogna. The micaschist consists of fine-grained rocks with a pervasive millimeter-spaced foliation marked by SPO of Wm and Grt. Micaschist is constituted by Wm (15-40%) + Qtz (15-50%) + Grt (15%) + Ep (5-10%) + Amp (5-10%). Metapelite outcropping nearby Lago del Giaspret (see interactive map) contains meter-sized metabasic boudins. Micaschist is alternated with fine-grained leucocratic Qtz-rich gneiss

in which the pervasive gneissic foliation is marked by Wm, Grt, and Ep. Leucocratic gneiss is constituted by Qtz (50%) + Grt (10-20%) + Wm (10-15%) + Ep (5-10%) + Amp (5%).

Metabasite

Metabasite occurs as meter- to decameter-sized lenses and as centimeter-sized boudins within metaintrusive, banded gneiss, and metapelite. The metabasite is characterized by a foliation marked by SPO of Cpx, Grt, and Wm, which locally is overprinted by the successive structural and metamorphic re-equilibrations.

Gneiss

Gneiss outcrops as fine-grained and meter- to decameter-tick rocks displaying a mylonitic contact with all the previous rock types. Gneiss is characterized by cataclastic-mylonitic fabric. Chl + Amp + Qtz + Op constitute the mylonitic millimeter-spaced foliation that transposed and obliterated all previous structures and lithologies.

4.1.4.2 Structural Analysis

The panels 1 and 2 of the interactive map show the location of the different strain domains for each rock type. In particular, they show coronitic domains wrapped by a network of superposed tectonitic foliations and mylonitic shear zones related to successive deformational stages. The identified mineral assemblages (Table 4.1.2) linked to the successive deformational stages (Table 4.1.3) allow defining the tectono-metamorphic history. Two groups of magmatic (M0, M6) structures and five groups of superposed tectonic structures (D1 to D5) are defined. Numbers associated with magmatic and tectonic structures refer to relative chronology. M0 stage consists of undeformed, most probably pre-Alpine, igneous intrusion (Zucali, 2011). D1 to D5 structures consist of fold systems, foliations, and shear zones that are comparable, in terms of their structural features and relative chronology, to the Alpine structures described by Zucali et al. (2002) and Delleani et al. (2012) in the nearby area of M. Mucrone. M6 stage is represented by andesite dykes intrusion that is quite common in the area and dated at the Oligocene (*e.g.* Kapferer, Mercolli, Berger, Ovtcharova, & Fügenschuh, 2012). Table 4.1.3 is a schematic representation of deformation timing and related pre-Alpine and Alpine meso-structures developed in metaintrusive, banded gneiss, and metapelite. The orientations of fabric elements are summarized in the structural data section of the interactive map. The relationships between the superimposed fabrics and mineral assemblages (Table 4.1.2) recognized at the multiscale have been used to reconstruct the following structural history.

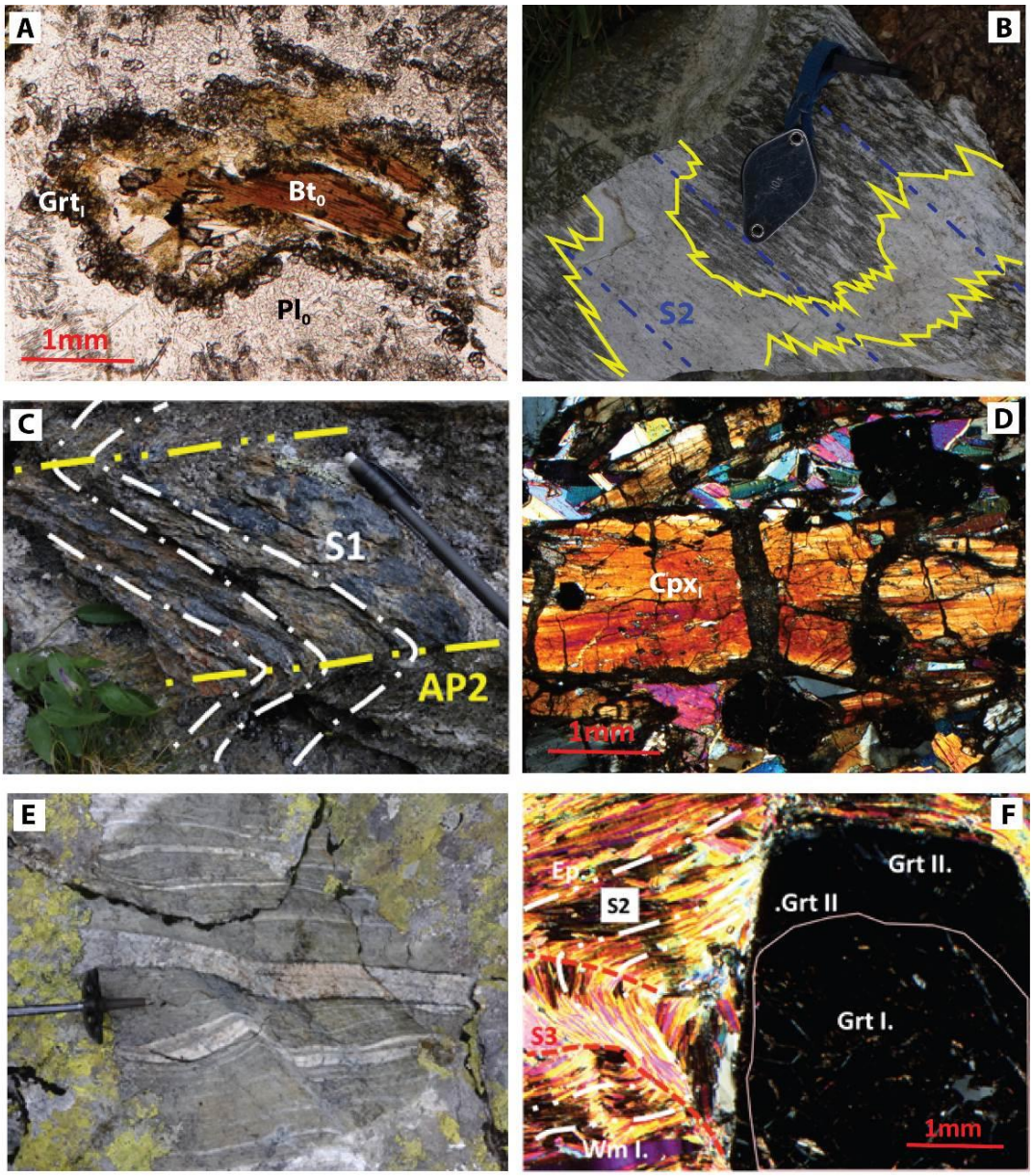

Figure 4.1.5. Multiscale structures. (A) Coronitic metaintrusive shows magmatic Bt_0 in single crystals rimmed by a continuous corona of Grt_I at the contact with magmatic Pl_0; plane polarized light (UTM: 417479-5059237). (B) Meta-aplite in tectonitic metaintrusive with boundaries deformed and stretched into parallelism with the S2 penetrative foliation (UTM: 415922-5059543). (C) Tectonitic metapelite with S1 foliation crenulated by D2 folding (UTM: 415716-5058620). (D) Relicts of S1 foliation marked by Cpx_I in metabasic boudin; crossed polars (UTM: 415731-5060114). (E) Mylonitic banded gneiss characterized by layering of Wm-Ep-bearing layers and minor leucocratic layers, overprinted by successive D3 shear zones (UTM: 416241-5058630). (F) Tectonitic metapelite shows millimeter-sized porphyroblasts of Grt displaying a Grt_I core rich in Wm and Zo inclusions surrounded by Grt_{II} inclusion free in equilibrium with Wm_{II}. S2 foliation (white dashed line) is marked by Wm_{II}, Ep_I and Ttn_{II}; S2 is crenulated during S3 foliation (red line) development. S3 is marked by fine-grained crystals of Wm_{III}, Ep_{II} and Chl_I; crossed polars (UTM: 416617-5057989).

M0. Isotropic textures are preserved in meter- to decameter-sized coronitic metaintrusive domains. Coronitic metaintrusive (at Rifugio Lago della Vecchia and west of P.ta Canaggio) preserves Bt0 (Figure 4.1.5A), Kfs_0, euhedral to subeuhedral Pl_0 grains, and interstitial Qtz. In the tectonitic and mylonitic domains, the magmatic textures are strongly deformed and the amount of igneous mineral relicts is lower than in coronitic metaintrusive. Primary magmatic contacts between granitoid and country rocks were not found. Metaintrusive is separated by metapelite by progressively high strain mylonitic domains that consist of banded gneiss and/or mylonitic metaintrusive themselves (east of Lago del Giaspret, SE of Rifugio della Vecchia, and ESE of Irogna). Aplite dykes intersect igneous fabric and mineral relicts in metaintrusive coronitic domains and are overprinted by Alpine foliations in tectonitic domains. In this last case, the igneous contact between aplite and metaintrusive is intersected at high angle by the Alpine foliations (Figure 4.1.5B).

D1. During D1 a well-preserved foliation (Figure 4.1.5C) developed within tectonitic micaschist (S1) nearby Colle d'Irogna (see interactive map) with dip azimuth clustering between 320°-140° and dip varying from 25° to 55°. Relicts of S1 foliation also occur in metabasite boudins (Figure 4.1.5D).

D2. During D2 stage a pervasive S2 foliation developed and previous structures, such as igneous structures, lithological surfaces, and S1 foliation were parallelized and often transposed into S2. S2 is characterized by 15-50° dip and dip azimuth varying from 90° to 320°, with cluster at dip azimuth of 125° and dip of 42°. In micaschist S2 occurs also as axial plane foliation of isoclinal to tight folds (SW-shore of Lago della Vecchia, east of Lago del Giaspret, and north of Colle d'Irogna).

Metaintrusive records the maximum variability of syn-D2 fabric types (coronite to mylonite). In tectonitic-mylonitic domains, S2-foliation wraps around coronitic domains and elongated metabasic boudins (for example toward SE of Lago del Giaspret) and overprints aplitic dykes. D2 is also responsible for the layering of the banded gneiss being parallel to S2 foliation (Figure 4.1.5E).

D3. This deformational stage mainly produced open folds characterized by sub-vertical SE dipping axial planes that affected all lithological boundaries. Generally, D3 folding is not associated with the development of a new pervasive foliation, however a differentiated S3 axial plane foliation is developed locally in metaintrusive and banded gneiss (at the top of Valle d'Irogna and between the Rifugio Lago della Vecchia and C.le della Vecchia), within 1-2 cm thick localized shear zones at high angle with the S2 foliation (Figure 4.1.5F).

D4. D4 produced open folds (NW of Olmo and north of C.le d'Irogna), characterized by a W-dipping sub-horizontal axial plane in micaschist and tectonitic metaintrusive. These folds are poorly recorded and are not associated with a new foliation.

Deformation stage	Metaintrusive	Banded gneiss	Metapelite
M0	Igneous Textures	Not Found	Not Found
D1	Not Found	Not Found	S1
D2	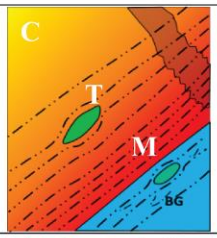	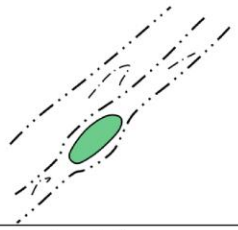	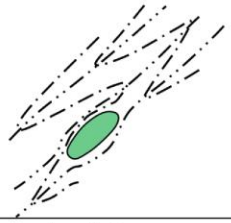
D3	cm-sized crenulation and open folds 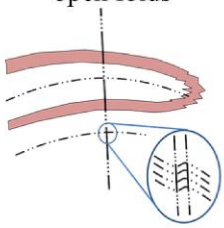	cm-sized shear zones 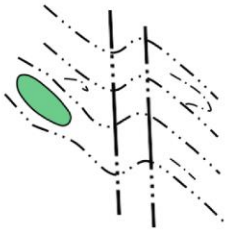	cm-sized shear zones 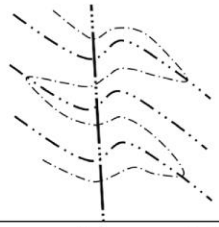
D4	metric open folds 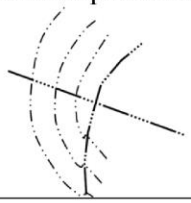	metric open folds 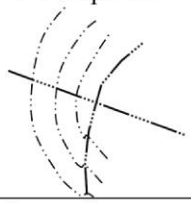	metric open folds 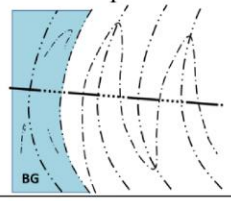
D5	m to km scale greenschist shear zones	m to km scale greenschist shear zones 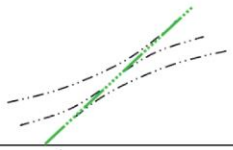	m to km scale greenschist shear zones 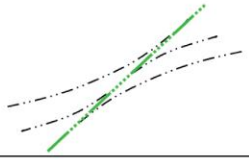
M6	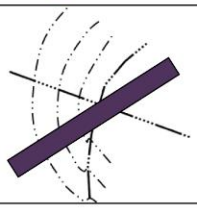	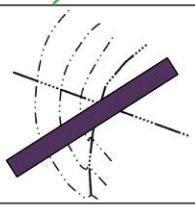	No andesitic dykes cut metapelite

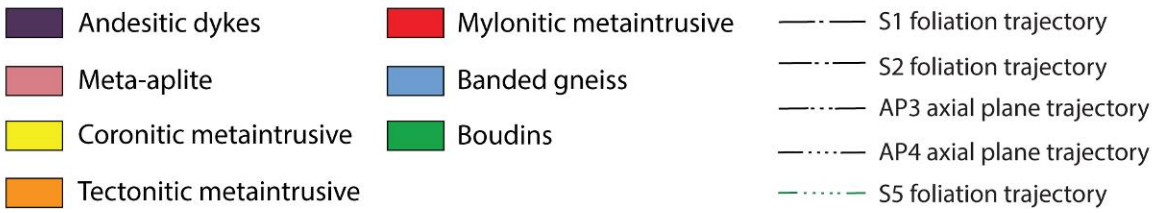

Table 4.1.3. Schematic representation of mesostructures developed in metaintrusive, banded gneiss, and metapelite during the pre-Alpine and Alpine evolution. BG: banded gneiss; C: coronitic domains; T: tectonitic domains; M: mylonitic domains.

D5. These structures are related to the development of ductile-brittle meter- to kilometer-long and meter-thick NE-SW trending shear zones. Within these shear zones, mylonitc fabrics are marked by greenschist-facies minerals (see the panel 1 and 2 within interactive map). These shear zones ubiquitously affect the contacts between the metaintrusive and banded gneiss (see the panel 2 and panel 5 within interactive map).

M6. This stage consists of andesitic dykes' intrusion. Sub-vertical andesitic dykes are 0.5 to 2-meter-thick and trend WNW-ESE. They crosscut all rock types and foliations (several outcrops between the Lago del Giaspret and C.le Irogna; NW Olmo, along the Torrente Irogna). Only the relationship with the D5 shear zones was not observed.

4.1.5 Conclusion

The analysis carried out on these metamorphic rocks show that the progress of metamorphic transformations was controlled by bulk rock, mineral compositions, but it was mainly affected by fabric evolution. The maps of degree of FE and MT support this conclusion showing that FE (panel 3) and MT (panel 4) are strictly correlated regardless the rock types. Moreover, the dominant tectono-metamorphic imprint is related to the D2 stage that is characterized by the highest degree of FE and MT.

Our observation agrees with results obtained in other portions of the subducted continental crust of the Western and Central Alps. For instance, in the nearby area of M. Mucrone the correlation between FE and MT shows that the dominant tectono-metamorphic imprint is related to high degree of FE and MT (Zucali et al., 2002; Delleani et al., 2012; Delleani et al., 2013). Similar results have been also obtained in the Mont Morion complex of the Dent Blanche nappe (Roda and Zucali, 2008) and in the Languard-Tonale unit in the central Austroalpine domain (Salvi et al., 2010). In this last example, the application of this method results in a 3-D model of the relationships between FE and MT and the estimation of the volumes affected by textural reworking during polyphase pre-Alpine and Alpine deformations.

In the area mapped in this work, the D2 event is more pervasive with respect to D1 and D3-D4 and S2 foliation displays the highest degree of FE and MT. In all rock types, blueschist facies mineral assemblages (Table 4.1.3) define S2. This finding is in contrast with the nearby metaintrusive of M. Mucrone, where eclogitic mineral assemblages mark the pervasive fabric (Zucali et al., 2002; Delleani et al., 2012; Delleani et al., 2013). Thus, different FE and MT would have affected the retrograde blueschist re-equilibration and potentially generated km-scale heterogeneities within the EMC.

4.1.6 Acknowledgements

Insightful reviews by Manuel Roda and an anonymous fellow helped us to clarify the ideas presented in the text and map panels. Steven Bernard provided useful advices on map plate layout. Funding from MIUR-PRIN 2010-2011 “Birth and death of oceanic basins: geodynamic processes from rifting to continental collision in Mediterranean and circum-Mediterranean orogens” and Linea B del Piano di potenziamento della ricerca Università di Milano “Analisi delle relazioni deformazione / metamorfismo e deformazione magmatismo applicata all’evoluzione degli orogeni collisionali”. Mr. Rizzetti facilitated the use of La Scala shepherd hut during fieldwork.

References are integrated at the end of the thesis.

4.2 Tectonometamorphic evolution of the Lago della Vecchia metaintrusive and its country rocks, Sesia-Lanzo Zone, Western Alps

The following sections refer to the published paper: Corti L., Alberelli G., Zanoni D., and Zucali M. (2018): Tectonometamorphic evolution of the Lago della Vecchia metaintrusive and its country rocks, Sesia-Lanzo Zone, Western Alps. Italian Journal of Geosciences, v. 137, p. 188-207, doi: 10.3301/IJG.2018.08

Abstract

In the Sesia-Lanzo Zone different complexes are separated on the basis of rock types and dominant metamorphic imprints: one of these is the Eclogitic Micaschists Complex (EMC) that is distinguished by a dominant Alpine eclogite facies fabric. In this contribution, we present the results of a multiscale structural analysis devoted to reconstruct the tectonometamorphic evolution of the Lago della Vecchia metaintrusive and its country rocks (upper Cervo valley, Biella), which are part of the EMC. Seven groups of superposed structures have been detected. Igneous pre-Alpine M0 relicts are preserved in metaintrusive. Alpine structures consist of: S1 foliation (D1) developed under eclogite facies conditions; S2 foliation (D2) is the most pervasive fabric and developed under low-pressure blueschist facies conditions; localised shear zones and open folds (D3 and D4) are associated with the development of greenschist facies assemblages; a kilometre-long shear zones (D5) developed under greenschist facies conditions. Finally, andesitic dikes intrusion postdates D1-D5 structures. On the basis of deformation-metamorphism relationships geothermobarometric estimates were performed to

constrain the PT conditions characterising subsequent deformation stages. The resulting Pressure-Temperature-relative time of deformation (*P*-*T*-d-t) path shows a pre-Alpine magmatic emplacement at around 15 km depth at *T*=710±19°C that is followed by re-equilibration indicating the conditions of the Alpine eclogitic peak (D1: 2.23±0.18 GPa; 537±43°C), compatible with a cold-subduction environment. A near-isothermal exhumation postdates D1, down to 1.12±0.11 GPa at 477±39°C during D2 deformation stage. Afterwards, temperature and pressure decreased from D2 low-pressure blueschist to D3-D4 greenschist re-equilibrations (*P*=0.6±0.10 GPa and *T*=302±24°C). In contrast with the most part of the EMC, where the dominant fabric developed under eclogitic facies conditions, at Lago della Vecchia the dominant fabric developed under low-pressure blueschist facies conditions. This difference suggests that the entire EMC should be characterised by kilometre-scale structural heterogeneities in the dominant tectonometamorphic record.

Keywords: multiscale structural analysis; blueschist-facies imprint; strain partitioning; metamorphic conditions; Eclogitic Micaschists Complex.

4.2.1 Introduction

The reconstruction of tectonometamorphic evolution of crustal slices is the primary tool for the study of tectonic processes in metamorphic terrains (Spalla et al., 2000; Spalla et al., 2005). Recently, it has been shown how only a multidisciplinary approach and multiscale structural correlation permit a robust reconstruction of the tectonic history (Gosso et al., 2015). Indeed, the combined use of *P*-*T* estimates and deformation histories (d-t) over large areas has recently became the basis for the individuation of tectonometamorphic units (TMUs of Spalla et al., 2000; Spalla et al., 2005). Deformation heterogeneities make this correlation difficult but allow the preservation of relict structures and related metamorphic assemblages that can be used to trace back the tectonometamorphic history. Thus, detailed structural analysis integrated with petrologic investigations allows the individuation of the boundaries of crustal slices sharing the same *P*-*T*-d-t evolutions (Zucali et al., 2002; Salvi et al., 2010). In the past twenty years, this approach has been intensively applied to the Sesia-Lanzo Zone (SLZ; Rebay & Spalla, 2001; Zucali et al., 2002; Spalla & Zucali, 2004; Zucali et al., 2004; Gosso et al., 2010; Zucali & Spalla, 2011; Delleani et al., 2012; Cantù et al., 2016; Delleani et al., 2018) and, combined with numerical models, it has been used to test the reliability of geodynamic models of subduction-collision processes (Meda et al., 2010; Roda et al., 2012). Since the end of eighties, this approach allowed recognising within the Eclogitic Micaschists Complex (EMC) of the SLZ, classically connoted by a dominant eclogite-facies Alpine fabric (Compagnoni et al., 1977),

structural and metamorphic heterogeneities. Therefore, the actual distribution of the dominant eclogitic imprint and the complexity of the tectonometamorphic evolution in the EMC are still debated (Pognante, 1989; Venturini, 1995; Babist et al., 2006; Zucali & Spalla, 2011; Regis et al., 2014; Giuntoli & Engi 2016).

This contribution aims at quantifying the tectonometamorphic evolution and degree of fabric development in an area of the EMC of the Sesia-Lanzo Zone, where only few data are available. With this aim, a multiscale structural analysis, combined with mineral chemistry and thermo-barometric estimates are performed to constrain the *P-T*-d-t evolution of the pre-Alpine Lago della Vecchia metaintrusive and its country rocks (upper Cervo valley, Biella), supported by a petrostructural map (Corti et al., 2017). The results are compared with the tectonic and metamorphic record of the EMC. In the following, mineral abbreviations are according to Whitney & Evans (2010).

4.2.2 Geological setting

In the western Austroalpine domain (Figure 4.2.1A), the SLZ is an elongated body (ca. 90x20 km) of pre-Alpine continental crust and it is interpreted as a slice of Adria active continental margin (Polino et al., 1990) that was subducted and exhumed during the Alpine convergence (Compagnoni et al., 1977). The SLZ is in contact with relicts of the oceanic domain of the Alpine Tethys to the north and with the Periadriatic line to the south, which separates the SLZ form the Southern Alps (Dal Piaz et al., 1972; Manzotti et al., 2014).

4.2.2.1 Lithostratigraphic-metamorphic outline

Taking into account the lithological composition and dominant metamorphic imprints, the SLZ has been classically subdivided into four main complexes (*e.g.* Gosso, 1977; Pognante, 1989; Figure 4.2.1B): 1) II Dioritic-Kinzigitic Zone (IIDK); 2) Eclogitic Micaschists Complex (EMC); 3) Gneiss Minuti Complex (GMC) and 4) Rocca Canavese Thrust Sheet (RCTS).

The IIDK consists of an association of high-grade metapelites, silicate marbles, amphibolites, and granulites with minor metagranitoids and few slices of mantle peridotite (Compagnoni et al., 1977; Gosso et al., 1982). The EMC and GMC rocks include micaschists, paragneisses, metaintrusives, quartzites, fine-grained gneisses, lenses of metabasites, and pure to impure marbles. Minor pre-Alpine high-grade metamorphic relicts, such as amphibolites of central EMC (Lardeaux et al., 1982; Gosso et al., 2010) and in kinzigites of the Monte Mucrone area (Compagnoni & Maffeo, 1973; Zucali et al., 2002; Zanoni, 2016) are preserved in the EMC. The RCTS includes pre-Alpine granulites and lenses of serpentinised lherzolite enclosed in metapelites and leucocratic gneisses (Pognante, 1989; Cantù et

al., 2016). The gabbroic and granitic to granodioritic bodies are diffused in EMC and GMC, but are most common in the northern Aosta valley, between Monte Mucrone (Compagnoni & Maffeo, 1973; Delleani et al., 2013), Lago della Vecchia (Corti et al., 2017), Gaby-Gressoney Valley and the Sesia Valley (Dal Piaz et al., 1972; Callegari et al., 1976; Compagnoni et al., 1977).

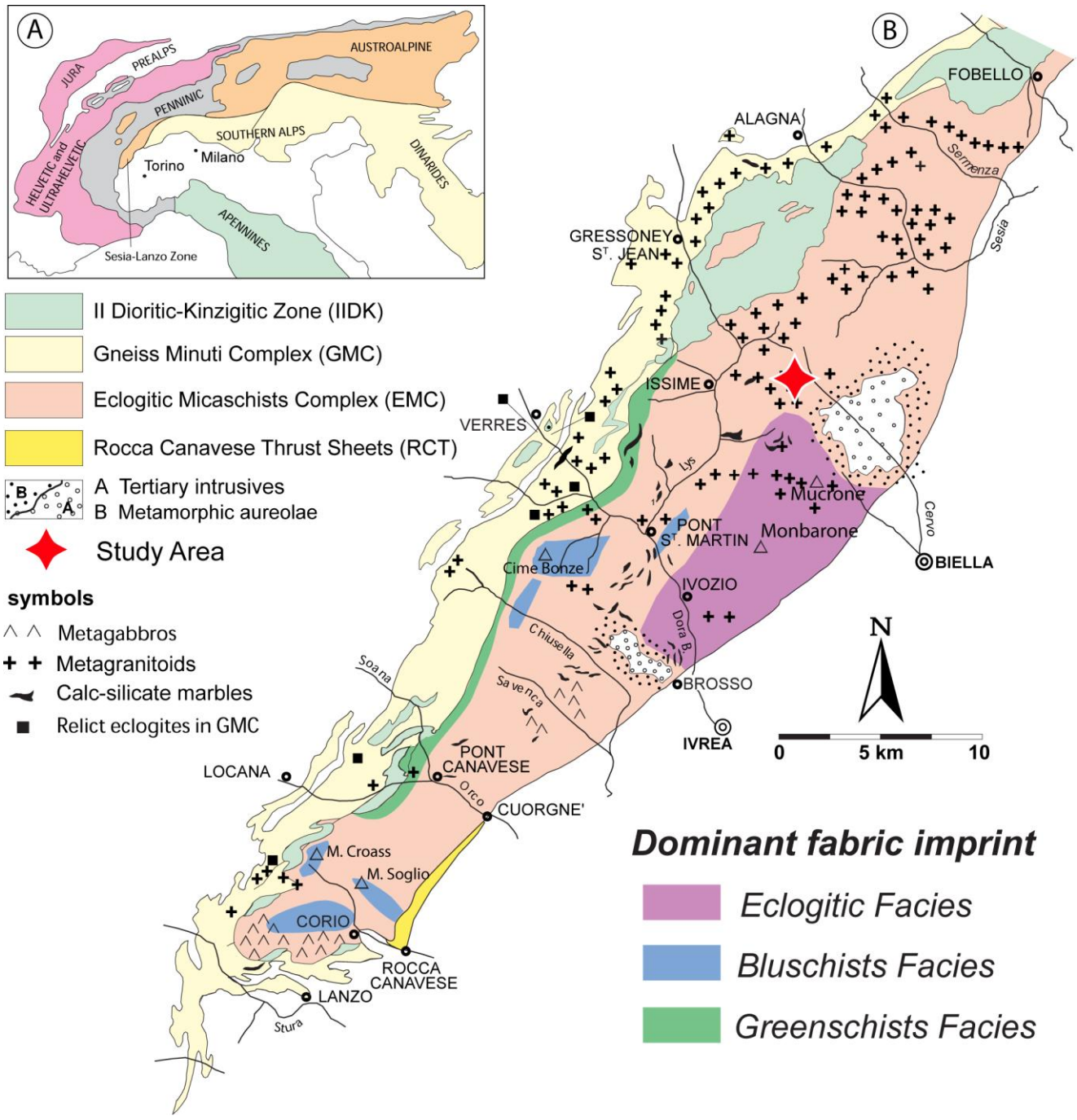

Figure 4.2.1. A) Simplified geological outline of the Alps and (B) tectonic map of Sesia-Lanzo Zone with the areas of different dominant fabrics imprint (modified after Spalla & Zulbiati, 2003; Zucali et al., 2004).

In the IIDK, large volumes of rocks that preserve pre-Alpine high temperature-low pressure (H*T*-L*P*) metamorphic imprints are dominant (*e.g.* Compagnoni et al., 1977; Gosso et al., 1982), and Alpine re-equilibration is pervasive exclusively along shear zones, and only incipient within low strain domains. The EMC and GMC pervasively record the Alpine metamorphic imprint; the EMC and GMC record an eclogitic and greenschist dominant fabric, respectively. The Alpine polyphasic deformation occurred under eclogite facies, followed by retrogression under blueschist to greenschist facies conditions (Lardeaux et al. 1982; Spalla et al., 1983; Spalla et al., 1996; Duchêne et al., 1997; Pognante, 1991; Gosso et al., 2010; Zucali & Spalla, 2011; Delleani et al., 2013; Lardeaux, 2014). The RCTS pervasively records a blueschist-facies metamorphic imprint (Pognante, 1989; Cantù et al., 2016) and was interpreted as escaping the eclogite facies conditions, even though a recent work documented an eclogite facies evolution (Roda et al., 2018).

<table>
<tr><th>COMPAGNONI et alii (1977)</th><th>VENTURINI (1995)</th><th>BABIST et alii (2006)</th><th>REGIS et alii (2014)</th><th>GIUNTOLI & ENGI (2016)</th></tr>
<tr><td rowspan="2">EMC</td><td>EMC</td><td>Mombarone nappe</td><td>Druer slice</td><td rowspan="2">Internal Complex</td></tr>
<tr><td>MCC (Scalaro and Bonze Units)</td><td>Bonze Unit</td><td>Fondo slice</td></tr>
<tr><td rowspan="2">GMC</td><td rowspan="2">Intermediate unit</td><td rowspan="3">Bard nappe</td><td rowspan="2">Intermediate unit</td><td>Barmet Shear Zone</td></tr>
<tr><td rowspan="2">External Complex</td></tr>
<tr><td>GMC</td><td>GMC</td></tr>
<tr><td>IIDK</td><td>IIDK</td><td>IIDK</td><td>IIDK</td></tr>
</table>

Not to scale

Table 1. Comparison of different names used in literature for the tectonic complexes of the SLZ (modified after Regis et al., 2014).

Alternative subdivisions for the SLZ (Table 4.2.1) have been proposed by several authors: Venturini (1995) identified a Monometamorphic Cover Complex, located between the EMC and GMC, while Babist et al. (2006) considered a subdivision based on the correlation of the structures at regional scale and widely mimicking the subdivision in the traditional metamorphic complexes. Regis et al. (2014) proposed an alternative subdivision of the inner part of the SLZ mainly based on geochronological data regarding H*P* assemblages that allow to identify two distinct H*P* metamorphism episodes. Giuntoli & Engi (2016) proposed for the central SLZ two basement complexes separated by a thin slice of monocyclic meta-sediments, called Barmet Shear Zone (Table 4.2.1).

4.2.2.2 Structural-metamorphic outline

The Alpine metamorphism and deformation are heterogeneously recorded and the relationships between deformation and metamorphism are not univocal in the three units of the SLZ and within them (Gosso, 1977; Pognante et al., 1980; Passchier et al., 1981; Williams & Compagnoni, 1983; Ramsbotham et al., 1994; Zucali et al., 2002; Babist et al., 2006; Giuntoli & Engi, 2016; Corti et al., 2017).

Pre-Alpine

The IIDK is escaped from the Alpine eclogitic re-equilibrations and widely preserves the pre-Alpine structures. On the contrary, in the EMC and GMC pre-Alpine structures occur in small-scale relics. In these three complexes, the pre-Alpine imprints show upper amphibolite to granulite facies assemblages (Compagnoni et al., 1977; Manzotti et al., 2014). *P-T* estimates indicate pressures of 0.6-0.9GPa and temperature of 700-850°C (Lardeaux et al., 1982; Lardeaux & Spalla, 1991). This stage is followed by a re-equilibration at 0.4-0.5GPa and 560-630°C (Lardeaux & Spalla, 1991).

Alpine

The Alpine evolution started with prograde blueschist facies imprint that is represented by a prograde foliation developed at pressure higher than 1.6GPa and temperature of 480-600°C (Pognante et al., 1980; Zucali et al., 2004; Babist et al., 2006; Zucali & Spalla, 2011). The eclogitic overprint is associated with a composite foliation related to a regional folding that produced isoclinal centimetre- to metre-sized folds. In the EMC the eclogitic foliation is penetrative and transposes the previous fabrics (Pognante et al., 1980; Williams & Compagnoni, 1993; Ramsbotham et al., 1994; Zucali et al., 2002; Babist et al., 2006; Zanoni et al., 2008; Zanoni, 2010, 2016) at conditions of 1.5-2.0GPa and 500-600°C (Pognante, 1989; Lardeaux & Spalla, 1991; Zucali & Spalla, 2011; Delleani et al., 2012). The eclogitic foliation was overprinted by a retrograde blueschist facies foliations developed at 1.2-1.6GPa and 450-600°C (Pognante, 1989; Zucali et al., 2002; Zucali, 2011) and that locally is dominant (Babist et al., 2006; Giuntoli & Engi, 2016; Corti et al., 2017). Exhumation-related greenschist facies metamorphism overprints all previous fabrics and in the EMC is only locally related to the development of a new foliation at $P<0.7$GPa and $T=320$-500°C (Stünitz, 1989; Pognante et al., 1987; Spalla et al., 1991; Regis et al., 2014). A synthesis of the pressure-temperature conditions of superposed fabrics and of the geochronological data in the EMC is shown in Table 4.2.2.

4.2.2.3 Geochronological outline

Pre-Alpine

The geochronological data for the gabbroic and granitic intrusion in the EMC indicates two clusters at ~ 350 Ma and 290 Ma, respectively: *i.e.* Mucrone granite has Permian age at 293±3Ma (Bussy et al., 1998); 297±18Ma (Rubatto et al., 1999); and 287±7Ma (Cenki-Tok et al., 2011); Cime Bonze gabbro is dated at 352±8Ma (Rubatto et al., 1999), Ivozio gabbro at 355±9Ma (Rubatto et al., 1998; Delleani et al., 2018), and Sermenza gabbro at 288±4Ma (Bussy et al., 1998). Older metaintrusives have been found in the Tavagnasco and Montestrutto areas and display monzogranitic silica-poor compositions and protolith ages of 435±8 Ma and 396±21Ma (Liermann et al., 2002). Relicts of pre-Alpine H*T* metamorphism in the EMC are dated between 313 and 230 Ma (Table 4.2.2).

Alpine

The prograde Alpine blueschist facies metamorphic imprint is described in southern and central EMC (Reinsch, 1979; Pognante et al., 1980; Zucali et al., 2004; Zucali & Spalla, 2011; Gosso et al., 2010; Giuntoli et al., 2017) and is dated between 85 Ma (Cenki-Tok et al., 2011) and 77 Ma (Giuntoli et al., 2017). Geochronological data of eclogitic assemblages highlight contrasting evolution within the EMC. Regis et al. (2014) and Rubatto et al. (2011) identified two distinct H*P* metamorphic episodes (dated respectively 79-75Ma and 70-65Ma) separated by a short exhumation period, whereas Giuntoli et al. (2017) described two crustal slices characterised by eclogitic assemblages dated around 67Ma and 64Ma, respectively. The retrograde blueschist facies is dated in the central EMC at 63-68Ma (Rubatto et al., 1999; Babist et al., 2006; Regis et al., 2014). The greenschist metamorphism in the central EMC is dated around 44 Ma (Babist et al., 2006; Giuntoli et al., 2017), coherently with Biella and Traversella Oligocenic plutons crosscutting the syn-greenschist facies structures (Zanoni, 2010; Zanoni et al., 2010; Zanoni, 2016).

The study area is located within the EMC in upper Valle del Cervo (Biella), ~5km north of Mt. Mucrone-Mt. Mars metagranitoids and surrounding metapelites that are characterised by a dominant Alpine fabric marked by mineral assemblages peculiar of eclogite-facies conditions (*e.g.* Zucali et al., 2002; Delleani et al.., 2012; Delleani et al.., 2013). In the Lago della Vecchia area Zucali (2011), through an exhaustive microstructural analysis on Alpine coronitic assemblages in metaintrusive rocks, proposed a pressure-peak conditions lower than those estimated in other sectors of the EMC and Corti et al. (2017) performed a detailed petro-structural mapping, constrained the mesostructural evolution and individuated homogeneous structural and metamorphic domains for the superposed syn-metamorphic structures.

	Pressure	Temperature	refs.	ages	refs
Pre-Alpine HT	7-9 kbar	700-800°C	(1)		
	0.24-0.44Gpa	680-750°C	(3)		
	4-5 kbar	560-630°C	(1)		
Blueschist - prograde	>1.8 GPa	>600°C	(5) (6)		
	1.8-2.0 GPa	550-580°C	(3)	~77Ma	(4)
	>2 GPa	480-580°C	(7)	~85 Ma	(16)
Eclogite	15-20 kbar	500-600°C	(8)		
	13-15 kbar	500-550°C	(1) (9)		
	>1.5 GPa	500-600°C	(10)	~65Ma	
	HP1; 2.2 GPa	580°C	(11)	79-75Ma	(11)
	HP1; 1.7-1.8 GPa	520-580°C	(12)	~75Ma	(12)
	HP2; 2 Gpa	560°C	(11)	70-65Ma	(11)
	HP2; 1.4-2 GPa	~550°C	(12)	~65Ma	(12)
Blueschist-retrograde	MP; <1.6 GPa	<520°C	(12)	~68Ma	(12)
	<1.6 GPa	<450°C	(13)		
	<1.5 GPa	<600°C	(10)	70-60Ma	(14)
	12.5 kbar	450-550°C	(2)		
Greenschist	<13 kbar	450-500°C	(8) (15)	Before 30Ma	
	<0.7 GPa	<350°C	(10)	Before 30Ma	(10)
	0.15-0.25 GPa	320-360°C	(12)	Before 30Ma	

References: (1) Lardeaux & Spalla (1991); (2) Zucali (2011); (3) Gosso *et alii* (2010); (4) Giuntoli *et alii* (2017); (5) Zucali *et alii* (2004); (6) Zucali & Spalla (2010); (7) Delleani *et alii* (2012); (8) Pognante *et alii* (1987); (9) Compagnoni *et alii* (1977); (10) Zucali *et alii* (2002); (11) Rubatto *et alii* (2011); (12) Regis *et alii* (2014); (13) Pognante (1989); (14) Rubato *et alii* (1999); (15) Williams & Compagnoni (1983); (16) Cenki-Tok *et alii* (2011).

Table 4.2.2. Relationships between deformation and metamorphism in the EMC of the Sesia-Lanzo Zone in terms of Pre-Alpine and Alpine fabrics, related P-T conditions and relatives ages.

4.2.3 Method

The integration of multiscale structural and petrographic analyses is the base for correlating different rock-volumes and for deciphering their tectonometamorphic evolution (Gosso et al., 2015). Field structural correlation exclusively based on geometric criteria is poorly reliable if deformation is heterogeneous (Table 4.2.2; Zucali et al., 2002; Spalla et al., 2000, Salvi et al., 2010). Indeed, during incremental strain, the deformation heterogeneity is responsible for producing poorly or pervasively deformed rock volumes (Spalla & Zucali, 2004). Equally, the metamorphic correlations without meso- and micro-structural constrains for different strain domains is not sufficient due to the catalysing effects of deformation (*i.e.* metamorphic transformations are favored in more deformed domains; Spalla et al., 2000; Spalla et al., 2005). As a consequence, the multiscale correlation of strain domains with mineral assemblages developed during polyphasic deformation is an indispensable tool for unraveling the size and structural and metamorphic evolution of crustal volumes involved in subduction-collision systems (Gosso et al., 2015).

According to Lardeaux & Spalla (1990), Salvi et al. (2010), Roda & Zucali (2011) and Gosso et al. (2015), in deformed rocks three fabric end-members of volumes can be defined: coronitic domains (randomly oriented fabric inherited from protoliths), tectonitic domains (normal planar/linear fabric), and mylonitic domains (pervasive oriented linear and planar fabric). Based on this assumption, mesoscale structural analysis aimed at recognizing strain gradients was performed in the study area (Corti et al., 2017). Microstructural analysis is used to define the relationships between deformation (different strain domains) and mineral growth for each deformation stage in order to identify equilibrium mineral assemblages in different rock types and strain domains. These constrains are the guide to select mineral compositions and perform *P-T* estimates for each superposed fabric. This approach allowed reconstructing the tectonometamorphic evolution of the Lago della Vecchia rocks to be compared with that of other portions of the EMC.

4.2.4 Mesostructural analysis

4.2.4.1 Rock types

According to Corti et al., (2017), four rock types are distinguished through petrostructural mapping (Figure 4.2.2): metaintrusive, banded gneiss, metapelite, and metabasite. In order to better constrain the rock types, a qualitative estimate of the whole rock chemistry is calculated starting from the modal amount of mineral (% area) and mineral chemistry.

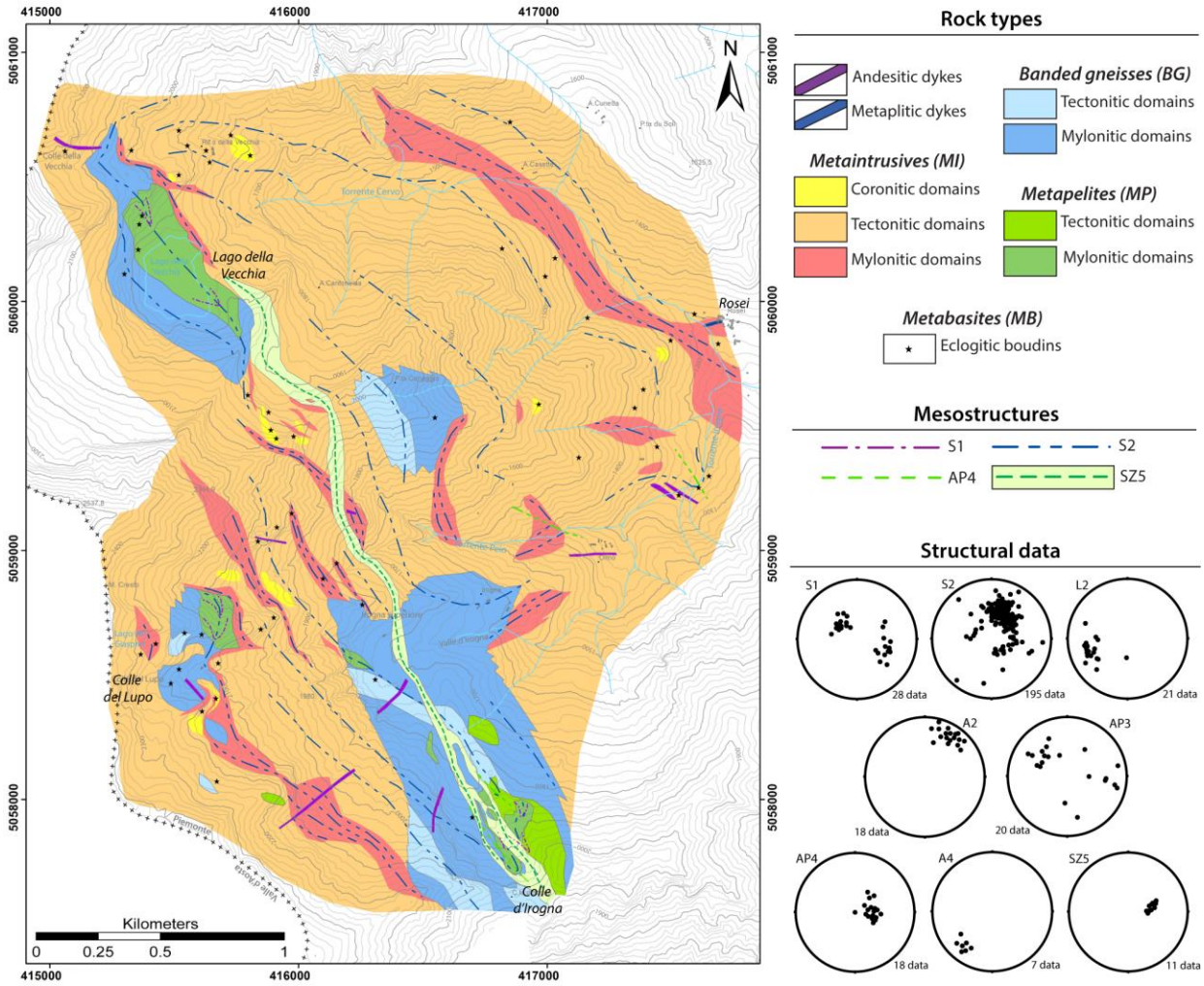

Figure 4.2.2. Petrostructural map and meso-structural data (S: foliation; L: lineation; AP: fold axial plane; A: fold axis; SZ: shear zone), modified after Corti et al. (2017).

1) Metaintrusive (MI) occurs as metre to kilometre-sized bodies that records all the three fabric end-members. Coronitic metaintrusive consists of Qz (30-35%), Pl (20-25%), Kfs (Figure 4.2.3A; 10-15%), Bt (10-15%), Ep (5-10%), ±Grt (<5%), ±Wm (<5%), ±Op (<5%) and have magmatic mineral relicts and igneous texture (Figure 4.2.3A). Tectonitic-to-mylonitic (Figure 4.2.3C) metaintrusives consists of Qz (30-50%), Wm (20-30%), Ep (15-20%), Grt (5%), Act (5%), and magmatic mineral relicts (5%; Kfs); shape preferred orientation (SPO) of Wm, Ep, Grt, and Kfs0 marks the tectonitic-to-mylonitic foliation. Where tectonitic-mylonitic fabric is dominant, metaintrusive preserves coronitic domains as metre- to decametre-sized bodies. On the base of estimated whole rock chemistry, a CIPW normative analysis (Figure 4.2.4) shows protoliths ranging from monzogranite to granodiorite compositions (red stars). According to the classification of granitic rocks (*e.g.* Frost et al., 2001), based on Fe-number (XFe > 0.7-0.8), modified alkali–lime index ($Na_2O + K_2O - CaO < 4$), and aluminium

saturation index (Al/(Ca – 1.67P + Na + K > 1), the protoliths show peraluminous composition (see supplemental material).

2) Banded gneiss (BG) consists of Qz (20-30%), Wm (15-20%), Ep (10-20%), Grt (10%), Ab (5-15%), ± Chl (<5%), ± Kfs (<5%), ± Op (<5%); it shows a mineral banding marked by leucocratic Wm-poor layers and melanocratic Wm-Ep-rich layers (Figure 4.2.3D).

3) Metapelite (MP) consists mostly of micaschists (Figure 4.2.3B) and minor gneisses that both form lenses within mylonitic metaintrusive and banded gneiss.

4) Metabasite (MB) occurs as metre-sized lenses and centimetre-sized boudins within all rock types and it is constituted by Omp (15-25%), Grt (10-20%), Gln (20%), Wm (10-20%), Ep (10-15%), ± Op (<5%). Based on estimated whole rock chemistry, a CIPW normative analysis (Figure 4.2.4) show protoliths with gabbro-diorite compositions (purple stars).

4.2.4.2 Mesostructural evolution

The relationships between the superposed fabrics and successive mineral assemblages recognized at the mesoscale (Figure 4.2.2; Corti et al., 2017) lead to infer two magmatic stages (M0 and M6) and five superposed deformation stages (D1 to D5).

M0 magmatic texture and igneous minerals (Kfs-Bt-Aln) are preserved in metaintrusive coronitic domains (Figure 4.2.3A); contacts between metaintrusive and country rocks are mylonitic all over the study area (Corti et al., 2017). The only magmatic contacts characterise aplite dykes in tectonitic-mylonitic metaintrusive and are overprinted by successive foliations.

During D1 the S1 foliation developed. S1 in metabasite and metapelite (Figure 4.2.3B) is marked by Wm-Cpx-Amp-Grt and Wm-Grt-Rt, respectively. In banded gneiss, S1 is relict and preserved discontinuously within S2 microlithons that are constituted by Wm-Grt-Ep-Rt. In metaintrusive only D1 mineral relicts (Wm-Grt-Zo) are preserved.

During D2, the dominant foliation (S2) developed heterogeneously at the map scale (Figure 4.2.2). S2 foliation transposed and often parallelised igneous structures, lithological surfaces and S1 foliation. In the metaintrusive S2, which consists of Wm-Ep-Pl-Grt, wraps coronitic domains, elongated metabasite boudins (Figure 4.2.3C) and transposed tabular rock bodies such as aplitic dykes. Only in metapelite, S2 is the axial plane foliation of isoclinal folds (Figure 4.2.3B) marked by Czo-Ep-Wm.

D3 structures mainly consist of open folds with sub-vertical axial planes; S3 developed only locally within centimetre-thick shear zones (Figure 4.2.3D) and it is marked by Wm-Amp-Chl.

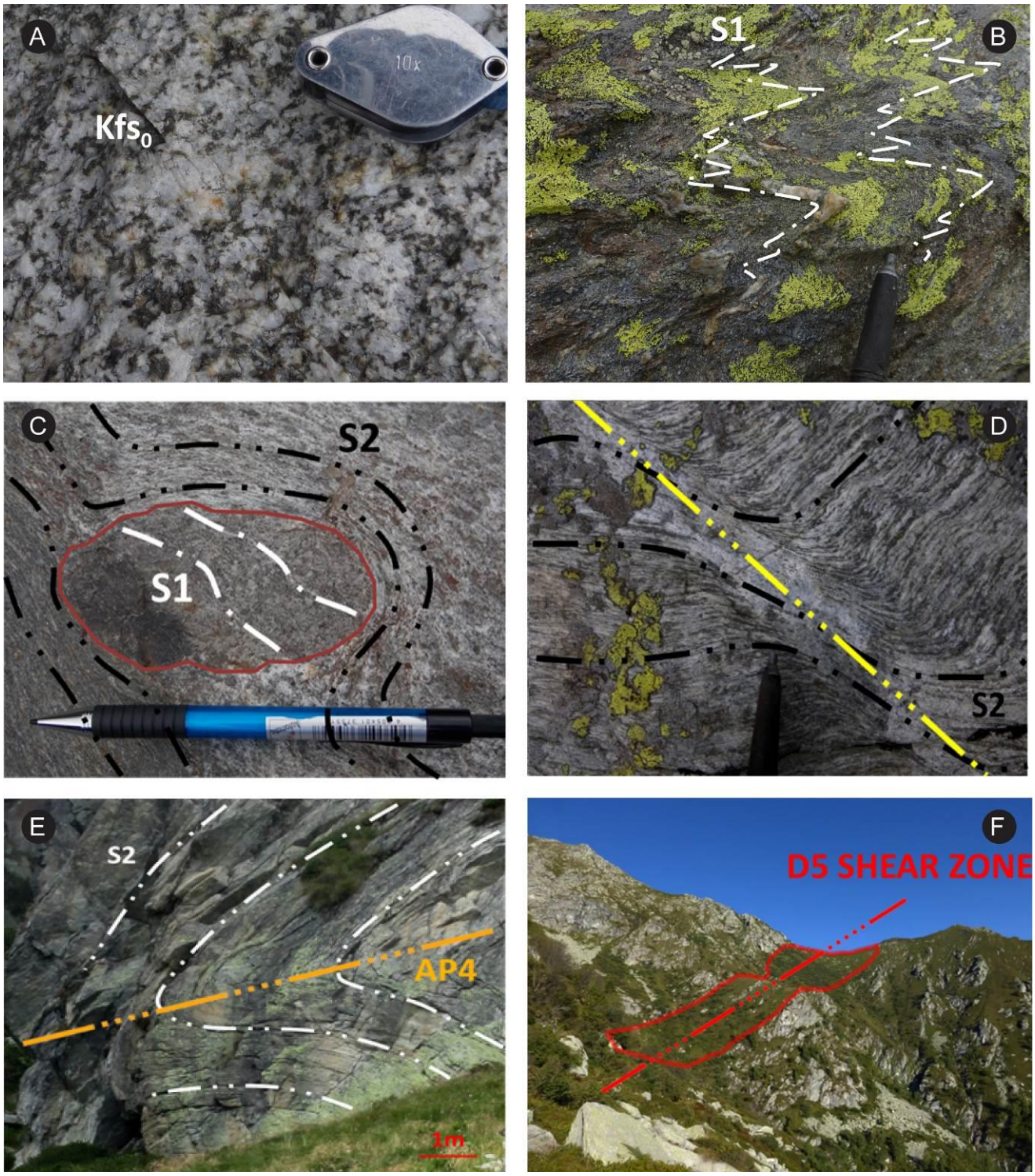

Figure 4.2.3. Mesostructural analysis. A) Igneous texture and magmatic mineral relics (e.g. Kfs and Bt) in coronitic metaintrusive. B) S1 foliation crenulated by D2 tight folding in metapelite. C) S1 preserved into a centimetre-sized metabasic boudin wrapped by S2 foliation in tectonitic metaintrusive. D) Ductile D3 shear zone (yellow line) in mylonitic banded gneiss. E) D4 decametre folding in tectonitic metaintrusive. F) Decametre-long D5 shear zone controlling the slope morphology.

D4 structures consist of metre-sized open folds with sub-horizontal axial plane (Figure 4.2.3E). These folds are better recorded within metapelite where they show a smaller wavelength and an intense crenulation in the hinge zone.

In metaintrusives and banded gneiss, D5 is related to the development of a NW-SE trending kilometre-long and metre-thick shear zone (Figure 4.2.3F) associated with a new mylonitic fabric marked by Wm-Chl-Act, locally overprinted by cataclastic fabric.

During M6 metre-thick andesitic dykes intruded all lithotypes and crosscut all previous structures in the whole area (see for details Corti et al., 2017). These sub-vertical and WNW-ESE trending dykes have been dated across the SLZ at 29-33 Ma (Scheuring et al., 1974; Kapferer et al., 2012).

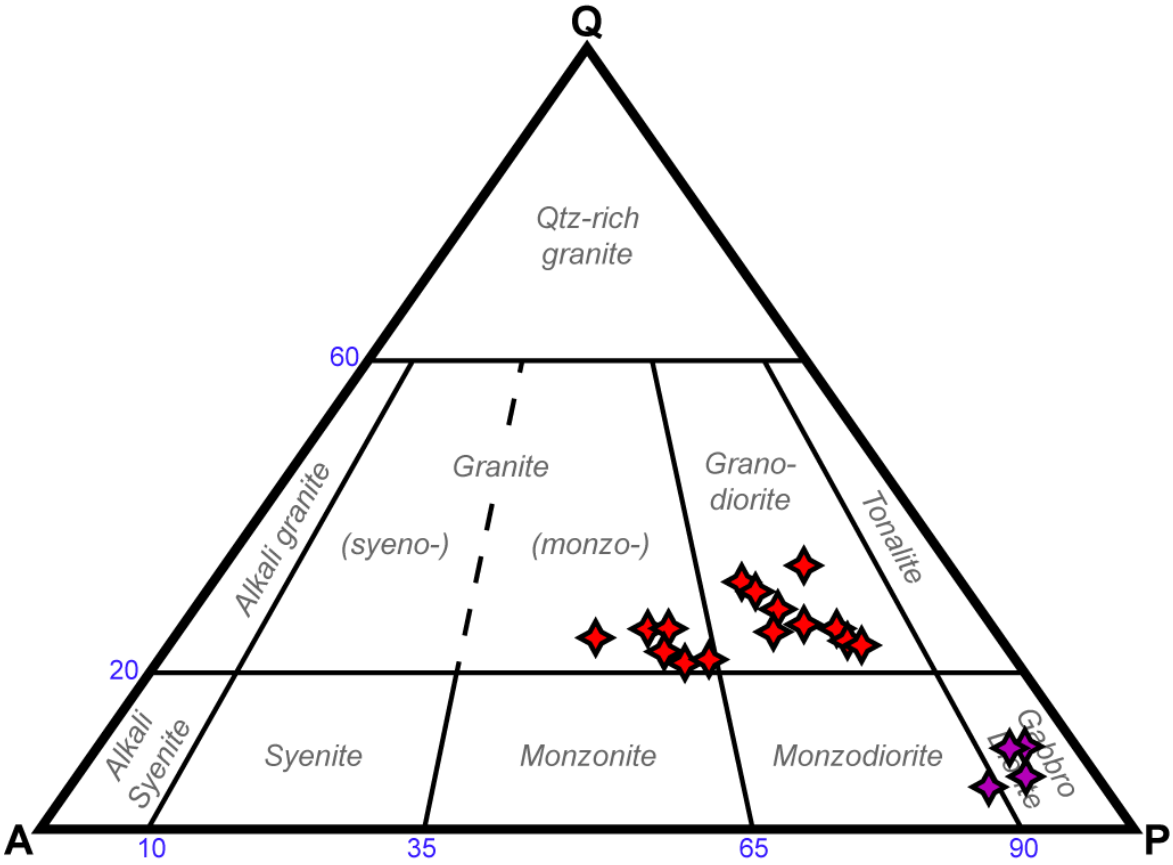

Figure 4.2.4. QAP diagram used to classify metaintrusive and metabasite rocks based on percentages of normative mineralogical composition of Q=quartz; A=alkali feldspar; P=plagioclase (normalised at 100%). Red stars: metaintrusive rocks; purple stars: metabasite rocks.

4.2.5 Microstructural evolution

Deformation-metamorphism relationships have been inferred based on the results of microstructural analysis of 42 thin sections, selected tacking into account the results of mesostructural analysis (Corti et al., 2017). Samples were selected with the aim of inferring the equilibrium mineral assemblages, marking the superposed fabrics individuated at the mesoscale. The relationships between microstructural evolution and growth of metamorphic assemblages are summarized in Table 4.2.3. In the following descriptions, the percentages of minerals are referred to each evolutionary stage and are estimated on the whole rock. Thus, the sum of percentage values gives the actual modal amount of minerals developed during each stage.

4.2.5.1 Pre-Alpine evolution

M0

M0 features are widely preserved in coronitic metaintrusive and as igneous mineral relicts (Kfs0 and Aln0) in tectonitic and mylonitic metaintrusive. These relicts are preserved also in banded gneiss that can be interpreted as deriving from igneous protoliths. Six igneous microdomains have been recognised in fine- to medium-grained phaneritic texture: biotite (7-10%), plagioclase (5-10%), K-feldspar (10-15%), allanite (~3%), white mica (~3%), and titanite (<2%). Bt0 forms 0.2-2 millimetre-sized crystals (Figure 4.2.5a) or aggregates of grains (Figure 4.2.5b). Bt0 shows a pleochroism from brown to reddish brown and is locally zoned with dark cores and light rims. Biotite microdomains are in contact with plagioclase, allanite and K-feldspar domains. Aln0 occurs in well preserved 3-5 mm sized single crystals (Figure 4.2.5b) characterised by varying pleochroism from dark-blue (cores) to light-blue (rims) that correspond to chemical zoning. Allanite microdomains are in contact with biotite, titanite, and plagioclase domains. Wm0 occurs as 0.5-1.0 mm sized single crystals characterised by perfect basal cleavage. Wm0 is locally kinked (Figure 4.2.5c) and is only in contact with plagioclase microdomains. Kfs0 occurs as 1-2 cm sized single crystals with undulose extinction or in aggregates rimmed by syn-D2 and syn-D3-D4 assemblages where it is in contact with plagioclase domains. Pl0 microdomains display millimetre-sized tabular shape and are completely pseudomorphosed by fine-grained syn-D2 assemblage (EpII, WmII, PlII). Ttn0 forms 1.0-2.0 millimetre-sized dark-brown grains with lobate rims. Ttn0 is in contact with Kfs0, Pl0 and Aln0.

Deformation phases	Metaintrusive	Metapelite	Metabasite	Banded Gneiss
M0	Bt_0+Kfs_0+$Wm_{0(?)}$ +Aln_0+Pl_0+Ttn_0 Igneous texture in coronitic domains	not found	not found	Kfs_0+Aln_0 Magmatic minerals relicts
D1	Wm_I+Zo_I+Grt_I +Qz_I±Pl_I±Rt_I no preserved D1 fabrics	Wm_I+Grt_I+Zo_I +Qz_I±Rt_I±Mnz_I in tectonitic fabric	Cpx_I+Grt_I+Wm_I +Amp_I±Czo_I ±Ttn_I±Rt_I in tectonitic fabric	Wm_I+Grt_I+Zo_I +Qz_I±Rt_I no preserved D1 fabrics
D2	Wm_{II}+Grt_{II}+Czo_{II} Ep_{II}+Zo_{II}+Qz_{II}+Pl_{II}+ Bt_{II}+Ttn_{II}±Mnz_{II}±Zrc_{II} in all fabrics	Wm_{II}+Grt_{II} +Czo_{II}+Ep_{II}+Qz_{II} ±Ilm_{II}±Ttn_{II} in tectonitic and mylonitic fabrics	Wm_{II}+Grt_{II} +Amp_{II}+Zo_{II}±Pl_{II} +Cpx_{II}±Op_{II} in all fabrics	Wm_{II}+Grt_{II} +Ep_{II}+Qz_{II}+Czo_{II} +Pl_{II}±Ttn_{II} in tectonitic and mylonitic fabrics
D3	Wm_{III}+Qz_{III}+Ep_{III} +Pl_{III}+Chl_{III}±Amp_{III} ±Ttn_{III}±Op_{III}	Wm_{III}+Ep_{III}+Qz_{III} +Chl_{III}+Amp_{III}	Wm_{III}+Qz_{III} +Amp_{III} ±Ttn_{III}±Op_{III}	Wm_{III}+Ep_{III}+Qz_{III} +Chl_{III}+Amp_{III}
D4	in coronitic and tectonitic fabric	in all fabrics	in coronitic and tectonitic fabric	in all fabrics
D5	Chl_V+Amp_V +Qz_V+Opv in shear zones	not found	not found	Chlv+Amp_V +Qz_V+Op_V in shear zones

Table 4.2.3. Minerals and mineral assemblages characterising superposed fabric types in different rock types.

4.2.5.2 Alpine evolution

D1 stage

D1 fabrics are preserved in MB and MP, while in the other rock-types only D1 mineral relicts are found. In MI and BG, millimetre-sized porphyroclasts of WmI (<5%), GrtI (2-3%), ZoI (2-5%) are observed both in microlithon and cleavage domains. ZoI and WmI show intra-crystalline deformation such as deformation bands and undulose extinction (Figure 4.2.5d). ZoI, WmI, and GrtI show core-

mantle microstructures and grain size reduction. ZoI is micro-boudinaged. GrtI cores show an internal foliation marked by fine-grained crystals of WmI, QzI, ZoI, and RtI with a smaller size than that of the grains constituting the matrix (Table 4.2.4).

MP has an S1 foliation marked by WmI (~15%), ZoI (~5%), and 0.2-0.5 mm RtI and MnzI (<3%) and is crenulated and overprinted by successive fabrics. Microstructural relicts of D1 are millimetre- to centimetre-sized porphyroclasts of WmI with evidence of dissolution and intra-crystalline deformation such as micro-kinks structures, undulose extinction, deformation bands and micro-boudinage. Millimetre-sized porphyroblasts of Grt display cores rich in fine-grained WmI inclusions, surrounded by inclusion free rims (Table 4.2.4); WmI porphyroblasts contain numerous RtI, ZoI, and MnzI.

In MB, S1 is marked by SPO (Shape Preferred Orientation) of CpxI (15-20%) with sharp equilibrium grain boundaries against GrtI (10-15%), WmI (~10%), AmpI (7-10%), and less than 5% of RtI, TtnI, and CzoI (Figure 4.2.5e, Table 4.2.4). WmI locally is characterised by undulose extinction and gentle folding. CpxI occurs as mm- to centimetre-sized porphyroblasts that are often boudinaged (Figure 4.2.5f) with boudin necks filled by fine-grained crystals belonging to successive assemblages grew. GrtI poikiloblasts contain randomly oriented CpxI, AmpI and RtI.

D2 stage

D2 fabrics are the most penetrative in all rock-types. In MI, the S2 spaced and discontinuous foliation is marked by millimetre-sized crystals of QzII (15-20%), WmII (10-15%), GrtII (10-15%), CzoII (~10%), PlII (5-7%), ZoII (3-5%) and less than 3% of ZrcII, MnzII, and TtnII. S2 wraps millimetre-sized porphyroblasts (Figure 4.2.6a) of WmI, ZoI, GrtI (D1-related), and Kfs0 and Aln0 (M0-related). Microlithon consists mostly of fine-grained aggregate of QzII, GrtII, PlII, subeuhedral and zoned CzoII and ZoII, and locally MnzII, ZrcII, and OpII. In low-strain domains, different D2 coronae and associations consist of fine-grained minerals that depend on the igneous microdomains they replaced. Between Bt0 and Pl0 a continuous composite corona of GrtII developed (Figure 4.2.5a). The contact between Aln0 and Ttn0 is marked by a corona constituted by coarse-grained CzoII (Figure 4.2.5b). Between Aln0 and Bt0 a double fine-grained corona occurs and is constituted by GrtII and BtII towards Bt0 and WmII and EpII towards Aln0. Fine-grained aggregates of WmII and GrtII mark the boundary between Wm0 and Pl0 domains (Figure 4.2.5c); the boundary between Kfs0 and Pl0 is marked by a fine-grained double corona made of WmII and PlII aggregates towards Kfs0, and a fine-grained aggregate of CzoII, WmII and GrtII towards Pl0. Between Ttn0 and Pl0 a corona is constituted by a fine-grained aggregate of GrtII, BtII, and OpII.

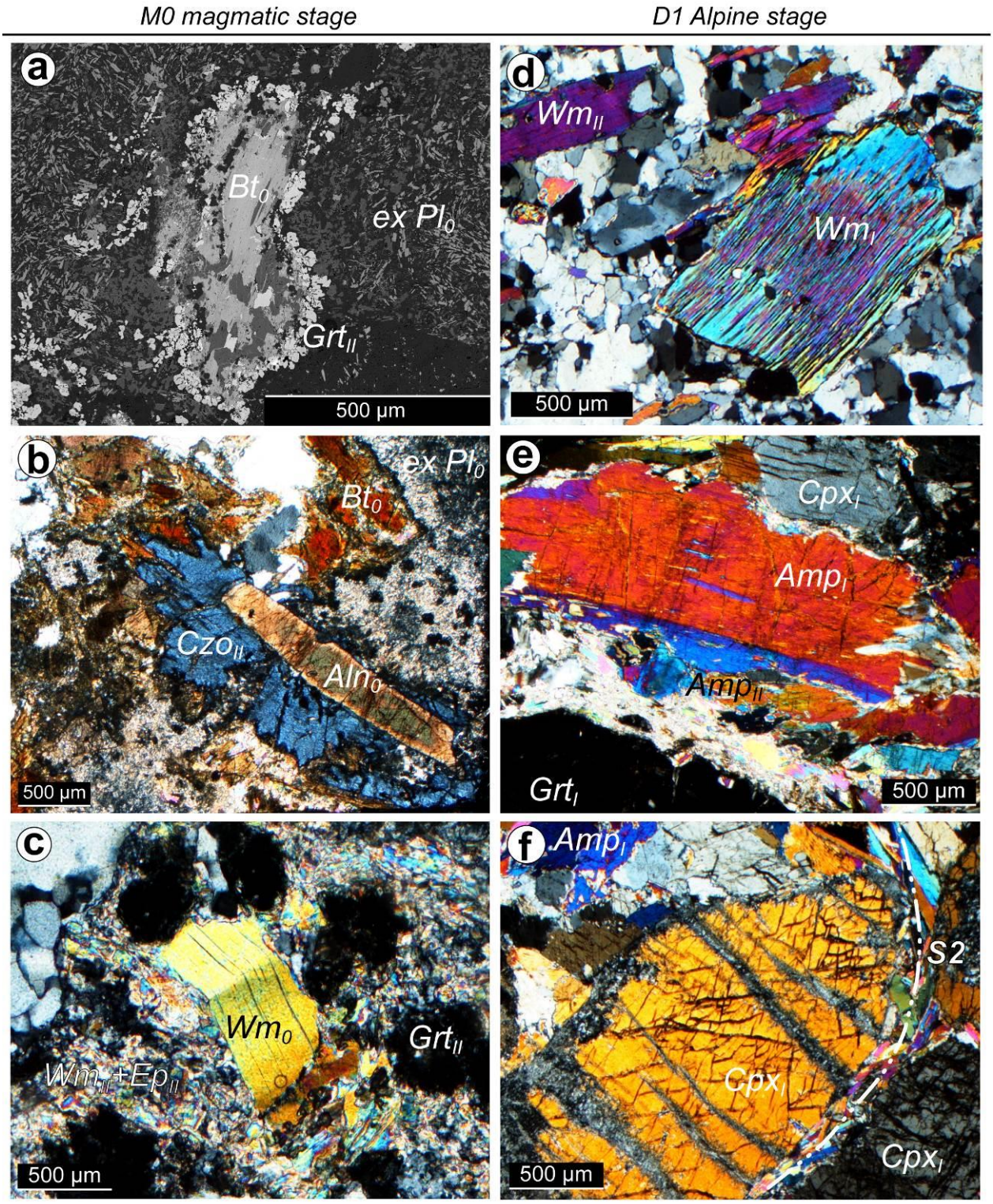

Figure 4.2.5 - Microstructural features of M0 and D1 stages. a) metaintrusive; Bt0 occurs as single crystals with a continuous corona of GrtII, BSE image; b) metaintrusive; Aln0 occurs in well-preserved single crystals, crossed polars; c) metaintrusive; between the single crystal of Wm0 and GrtII fine-grained corona of WmIII and EpIII developed, crossed polars. d) metaintrusive; WmI shows kinked basal cleavages, crossed polars; e) metabasite; S1 marked by AmpI, CpxI, and GrtI; AmpII rims AmpI, crossed polars; f) metabasite; millimetre-sized CpxI is boudinaged and partially re-crystallised at the grain boundaries, crossed polars.

BG are characterised by a spaced and discontinuous S2 foliation (Table 4.2.4) that is marked by WmII (~10%), GrtII (7-10%), EpII (5-7%), CzoII (~5%), and TtnII (<3%) and by microlithon domains consisting of fine-grained QzII (25-30%) and PlII (5-7%) grains elongated parallel to S2. Some samples display locally fine-grained euhedral GrtII levels alternating to Grt-poor levels often contain magmatic relicts (Kfs0 and Aln0).

In MP a pervasive S2 foliation is continuous in micaschists and spaced in gneisses. S2 foliation wraps the D1 relicts (Table 4.2.4) and is marked by millimetre-sized crystals of WmII (~20%), GrtII (7-10%), EpII (~5%), CzoII (<3%), IlmII (<3%), TtnII (<3%).

In high-strain domains, MB shows a continuous S2 foliation (Figure 4.2.6b) that is marked by SPO and LPO (Lattice Preferred Orientation) of 0.5-1.0 millimetre-sized crystals of AmpII (~10%), CpxII (5-7%), WmII (~5%), and ZoII (<5%). Euhedral millimetre-sized inclusion-free GrtII (~5%) shows rational grain boundaries (Table 4.2.4) with WmII and CzoII (~5%). In low-strain domains the fine-grained WmII and CpxII form a mineral assemblage in the boudin necks of CpxI (Figure 4.2.6c). 0.1-0.5 mm sized AmpII, PlII and ZoII crystals developed between CpxI and GrtI (Table 4.2.4).

Deformation stage	MB	BG	MP
M0	Not found	Magmatic relicts Kfs; Aln	Not found
D1	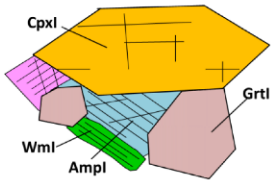	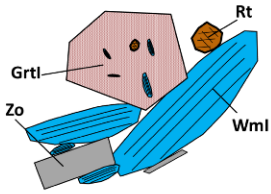	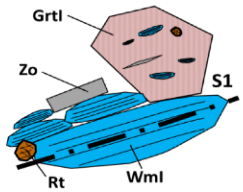
D2	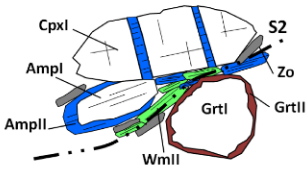	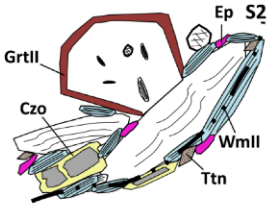	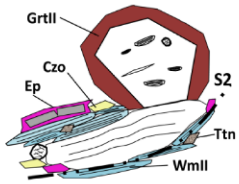
D3	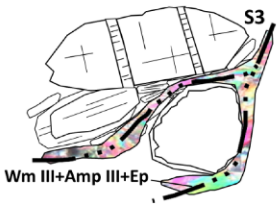		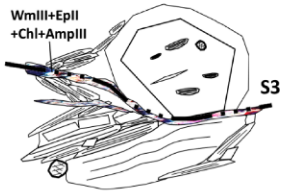
D4			

Table 4.2.4 – Synoptic representation of microstructural evolution during the successive deformation stages in metabasite (MB), banded gneiss (BG), and metapelite (MP).

D3-D4 stages

D3 and D4 structures are locally related to the development of a S3 and S4 foliations, at low angle with respect to the S2 foliation, that is dominant in mylonitic domains; in coronitic fabrics, D3 and D4 are characterised by mimetic growth and development of coronae.

In MI the local S3 foliation is marked by fine-grained WmIII (5-10%), EpIII (~7%), ChlIII (5-7%), AmpIII (~5%), PlIII (~5%), and less than 5% of TtnIII and OpIII. SPO of millimetre-sized crystals of PIIII, 0.2-0.7 millimetre-sized WmIII, TtnIII, and EpIII aggregate mark an incipient S3 foliation (Figure 4.2.6d). 0.1-0.2 millimetre-sized grains of WmIII and ChlIII developed along cleavages of WmI and WmII porphyroclasts and grain boundaries and microfractures of Grt porphyroblasts.

In the medium-strained BG and MP, D3 stage is associated with micro-folding marked by an incipient S3 foliation (Figure 4.2.6e) constituted by fine-grained crystals of WmIII (3-5%), EpIII (3-5%), ChlIII (~3%), and AmpIII (~3%). In BG and MP high-strain domains a pervasive S4 foliation developed (Table 4.2.4) involving a grain-size reduction (Figure 4.2.6f).

MB are characterised by the local development of D3 assemblages that consist of fine-grained WmIII (5-7%), AmpIII (~5%), EpIII (<5%), TtnIII (2-3%), OpIII (<2%) between boudinaged CpxI and along porphyroblast boundaries (Table 4.2.4).

D5 stage

D5 affects only MI and BG and is associated with extremely localised overprint related to D5 meso-shear zones marked by 0.3-0.5 millimetre-sized grains of ChlV (3-5%area), AmpV (~3%area) and OpV (<3%area).

4.2.6 Mineral chemistry

WDS mineral chemical analyses were acquired based on the reconstructed mineral-growth sequence for each deformation stage. The Electron Microprobe (JEOL 8200 Super Probe – EMPA operation software) operating at the Dipartimento di Scienze della Terra “A. Desio” – Università degli Studi di Milano was used. Accelerating voltage was 20 kV and filament intensity was 1.70 A; beam sizes of 5µm was enlarged at 10 µm to analyse phyillosilicates. Natural silicates were used as standards and matrix corrections were calculated with ZAF (Z=atomic number, A=absorption, F=fluorescence) procedure (Armstrong & Buseck, 1975). Mineral chemical analyses are reported in the supplemental material as function of rock types and evolutional stages.

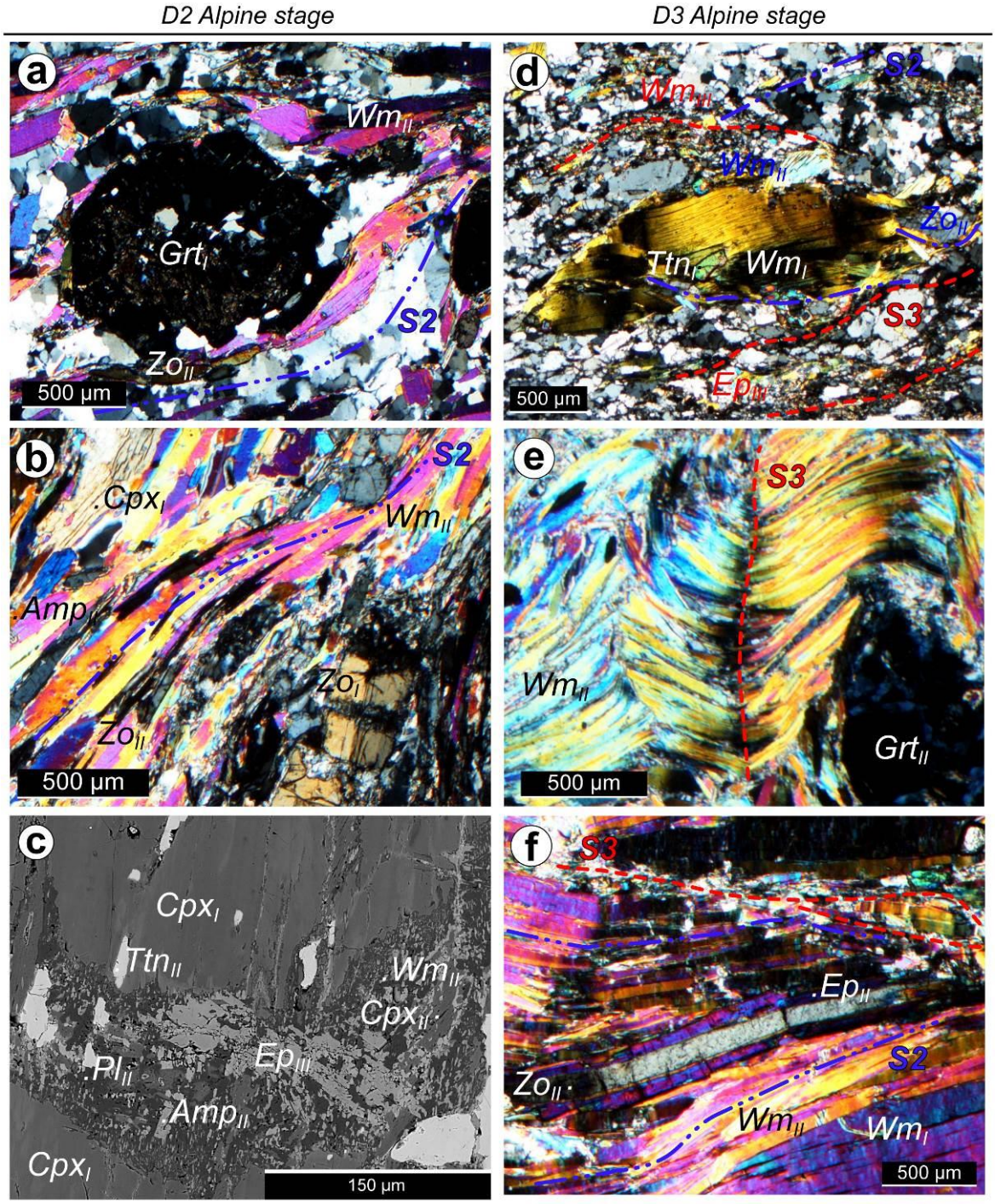

Figure 4.2.6 - Microstructural features of D2 and D3 stages. a) metaintrusive; S2 foliation marked by SPO of WmII and ZoII wraps GrtI, crossed polars; b) metabasite; S2 foliation marked by SPO and LPO of AmpII, WmII and ZoII, wrapping a ZoI porphyroclast, crossed polars; c) metabasite; syn-D2 mineral assemblage consists of WmII+PlII+CpxII+AmpII and grew in the boudin neck of CpxI; syn-D3 EpIII replaced syn-D2 minerals, BSE image; d) banded gneiss; S3 foliation crosscuts S2 and is marked by fine-grained crystals of WmIII, EpIII and ChlIII; S2 is marked by WmII, ZoII, PlII, crossed polars; e) metapelite; WmII is crenulated during D3, crossed polars; f) metapelite; S3 foliation, marked by fine-grained crystals of WmIII, EpIII and ChlIII, crosscut S2 foliation marked by WmII, ZoII, EpII, crossed polars.

Mineral formulae of amphibole and clinopyroxene were calculated following Locock (2014) and Morimoto (1988), respectively. All other mineral formulae were calculated according to Deer et al. (1992) with jPTGUI software (Zucali, 2005). The stoichiometric formulae are based on 12 oxygen atoms for Grt, 22 oxygen atoms for Wm and Bt, 23 oxygen atoms for Amp, 6 oxygen atoms for Cpx, 12.5 oxygen atoms for Ep, 10 oxygen atoms for Ttn, and 14 oxygen atoms for Chl.

Garnet. In MI GrtII mainly consists of Ca (1.11-1.94 a.p.f.u.), Fe^{2+} (0.97-1.62 a.p.f.u.), and minor Mg (0.03-0.22 a.p.f.u.) contents. Within this broad composition GrtII shows chemical variations depending on the magmatic microsites it replaces (Figure 4.2.7A). GrtII replacing Aln0 shows the highest Ca (1.88-1.94 a.p.f.u.) and the lowest Fe^{2+} (0.97-1.13 a.p.f.u.) and Mg (0.03-0.07 a.p.f.u.) contents. GrtII replacing Pl0 shows a lower Ca (1.31-1.38 a.p.f.u.), higher Fe^{2+} (1.13-1.21 a.p.f.u.) and similar Mg (0.03-0.07 a.p.f.u.) contents with respect to the GrtII that rims Aln0 microsites. In the coronitic structure around Bt0, GrtII shows a Ca content of 1.38-1.71 a.p.f.u. and is richer in Fe2+ (1.42-1.48 a.p.f.u.) and Mg (0.13-0.14 a.p.f.u.) than the two types of GrtII mentioned above. In the Ttn0 corona, GrtII shows the highest amount of Fe^{2+} (1.60-1.62 a.p.f.u.) and Mg (0.22 a.p.f.u.) and the lowest amount in Ca (1.11-1.20 a.p.f.u.).
In MP and BG, GrtII is extremely rich in Ca (2.39-2.66 a.p.f.u.) and shows Ca-rich cores and Ca-poor rims. GrtI has lower Ca (0.52-0.57 a.p.f.u.) and higher Fe^{2+} contents (2.02-2.08 a.p.f.u.) than GrtII.
GrtI in MB is Mg-rich where it is associated with WmI; in this case, Mg content decreases and Ca content increases from cores to rims. GrtI is Mg-poor where it is associated with CpxI, and Mg content increases and Ca decreases from core to rims.

White mica. In all rock types, Si content decreases progressively from WmI to WmIII. In MI, Wm is mostly phengitic and displays a wide compositional range. WmI has higher Si contents, ranging between 6.78 and 7.00 a.p.f.u., and lower Al^{tot} (3.90-4.30 a.p.f.u.) and Mg contents (0.41-0.70 a.p.f.u.) than WmII (Si = 6.60 - 6.80 a.p.f.u.; Figure 4.2.7B; Mg ca. 0.32 a.p.f.u.; Al^{tot} =3.90-4.40 a.p.f.u.). WmIII has Si and Al^{tot} content of 6.38-6.52 a.p.f.u. and 4.80-5.45 a.p.f.u., respectively.
In BG, WmI has Si contents ranging between 6.78 and 7.00 a.p.f.u. and Altot between 3.90 and 4.30 a.p.f.u.. Whereas, WmII has Si contents varying from 6.75 to 6.85 a.p.f.u., Al^{tot} from 4.1 to 4.3 a.p.f.u., Fe^{tot} from 0.3 to 0.46 a.p.f.u., and Mg from 0.5 to 0.64 a.p.f.u.. WmIII has Si and Al^{tot} content of 6.46 a.p.f.u. and 4.78 a.p.f.u., respectively.
MP contains WmI with Si content ranging from 6.75 to 7.00 a.p.f.u., Al varies from 4.10 to 4.60 a.p.f.u., Fe^{tot} from 0.37 to 0.54 a.p.f.u., and Mg from 0.32 to 0.47 a.p.f.u.. Whereas, WmII displays a Si contents varying from 6.61 to 6.78 a.p.f.u. and Al^{tot} from 4.20 to 4.46 a.p.f.u.

In MB, Wm is phengitic and displays higher #Mg with respects to Wm in other rock-types, due to the basic bulk rock composition. In WmI Si contents vary from 6.75 to 6.85 a.p.f.u., Al from 4.1 to 4.3 a.p.f.u., Ti content does not exceed 0.65 a.p.f.u., Mg contents vary from 0.50 to 0.70 a.p.f.u., and Al^{tot} content, from 4.25 to 4.50 a.p.f.u.. In WmII Si contents varying from 6.69 to 6.78 a.p.f.u. and Al^{tot} from 4.05 to 4.72 a.p.f.u.

Amphibole. The analysed amphiboles in MB and MI are ascribed to the Alpine evolution (D1, D2 and D3-D4) and cover the winchite, edenite-hornblende, and actinolite compositional fields (Figure 4.2.7C). AmpI has winchite composition, AmpII is edenite-hornblende, and AmpIII shows actinolite compositions. AmpI displays the highest Na/Ca ratio and Al^{VI} content, whereas the Al^{VI} content progressively decreases in AmpII and AmpIII.

Clinopyroxene. In MB, CpxI is omphacite and displays compositions strongly controlled by the adjacent mineral phases and assemblage. CpxI adjacent to WmI is richer in Fe^{2+} (0.2-0.25 a.p.f.u.), in Ca (0.39-0.5 a.p.f.u.) (Figure 4.2.6A) and poorer in Jd (50-60%) than CpxI in contact with GrtI (Fe^{2+} from 0.1 to 0.2 a.p.f.u.; Ca from 0.21 to 0.38 a.p.f.u; Jd from 68 to 75%). CpxII is diopside and contains Fe^{2+} ranging from 0.2 to 0.5 a.p.f.u. and Ca from 0.78 to 1.00 a.p.f.u. (Figure 4.2.7D).
Biotite. In MI, igneous biotite Bt0 shows high Ti contents (0.37-0.52 a.p.f.u.; Figure 4.2.7E) and XMg contents around to 0.4-0.5. BtII is strongly depleted in Ti (lower than 0.11 a.p.f.u.) and has similar in XMg contents (0.4-0.6) with respect to Bt0.

Epidote. Epidote covers a large compositional field and is represented by Zo, Ep, Czo, and Aln. In all rock-types the EpI is mainly Zo with Fe^{3+} content ranging from 0.1 to 0.2 a.p.f.u., Al^{VI} and Ca contents are higher than 2.8 a.p.f.u. and 1.8 a.p.f.u., respectively. EpII/III consist of Ep and Czo with a content in Fe^{3+} from 0.2 to 1.0 a.p.f.u., Al^{VI} from 2.0 to 2.6 a.p.f.u., and Ca from 2.0 to 2.6 a.p.f.u.. In MI magmatic Aln0 displays higher Fe^{3+} (0.74-1.24 a.p.f.u.) and lower Ca (1.02-1.22 a.p.f.u.) contents than the other types of Ep. Furthermore, from cores to rims Fe^{2+} and total REE content decrease with the increasing of Ca and Al^{VI} content (0.32 -0.98 a.p.f.u.).

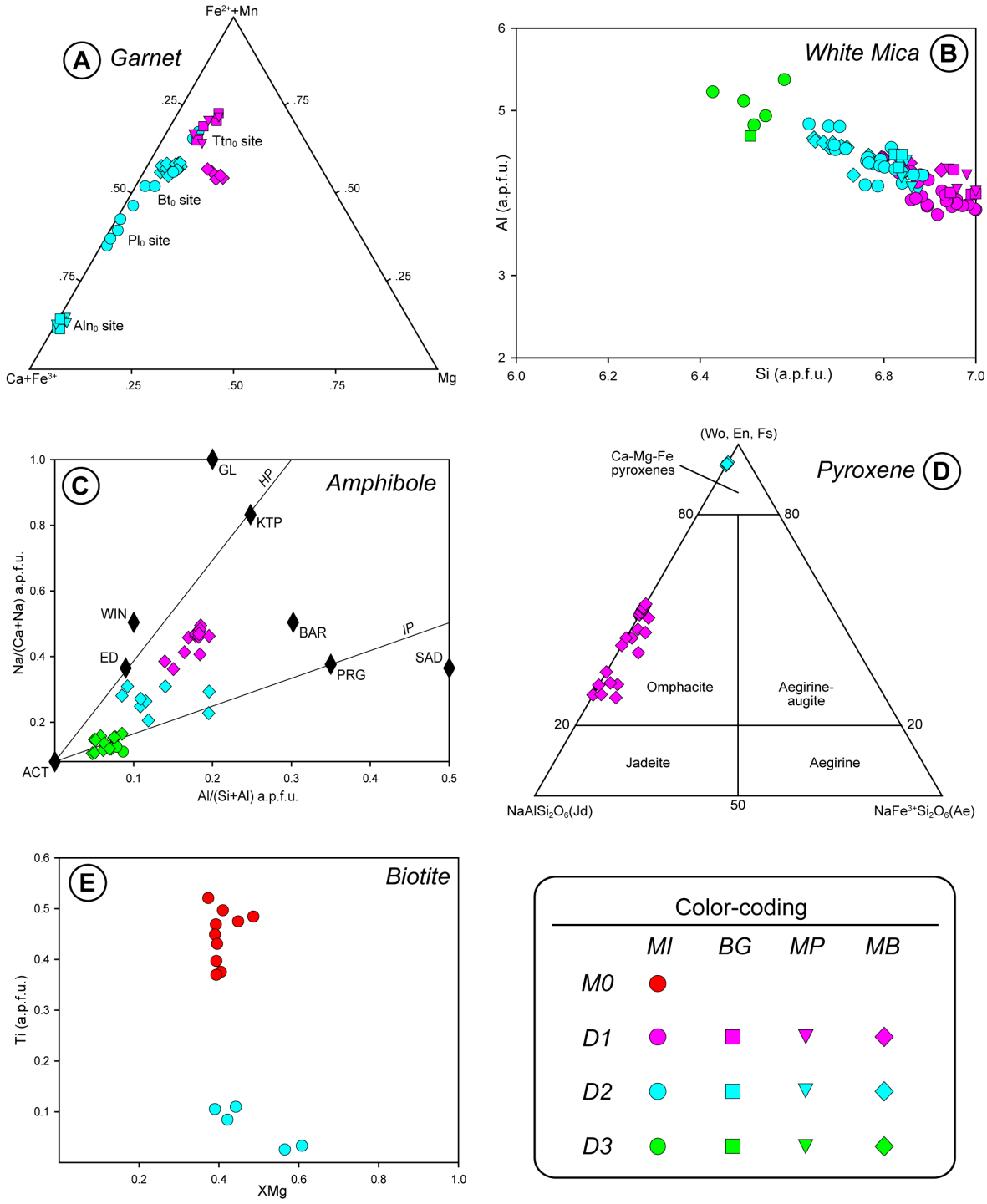

Figure 4.2.7 - A) ternary diagram showing the Grt compositional variations in terms of $Ca+Fe^{3+}$, $Mn+Fe^{2+}$, and Mg contents and also with respect to the magmatic mineral replaced; B) variations of Si and Al contents in Wm; C) Al/(Si+Al) vs. Na/(Na+Ca) diagram showing the compositional variation of Amp. Diamonds locate end-member compositions (ACT=actinolite; BAR=barroisite; ED=edenite; GL=glaucophane; KTP=katophorite; PRG=pargasite; SAD=sadanagaite; WIN=winchite). Straight lines define high-pressure (HP) and intermediate pressure (IP) amphibole trends from Vermont (after Laird & Albee, 1981); D) Ternary diagram showing the compositional variation of Cpx in terms of (Ca – Mg – Fe), Na and Fe^{3+}; E) diagram showing the Bt chemical variation in XMg and Ti content.

Titanite. Ttn has a variable Ti content ranging from 0.82 to 0.94 a.p.f.u. in MI, from 0.85-0.95 a.p.f.u. in BG, from 0-85-0.88 a.p.f.u. in MP, and from 0.86 to 0.88 a.p.f.u. in MB. Al content varies from 0.04 to 0.16 a.p.f.u..

Chlorite. In BG and MB, chlorite ascribed to D3-D4 stage is pycnochlorite, whereas in MI and BG D5 chlorite has compositions between ripidolite and brunsvigite (Hey, 1954). D3-D4 Chl displays Si contents around 5.55 a.p.f.u. and XFe ca. 0.49, whereas D5 Chl shows Si contents of ca. 6.0 a.p.f.u and XFe of 0.7.

4.2.7 Metamorphic conditions

Thermobarometric estimates have been performed to constrain the metamorphic conditions and *P*/*T* ratios under which the successive tectonometamorphic stages developed. For each metamorphic assemblage, *P-T* estimates were performed by the application of different well-constrained geothermobarometers (Table 4.2.5) to mineral pairs in mutual contact with rational grain boundaries, indicating textural equilibrium. Moreover, average *P-T* calculations were performed using the THERMOCALC thermodynamic dataset on the basis of the activity of end-members calculated by AX software (Holland & Powell, 1998). Geothermobarometers were applied considering the calibration conditions and constraints on minerals and bulk rock chemistry. The results obtained for each stage are reported in Table 4.2.5.

M0 stage. The M0 mineralogical relicts are Bt0, Kfs0, Wm0, Aln0, and Ttn0. The *P-T* estimates for the igneous stage indicate *T*=710±19°C based on Ti-XMg content in Bt0 (thermometer calibrated for metapelites and extended for peraluminous metamorphic rocks; Henry et al., 2005) and *P*=0.52±0.21 GPa using the normative contents of Qz, Ab, and Or (Yang, 2017).

D1 stage. In MB the tectonitic fabric D1 is associated with the mineral assemblage CpxI (Omp), AmpI, WmI, GrtI and CzoI. The THERMOCALC average PT calculation suggests a *P*=1.9-2.3GPa and a *T*=475-530°C. Pressures of 2.33±0.06GPa are estimated with the barometer Grt-Cpx-Wm ((Krogh-Ravna & Paquin, 2003) and pressure values higher than 1.38±0.01 GPa are based on Xjd content in CpxI (Holland, 1980). The Mg-Fe^{2+} exchange thermometer between Grt-Cpx suggests temperatures of 566±10°C (Sengupta et al., 1989) and of 533±35°C (Powell, 1985) and considering these temperatures, the pressure suggested by the barometer based on Si^{4+} content in Wm (Massonne & Schreyer, 1987) is higher than 1.0-1.2GPa. Even though the Si^{4+} barometer is calibrated for feldspar-bearing systems it is largely used also in basic systems (*e.g.* Escuder-Viruete & Pérez-Estaún, 2006).

In MP the tectonitic fabric is associated with the mineral assemblage WmI, GrtI, ZoI, QzI and RtI. The Grt-Wm (WU et al., 2002) thermometer suggests a *T*=452±17°C and the Si^{4+} content (Massonne & Schreyer, 1987) in phengitic mica suggests a *P*>1-1.4GPa for that *T* interval. The average PT gives *P*=1.85-2.10GPa and *T* of 450-550°C.

In tectonitic MI the D1 is characterised by the assemblage: WmI, GrtI, ZoI. The Grt-Wm (Wu et al., 2002) thermometer suggests a *T*=501±22°C and the Si^{4+} content (Massonne & Schreyer, 1987) in phengitic mica suggests a *P*>1-1.2GPa for that *T* interval.

In BG the D1 is characterised by the assemblage: WmI, GrtI, ZoI and EpI. The Grt-Wm (Wu et al., 2002) thermometer suggests a *T*=500±54°C and the Si^{4+} content (Massonne & Schreyer, 1987) in phengitic mica suggests a *P*>1-1.4GPa for that *T* interval. The average PT gives *P*=2.09-2.18GPa and *T* = 460-520°C

thermobarometer	T (°C)	P (GPa)	Refs
M0 magmatic stage			
	coronitic metaintrusive		
Ti/XMg in Bt0	710±19		(1)
(1) Qz normative contents		0.52±0.21	(2)
(2) Ab, Or normative contents		0.52±0.21	(2)
D1 Alpine stage			
	metabasite		
GrtI-CpxI (Mg-Fe2)	533±35		(3)
GrtI-CpxI (Mg-Fe2)	570±31		(4)
Grt+Wm+Cpx+Amp	475-530	1.90-2.30	(5)
Xjd in CpxI		1.38±0.01	(6)
Si4+ in WmI		>1-1.4	(7)
GrtI-CpxI-WmI (Mg-Fe2)		2.33±0.06	(8)
GrtI-CpxI (Mg-Fe2)	566±10		(9)
GrtI-CpxI (Mg-Fe2)	510±16		(10)
	metapelite		
Si4+ in WmI		>1-1.4	(7)
GrtI-WmI (Fe2-Mg)	452±17		(11)
Wm+Grt+Zo+Qz	450-550	1.85-2.10	(5)
	banded gneiss		
Si4+ in WmI		>1-1.4	(7)
GrtI-WmI (Fe2-Mg)	500±54		(11)
Wm+Grt+Zo+Qz	460-520	2.09-2.18	(5)
	tectonitic metaintrusive		
GrtI-WmI (Fe2-Mg)	501±22		(11)
Si4+ in WmI		>1-1.2	(7)

thermobarometer	T (°C)	P (GPa)	Refs
D2 Alpine stage			
	metabasite		
GrtII-CpxII (Mg-Fe2)	491±28		(3)
GrtII-CpxII (Mg-Fe2)	461±17		(4)
Xjd in CpxII		1.21±0.01	(6)
Si4+ in WmII		>0.9-1.1	(7)
GrtII-AmpII (Mg-Fe2)	575±14		(12)
	metapelite		
GrtII-WmII (Fe2-Mg)	419±19		(11)
Si4+ in WmII		>1-1.2	(7)
	banded gneiss		
GrtII-WmII (Fe2-Mg)	472±64		(11)
Si4+ in WmII		>0.9-1.2	(7)
	coronitic metaintrusive		
Ti/XMg in BtII	392±46		(1)
Si4+ in WmII		>1-1.2	(7)
	tectonitic metaintrusive		
GrtII-WmII (Fe2-Mg)	425±65		(11)
Si4+ in WmII		>1-1.2	(7)
D3-D4 Alpine stage			
	metabasite		
WmIII+PIII (Na-K)	357±20		(13)
	metapelite		
AlIV in ChII	298±14		(14)
Fe2-Mg in ChII	305±7		(15)
	banded gneiss		
AlIV in ChII	309±19		(14)
Fe2-Mg in ChII	317±20		(15)
	coronitic metaintrusive		
WmIII+PIII (Na-K)	390±72		(13)
AlIV in ChII	295±7		(14)
Si4+ in WmIII		>0.5-0.7	(7)
	tectonitic metaintrusive		
WmIII+PIII (Na-K)	245±20		(13)
AlIV in ChII	315±11		(14)

References

(1) Henry et alii, 2005
(2) Yang, 2017
(3) Powell, 1985
(4) Krogh-Ravna, 2000
(5) Av.PT - Holland & Powell, 1998
(6) Holland, 1980
(7) Massone & Schreyer, 1987
(8) Krogh-Ravna & Paquin, 2003
(9) Sengupta et alii, 1989
(10) Ai, 1994
(11) Wu et alii, 2002
(12) Graham & Powell, 1984
(13) Green & Usdansky, 1986
(14) Chatelineau, 1988
(15) Jowett, 1991

Table 4.2.5. PT estimates of magmatic and superposed deformation stages in metabasite, banded gneiss, coronitic and tectonitic metaintrusive.

D2 stage. In MI the coronitic fabric consists of WmII, QzII, BtII, CzoII, ZoII, GrtII, PlII, TtnII and OpII. Temperature obtained using Ti-XMg in Bt (Henry et al., 2005) is 392±46°C. Upon these temperatures, the Si^{4+} content (Massone & Schreyer, 1987) in Wm gives pressure higher than 1.0-1.2 GPa. The tectonitic fabric is marked by WmII, GrtII, CzoII, QzII, TtnII and OpII mineral assemblage. Temperature obtained using the Grt-Wm (Wu et al., 2002) thermometer is 425±65°C and the Si^{4+} content (Massone & Schreyer, 1987) in Wm suggests *P*>1.0-1.2GPa.

D2 in MB is associated with the mineral assemblage constituted by AmpII, GrtII, CpxII (Di), WmII, CzoII, EpII, PlII and TtnII. Pressure obtained using the Si^{4+} content in phengitic mica is higher than 0.9-1.1GPa for *T* interval of 500-600°C, whereas Xjd content in Cpx indicates *P*>1.21±0.01 (Holland, 1980). The Grt-Amp (Graham & Powell, 1984) and Ti content in Amp (Otten, 1984) suggest *T* range of 575±14°C and 554±28°C, respectively.

In MP the tectonitic fabric is associated with mineral assemblage WmII, GrtII, CzoII, QzII and TtnII. The Si^{4+} content (Massone & Schreyer, 1987) in phengitic mica indicates *P*>1.0-1.2GPa for *T* interval derived by the Grt-Wm (Wu et al., 2002) thermometer that suggests *T*=419±19°C.

D2 in BG is characterised by the mineral assemblage WmII, GrtII, CzoII, EpII, QzII, PlII and TtnII. The Si^{4+} content (Massone & Schreyer, 1987) in phengitic mica indicates *P*>0.9-1.2GPa for *T* interval of 400-550°C. The Grt-Wm (Wu et al., 2002) thermometer suggests *T*=472±64°C.

D3-D4 stage. MI contains the mineral assemblage: WmIII, EpIII, AmpIII, QzIII, ChlIII, PlIII TtnIII. In the tectonitic fabric, Wm-Pl equilibrium (Green & Usdansky, 1986) and Al^{IV} content in Chl (Cathelineau, 1988) suggest temperatures of 245±20°C and 315±11°C, respectively. In coronitic MI Wm-Pl (Green & Usdansky, 1986) and Al^{IV} in Chl (Cathelineau, 1988) thermometers suggest temperatures of 390±72°C and 295±7°C, respectively; for these ranges of temperatures, Si^{4+} in Wm (Massone & Schreyer, 1987) indicates a *P*>0.5-0.7GPa.

MP is characterised by the mineral assemblage: WmIII, AmpIII, EpIII, PlIII, QzIII and ChlIII. The Al^{IV} contents (Cathelineau, 1988) and Fe-Mg exchange (Jowett, 1991) thermometers for Chl suggest temperatures of 298±14°C and 305±7°C.

MB shows the assemblage: WmIII, AmpIII, EpIII, PlIII, QzIII and TtnIII; the Wm-Pl (Green & Usdansky, 1986) thermometer, calibrated for peraluminous rocks, indicates temperature of 357±20°C, which we consider anyway as these values are consistent with those obtained with the same calibration for the other rock types (Table 4.2.5).

BG is characterised by the assemblage WmIII, EpIII, QzIII, PlIII and ChlIII. The Al^{IV} contents (Cathelineau, 1988) and Fe-Mg exchange (Jowett, 1991) thermometers for Chl suggest temperatures of 309±19°C and 317±20°C, respectively.

The inferred metamorphic conditions with standard deviations obtained from the different thermobarometric calibrations applied in any rock type (MI, MP, BG, MB) are synthesised in Figure 4.2.8, which shows four resulting clusters of *P-T* estimates related to the successive stages (M0, D1, D2 and D3-D4).

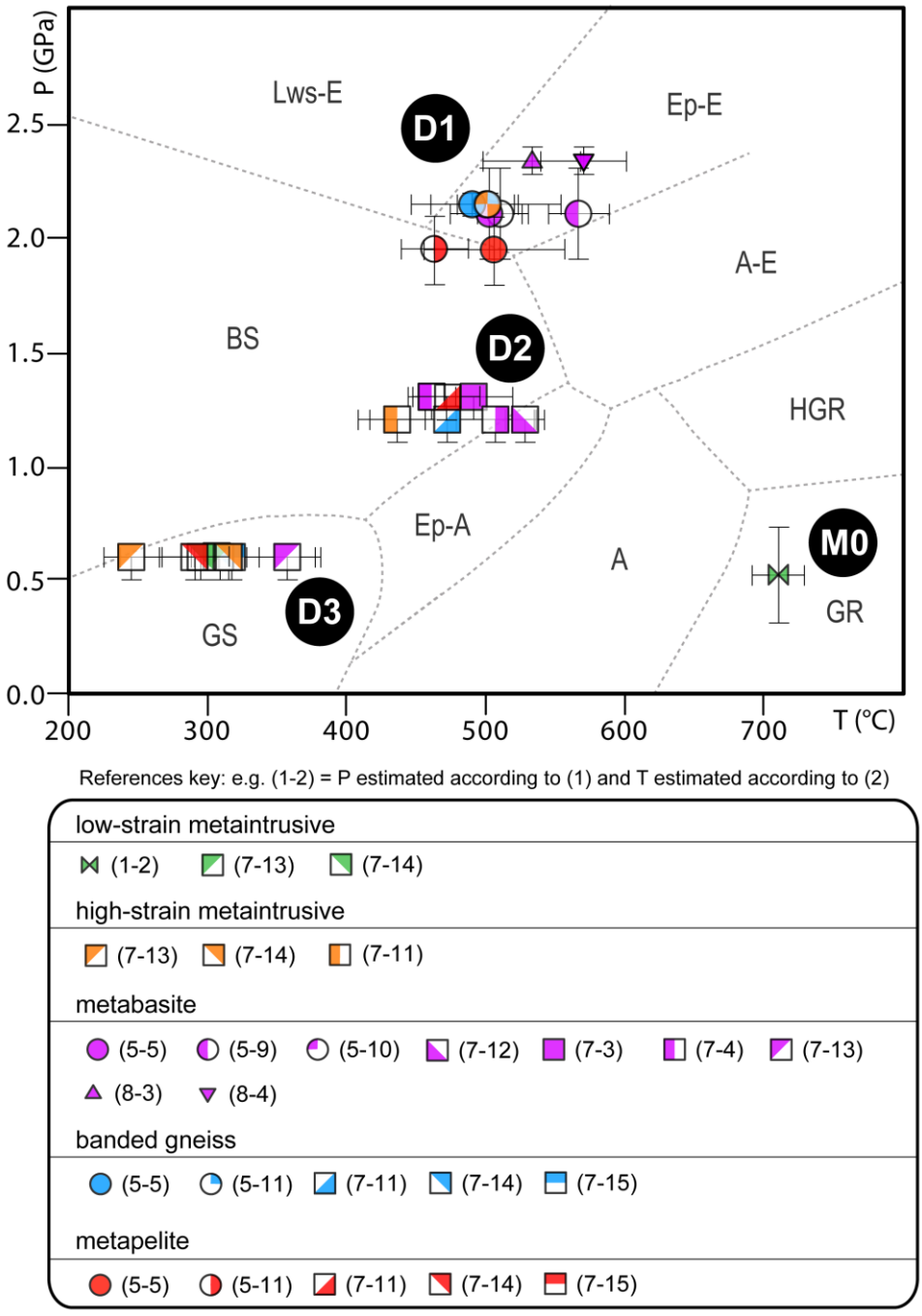

Figure 4.2.8. P-T estimates of different rock types inferred from relative timing of microstructures and metamorphic assemblage superposition. The geothermobarometers are indicated in brackets, according to Table 4.2.5. Facies fields from Ernst & Liou (2008).

4.2.8 Discussion

4.2.8.1 Tectonometamorphic and geodynamic evolution

The *P-T* conditions for the different rock types related to M0 magmatic assemblage and overprinting syn-tectonic assemblages (D1, D2 and D3+D4) allow inferring the tectonometamorphic evolution of the Lago della Vecchia metaintrusive and its country rocks.

Taking into account the wet solidus reaction for granites, **M0** conditions can be refined at pressure between 0.31 and 0.60 GPa at temperature around of 710°C. These conditions may represent the emplacement crustal level of the metaintrusive protholiths.

D1 stage is well preserved in MB and MP (Figure 4.2.8). Although the other lithologies preserve only D1 mineral relicts and considering that MB occurs as layers or lenses in BG and MI, the *P*-peak conditions inferred for MB can be extended to these rock types and are characteristic of eclogite facies (Figure 4.2.9).

D2 is recorded in all rock types and all fabric types. Temperatures and pressures estimated in all rock types are similar (within errors) and indicate low-pressure blueschist-facies conditions (Figure 4.2.8), according to the Pl stability in syn-D2 mineral assemblage (Figure 4.2.9), justified by the reaction Jd + Qz = Ab (Liou et al., 2004).

D3-D4 PT conditions are similar in the all rock types and are characteristic of greenschist facies conditions (Figure 4.2.9).

The traces of the oldest event recorded in the studied metaintrusives belong to the M0 group of structures and textures. M0 includes the textures and mineral relicts of the metaintrusive protoliths that survived the Alpine structural and metamorphic history. The metaintrusives could have been emplaced at ~ 13 km depth into the pre-Alpine continental crust (Table 4.2.6).

Stage	*P* (GPa)		*T* (°C)		*P/T* (10exp-3*GPa/°C)	*D* (km)		*T/D* (°C/km)	
	mean	dev.st	mean	dev.st	mean	min	max	min	max
M0	0.46	±0.15	710	±19	0.65	9	17		
D1	2.23	±0.18	537	±43	4.15	59	70	7	10
D2	1.12	±0.11	477	±39	2.35	29	36	12	18
D3-D4	0.60	±0.10	302	±24	1.99	15	20	14	22

Table 4.2.6. Variation of conditions during magmatic and superposed deformation stages recorded in the Lago della Vecchia rocks. Pressure (P), temperature (T), pressure-temperature ratio (P/T), depth (D), and temperature-depth ratio (T/D) are indicated. The M0 condition is refined considering the wet solidus reaction for granites. Depth is estimated considering an average density for the continental crust of 2.9 g/cm^3.

The Alpine evolution shows an eclogitic metamorphic peak at 2.23±0.18 GPa and 537 ±43 °C and characterised by a temperature-depth ratio between 7 and 10°C/km (Table 4.2.6). The D1 temperature-depth ratio is compatible with the thermal regime characterising a cold subduction (Figure 4.2.9). Between D1 and D2 stages, a near-isothermal exhumation down to D2 conditions of 1.12±0.11 GPa and 477±39 °C took place. The estimated D2 temperature-depth ratio is between 12 and 18°C/km (Table 4.2.6) and it is close to a warm subduction geotherm (Figure 4.2.9). Afterwards, *T* and *P* progressively decreased from D2 to D3-D4 stage at conditions of 0.60±0.10 GPa and 302±24 °C (Table 4.2.6; Figure 4.2.9). D3-D4 is characterised by a temperature-depth ratio between 14 and 22°C/km that is consistent with a warm subduction geotherm. The *P*/*T* ratios highlight a thermally depressed environment characterising the retrograde path of the Lago della Vecchia rocks (Figure 4.2.9; Table 4.2.6), which suggests that exhumation took place during the ongoing Alpine subduction, coherently with other portions of SLZ (*e.g.* Compagnoni et al., 1977; Pognante, 1989; Rebay & Messiga, 2007; Gosso et al., 2010; Zucali & Spalla, 2011; Delleani et al., 2013; Regis et al., 2014; Giuntoli et al., 2017). According to the temperature-depth ratio (Table 4.2.6), the final stage of exhumation (D3-D4) may have taken place at the end of the Alpine subduction, since it developed under a temperature-depth ratio lower than ratios characteristic of continental collision.

4.2.8.2 Contrasting histories vs. Contrasting memories along EMC

The tectonometamorphic evolution inferred for the Lago della Vecchia rocks is consistent with *P*-*T*-d-t paths reported in the literature (Figure 4.2.10; Table 4.2.2) for the Mucrone area in the EMC (Zucali et al., 2002; Delleani et al., 2012; Regis et al., 2014). Some tectonometamorphic evolutions, previously inferred for other sectors of the EMC, differ from that of the Lago della Vecchia area, such as the areas of Val Malone (Pognante, 1989), Corio and Monastero (Rebay & Messiga, 2007), Ivozio (Zucali & Spalla, 2011), Cime Bonze (Regis et al., 2014), and Pont S. Martin (Giuntoli et al., 2017). Furthermore, the development of pervasive D2 fabric under low-pressure blueschist facies at Lago della Vecchia is in contrast with the developed of the dominant fabric under eclogitic conditions, generally recorded in the nearby central portion of EMC (Figure 4.2.10).

This difference in the dominant tectonometamorphic imprint opens the question about the actual distribution of the eclogitic tectonometamorphic imprint within the EMC. These contrasting dominant fabric imprints and *P*-*T*-d-t paths (Figure 4.2.10) may suggest that the entire EMC could be characterised by kilometre-scale heterogeneities in the tectonometamorphic record and it may represent a composite object formed by several sub-units coupled during Alpine subduction and/or exhumation; the spatial shortage of comparable *P*-*T*-d-t data makes this interpretation arduous. These

heterogeneities in tectonometamorphic evolution, geochronological data (Figure 4.2.10; Table 4.2.2), and distribution of dominant fabric evolution are compatible with predictions of numerical modelling (Gerya et al., 2002; Stöckhert & Gerya, 2005; Meda et al., 2010; Roda et al., 2010; Roda et al., 2012), suggesting that the exhumation of HP units could be promoted by flow dynamics within the hydrated subduction mantle channel and occurred in a depressed thermal regime preserved by the still active oceanic subduction.

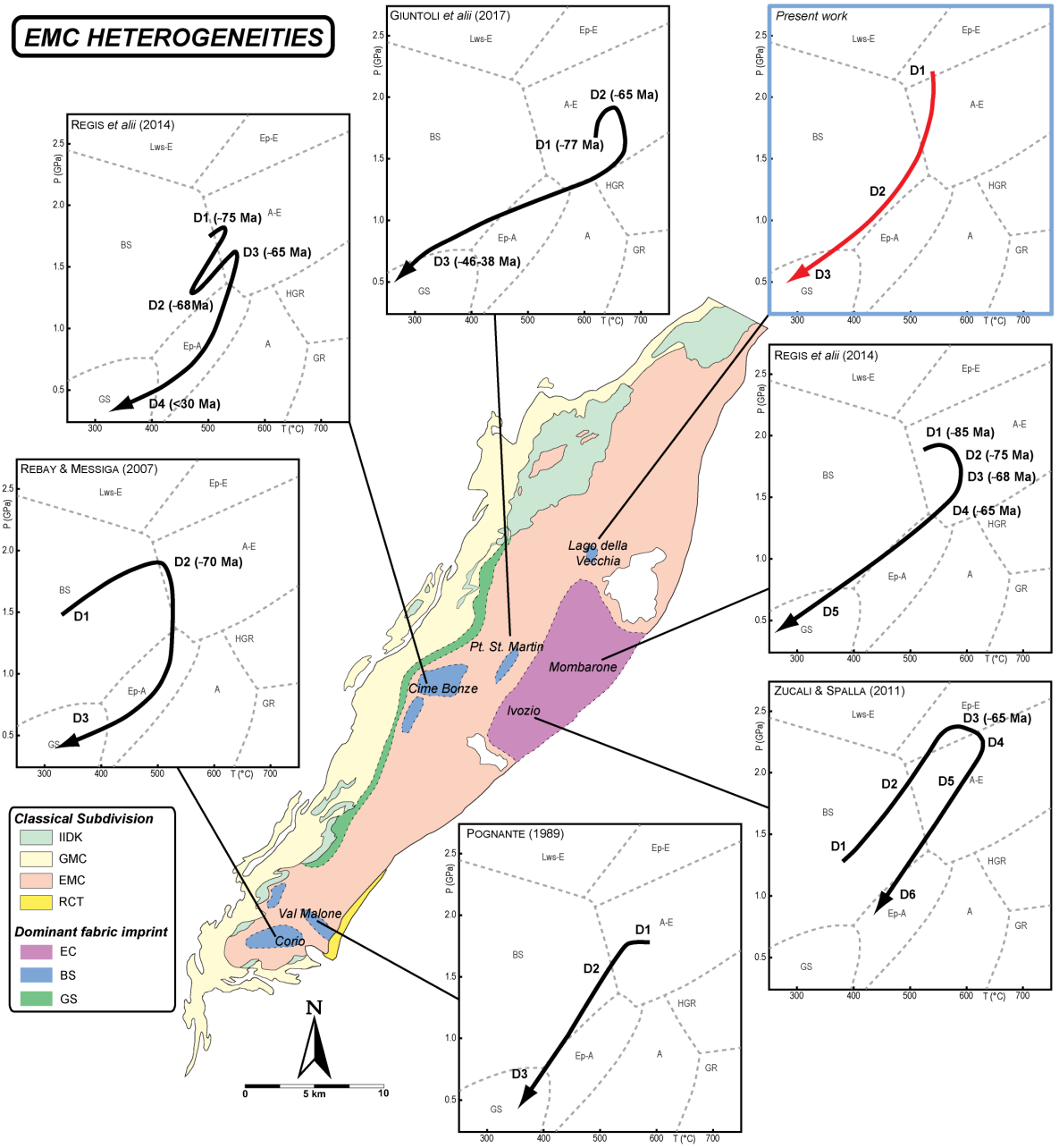

Figure 4.2.10. Spatial distribution of heterogeneities in dominant fabric imprints and tectonometamorphic evolution along EMC. Blue rectangle indicates the P-T-d-t path of the studied rocks. The metamorphic facies fields shown are after Ernst & Liou (2008).

4.2.9 Conclusion

- A multidisciplinary approach based on multiscale structural correlation of superposed metamorphic and structural imprints (Spalla et al., 2005; Salvi et al., 2010; Gosso et al., 2015) is a powerful method to reconstruct the tectonometamorphic evolution and volume sizes of lithospheric slices affected by heterogeneous fabric reworking and metamorphic transformation in polydeformed basement. For instance, the preservation of D1 fabric only in metabasite boudins and tectonitic metapelites points out the control of rock composition on deformation partitioning. Conversely, metaintrusive was intensely reworked during D2 and only pre-D2 mineral relicts are preserved.
- Exploitation of deformation heterogeneity permitted the reconstruction of a deformation-metamorphism history, which reveals that Lago della Vecchia rocks were exhumed during the ongoing Alpine subduction.
- The studied rocks followed a *P*-*T*-d-t path comparable with that of the Mucrone rocks (Figure 4.2.9; Zucali et al., 2002; Delleani et al., 2012; Regis et al., 2014). The difference between the two rock volumes concerns the metamorphic condition of the dominant fabric. At Lago della Vecchia it developed under low-pressure blueschist facies conditions, whereas at Mt. Mucrone it developed under eclogite facies conditions.
- The development of pervasive low-pressure blueschist facies D2 fabric in this area of EMC is in agreement with the results of the recent literature (Babist et al., 2006; Zucali & Spalla, 2011; Regis et al., 2014; Giuntoli & Engi 2016) that describes this heterogeneity along strike of the EMC. This heterogeneous structural and metamorphic record of the dominant fabric suggests that entire SLZ record kilometre-scale heterogeneities in the dominant tectonometamorphic imprint.
- Geochronological analysis is necessary for a better constraint of the timing of tectonometamorphic stages inferred from this work. Microscale analysis reveals that superposed assemblages contain minerals suitable to dating techniques, such as allanite (pre-Alpine magmatic intrusion), rutile, and zircon (Alpine eclogitic and low-pressure blueschist stages).
- Reconstructing and comparing *P*-*T*-d-t paths integrated with geochronological data and fabric evolution analysis of other portions of the EMC could highlight the shape and dimension of different crustal slices within the EMC and provide a more accurate interpretation about the *P*-*T* trajectories of crustal slices involved in the Alpine subduction-collision system.

- Finally, the individuated low-strain domains in the metaintrusive rocks could be good samples for modelling the metamorphic petrology of coronitic reactions and quantify the element diffusion.

4.2.10 Acknowledgements

We would like to thank Chiara Groppo and two anonymous reviewers for providing useful suggestions and constructive criticisms that greatly improved quality of the work. Funding from MIUR-PRIN 2010-2011 “Birth and death of oceanic basins: geodynamic processes from rifting to continental collision in Mediterranean and circum-Mediterranean orogens” and by “Evoluzione strutturale delle zone attive della litosfera e modellazione geodinamica” PSR2015-1716DZANO_M Università di Milano.

References are integrated at the end of the thesis.

4.3 LREE distribution in allanite during subduction controlled by strain partitioning in rock matrix

The following sections refer to the submitted paper: Corti L., Zanoni D., Gatta G.D., and Zucali M.: LREE distribution in allanite during subduction controlled by strain partitioning in rock matrix. Mineralogical Magazine.

Abstract

Combined microstructural, mineral chemical, X-ray maps, and X-ray single-crystal diffraction analyses are used to reveal the behaviour of individual grains of magmatic allanite relicts hosted in variably deformed metagranitoids at Lago della Vecchia (inner part of the Sesia-Lanzo Zone, Western Alps, Europe), which experienced H*P*-L*T* metamorphism during the Alpine subduction. The X-ray single-crystal diffraction shows that all the allanite crystals, irrespectively of the strain state of the host rock, do not record any evidence of plastic deformation, as proved by the shape of the Bragg diffraction spots, the atomic site positions and their displacement around the centre of gravity. On the contrary, strong plastic deformation affected matrix minerals, such as quartz, white mica, and feldspar of the hosting rocks, during the development of the Alpine eclogitic- and blueschist-facies metamorphism. Despite the strain-free atomic structures of allanite, different patterns of chemical

zoning, as a function of strain accumulated in the rock matrix, are observed. Since allanite occurs in magmatic and metamorphic rocks and it is stable at H*P*-L*T* conditions, we infer that allanite could behave as one of the main carriers of LREE into the mantle wedge during subduction of continental crust. In particular, the release of LREE from allanite, under H*P* conditions in subduction zones, is facilitated by high strain accumulated in the surrounding rock matrix.

Keywords: Allanite; Sesia-Lanzo Zone; Strain partitioning; Single-crystal X-ray diffraction; LREE release; Chemical imaging.

4.3.1 Introduction

Allanite, ideally $^{A1}(Ca)^{A2}(LREE^{3+})^{M1,M2}(Al)_2{}^{M3}(Fe^{2+},Fe^{3+})(SiO_4)(Si_2O_7)O(OH)$, is a sorosilicate belonging to the epidote group minerals, with monoclinic symmetry and structure topology consistent with the space group $P2_1/m$ (Dollase, 1971; Catlos et al., 2000; Franz and Liebscher, 2004; Armbruster et al., 2006). With respect to the other epidotes, allanite preferentially incorporates a significant fraction of light rare earth elements (LREE), and minor Th, U, Sr, Zr, and Cr into its structure (Deer et al., 1992; Catlos et al., 2000). The crystal structure is characterised by single silicate tetrahedra (SiO_4), double silicate tetrahedra (Si_2O_7), and continuous chains of MO_6 and $MO_4(OH)_2$ octahedra parallel to the crystallographic *b*-axis (Dollase, 1971; Gieré and Sorensen, 2004; Armbruster et al., 2006).

The crucial role of allanite for metamorphic petrology is due to its wide compositional range and *P*-*T* stability field. Allanite shows variable phase relations depending on *P*-*T* conditions and on the reacting chemical system (*e.g.*, Finger et al., 1998; Cox at al., 2003; Gregory et al., 2007): it occurs in igneous and metamorphic rocks (Franz et al., 1986; Moore and McStay, 1990; Sorensen, 1991; Schmidt and Thompson, 1996; Tribuzio et al., 1996; Liu et al., 1999; Carswell et al., 2000; Cenki-Tok et al., 2011; Cenki-Tok et al., 2014; Cliff et al., 2015; Manzotti et al., 2018) and it can incorporate up to about 60 wt% of the bulk rock LREE (especially Ce, La, and Nd) as well as Th (Exeley, 1980; Brooks et al., 1981; Gromet and Silver, 1983; Tribuzio et al., 1996). Allanite capability to incorporate LREE is counteracted by monazite, which can carry between 40 and 80 wt% of the LREE content in the bulk rock (*e.g.*, Bea, 1996; Finger et al., 1998). For this reason, the two minerals are considered the main potential carriers of LREE in the Earth's mantle through subduction (*e.g.*, Hermann, 2002; Giere and Sorensen, 2004; Hermann and Rubatto, 2009).

The *P*-*T* stability fields of these LREE-bearing minerals is mostly controlled by the temperature and Ca activity (*e.g.*, Rasmussen et al., 2006; Boston et al., 2017; Engi, 2017). Allanite stability at high-temperature and high-pressure conditions increases in Ca-rich rocks (*e.g.*, Janots et al., 2008; Kim et

al., 2009; Radulescu et al., 2009). In metapelitic systems, monazite-to-allanite reaction develops between low grade and amphibolite facies conditions (*e.g.*, Smith and Barreiro, 1990; Wing et al., 2003; Tomkins and Pattison, 2007; Janots et al., 2007, 2008; Spear, 2010). In magmatic environment, the crystallisation temperature of these LREE-rich phases is relatively similar (*e.g.*, Lee and Silver, 1964; Casillas et al., 1995), the Ca content and H_2O activity during magma crystallisation are the major parameters controlling allanite and monazite *P-T* stability (*e.g.*, Broska et al., 2000; Wing et al., 2003; Janots et al., 2008; Berger et al., 2009; Dini et al., 2014; Engi, 2017). In addition, allanite is characteristic of Ca-rich metaluminous granitoid rocks, whereas monazite is widespread in Ca-poor peraluminous granitoid rocks (*e.g.*, Broska and Siman, 1998; Catlos et al., 2000).

Whereas the knowledge of the crystal chemistry and *P-T* stability of allanite in natural systems have been thoroughly studied in the last decade (*e.g.*, Wing et al., 2003; Janots et al., 2007, 2008; Gregory et al., 2012), little is known about the behaviour of its structural properties during deformation and diffusion processes. Very recently, Gatta et al. (2019) described the compressional behaviour of allanite by *in-situ* single-crystal synchrotron X-ray diffraction with a diamond anvil cell. The experiments, conducted under hydrostatic conditions on natural allanite crystals, demonstrated that allanite preserves its crystallinity along with an elastic compressional behaviour at least up to 16 GPa, without any *P*-induced phase transition within the *P*-range investigated. The thermodynamic elastic parameters have been obtained by an isothermal Birch-Murnaghan Equation of State fit to the *P-V* data, and the evolution of the lattice parameters with *P* showed a slight anisotropic compression pattern (governed by the monoclinic symmetry of the structure). The main deformation mechanisms at the atomic scale were described on the basis of a series of structure refinements at different pressures. Comparing the (isothermal) compressional patterns with those obtained in previous studies, the effect of LREE on the elastic behaviour of epidote-group minerals was inferred (Gatta et al., 2019).

Recent works reported contrasting chemical and physical behaviours for allanite, preserving its primary chemical and isotopic fingerprint in crystals hosted in shear zones within eclogitised metagranitoid (*e.g.* Monte Mucrone, Western Austroalpine domain), suggesting a high shielding property due to high Young's modulus and low diffusion rates (Cenki-Tok et al., 2011). Conversely, allanite grown during shearing and metamorphism appears to have higher diffusion rate and lower Young's modulus (*e.g.* Dabie Shan; Liu et al., 1999; Monte Bianco, External Crystalline Massifs domain; Cenki-Tok et al., 2014; Sesia-Lanzo Zone, Regis et al., 2014).

In this light, this study aims at investigating structural parameters, chemical compositions, and texture patterns of natural allanite crystals from the Lago della Vecchia metagranitoids in the Sesia-Lanzo Zone, Western Alps, in order to: 1) describe any potential crystal structure and mineral chemistry variation in response to the different conditions of the surrounding plastically deformed matrix during

strain partitioning, and 2) estimate the LREE fraction released from allanite as function of the accumulated strain in the host rocks. Allanite crystals were sampled in rock volumes that recorded different degree of fabric evolution and metamorphic reaction progress (Corti et al., 2017) during the development of the blueschist-facies dominant fabric (Corti et al., 2018).

Hereafter, mineral abbreviations are used according to Whitney and Evans (2010).

4.3.2 Material and methods

4.3.2.1 Geological outline

The allanite crystals used in this study were sampled from the Lago della Vecchia metagranitoids, which are part of the Eclogitic Micaschist Complex of the Sesia-Lanzo Zone (EMC-SLZ), in the Austroalpine domain of the Western Alps (Fig. 4.3.1a). SLZ is a slice of continental crust that experienced H*P*-L*T* conditions during the Alpine subduction (*e.g.*, Compagnoni et al., 1977; Spalla et al., 1991; Zucali et al., 2002; Gosso et al., 2010; Roda et al., 2012; Giuntoli et al., 2016; Roda et al., 2018; 2019). Metagranitoids occur as metre- to kilometre-sized bodies in tectonic contact with micaschists and gneisses (Corti et al., 2017). They spectacularly preserve magmatic textures and igneous minerals, within metre to decametre domains. These domains are only weakly affected by superposed Alpine tectonometamorphic imprints developed under eclogite- and blueschist-facies conditions (Zucali, 2011; Corti et al., 2018). The multiscale structural analysis and geothermobarometric estimates allow inferring the tectono-metamorphic evolution of the Lago della Vecchia metagranitoids (Corti et al., 2017; 2018). Pre-Alpine M0 magmatic stage consists in magmatic textures and igneous relicts in coronitic domains and allanite crystals in all-strain domains (P = 0.46±0.15 GPa; T = 710±19 °C). The first Alpine stage is D1that developed the S1 foliation at P = 2.23±0.18 GPa and T = 537±43 °C, under eclogitic-facies conditions. D1 structures were transposed and obliterated by D2 stage that developed the pervasive S2 foliation at P = 1.12±0.11 GPa and T = 477±39 °C, under blueschist-facies conditions. The D2 stage is retrograde with respect to D1 eclogitic-peak and took place under a depressed thermal state compatible with oceanic subduction (Corti et al., 2018; Fig. 4.3.1c). D3 and D4 stages (P = 0.6±0.10 GPa; T = 302±24 °C) consist of localised shear zones and open folds marked by greenschist facies assemblages and D5 developed km-long brittle-to-ductile mylonitic shear zones at shallow crustal level (Corti et al., 2017, 2018). In contrast with most of the EMC, where the dominant fabric developed under eclogitic facies conditions, the dominant fabric of the Lago della Vecchia metagranitoids developed under the D2 blueschist-facies conditions. In response to deformation partitioning, D2 produced low-strain domains (*i.e.*, coronitic domain)

wrapped by intermediate (*i.e.*, tectonitic domain), and high (*i.e.*, mylonitic domain) finite strain domains (Fig. 4.3.1b; *e.g.*, Gosso et al., 2015; Corti et al., 2017).

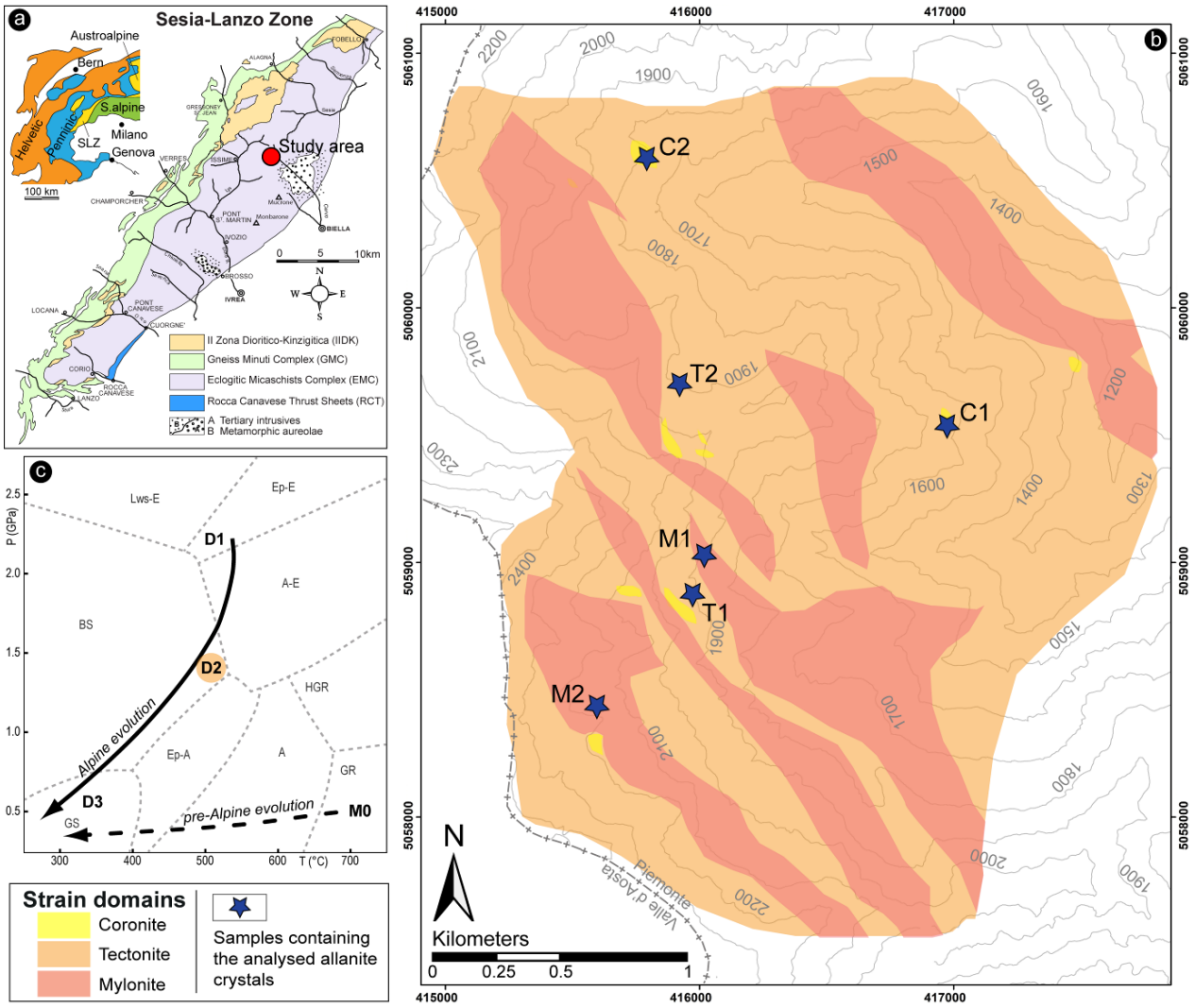

Figure 4.3.1. a) Study area of the Sesia-Lanzo Zone, Western Alps. b) D2 fabric domains and location of analysed allanite crystals (UTM 32N-WGS84; modified after Corti et al., 2017). c) P-T-d-t path and D2 dominant fabric conditions as inferred by Corti et al. (2018).

4.3.2.2 Allanite sampling

Six metagranitoid samples with allanite crystals were selected using the D2 domains of the degree of fabric evolution (DFE) as structural reference (Fig. 4.3.1b). While in mylonitic domains the rock fabric is entirely related to the new metamorphic conditions, in tectonitic to coronitic domains relic fabrics and mineral associations are preserved. The contouring of such domains with homogeneous DFE is facilitated by integrating meso- and micro-scale structural analysis (*i.e.*, Gosso et al., 2015). The estimation of the DFE is based on the volumes occupied by different degree of grain-scale reorganization during D2, which span from coronitic to mylonitic domains (Lardeaux and Spalla,

1990; Gosso et al., 2015) (planar fabric: coronitic: 0-20%; tectonitic: 21-60%; mylonitic: 61-100%). Thus, two samples were chosen from coronitic (C1 and C2 samples), tectonic (T1 and T2 samples, and mylonitic (M1 and M2 samples) metagranitoids, respectively (Fig. 4.3.1b). Location of samples is shown in Fig. 4.3.1b and is indicated in the following analytical tables and figures.

4.3.2.3 Methods

The rock microstructures and the cristallochemical features of the allanite crystals in different D2 fabric domains have been investigated by (transmitted) polarised light microscopy, scanning electron microscopy in wavelength-dispersive mode (WDS-EMPA), and single-crystal X-ray diffraction.

Quantitative WDS chemical micro-analyses were obtained with a JEOL 8200 Super Probe system at the Earth Sciences Department, University of Milan, with operating conditions of 15 kV and 5nA, 5μm beam diameter, and counting times of 30s on the peaks and 10s on the backgrounds. Natural minerals were used as standards and the results were corrected for matrix effects using a *ZAF* routine (Armstrong and Buseck, 1975), set in the JEOL suite of programs. Selected mineral chemical data for each strain domain are reported in Table 1. The chemical formula of allanite was calculated following the IMA procedure, based on $\Sigma(A+M+T) = 8$ cations per formula unit (Armbruster et al., 2006). X-ray elemental maps (elements: Al, Ca, Ce, Fe, La, Mg, Nd, Pr, Si, and Th) of one Aln crystal within each strain domain were acquired under 60 ms dwell time, 15 kV accelerating voltage and a probe current of 100 nA. A step size of 0.40 μm on both the orthogonal reference directions (*x* and *y*) was used for acquiring an image with a resolution of 625x625 pixels.

The Quantitative X-Ray Map Analyser (QXRMA; Ortolano et al., 2018) was used to classify rock-forming minerals starting from an array of X-ray elemental maps and to quantify the chemical zoning of Aln crystals and their chemical and textural relationships with the surrounding rock-matrix. The QXRMA first cycle is useful to distinguish mineral phases as well as to extrapolate their modal fractions by a multivariate statistical analysis that allowed the handling of the X-ray maps through the Principal Components Analysis (PCA) and the supervised Maximum Likelihood Classification (MLC; Ortolano et al., 2014). The second cycle allows performing a deeper analysis of Aln crystals, identified during the first cycle, for detecting occurrences of mineral zoning.

A series of sub-millimetric crystals of Aln from all strain domains were picked up for the single-crystal X-ray diffraction investigation. In particular, three crystals from a coronitic allanite, two from tectonitic, and one from mylonitic domain were used. Intensity data were collected with an Xcalibur-Oxford Diffraction diffractometer, equipped with CCD, using a graphite monochromatised Mo-*K*α radiation, and operated at 50 kV and 40 mA. A combination of omega and phi scans was used to

maximize the reciprocal space coverage and redundancy, fixing a scan width of 0.5°, an exposure time of 30 s/frame, and a crystal-detector distance of 80 mm. The unit-cell was found to be monoclinic for all the crystals, and absence conditions always compatible with the $P2_1/m$ space group. Intensities from all the datasets were integrated and corrected for Lorentz-polarization (Lp) effects using the CrysAlis^{TM} software. Correction for absorption was applied by the semi-empirical *ABSPACK* routine implemented in CrysAlis^{TM}. The anisotropic structure refinements were conducted using the software SHELXL97 (Sheldrick, 1997), starting from the structure model of Dollase (1971) and Bonazzi et al. (2009) in the space group $P2_1/m$. The atomic sites were modelled as follows: the *A1* and *A2* sites were modelled with a mixed (Ca + Ce) X-ray scattering curve; the *M1* and *M2* octahedral sites as populated by Al only and the *M3* site as populated by (Fe + Al); the three independent tetrahedral sites (*i.e.*, *Si1*, *Si2* and *Si3*) were modelled as fully occupied by Si. The proton site was located in all the refinements. Convergence was rapidly achieved for all the refinements and no significant correlation was observed in the variance-covariance matrix of the refined parameters. CIFs are deposited as electronic supplementary material.

4.3.3 Results

4.3.3.1 Microstructures

The microstructural analysis (in optical microscopy) reveals that, in all strain domains, Aln occurs as mm-sized single crystals characterised by high birefringence, dark-brown (cores) to light-brown (rims) pleochroism. The Aln crystals are surrounded by blueschist-facies metamorphic assemblages consisting of Czo rims, fine-grained aggregates of Wm+Pl+Ep, and large crystals or aggregates of Qz. The photolith of the analysed metagranitoids consists of a granodiorite (Figs 4.3.2a and 4.3.2b), according to the bulk-rock chemistry estimated on modal mineral content and mineral chemistry (data in Corti et al., 2018).

Coronitic domains are medium- to coarse-grained rocks showing a well-preserved magmatic texture with igneous mineral relics only partially replaced by Alpine metamorphic assemblages. These domains are (volumetrically) constituted by Qz (30-35%), Pl (15-20%), Ep (5-10%), Aln (5%), ±Grt (10%), ±Wm (<5%), ±Amp (<5%), and ±Op (<5%). The igneous minerals such as Bt, Kfs, and Aln constitute ≈ 20-30 % of the rock volume. Tectonitic domains consist of fine- to medium-grained rocks that contain Qz (30-50%), Wm (20-30%), Ep (15-20%), Grt (5%), Amp (5%), Kfs (5%), and Aln (3%). These domains mostly show a well-developed foliation marked by shape-preferred orientation (SPO) of Qz and aggregates of Wm and Ep. Mylonitic domains consist of fine-grained rocks showing a millimetre-spaced foliation defined by SPO of Wm, Ep, and Amp that wraps porphyroblasts of Grt

and porphyroclasts of Kfs. These rocks are constituted by Qz (40-50%), Wm (15-20%), Ep (15-20%), Grt (5-10%), Amp (5-10%), and Aln (5%). In tectonitic and mylonitic domains, igneous Kfs (<5%) and Aln (<5%) constitute less than 10 % of the rock volume and the new planar fabrics largely overprint igneous textures.

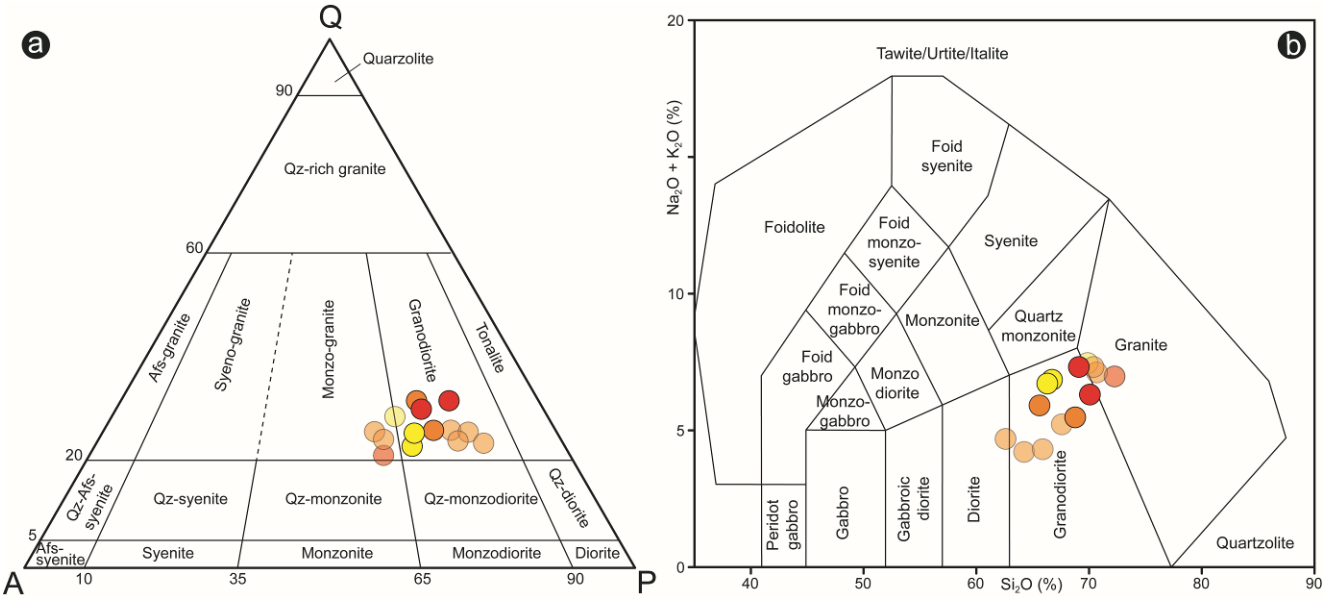

Figure 4.3.2. Estimated bulk-rock composition. a) QAP diagram used to classify granitoid rocks is based on the integration of modal mineral content, mineral chemistry and CIPW normative analysis. Q: quartz; A: alkali feldspar; P: plagioclase (normalized to 100%). b) Metagranitoid samples plotted on TAS diagram (modified after Middlemost, 1985). Yellow: coronitic samples; orange: tectonitic samples; red: mylonitic samples. Allanite crystals of this study are from the samples represented by the six non-transparent symbols; the others are from Corti et al., (2018).

In coronitic domains, Aln occurs in well-formed 50-200 µm-sized crystals (Fig. 4.3.3a), surrounded by Czo, Wm, and Ep (Fig. 4.3.3b). In tectonitic domains, the Aln crystal size is similar but the corona of Czo is more developed (Fig. 4.3.3c) and is wrapped by the dominant foliation (Fig. 4.3.3d). The microstructural analysis of evolution of superposed fabrics and related mineral assemblages suggests that Aln pre-dates the Alpine metamorphism and it is interpreted as a magmatic relict.

In mylonitic domains, the dominant S2 is a spaced and discontinuous foliation, marked by Qz, Wm, Ep, Czo, and Fsp and it wraps millimetre sized Aln porphyroclasts. The Aln crystals are aligned and often boudinated along S2 (Fig. 4.3.3e), without evidences of plastic deformation. In contrast, the matrix minerals, such as Qtz, Wm, Fsp, Czo, and Ep show evidence of plastic deformation and grain-size reduction (Fig. 4.3.3f). Details on petrography and microstructures of metagranitoids are in Corti et al. (2017, 2018).

4.3.3.2 Chemical imaging

X-ray elemental mapping of the selected Aln crystals from the different strain domains reveals evident mineral zonation, especially related to the relative concentration of Ca, Ce, Fe, and Th (Fig. 4.3.4). The Ca and Fe relative concentration increase towards the Aln rim and in the mineral matrix around the Aln crystals, whereas Ce and Th relative concentration is highest in the core of the Aln grains.

The QXRMA procedure is a powerful tool for quantitatively defining the spatial distribution of Aln chemical zoning and to discuss this chemical variation in relation with the strain domains. The first cycle of QXRMA analysis allows the mineral classification within the three microdomains. The classified pixels are 99.98%, 99.87%, and 99.93% for the images related to coronitic, tectonitic, and mylonitic domains, respectively. The identified mineral phases are Aln, Czo, Ep, Wm, and Qtz (Fig. 4.3.5), which correspond to the pre-Alpine Aln porphyroclasts, and Alpine Czo, Ep, Wm, and Qtz blueschist-facies mineral associations.

The second cycle of QXRMA analysis reveals three major chemical zoning in Aln: Aln1, Aln2, and Aln3 as shown in Figure 4.3.5a. In general, Aln1 constitutes the core and Aln3 the rim in the crystals from all strain domains, though the relative proportion of Aln1, Aln2, and Aln3 may change (Fig. 4.3.5a). These three zonations are separated mainly based on total LREE *vs.* Al-Fe-Ca relative concentration, which is characterised by LREE depletion and Al-Fe-Ca enrichment from Aln1 to Aln3 (Fig. 4.3.5b). The LREE partitioning shows as the concentric zonation in coronitic domain is given by Ce-rich core and Th/Nd-rich rim, whereas the chemical zoning in tectonitic and mylonitic domains is elongated according to the S2 foliation. More in details, RGB X-ray map analysis reveals differences in chemical pattern of LREE elements, such as Ce, Nd, Th, in relation with the strain domains (Fig. 4.3.5b). These elements generate patchwork and en-echelon-like chemical zonation in tectonite and mylonite domains, respectively (Fig. 4.3.5b). En-echelon-like chemical zonation forms an angle of about 30° with respect to S2 in rock matrix.

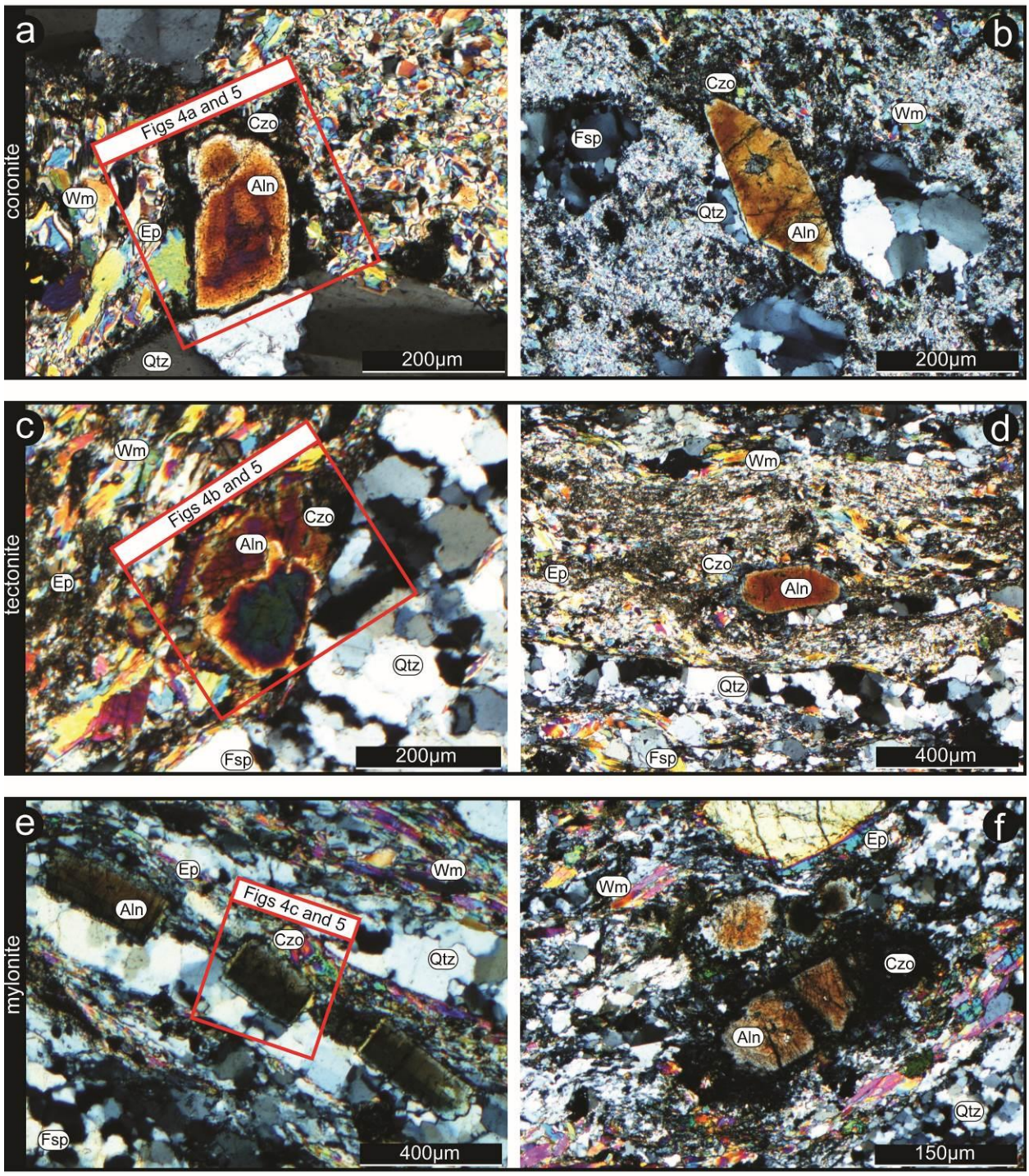

Figure 4.3.3. Microstructural features of the analysed Aln crystals (crossed polars). In coronitic domains (a: UTM: 417087 – 5059526; b: UTM: 415879 – 5060637), Aln occurs in well-preserved single crystals rimmed by Czo and surrounded by fine grainsize rock-matrix constituted by Wm + Ep + Qtz. In tectonitic domains (c: UTM: 415994 – 5058867; d: UTM: 4159071 – 5059737), Aln porphyroclast is partially replaced by Czo and it is wrapped by Wm + Ep + Qtz + Fsp assemblage marking the S2 foliation. In mylonitic domains (e: UTM: 416137 – 5059099; f: UTM: 415699 – 5058603), Aln crystals are aligned and boudinated along S2 that is constituted by Qtz + Wm + Fsp + Czo + Ep assemblage. The extension of the X-ray maps is shown (red rectangle).

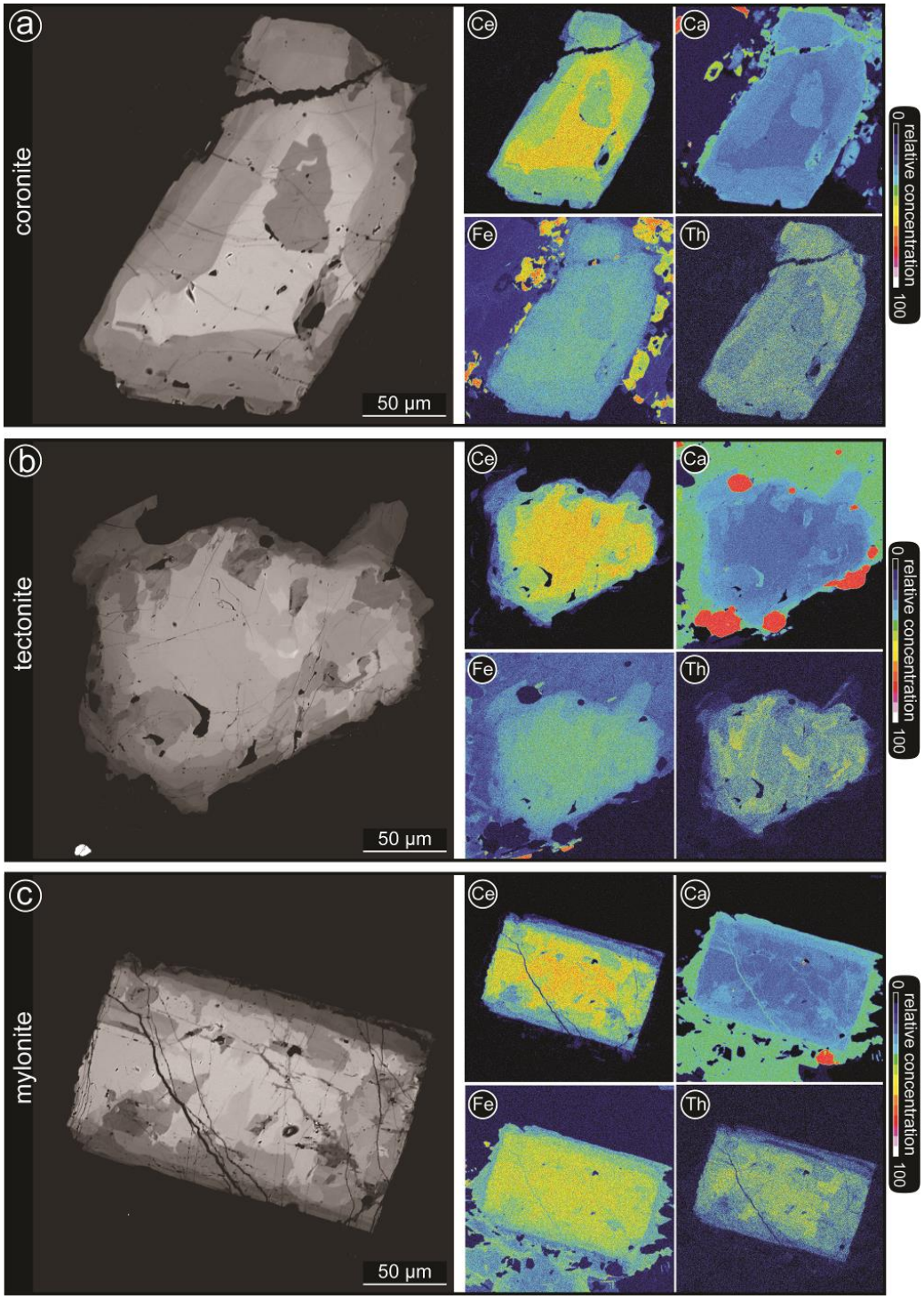

Figure 4.3.4. BSE images and X-Ray elemental maps (Ce, Ca, Fe, and Th) of an Aln crystal in (a) coronitic domain, (b) tectonitic domain, and (c) mylonitic domain. The chemical pattern shows how the concentric zonation in coronitic domain is mostly given by the decrease of Ce content and the increase of Ca/Fe contents towards the crystal rim. The element partitioning generate patchwork and en-echelon-like chemical zonation in tectonite and mylonite domains, respectively.

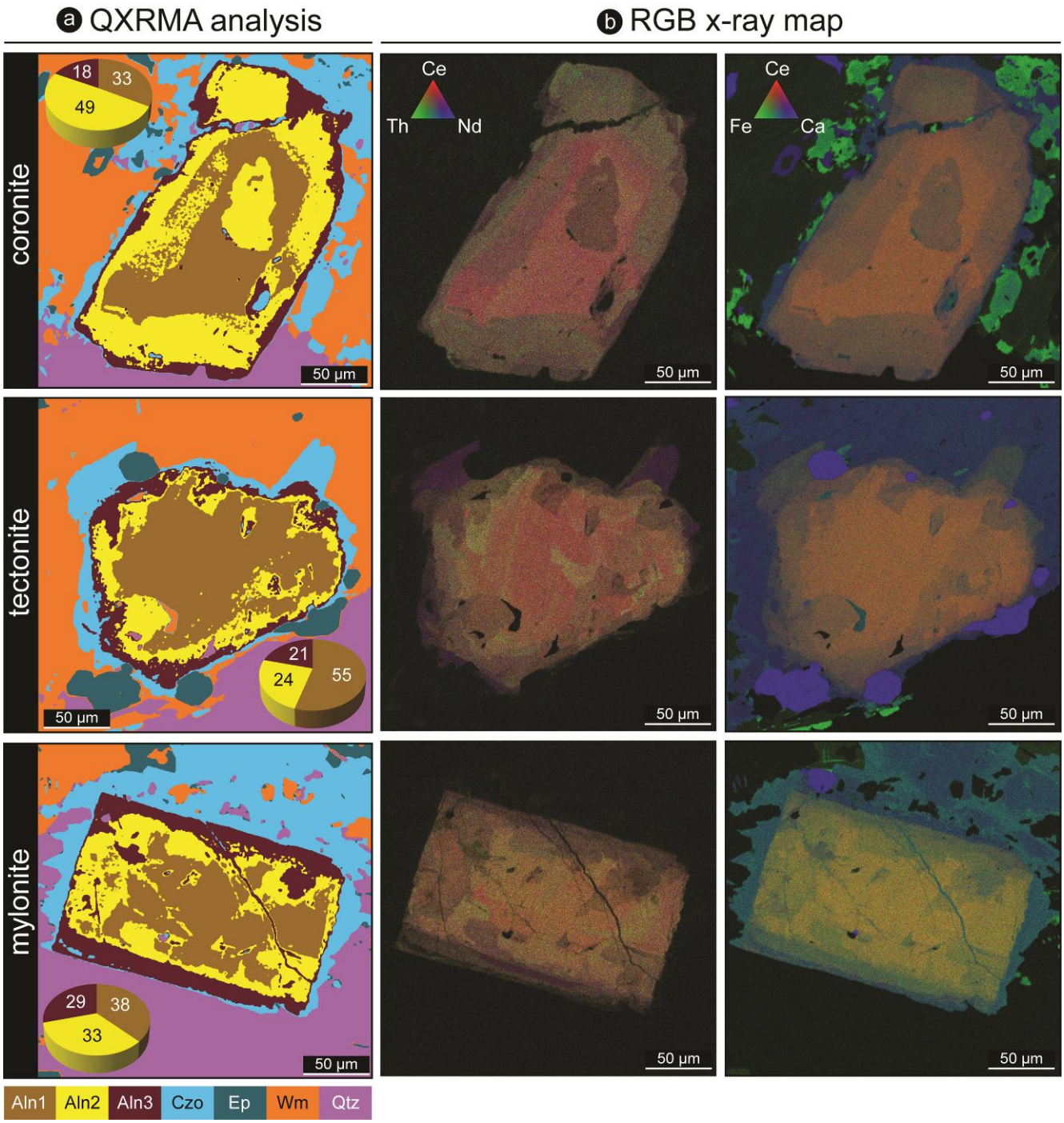

Figure 4.3.5. (a) QXRMA results, with nature and spatial distribution of the mineral species, along with the modal fraction of the Aln chemical zoning in relation with the progressive strain domains. (b) Ce-Th-Nd and Ce-Fe-Ca pattern within Aln crystals, showing a clear decrease of Ce content in all strain domains, concentric zonations in the coronitic domains, and en-echelon-like zonation in the mylonitic domains, oblique with respect to S2.

4.3.3.3 Mineral Chemistry

Aln crystals show homogeneous chemical variation from core to rim (LREE depletion and Al enrichment from Aln1 to Aln3; Fig. 4.3.6a). Regardless the strain domain, allanite crystals show Ce depletion and Th enrichment from Aln1 to Aln3 (Fig. 4.3.6b). The chemical zoning is highlighted by the Ce/LREE and Ca/LREE ratios *vs.* Al partitioning, and follow a linear trend of LREE depletion and Al enrichment from Aln1 to Aln3 (Figs 4.3.6c and 4.3.6d).

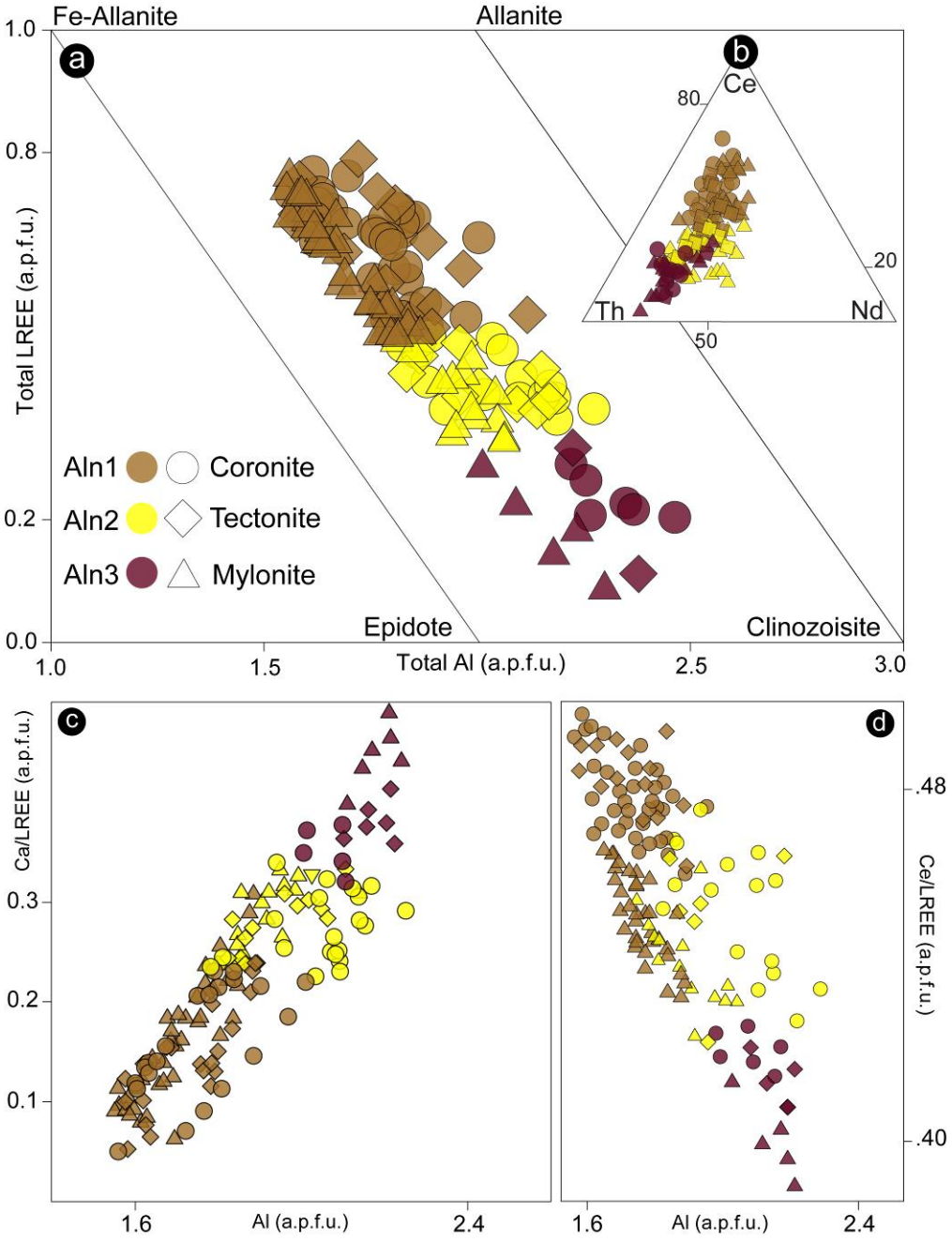

Figure 4.3.6. Chemical variation in allanite crystals from core (Aln1) to rim (Aln3) in the different strain domains (circle: coronite, diamond: tectonite, triangle: mylonite). a) Total LREE vs. Al content. b) Ce-Th-Nd triangular plot. c) Ca/LREE ratio vs. Al content. d) Ce/LREE ratio vs. Al content.

Allanites in coronitic and tectonitic domains display a similar chemical pattern: Ce/LREE-richer core (Fig. 4.3.6d) and a generally higher Al content than Aln in mylonitic domains. The lowest Ce/LREE values in all Aln zonations represent a common feature in mylonitic domains (Fig. 4.3.6d). In Aln3 from mylonitic domains, Ca/LREE ratio shows the highest values, and this ratio in Aln3 progressively decreases in tectonitic and coronitic domains (Fig. 4.3.6c).

Sample	Coronite 1 (C1)			Coronite 2 (C2)			Tectonite 1 (T1)			Tectonite 2 (T2)			Mylonite 1 (M1)			Mylonite 2 (M2)		
Subphase	Aln1	Aln2	Aln3	Aln1	Aln2	Aln3	Aln1	Aln2	Aln3	Aln1	Aln2	Aln3	Aln1	Aln2	Aln3	Aln1	Aln2	Aln3
MgO	0.66	0.57	0.37	0.74	0.40	0.24	0.69	0.32	0.21	0.65	0.51	0.14	0.84	0.37	0.16	0.53	0.25	0.04
TiO2	0.75	0.53	0.30	0.77	0.46	0.18	0.86	0.57	0.12	0.26	0.34	0.06	0.84	0.21	0.20	0.64	0.37	0.19
Pr2O3	2.36	1.57	0.93	2.36	1.71	1.17	2.39	1.78	1.07	2.28	1.71	0.71	2.56	1.65	0.78	2.33	1.15	0.73
ThO2	1.49	0.83	0.45	0.92	1.00	0.91	1.78	1.03	0.60	0.77	0.97	0.46	1.25	0.88	0.47	1.36	0.63	0.34
Al2O3	16.55	20.19	23.97	17.35	20.90	24.83	16.25	19.92	24.05	18.41	19.69	26.91	16.30	21.65	26.55	17.22	21.81	25.19
SiO2	33.02	34.45	35.83	32.05	34.76	36.05	32.77	34.84	36.08	33.18	34.37	37.00	32.71	34.35	36.16	33.08	35.95	38.10
La2O3	6.00	2.87	1.86	6.23	3.52	3.04	5.21	3.57	2.36	5.45	3.51	1.51	5.38	3.61	1.56	5.64	2.60	1.37
Nd2O3	3.10	4.06	2.42	4.01	3.27	2.16	3.81	2.88	2.07	3.72	3.00	1.55	3.48	2.81	1.71	3.24	2.51	1.23
CaO	10.67	13.63	16.96	9.88	14.32	16.32	10.08	14.43	17.11	10.65	14.21	18.93	10.42	14.31	19.10	10.97	16.31	19.45
Ce2O3	11.43	7.39	4.12	12.50	7.82	6.58	11.23	7.52	5.37	10.93	7.83	3.24	11.65	7.75	3.58	11.32	6.04	3.12
Sm2O3	0.49	1.01	0.83	0.59	0.60	0.33	0.66	0.44	0.30	0.71	0.79	0.25	0.45	0.43	0.44	0.61	0.64	0.23
FeO	13.67	12.38	11.04	12.37	11.11	7.57	14.29	11.90	9.74	12.77	12.24	8.58	13.83	11.28	8.09	13.21	11.08	8.96
Total	100.20	99.48	99.08	99.78	99.86	99.38	100.01	99.20	99.07	99.78	99.17	99.34	99.71	99.29	98.79	100.15	99.34	98.95
Formulae are based on 8 cations (IMA procedure; Armbruster et al., 2006)																		
Mg	0.08	0.07	0.04	0.09	0.05	0.03	0.08	0.04	0.02	0.08	0.06	0.02	0.10	0.04	0.02	0.06	0.03	0.00
Ti	0.05	0.03	0.02	0.05	0.03	0.01	0.05	0.03	0.01	0.02	0.02	0.00	0.05	0.01	0.01	0.04	0.02	0.01
Pr	0.07	0.05	0.03	0.07	0.05	0.03	0.07	0.05	0.03	0.07	0.05	0.02	0.08	0.05	0.02	0.07	0.03	0.02
Th	0.03	0.01	0.01	0.02	0.02	0.02	0.03	0.02	0.01	0.01	0.02	0.01	0.02	0.02	0.01	0.03	0.01	0.01
Al	1.60	1.88	2.15	1.72	1.96	2.32	1.58	1.86	2.19	1.78	1.84	2.39	1.58	2.02	2.39	1.67	1.99	2.23
Si	2.72	2.73	2.72	2.70	2.76	2.86	2.70	2.77	2.78	2.73	2.73	2.78	2.70	2.72	2.76	2.72	2.79	2.87
La	0.18	0.08	0.05	0.19	0.10	0.09	0.16	0.10	0.07	0.17	0.10	0.04	0.16	0.11	0.04	0.17	0.07	0.04
Nd	0.09	0.11	0.07	0.12	0.09	0.06	0.11	0.08	0.06	0.11	0.09	0.04	0.10	0.08	0.05	0.10	0.07	0.03
Ca	0.94	1.16	1.38	0.89	1.22	1.38	0.89	1.23	1.42	0.94	1.21	1.53	0.92	1.22	1.56	0.97	1.36	1.57
Ce	0.34	0.21	0.11	0.39	0.23	0.19	0.34	0.22	0.15	0.33	0.23	0.09	0.35	0.22	0.10	0.34	0.17	0.09
Sm	0.01	0.03	0.02	0.02	0.02	0.01	0.02	0.01	0.01	0.02	0.02	0.01	0.01	0.01	0.01	0.02	0.02	0.01
Fe2+	0.82	0.70	0.59	0.77	0.64	0.44	0.86	0.68	0.53	0.77	0.69	0.45	0.83	0.64	0.43	0.79	0.61	0.48
Fe3+	1.06	0.94	0.81	0.98	0.84	0.56	1.11	0.90	0.72	0.99	0.93	0.63	1.08	0.86	0.60	1.02	0.83	0.65
REE sum	0.70	0.49	0.28	0.79	0.49	0.38	0.70	0.47	0.31	0.69	0.49	0.20	0.71	0.47	0.22	0.69	0.37	0.18

Table 4.3.1. WDS-EPMA data of 18 selected allanite crystals from the three strain domains (i.e., C: coronite, T: tectonite, and M: mylonite). Chemical formulae, in atoms per formula units (a.p.f.u.), were calculated following the IMA procedure based on 8 cations p.f.u. (Armbruster et al., 2006). The crystals used for the single crystal X-ray diffraction experiments are from the domains C1 (i.e., crystals #3.10, #3.11 and #1.10), T1 (#5.3, #5.5), and M2 (#8.1) (see the CIFs).

4.3.3.4 Single crystal X-ray diffraction

As shown in Fig. 4.3.7, the X-ray diffraction patterns of the investigated crystals of allanite, belonging to three different domains (*i.e.*, coronitic C1, tectonitic T1 and mylonitic M2), show diffraction spots with approximately circular sections (max ellipticity ratio: 1.2:1) and similar full-width-at-half-maximum (FWHM), in turn similar (within 3σ) to those of unstrained gem-quality epidote crystals (previously studies by Gatta et al. 2010, 2011a, and using the same experimental set-up here used). In

other words, there is no evidence of potential textured patterns (on some specific crystallographic planes) and this is irrespective of the different strain domains of the sample (*i.e.*, coronite, tectonite, mylonite). The structure refinements based on the six data sets (*i.e.*, #3.10, #3.11 and #1.10 from the coronitic C1, #5.3 and #5.5 from the tectonitic T1, and #8.1 from mylonitic M2 domains; see the CIFs) are of similar quality, as shown by the values of the statistical parameters: $R_{int} \approx 0.03 - 0.04$, $R(F)_{obs} \approx 0.03 - 0.04$, $wR(F^2)_{obs} \approx 0.05 - 0.06$ (see the CIFs).

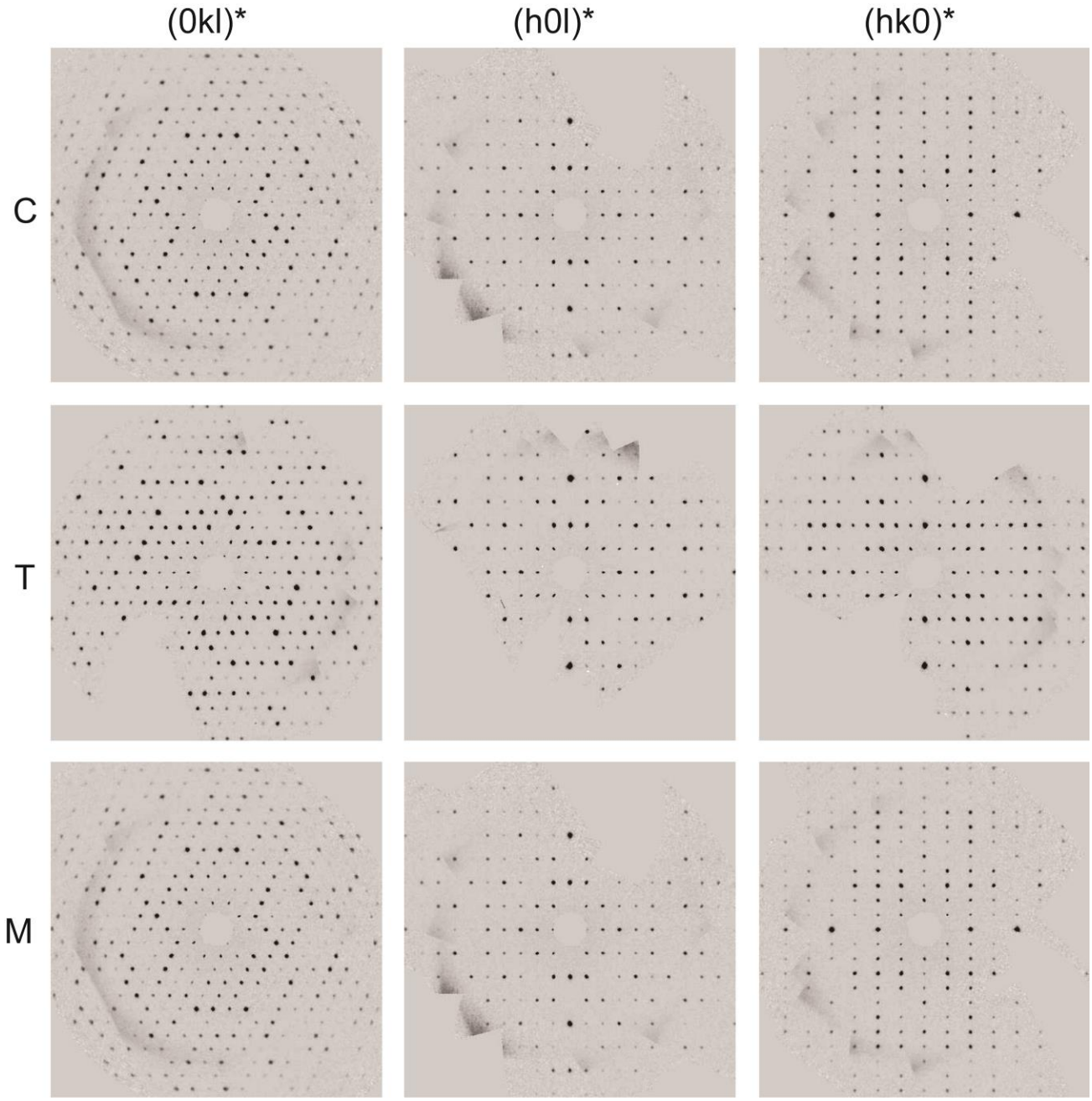

Figure 4.3.7. Unwarped single-crystal diffraction patterns (based on raw data) of the allanite crystals from the different strain domains (C = coronitic, #1.10; T = tectonitic, #5.5; M = mylonitic, #8.1, see also the CIFs).

All the least-squares refinements produce similar atomic coordinates (and therefore similar bond distances and angles of the coordination polyhedra) along with their anisotropic displacement parameters (excluding the proton site, which was modelled isotropically). In the structure refinements of this study, the anisotropic displacement factor exponent of each atomic site is modelled on the Gaussian approximation, with the form: $-2\pi^2[(ha^*)^2U^{11} + (kb^*)^2U^{22} \ldots + 2hka^*b^*U^{12}]$, according to Fischer and Tillmanns (1988). The individual atomic anisotropic displacement parameters may represent atomic motion or possible static displacive disorder. When a given crystallographic site is populated by a multi-elemental population, its anisotropic displacement parameter can be virtually pronounced in response to the different displacement of the elements from the center of gravity. This could be the case of allanite, in which (at least) *A1*, *A2* and *M3* sites are affected by multi-elements site population. Despite that, the refined atomic displacement ellipsoids, pertaining to all the six structure refinements of this study, are all in line with those usually found in gem-quality unstrained crystals (*i.e.*, with a modest ratio of the longest and shortest root-mean-square components of the ellipsoids, < 1.7-2.0) and, in turn, very similar (*per* each relative crystallographic site) among the six refinements. As an example, in Fig. 4.3.8 it is shown the refined structure model based on the X-ray intensity data generated by the crystal #8.1, belonging to the mylonitic domain M2 (*i.e.*, the most strained one), with atomic displacement probability factor at 99%.

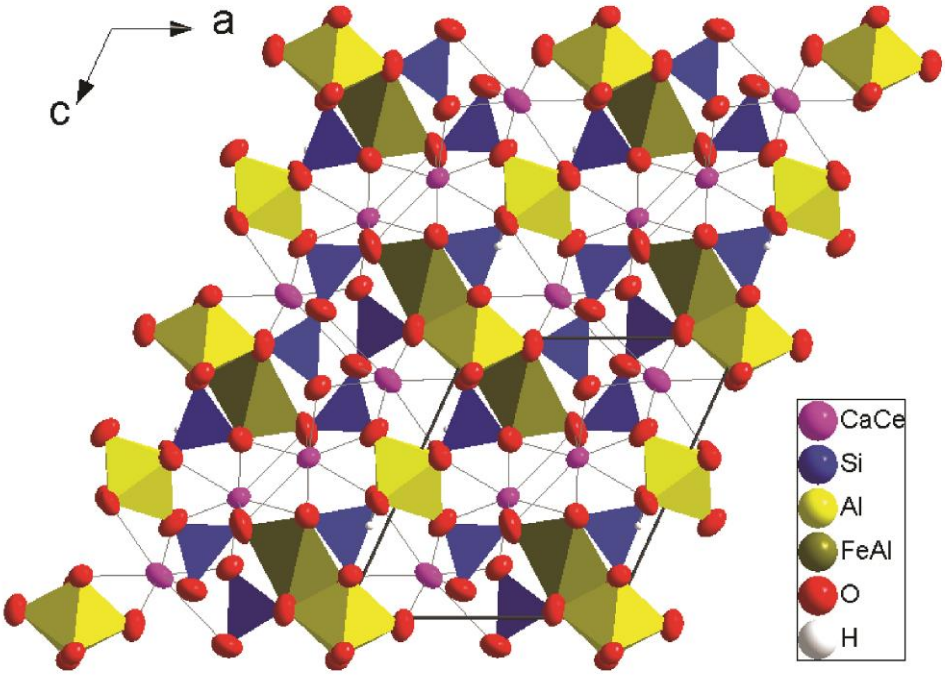

Figure 4.3.8. Output of the anisotropic structure refinement of the Aln crystal (#8.1) from a mylonitic domain (atomic displacement probability factor: 99%). It is evident the modest anisotropy of the atomic displacement ellispoids.

4.3.4 Discussion

4.3.4.1 Crystallography constrains

As observed by Gatta et al. (2009) for strained kyanite crystals from the Eclogitic Micaschists Complex of the Sesia Lanzo Zone (EMC-SLZ), the X-ray single-crystal diffraction experiments can provide evidence of plastic deformation at two different levels, which are mutually related: *i*) the first reflects the 3-dimentional periodic arrangement of the atomic sites, and it is represented by shape and size of the Bragg diffraction spots, *ii*) the second reflects the displacement from the center of gravity of any given atomic site, and it is represented by magnitude and orientation of the displacement ellipsoid produced by the structure refinement. More specifically, the single-crystal X-ray experiment of the EMC-SLZ kyanite showed diffraction patterns severely textured on the (*h*0*l*)*-plane; such an evidence was not observed in the patterns on the (0*kl*)* and (*hk*0)* planes. The diffraction spots of kyanite were affected by large FWHM (compared to those of untrained gem-quality crystals), elliptical shape with significantly relevant ellipticity ratio (up to 3:1) and a severe bending (see Fig. 5 in Gatta et al., 2009). In addition, the anisotropic displacement ellipsoids of all the atomic sites were larger (*i.e.*, with a drastic ratio of the longest and shortest root-mean-square components of the ellipsoids, up to 4.0) than those previously reported in the literature for unstrained crystals, and systematically oriented with the largest elliptic section (almost) $\perp$ [010] (see Fig. 6 in Gatta et al. 2009). As discussed by Gatta et al. (2009), the large displacement ellipsoids reflected the displacement from the center of gravity of the electron distribution, rather than an anomalous atomic thermal motion. The effect usually called "crystal mosaicity" can be ascribed to randomly located dislocations, which is usually associated with a homogeneous enlargement of the X-ray diffraction spots. If dislocations are arranged continuously within the crystal, a long-range "bending" of the structure occurs, with a consequent bending of the diffraction spots emulating a polycrystalline-like (*i.e.*, powder-like) diffraction pattern. On the whole, Gatta et al. (2009) ascribed the anomalous magnitude (and orientation) of the displacement parameters and the features of the diffraction pattern of Ky to two potentially combined effects: *i*) crystals were actually composed by several blocks; *ii*) crystals were affected by pervasive residual strain, as a result of plastic deformations and re-crystallization (with at least two stages of growth) during the long-lived tectono-metamorphic evolution.

Aln crystals of this study do not show any evidence of pervasive residual strain ascribable to a plastic deformation: 1) the single-crystal X-ray diffraction patterns are those of clearly unstrained crystals, with Bragg spots of almost circular section (ellipticity ratio up to 1.2:1) and FWHM comparable (within 3σ) to that of gem-quality unstrained epidote crystals; 2) the structure refinements provide structural models virtually identical to those of other (unstrained) allanite reported in the literature, in

particular with atomic displacement parameters which are, in shape and magnitude, comparable to those previously reported.

The different behaviour of Aln and Ky cannot simplistically be ascribed to the different general symmetry of the structures (as symmetry governs the deformation mechanisms): Aln and Ky are both low-symmetry minerals (Aln is monoclinic, Ky is triclinic), with high-degrees of freedom of deformation. However, they show a remarkable contrasting physical behaviour in relation to the incremental deformation, even under similar *P/T* ratios (*e.g.*, Delleani et al., 2012; Corti et al., 2018) and hosting rock-matrix (in both cases Qz-rich). Moreover, the response to the tectono-metamorphic conditions appears not to be related to the bulk compressibility: the isothermal bulk modulus (valid at room conditions, $K_{P0,T0}$) of kyanite is $K_{P0,T0}$= 190-200 GPa (Liu et al., 2009), that of allanite is $K_{P0,T0}$=131(4) GPa (Gatta et al., 2019); therefore, kyanite is drastically stiffer than allanite.

As the plastic behaviour is expected to be governed by the crystal structure, the further question is: how the isomorphic substitution can influence the plastic response among the (isostructural) epidote-group minerals? The answer to this question is not trivial. The recent study of Gatta et al. (2019) on the elastic behaviour of allanite under compressional regime, which provided also a comparative analysis among the epidote-group minerals (based on previous data by Gatta et al., 2011b, and Qin et al., 2016), reported that the compressional patterns among this group of minerals are different at a significant level, in terms of bulk compression and elastic anisotropy, though not drastically. The following isothermal bulk moduli were obtained: $K_{P0,T0}$=131(4) GPa for allanite, $K_{P0,T0}$=111(3) GPa for epidote with 0.74 Fe a.p.f.u. and $K_{P0,T0}$=115(2) GPa for epidote with 0.79 Fe a.p.f.u., and $K_{P0,T0}$=142(3) GPa for clinozoisite with 0.40 Fe a.p.f.u.. Epidote is the softest one, clinozoisite is the stiffest and allanite lies in between. On the basis of the structural homology among the aforementioned minerals, which governs their "similar" compressional behavior, we cannot exclude that even the other epidote-group species would experience a similar plastic behavior as that of allanite under the same tectono-metamorphic conditions of the samples here investigated.

4.3.4.2 LREE released vs. rock matrix total strain

The multidisciplinary approach of this study reveals that Aln can be remarkably resistant to deformation and metamorphism under cold subduction thermal state (see Corti et al., 2018). Under these conditions, Aln crystals do not show evidence of intra-crystalline plastic deformation from micro- to atomic-scale and along strain gradients. Aln behaves as a "rigid" object, at a first approximation, in a weak matrix (metagranitoids with modal amount of Qz + Wm>60%) and it is characterised by high mechanical strength and it is reluctant to recrystallize during polyphasic tectono-

metamorphic history. Even in mylonitic domains, Aln is rigid because deformation is accommodated by the recrystallization of Qz and Pl grains and crystal folding (*e.g.*, Wm).

Quantitative mineral chemical analysis and chemical imaging procedure were performed to decipher the chemical features of the Aln zoning in relation to the rock-matrix strain accumulation. The Aln chemical zoning is mostly defined by the Ca/ and Ce/LREE ratio. The high Ca fraction in the Aln3 sample may be due to a more progressed metamorphic transformation, especially in mylonitic domains. Despite a general Al depletion in the mylonitic domains, the analysed Aln crystals show a similar LREE content within the inner zoning (*i.e.*, Aln1, Aln2). The chemical variation became appreciable in the outermost zoning (*i.e.*, Aln3) and in mylonitic domains, the Aln3 shows even lower LREE contents than Aln3 in coronitic and tectonitic domains (Figs. 4.3.6c and 4.3.6d).

The QXRMA procedure reveals that elements such as Ce, Nd, and Th build up patchwork and en-echelon-like re-arrangement of Aln zoning in tectonitic and mylonitic domains, respectively (Fig. 4.3.5). These chemical features might therefore be the effect of the strong strain partitioning between Aln and the matrix mineral at H*P*-L*T* conditions during subsequent tectono-metamorphic stages.

Allanite is known as one of the main potential carriers of LREE in the mantle wedge (*e.g.*, Hermann, 2002; Giere and Sorensen, 2004; Hermann and Rubatto, 2009) because of high shielding property during subduction processes (Cenki-Tok et al., 2011). Combining the Ca/LREE ratio of the Aln crystals with the DFE rock-matrix estimation of each analysed sample (Corti et al., 2017), it is possible to estimate the LREE release in relation with the strain accumulated by the rock-matrix during D2 (responsible for the S2 dominant foliation) tectono-metamorphic stage (Fig. 4.3.9). The LREE released during the exhumation in the subduction mantle wedge for the six analysed Aln crystals was estimated through two parameters in relationship with the DFE (Fig. 4.3.9). The first is the difference between Ca/LREE ratio in Aln1 and Aln3, normalised to the sum of Ca/LREE ratio in the three zoning of a single grain. Figure 4.3.9a shows a well-defined linear regression ($y = 0.2x + 18.9$, with $R^2 = 0.92$) between the normalised Ca/LREE ratio and the strain accumulation in the rock matrix. The second parameter is the difference between the LREE contents in Aln1 and Aln3, normalised to the sum of LREE in the three zoning of a single grain (Fig. 4.3.9b), and it reflects a LREE loss parameter. The relation between LREE variations and DFE is characterised by an exponential regression ($y = 0.8e^{0.6x}$, with $R^2 = 0.96$). These two correlations allowed quantifying the release of LREE from Aln grains in the three strain domains.

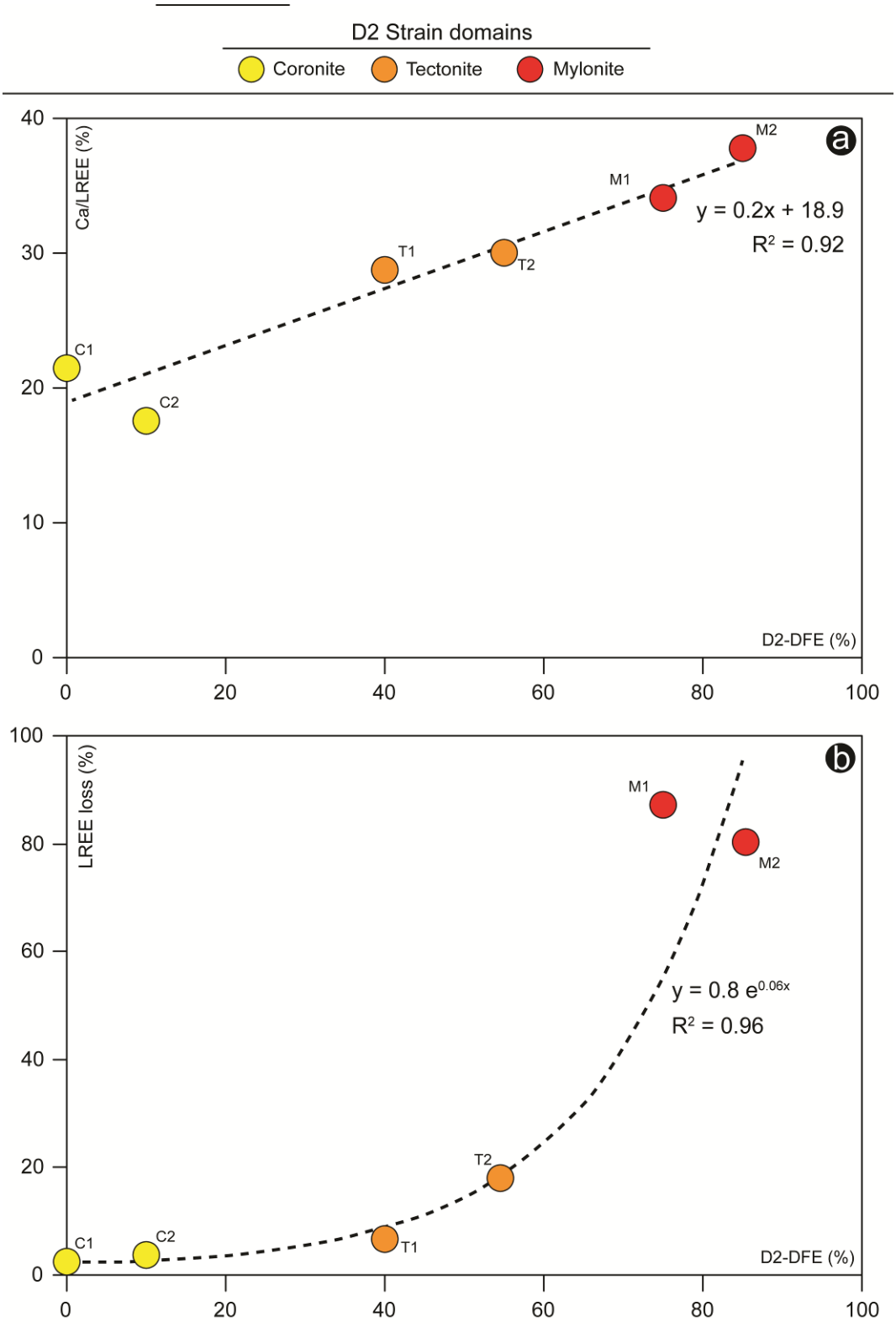

Figure 4.3.9. LREE release. a) Normalised Ca/LREE ratio vs. D2-stage Degree of Fabric Evolution estimated for each sample. The label of each sample is reported. The linear regression and the related coefficient of determination between Ca/LREE ratio during the D2 strain accumulation is reported. b) LREE loss vs. D2-stage Degree of Fabric Evolution estimated for each sample. The exponential regression and the related coefficient of determination between LREE released during the D2 strain accumulation is reported.

Our results show that the Aln appears to be able to carry and release LREE under H*P*-L*T* conditions if the surrounding rock matrix accumulates high total strain and metamorphic transformation. Indeed, Aln in mylonitic rocks shows higher Ca/LREE and LREE loss parameters than Aln in tectonitic and coronitic domains (Figs 4.3.6c and 4.3.9). The diagram in Fig. 4.3.9 shows that from coronite to mylonite the increase of the two parameters is continuous. Therefore, a LREE loss of 1-2%, 5-16%, and 82-84% (Fig. 4.3.9b) and increase of Ca/LREE parameter of 18-21%, 29-30%, and 34-38% (Fig. 4.3.9a) are estimated for coronitic, tectonitic, and mylonitic domains, respectively. The two parameters increase from coronite to mylonite but with a linear and exponential trend for Ca/LREE and LREE loss, respectively. The high Ca/LREE and LREE loss parameters may be due to a more progressed metamorphic transformation facilitated by high strain accumulation in mylonitic domains.

4.3.5 Conclusion

This work shows that allanite enclosed in metagranitoids under subduction thermal state and blueschist facies conditions do not record any plastic deformation regardless the total strain accumulated by the host rock. The plastic deformation is accommodated by the rock matrix minerals, such as quartz, feldspar, and white mica. The only evidence of deformation in allanite is represented by brittle boudinage in mylonitic rocks. The deformation in the rock matrix appears to be responsible for the linear chemical zoning patterns in tectonite and mylonite crystals. The total strain accumulated by hosting rocks under H*P*-L*T* has also a strong control on LREE in allanite. The release of LREE from allanite is indeed facilitated if high strain and metamorphic transformation is accumulated in the surrounding rock matrix (*i.e.*, mylonitic shear zones). Therefore, strain is a fundamental parameter to provide subduction wedge with LREE.

4.3.6 Acknowledgment

We tank Davide Comboni for his help with the single-crystal X-ray data collections, Andrea Risplendente for his assistance during the X-ray maps and WDS-EMPA analysis, and Manuel Roda for reading the first draft of the text. Funding by MIUR-PRIN 2010-2011 “Birth and death of oceanic basins: geodynamic processes from rifting to continental collision in Mediterranean and circum-Mediterranean orogens”, PSR2018_DZANONI, and FFABR2018DZANONI, Univ. Milano. The authors acknowledge the support of the Italian Ministry of Education (MIUR) through the project “Dipartimenti di Eccellenza 2018–2022, Le Geoscienze per la Società: Risorse e loro evoluzione”.

References are integrated at the end of the thesis.

Chapter 5

Second case study: Mt. Mucrone area

5.1 3D reconstruction of fabric and metamorphic domains in a slice of continental crust involved in the Alpine subduction system: the example of Mt. Mucrone (Sesia-Lanzo Zone, Western Alps)

The following sections refer to the submitted paper: Corti L., Zucali M., Delleani F., Zanoni D., and Spalla M.I.: 3D reconstruction of fabric domains in the eclogitised continental crust of the Mt. Mucrone area, Sesia-Lanzo Zone, Western Alps. International Journal of Earth Sciences

Abstract

Geological mapping, multiscale structural analysis, and estimations of the degree of fabric evolution and of reaction progress allow the construction of a 3D quantitative model of structural and metamorphic gradients in a portion of continental crust deeply involved in the Alpine subduction system, and mainly structured under eclogite-facies conditions before the continental collision. The investigated and modelled rocks are exposing in the surroundings of Mt. Mucrone, in the central Sesia-Lanzo Zone. The Geomodeller® software allowed a quantitative 3D estimation of domains characterized by homogeneous domains of fabric evolution and metamorphic reaction progress (DFE and DRP, respectively) for two of the seven structural and metamorphic imprints detected in this area: the D2-eclogitic and D5-greenschist stages, that are the more pervasive tectono-metamorphic stages at km-scale. Such a 3D modelling, clarifying mutual relationships between fabric and metamorphic gradients, indicates that: i) the DFE and DRP are closely related regardless the rock type; ii) the syn-deformational thermal regime can influence the degree of metamorphic transformation, if the DFE remains below to the 60% threshold; iii) the phase transitions cannot be properly implemented in quantitative geodynamic modelling without considering the heterogeneity of reaction progress and fabric evolution.

Keywords: Strain partitioning, metamorphic reaction progress, eclogitised granitoids, Austroalpine domain.

5.1.1 Introduction

The relationship between deformation and metamorphism in basements have long been studied (Turner and Weiss 1963; Park 1969; Hobbs et al. 1976) and it is currently generally accepted that the single use of geometric criteria during structural correlation turns out to be poorly reliable (Spalla et al. 2000), mainly due to deformation partitioning commonly affecting crystalline basements (*e.g.* Myers 1970; Mørk 1985). Similarly, the metamorphic correlations without structural constrains it often turns out to unconvincing, again because strain partitioning may influence the heterogeneous distribution of metamorphic assemblages or, even worst, it can result in gaps in the metamorphic memory of rocks (Spalla et al. 2005; Pearce and Wheeler 2010). These vacancies are referenced to be due to the catalysing effect of deformation on the metamorphic reaction progress (*e.g.* Spalla et al. 2000; Spalla et al. 2005; Hobbs et al. 2010; Chapman et al. 2019) or local instabilities due to diffusion processes (*e.g.* Pearce and Wheeler 2010) or stress-driven reaction heterogeneities (Schmalholz and Podladchikov 2014; Tajcmanova et al. 2014; Zhong et al. 2017). Detailed multiscale correlation among superposed fabric elements and metamorphic assemblages is known to be of first order importance to infer relationship between fabric and metamorphic gradients (*e.g.* Williams 1985; Stünitz 1989; Lardeaux and Spalla 1990; Passchier et al. 1990; Johnson and Vernon 1995; Spalla et al. 1999; Zucali et al. 2002; Spalla and Zucali 2004; Gosso et al. 2010; Salvi et al. 2010; Hobbs et al. 2011; Delleani et al. 2012; Gosso et al. 2015; Rebay et al. 2015; Cantù et al. 2016; Corti et al. 2017, 2018; Delleani et al. 2018).

Indeed, syn-metamorphic finite strain gradients from domains that completely escaped deformation (coronite) or that partially (tectonite) or pervasively (mylonite) deformed are common in adjacent rock volumes (*e.g.* Bell and Rubenach 1983; Lardeaux and Spalla 1990; Bell and Hayward 1991; Spalla and Zucali 2004; Salvi et al. 2010). More in details, in coronitic domains metamorphic reactions take place without the development of a new oriented fabric. In contrast, where the strain is accumulated, tectonitic and mylonitic fabric develop and the new metamorphic assemblages define the new fabrics (Spalla et al. 2005; Salvi et al. 2010; Gosso et al. 2015). Heterogeneities, accompanying fabric evolution, also characterize metamorphic reaction progress facilitating the reconstruction of structural and metamorphic evolution back in time. The resulting distribution of the superposed fabrics elements and metamorphic assemblages allows the evaluation of the mechanically and chemically reacting volume percentage during the successive tectono-metamorphic stages. The correlation between degree of fabric evolution (DFE) and degree of metamorphic reaction progress (DRP) of superposed tectono-metamorphic imprints can be used for quantifying the size of rock volumes affected by such structural and metamorphic heterogeneities in crustal portions implicated in convergent dynamics (*e.g.* Salvi et

al. 2010; Gosso et al. 2015). Estimates of the DFE and DRP relationships made on rock-volumes reworked during various thermo-mechanical evolutions shows that the dominant tectono-metamorphic imprint is related to the high degree of fabric evolution and metamorphic reaction progress (*e.g.* Southalpine domain: Spalla et al. 2000; Sesia-Lanzo Zone: Zucali et al. 2002; Delleani et al. 2012, 2013; Corti et al. 2017; Dent Blanche nappe: Roda and Zucali 2008; Baletti et al. 2012; Languard-Tonale unit: Salvi et al. 2010).

The Sesia-Lanzo Zone, and in particular the Monte Mucrone area, has long been a training area for multiscale structural analysis and for study in detail the correlation between deformation and metamorphism thanks to the remarkable fabric and metamorphic partitioning from micro- to km-scale (Hy 1984; Koons et al. 1987; Ridley 1989; Ildefonse et al. 1990; Zucali et al. 2002; Babist et al. 2006; Cenki-Tok et al. 2011; Delleani et al. 2013). This area offers the opportunity to investigate the relationships between DFE and DRP. 2D representations of the fabric gradients and the metamorphic transformation have already been performed (Zucali et al. 2002; Delleani et al. 2012). For these reasons, this area can be an ideal place to develop a 3D model that allows a quantitative evaluation of the interaction between the fabric evolution and the metamorphic reaction progress.

In this contribution, we integrate geological mapping, multiscale structural analysis, DFE and DRP estimations of Zucali et al. (2002) and Delleani et al. (2012, 2013) with new original data to construct a 3D quantitative DFE and DRP models of the area between Mombarone, Mt. Mucrone, and Mt. Mars. HP-LT metamorphic rocks derived from pre-Alpine continental protoliths are poly-deformed when involved in the Alpine subduction-collision system, and pre-Alpine igneous and HT metamorphic relicts are preserved in heterogeneously deformed and eclogitized metagranitoids and metapelites, respectively.

Multiscale structural analysis revealed a pre-Alpine structure (pre-D1) and six groups of superposed Alpine structures developed under eclogite-facies conditions (D1 to D3) during subduction, and successively under blueschist- (D4) to greenschist-facies conditions (D5 to D6) during the exhumation. D2 structures are dominant at the regional scale and are characterized by isoclinal folding associated with a pervasive foliation. We synthesize the multiscale data, defining syn-D2 (H*P*-L*T*) and syn-D5 (L*P*-L*T*) structural and metamorphic heterogeneities, on maps showing the degree of fabric evolution and metamorphic reaction progress. We apply the GeoModeller ® software that allows to build a 3D model in which it is possible to discriminate the volumes characterized by different degree of fabric evolution and metamorphic reaction progress developed during D2- and D5-stages and their quantitative estimation in volume percentage together with their spatial distribution.

The 3D modelling allows a quantitative comparison between volumes preserving textural and mineral relicts after, regardless the possible influence of fluids, during incomplete accomplishment of

structural and/or metamorphic re-equilibrations; moreover, the proposed 3D model quantify structural and metamorphic re-equilibrations in rock volumes translated through different structural levels, in which evolving thermomechanical regimes drive the change of dominant active deformation mechanisms.

5.1.2 Geological outline

The Sesia-Lanzo Zone (SLZ, Fig. 5.1.1) represents the widest portion of continental crust in the Western Alps that underwent high pressure (H*P*) metamorphism during the Alpine subduction (*e.g.* Dal Piaz et al. 1972; Compagnoni et al. 1977; Pognante 1991; Babist et al. 2006; Meda et al. 2010; Roda et al. 2012; Regis et al. 2014). The Alpine metamorphic history of the SLZ comprises the record of an eclogite-facies imprint followed by blueschist- and greenschist-facies re-equilibrations (*e.g.* Compagnoni and Maffeo 1973; Compagnoni 1977; Gosso 1977; Lardeaux 1981; Lardeaux et al. 1982a; Lardeaux et al. 1983; Spalla et al. 1983; Pognante 1989a; Venturini et al. 1994; Castelli and Rubatto 2002; Zucali et al. 2004; Rebay and Messiga 2007; Zucali and Spalla 2011; Giuntoli and Engi 2016; Giuntoli et al. 2018a; Roda et al. 2018a; Roda et al. 2019). Mineral ages ranging between 90 and 65 have been related to the Alpine eclogite-facies peak (Rubatto et al. 1999; Cenki-Tok et al. 2011; Regis et al. 2014; Giuntoli et al. 2018b; Halama et al. 2018). The very low *T*/*P* ratio characterising this evolution assists the preservation of pre-Alpine igneous and metamorphic relics in rocks with an Alpine polyphasic recrystallization. *P*-*T* conditions for the early-Alpine H*P* imprints range between 500–625 °C and 1.3–2.5 GPa (see Roda et al. 2012 for a review of available PT estimates). The external margin of the SLZ is bounded by eclogitized ophiolitic relics of the Liguria-Piedmont Ocean, the Piedmont Zone, and its internal margin is a thick mylonitic belt (the Canavese Line), separating SLZ from the lower crustal rocks of the Southalpine Ivrea Zone, which escaped the Alpine HP evolution (*e.g.* Bigi et al. 1990; Rebay et al. 2018; Balestro et al. 2019).

A pre-Alpine polyphasic metamorphic evolution, from granulite- to amphibolite-facies conditions, is still preserved in marbles, metapelites, metagranitoids and metabasics (Compagnoni et al. 1977; Lardeaux et al. 1982b; Castelli 1991; Lardeaux and Spalla 1991; Rebay and Spalla, 2001): the pre-Alpine *T*-climax has been constrained at *T*=730–830 °C *P*=0.7-0.9 GPa (Lardeaux and Spalla 1991). Granulite- and amphibolite-facies imprints have been interpreted as the result of an extension-related uplift of a portion of the Variscan crust, occurred in Permian–Triassic times during the lithospheric thinning leading to the Tethys opening (*e.g.* Lardeaux and Spalla 1991; Marotta et al. 2009; Roda et al. 2018b).

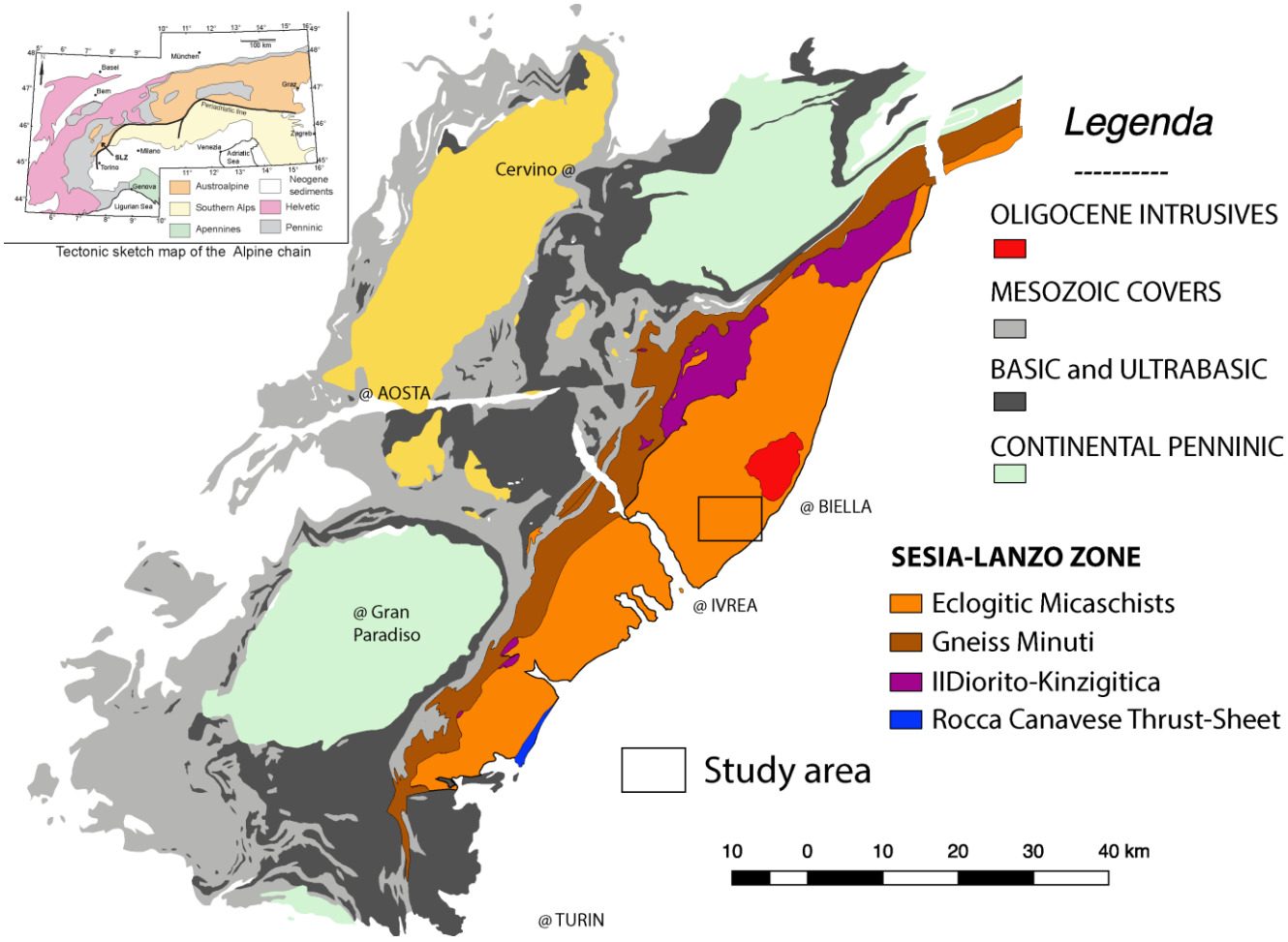

Figure 5.1.1. Tectonic scheme of the Western Alps with the different metamorphic complexes of the Sesia-Lanzo Zone. The studied area is located.

This pre-Alpine tectono-metamorphic evolution is preserved in the metamorphic complexes forming the SLZ: the Eclogitic Micaschist Complex (EMC), the Gneiss Minuti Complex (GMC), the II Dioritic–Kinzigitic Zone (IIDK) and the Rocca Canavese Thrust Sheets (RCTS) (*e.g.* Compagnoni et al. 1977; Pognante 1989a, 1989b; Spalla et al. 1991; Cantù et al. 2016; Roda et al. 2018a; Roda et al. 2019). The IIDK consists of kilometric lenses, lying between EMC and GMC, in which Alpine eclogitic assemblages are not described, even if in the Vogna Valley the tectonic contact underlying the margin between IIDK and EMC is marked by eclogite-facies mylonites (Lardeaux 1981; Lardeaux et al. 1982b). Eclogitic parageneses are widely described both in EMC and GMC with a strong difference in the volume affected by the greenschist re-equilibration: the GMC, which lies along the tectonic boundary with the Piedmont Zone, is widely re-equilibrated under greenschist facies conditions, while the EMC, constituting the internal part of the SLZ, records the greenschist-facies re-equilibration mainly along discrete shear zones and shows a dominant metamorphic imprint under

eclogite-facies conditions (*e.g.* Spalla et al. 1983; Stuenitz 1989; Spalla et al. 1991; Giuntoli and Engi 2016).

The EMC protoliths are high-grade paragneisses, granulites, amphibolites and minor marbles and quartzites, which are the country rocks of Permian granitoids and gabbros (Compagnoni and Maffeo 1973; Callegari et al. 1976; Compagnoni et al. 1977; Lardeaux 1981; Oberhaensli et al. 1985; Castelli 1987; Bussy et al. 1998; Cenki-Tok et al. 2011; Zucali 2011) and from which the Mt. Mucrone body is the most renown. The deformation history of EMC, in this area, comprises four generations of Alpine folds, two of which are associated with the high-pressure (H*P*) mineral assemblages, and two generations of shear zones synchronous with the blue- and greenschist-facies re-equilibrations, respectively (Hy 1984; Zucali et al. 2002; Delleani et al. 2012; 2013). According to Zucali (2002) D1 and D2 groups of folds are generally associated with axial plane foliations marked by Ph, Pg, Na-Cpx, Grt, Rt and Zo (mineral abbreviations are used according to Whitney and Evans 2010); the same mineral assemblage is stable during D3 folding. D4 is accompanied by a widespread re-equilibration under blueschist-facies conditions, confined along metre-wide mylonitic shear zones, which locally developed at the boundary between metagranitoids and country rocks. D5 mega-scale folds, D6 centimetre-thick mylonitic shear zones and gentle folding, overprinting blueschist mylonites and the eclogitic foliations, are synchronous with the formation of the greenschist-facies paragenesis Qtz, Ab, Wm, Ep, Ttn and green-Amp.

5.1.3 Lithostratigraphy and mesostructures

The interpretative map reported in Figure 5.1.2 shows the distribution of main lithotypes and structures in the area from the Mt. Mucrone to the East and Mombarone-Mt. Mars ridge to the West. Here the main lithologic types are: 1) metaintrusives, comprising metagranites, meta-quartzdiorites and metadiorites; 2) metaaplites; 3) eclogites and glaucophanites; 4) micaschists; 5) gneisses; 6) marbles and quartzites; 7) zoisitites and 8) andesitic dykes. The interpretative map in Figure 5.1.2 and the 3D modelling have been built grouping lithotypes with structural and lithostratigraphic affinities to increase readability and modelling. Five groups have been assembled: 1) micaschists; 2) gneisses; 3) metabasites; 4) metaintrusives; 5) marbles and "quartzites" (Figs. 5.1.2, 5.1.3 and Tab. 5.1.1). Mineral assemblages marking coronitic, tectonitic and mylonitic fabrics developed during successive deformation stages (D1 to D6) in the different lithologic groups are summarized in Table 5.1.1. Below, a brief description of each group is given, though more details can be found in original papers (Zucali 2002; Zucali et al. 2002; Delleani et al. 2012, 2013).

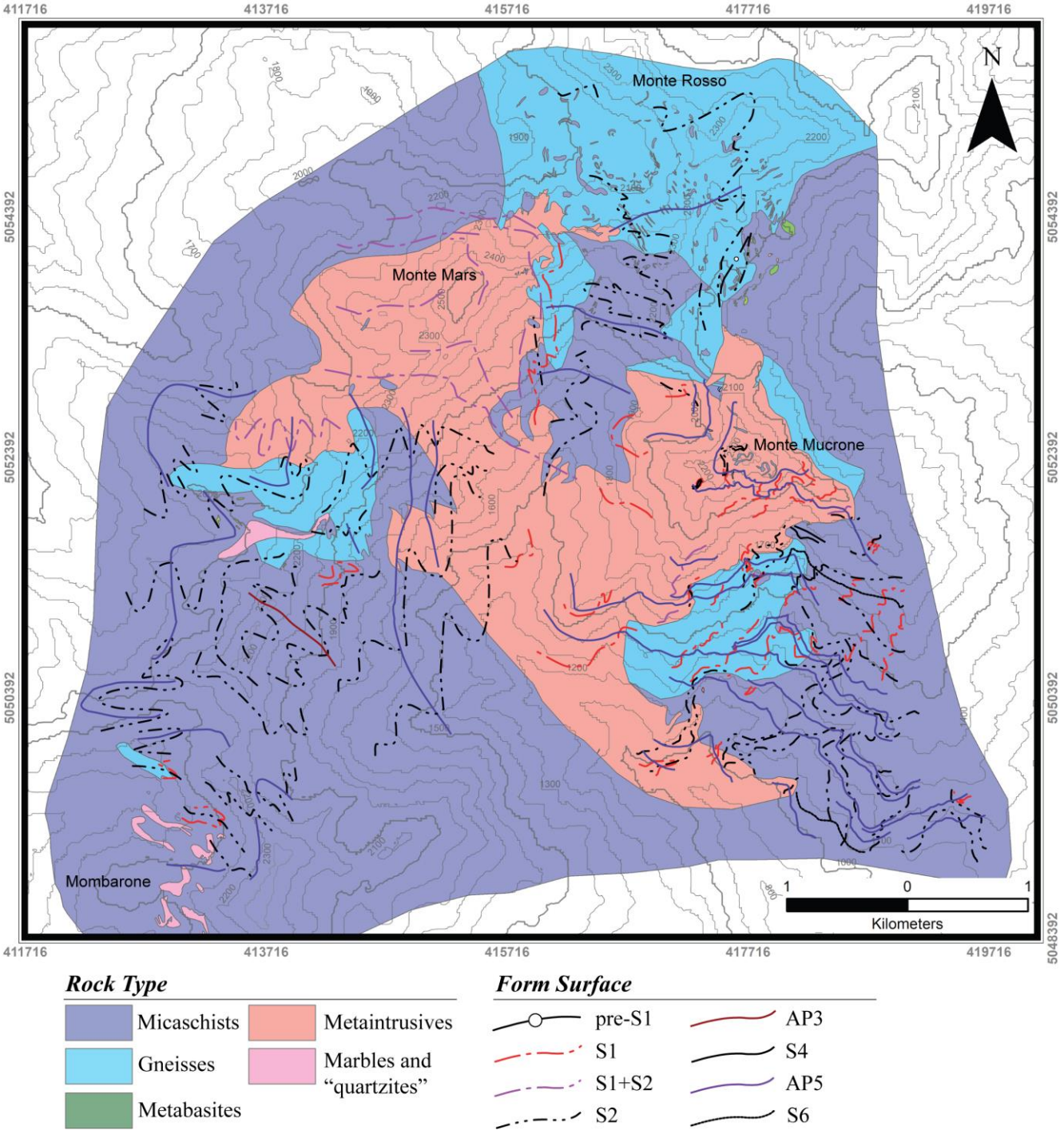

Figure 5.1.2. Petrostructural map with foliation and axial plane trajectories (S: foliation; AP: fold axial plane), synthesized by Zucali (2002), Zucali et al. (2002), Delleani et al. (2012) and Delleani et al. (2013) integrated with original data.

5.1.3.1 Metaintrusives

Protoliths consist of granitoids that occur as 10-m to km-sized bodies, including minor meter-sized granodioritic lenses. The metagranitic complex ("grey-type" metagranitoids and "green-type" metagranitoids according to Delleani et al. 2012, 2013) forms the upper part of Mt. Mucrone and Mt. Mars and derives from Permian intrusive rocks (Oberhänsli et al. 1985; Bussy et al. 1998; Rubatto et al. 1999; Cenki-Tok et al. 2011), locally in primary contact with metasedimentary country rocks (Compagnoni and Maffeo 1973; Hurford and Hunziker 1985; Delleani et al. 2013) that preserve the pre-Alpine HT-LP metamorphic imprint (Zucali et al. 2002).

Metagranitoids comprise medium- to coarse-grained lithotypes, showing a well-preserved isotropic and hypidiomorphic igneous texture, with igneous mineral relics as Bt, Aln, and Kfs, only partially replaced by Alpine Jd, Grt, Zo and Phn; meta-quartzdiorites consist of fine- to medium-grained rocks, showing a dominant foliation marked by Omp, Grt, Wm, Gln and Czo. In the metaintrusives, the partitioning of Alpine deformation is responsible for the preservation of igneous texture in low-strain volumes, wrapped by finely foliated domains (mylonitic textures) where Alpine eclogite-facies assemblages are dominant. Blueschist- and greenschist-facies assemblages are poorly developed, being associated to localized deformation bands, shear zones or large-scale recumbent folds.

Zoisitites layers may occur as enclaves with a thickness of 1-to-10 m in metagranitoids at Mt. Mars and Mt. Mucrone; these rocks are characterized by garnet grains up to 10 cm in size associated with epidotes.

Meter to ten-meters thick metaaplite dikes show a well-developed foliation, marked by the Shape Preferred Orientation (SPO) of phengitic mica, quartz, feldspar and omphacite. The foliation and the lithological boundaries commonly are parallelised with the D2 eclogitic foliation within micaschists, gneisses and large metaintrusives bodies.

5.1.3.2 Micaschists

The micaschists are coarse- to fine-grained, with a pervasive foliation, with millimetre-scale spacing marked by Qtz + Omp + Gln + Grt and Wm-rich layers. They can be characterized by mm- to cm-sized rootless folds, generally marked by Qtz-rich veins or layers. Omp and/or Gln SPO is common and generally lie parallel to the most penetrative D2 eclogitic foliation.

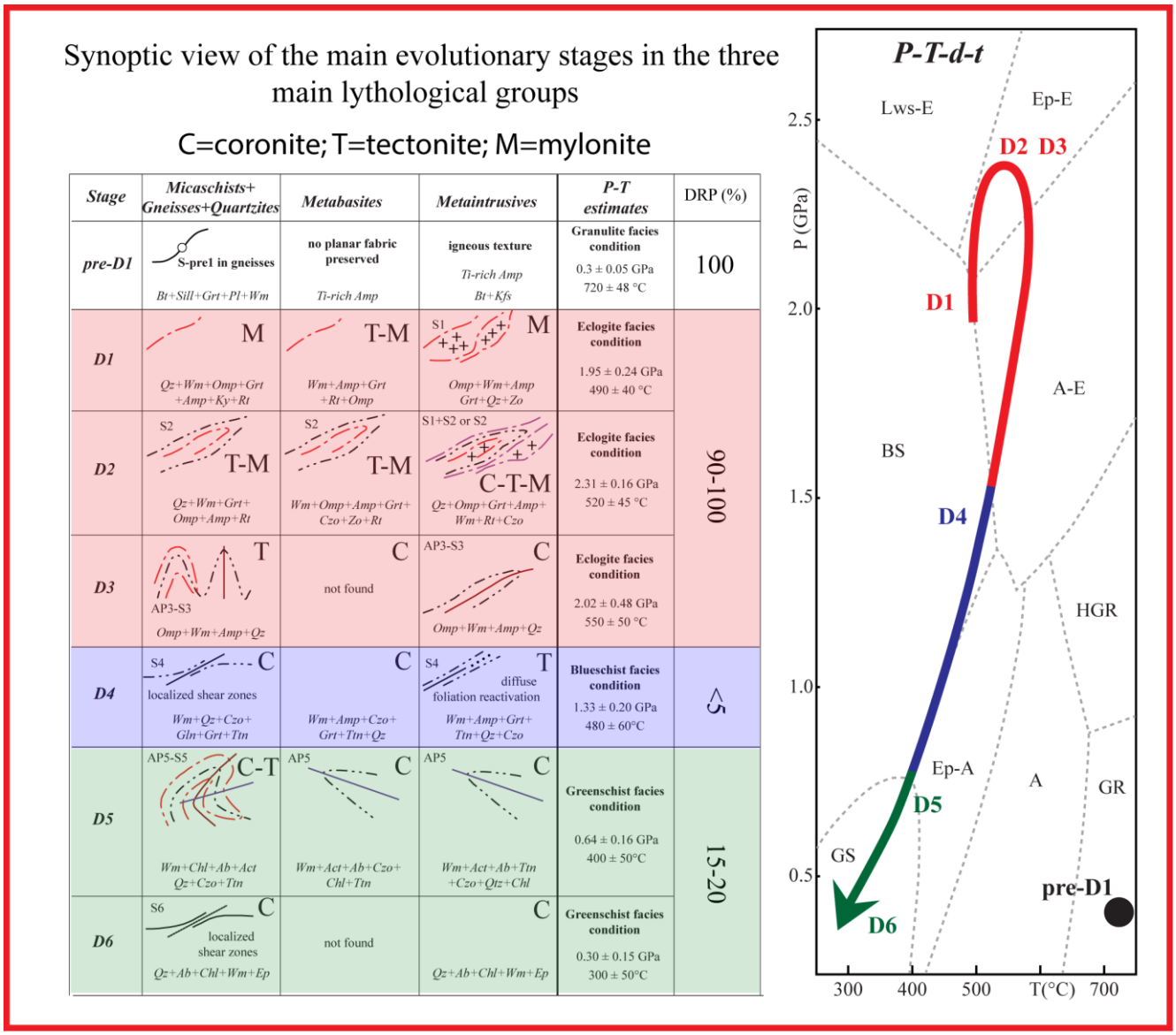

Table 5.1.1. Summary of the structures developed in each rock type during pre-Alpine and Alpine polyphase tectonic evolution. the degree of fabric evolution (C: coronite; T: tectonite; M: mylonite) and degree of metamorphic reaction progress (DRP: percentage of syn-metamorphic minerals) have been quantified for each deformational stage. The pressure-temperature estimated for successive structural and metamorphic stages and the inferred P-T-d-t path are also reported (modified after Zucali et al. 2002 and Delleani et al. 2012).

5.1.3.3 Gneisses

The gneisses are structured as Qtz- and Grt-bearing layers alternating with more mafic layers, primarily consisting of Omp, Grt and Gln with minor Qtz and Wm; this layering marks the gneissic penetrative D2 eclogitic foliation. Meter-thick layers of porphyric gneiss and coarse-grained Kfs crystals occur. In agreement with the observations of adjacent areas by Zucali (2002), these latter rocks are interpreted as derived from pre-Alpine partially melted paragneisses, named kinzigites (high-grade Bt + Grt + Sil-bearing gneisses) in the Alpine literature. The lithological boundary between gneisses

and micaschists is never sharp but consists in a gradual transition from portion of mica-rich gneisses to micaschists. Micaschists and gneisses may generally bear metre-sized lenses or boudins of mafic rocks as eclogites and glaucophanites, or marbles and quartzites or meta-aplitic layers.

5.1.3.4 Metabasites (eclogites and glaucophanites)

Eclogites mainly consist of omphacite and garnet and secondarily of glaucophane, white mica and minor carbonates. They locally display a foliation, commonly marked by the SPO of omphacite but generally eclogites do not display an oriented fabric. Locally, eclogite boudins within micaschists or gneisses, have a reaction rim rich in glaucophane and white mica. Glaucophanites may display a spaced foliation marked by the SPO of Gln, while Omp is normally randomly oriented.

5.1.3.5 Marble and "quartzites"

Meter- to ten-meter-thick marbles and quartzites may occur in layers or boudins in micaschists and gneisses. Pure and silicate-rich marbles (Pognante et al. 1980; Castelli 1991; Zucali 2002) are characterized by penetrative foliation generally marked by compositional layering in marbles and by mineral white mica SPO in impure marbles. "Quartzites" correspond to quartz-rich micaschists and occur as few-meter-sized boudins, with a D2 dominant foliation marked by white mica, chloritoid, garnet and kyanite (Pognante et al. 1980; Zucali 2002; Gatta et al. 2009; Regis et al. 2014) indicating eclogite facies conditions (Zucali et al. 2002).

5.1.4 Structural and metamorphic evolution

Seven groups of structures were recognized (Table 5.1.1), from pre-Alpine to Alpine in age, named as follows: D1 to D3 took place under eclogite- facies, D4 under blueschist- facies and D5 – D6 under greenschist-facies conditions, respectively (Zucali et al. 2002; Delleani et al. 2012, 2013). A pre-D1 foliation has also been recognized in paragneisses as relict of the pre-Alpine high-temperature fabric (Zucali 2001).

D1 and D2 are the most pervasive fabrics, developed under eclogite-facies conditions as testified by SPO of white mica, omphacite and garnet ± glaucophane: S1 and S2 foliations developed in all lithotypes (Tab. 5.1.1 and Fig. 5.1.2). In metaintrusives, S1 can be separated from S2 only in the Mt. Mucrone area, while in Mt. Mars a S1+2 composite fabric occurs (Fig. 5.1.2). D3 isoclinal folding is locally associated with a S3 axial plane foliation, marked by omphacite SPO in micaschists and gneisses while it is lacking in the other rocks (Tab. 5.1.1 and Fig. 5.1.2). In D4 meter-thick shear zones SPO of blueschist facies minerals marks the new planar fabric S4 (Tab. 5.1.1). D5 and D6 are close to

open fold systems, associated with greenschist-facies mineral growths (Tab. 1). D6 consists of centimetre- to ten-centimetre-thick shear zones in which greenschist-facies minerals mark the localized S6 foliation (Tab. 5.1.1).

5.1.5 3D reconstruction method

3D geological modelling in metamorphic basements proved to be an excellent tool for quantitative estimates of rock volumes that recorded different fabric evolution and metamorphic transformation during a polyphase structural and metamorphic history (Salvi et al. 2010). To verify the effectiveness of the approach also in rocks forged in a subduction complex, we perform a quantitative 3D representation of domains characterized by homogeneous Degree of Fabric Evolution (DFE) and Degree of metamorphic Reaction Progress (DRP) for D2-eclogitic and D5-greenschist stages, which develop the two more pervasive tectono-metamorphic imprints at km-scale.

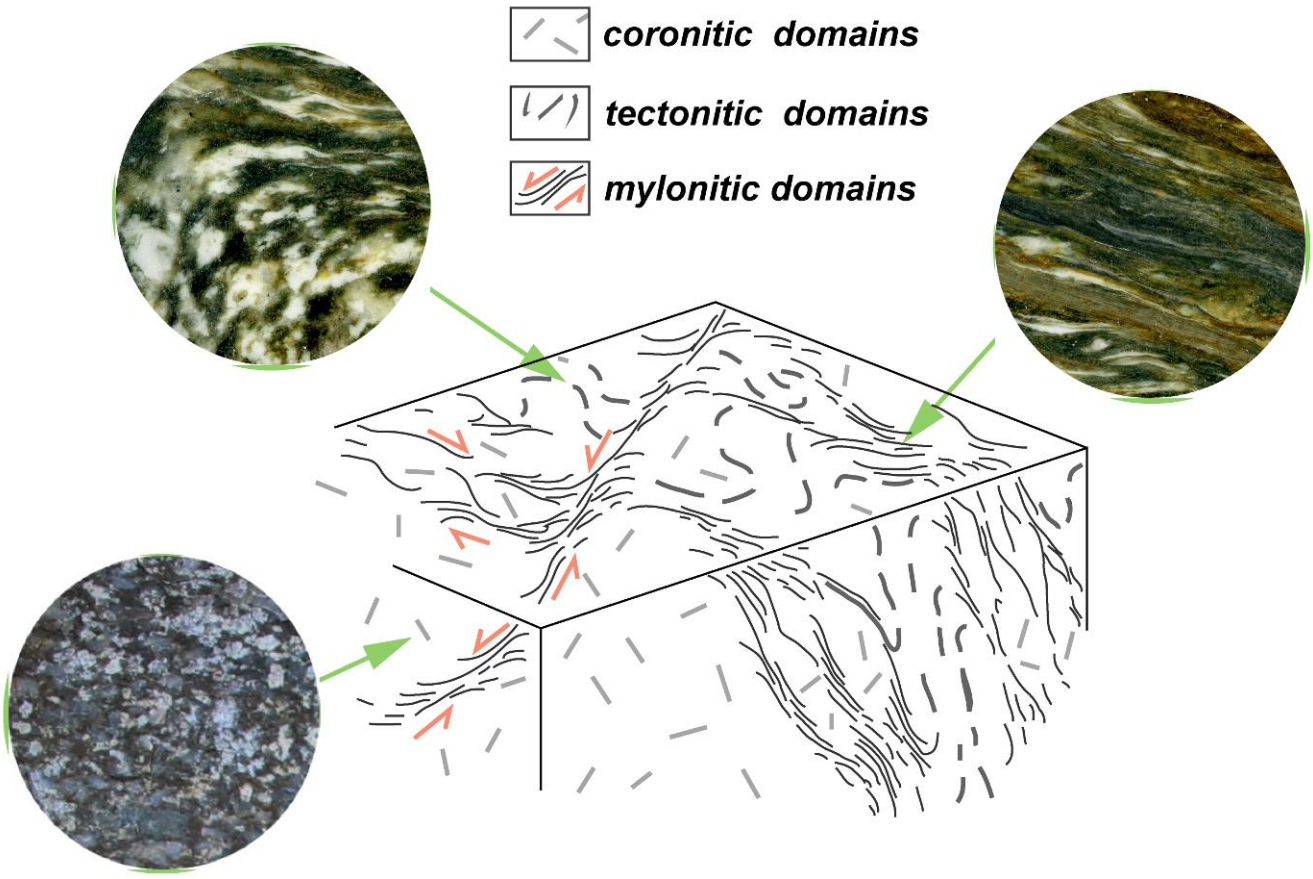

Figure 5.1.3. Idealized block diagram showing the heterogenous fabric evolution due to the multiscale strain partitioning (modified after Lardeaux and Spalla 1990 and Baletti et al. 2012). In the loops coronitic, tectonic and mylonitic fabrics of the eclogitised metagranitoid surfacing at the base of NE slope of Mt. Mucrone.

The contouring of domains that show homogeneous fabric development and metamorphic transformation is facilitated by integrating meso- with micro-scale structural analysis to estimate the DFE and DRP in volume percentage (Salvi et al. 2010; Delleani et al. 2012; Gosso et al. 2015; Corti et al. 2017). During incremental deformation related to a specific tectono-metamorphic stage, rock volumes may escape deformation in coronitic domains or may be partially or pervasively deformed in tectonic and mylonitic domains (Fig. 5.1.3), respectively. In the coronitic domains, metamorphic reactions take place without the formation of a new oriented fabric. Where the strain is accumulated, tectonitic and mylonitic fabric develop planar/linear tectonites or mylonites, marked by metamorphic assemblages peculiar of PT conditions under which the strain is accumulated (Bell and Rubenach 1983; Lardeaux and Spalla 1990; Passchier and Trouw 2005). Microstructural analysis was performed on 175 thin sections, strategically distributed throughout the area (≈52 km^2). The DFE is estimated on the basis of the amount of newly formed fabric compared to relic fabrics following the method of Salvi et al. (2010). The DFE is made explicit into three groups: Coronite (C) 0-20%; Tectonite (*T*) 21-60%; Mylonite (M) > 60% (Fig. 5.1.3 and Tab. 5.1.1). The DPR reflects the modal proportion of mineral phases, related to a specific deformation phase, as inferred using graphical comparison at optical microscope. Three class of DRP domains have been individuated: Low (L) 0-20%; Medium (M) 21-60%; High (H) > 60%. The flowchart shown in Fig. 5.1.4 summarizes the main method steps that combines both field-based structural and petrographic analysis and software-based modelling.

5.1.5.1 2D interpolation

The whole multiscale dataset was georeferenced and stored in a GIS (Geographic Information System) database. The GIS environment allows rapid data management, representation, querying and manipulation to predispose the multiscale structural and metamorphic dataset to 3D modelling by interfacing GIS to the GeoModeller® software.

The topography shape file was acquired on the Geoportal of Piemonte Region (http://www.geoportale.piemonte.it/cms/) and the digital elevation model DEM20 on SINAnet (ISPRAmbiente - website - http://www.sinanet.isprambiente.it/it/sia-ispra/download-mais/dem20/view).

The multiscale DFE and DRP punctual data combined with the foliation trajectories map are the starting point to constrain the area and the shape of the D2- and D5-related homogenous fabric evolution and metamorphic transformation domains. The results are synthetized in DFE and DRP thematic maps representing strain and metamorphic gradients in categorized domains (Fig. 5.1.4). The fabric evolution and metamorphic transformation domain maps linked to digital elevation model, eight

interpretative cross-sections, foliation trajectories map, and orientation data of the structural elements are used to constrain volumes during the 3D modelling with Geomodeller ®.

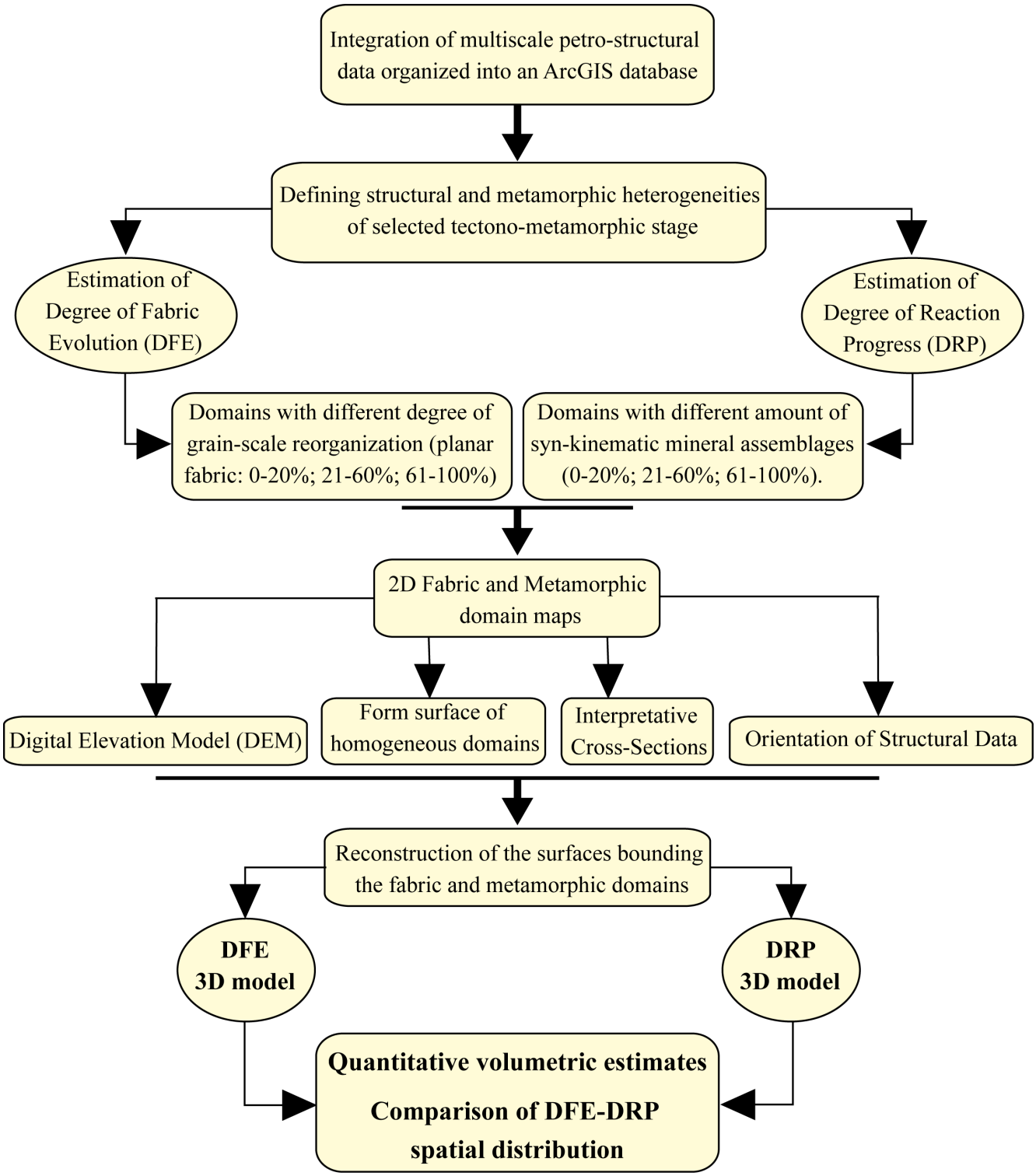

Figure 5.1.4. Flowchart for the 3D model set up.

5.1.5.2 3D modelling

Geomodeller® is based on the surface potential-field method to build 3D geological models from geological map, DEM, and structural orientations as data input (Chilès et al. 2004). Each geological interface is treated as an iso-potential surface of a potential-field defined in 3D space. The potential-field interpolation is based on a co-kriging statistical analysis defining the correlation between geological and structural data values as a function of the distances between data points. These distances are calculated using a system of parametric coordinates defined internally to the potential-field (Lajaunie et al. 1997). The software takes into account the iso-potential surfaces (*i.e.* geological interfaces) to compute those distances through an implicit method based on a system of potential-field functions (Calcagno et al. 2008). In details, it is able to model geological bodies integrating the location of geological interfaces (iso-potential data) used as spatial distribution parameters and their structural data orientation (potential gradients) used as anisotropy shape parameters. The combination of these functions allows a full spatial and volumetric description of shapes of geological bodies (Guillen et al. 2011).

The 3D quantification of the relationships between the DFE and DRP during polyphasic tectono-metamorphic evolution are feasible trough the reconstruction of the boundaries between homogeneous domains using the foliation trajectories map (Fig. 5.1.2) and several cross-sections as structural guide. The location precision of these boundaries varies between 5 and 50 m, depending on the density of the input petro-structural data. Taking advantage of the rapidity of the Geomodeller® elaborations, 3D modelling is performed for D2- and D5-stages. The first step consists in merging the digital elevation model with the 2D maps of DFE and DRP, locating the cross sections and structural orientation data to constrain the boundaries between homogeneous domains in three dimensions (Fig. 5.1.4). The modelled volume of 61.54 km^3 is voxelized into a regular and orthogonal 3D triangular mesh and the geological properties have been attributed to each cell. In the x-y-z directions the voxel dimension is 50-50-25m discretizing the entire volume in 3.534*e6 voxels. The consistency of the 3D results has been verified by visual inspection, to check the geologically coherent geometries and intersection relationships, plotting the modelled surfaces on the 2D maps and cross-sections in order to verify the model reliability with respect to the input data. The model allows defining the size, shape, and spatial relations of rock volumes showing homogeneous DFE and DRP for the two selected tectono-metamorphic stages. Comparing the DFE and DRP models for each analysed stage it is possible to calculate the volumetric misfit between the corresponding homogeneous DFE and DRP volumes.

5.1.6 Results

The degree of fabric evolution does not necessarily correspond with the degree of metamorphic reaction progress during each tectono-metamorphic stage as qualitatively suggested by Zucali et al. (2002) and, quantitatively, by Salvi et al. (2010). The DFE and DRP can evolve independently at different rates, but from DFE above 60% the mechanical and chemical transformation increase proportionally (Salvi et al. 2010).

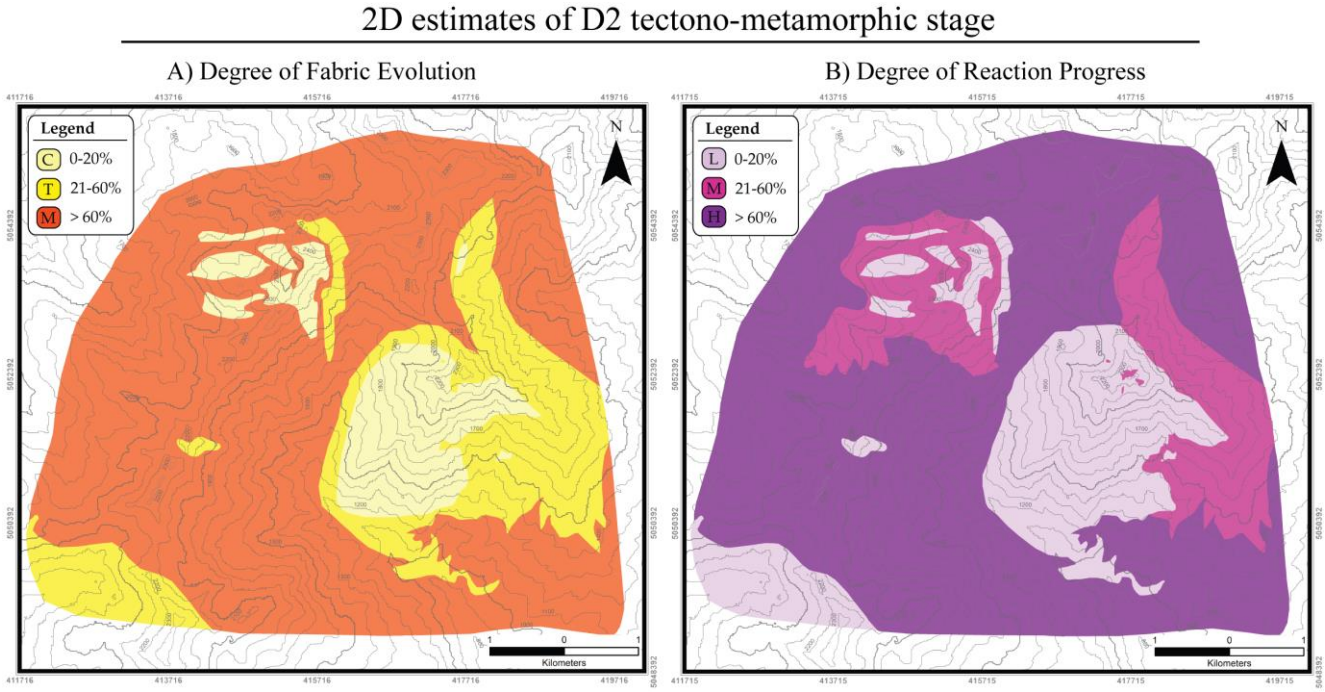

Figure 5.1.5. Domains of homogeneous degrees of fabric evolution and metamorphic reaction progress reconstructed for D2 stage (inferred from Zucali 2002, Zucali et al. 2002, Delleani et al. 2012, and Delleani et al. 2013 integrated with original data).

To investigate this heterogeneity at the km-scale the DFE and DRP models are separately constructed. The 2D contouring of the fabric and metamorphic gradients are performed for D2 (Fig. 5.1.5) and for D5 stages (Fig. 5.1.6). As already pointed out, these maps of fabric and metamorphic domains include the previous works of Zucali (2002), Zucali et al. (2002), Delleani et al. (2012, 2013) integrated with original structural and petrologic data.

Quantitative results of 3D modelling on syn-D2 and -D5 structural and metamorphic heterogeneities are compared in Figure 5.1.7 where the volumetric estimates for D2 fabric domains (coronitic domain: 5.83%; tectonitic domain: 8.51%; mylonitic domain: 85.66%) and for metamorphic domains (low-transformation domain: 5.93%; medium-transformation domain: 11.13%; high-transformation domain: 82.95%) are shown. In the same way, Figure 5.1.8 shows the D5 volumes for the fabric domains (88.62% for the coronitic domain and 11.38% for the tectonitic domain) and for the metamorphic

domains (86.77% for the low-transformation domain; 9.42% for the medium-transformation domain; and 3.81% for the high-transformation domain).

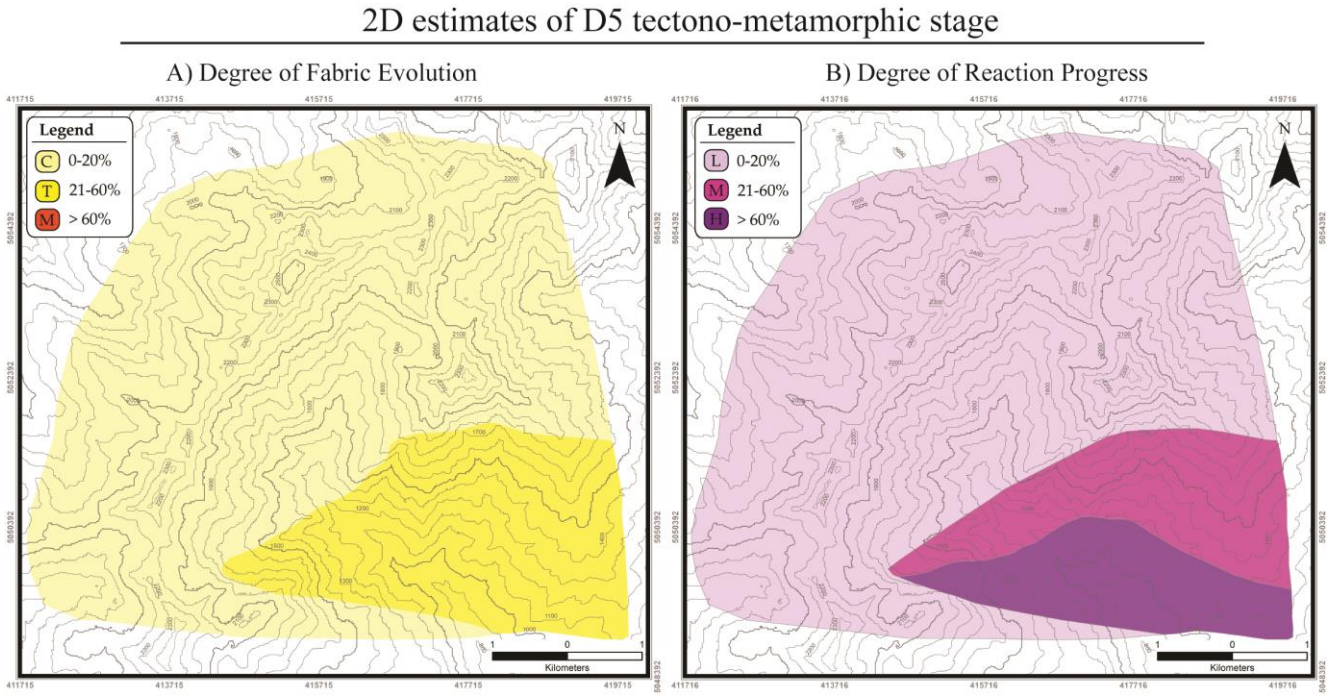

Figure 5.1.6. Domains of homogeneous degrees of fabric evolution and metamorphic reaction progress reconstructed for D5 stage (inferred from Zucali 2002, Zucali et al. 2002, Delleani et al. 2012, and Delleani et al. 2013 integrated with original data).

In general, the dominant D2 stage is characterized by the highest DFE values and the widespread tectonitic-mylonitic domains reach the 94.17% of the modelled rock volume. The D2-related syn-kinematic mineral assemblage reach the DRP of 100% only above the 60% DFE threshold. Regardless the spatial distribution, the DFE-DRP relations is quite proportional and the absolute volumetric misfit between the corresponding DFE-DRP domains is lower than 4% for both the considered stages (Figs. 5.1.7, 5.1.8). The comparison of the tectono-metamorphic map (Fig. 5.1.2) with the DFE-DRP map (Figs. 5.1.5, 5.1.6) and the 3D models (Figs. 5.1.7, 5.1.8) of the considered stages clearly shows that the distribution of the high- and low-strain domains is not controlled by lithology as high-strain domains intersect lithological boundaries.

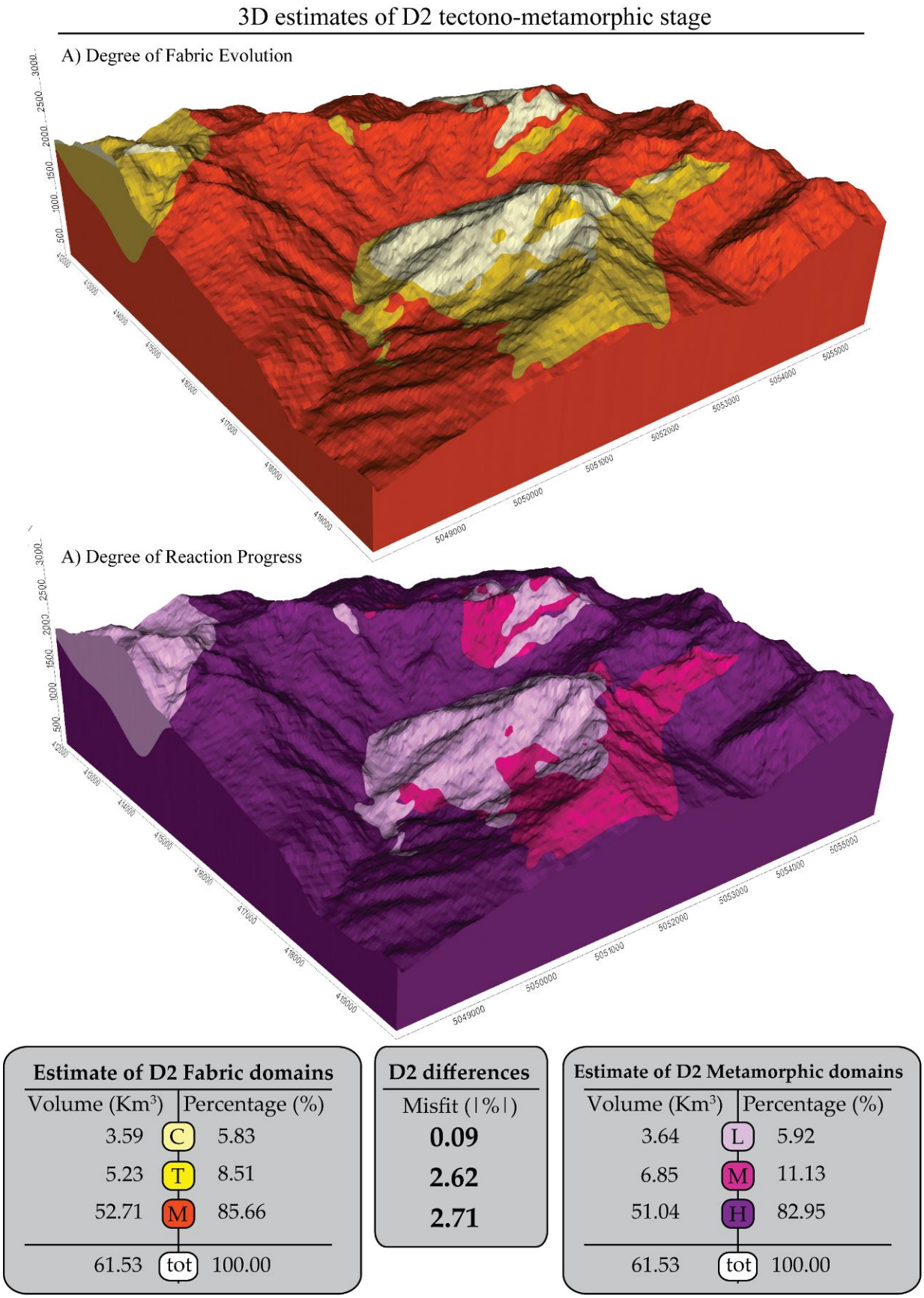

Figure 5.1.7. 3D models of DFE and DRP for the D2 stage. Volumetric estimation and misfit between DFE and DRP domains are reported.

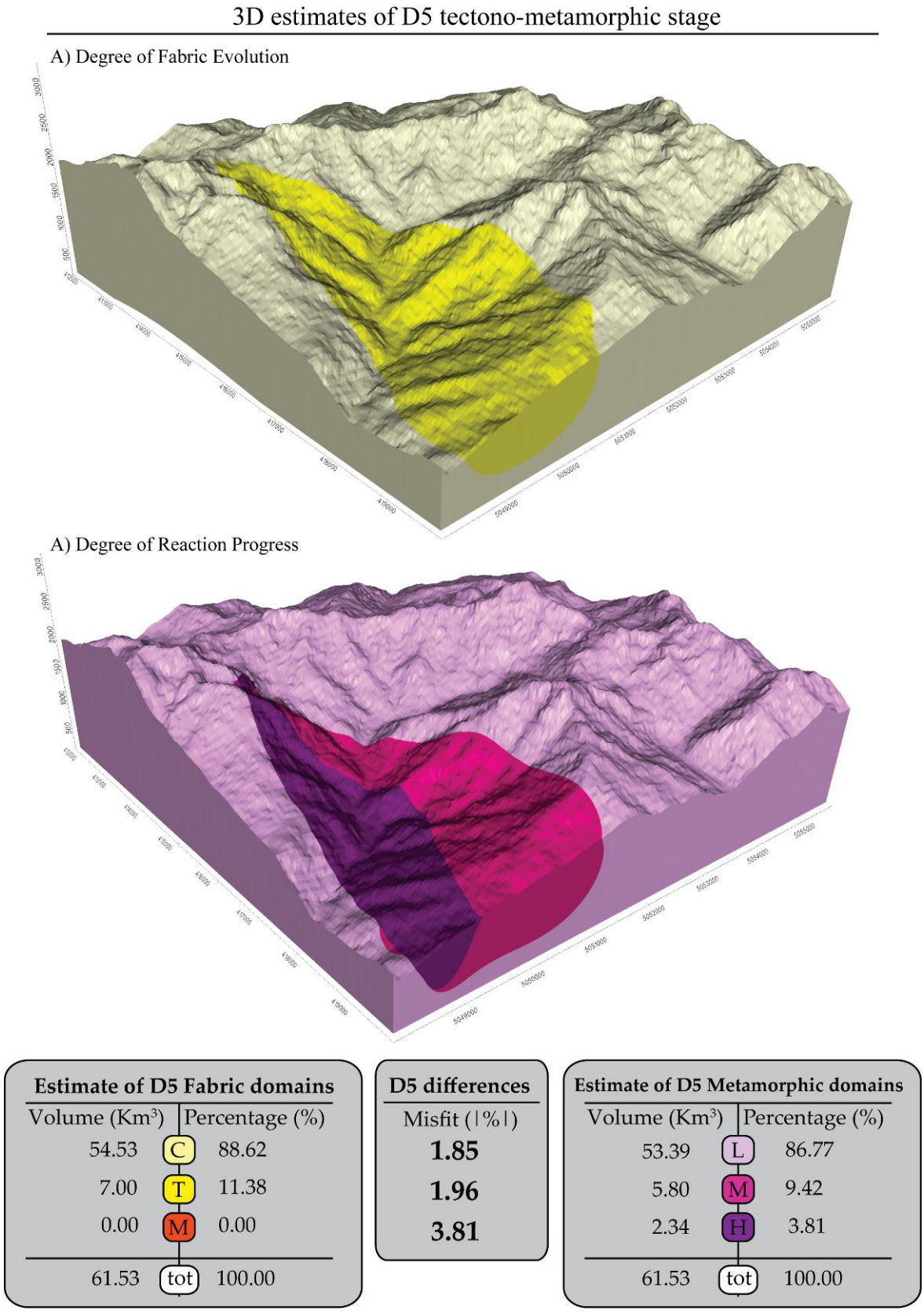

Figure 5.1.8. 3D models of DFE and DRP for the D5 stage. Volumetric estimation and misfit between DFE and DRP domains are reported.

During D2, high variation rate of the DFE and DRP occurred. Large rock volumes totally escaped deformation and metamorphic re-equilibration effects. In the Mars metagranitoids larger undeformed volumes are preserved during D1 stage than in the Mucrone metagranitoids, influencing the different D2 structural and metamorphic evolution. In the Mars metagranitoids the transition between mylonitic-DFE to coronitic-DFE domains is sharp with narrow or absent tectonitic domains, whereas in Mucrone metagranitoids the transition from coronitic to mylonitic domains is gradual (Fig. 5.1.7). The Low- to Medium-DRP domains show a spatial mismatch with respect to the corresponding coronitic- to tectonitic-DFE domains, especially along the Mars-Mombarone ridge and along the Elvo valley, where the transition from mylonitic- to coronitic domains is sharp. The DFE does not show drastic changes for D5 stage showing a gradual transition from coronitic- to tectonitic-domains. The 60% DFE threshold is never reached for the D5 stage and the tectonitic fabric is developed with high-DRP accumulation. The highest DFE and DRP volumes are localized in the southeast part of the 3D model (Fig. 5.1.8).

5.1.7 Discussion

The analysis of diffuse textural and metamorphic heterogeneities in the studied rock-volume through the 3D quantification of fabric and metamorphic gradients developed during a polyphasic tectono-metamorphic evolution shows that only ~15% of the total rock volume was mechanically and chemically re-equilibrated during the late D5 stage developed under greenschist facies condition (Fig. 5.1.8). Around 5% of the total volume preserves structural and metamorphic imprints related to the earlier stages (pre-D1 and D1 events) due to a poor mechanical reactivation during the whole Alpine history. Moreover, the eclogitic D2 dominant tectono-metamorphic imprint show the highest degree of fabric evolution and reaction progress (Fig. 5.1.7). The D2 mylonitic and high-transformation domains (above the 60% DFE-DRP threshold) make up about 85% of the modelled volume. Both the considered stages (Figs. 5.1.7, 5.1.8) display differences concerning the DFE-DRP relations in terms of absolute volumetric estimation and spatial distribution. The structural pattern (*i.e.* orientation data, foliation trajectories map, and intersection relationships) is used as geometric constrain to interpolate the point of DFE estimates in volumetric domains. Conversely, the reconstruction of the boundaries of DRP domains can be attained through two different approaches, namely 1) contouring using co-kriging algorithm and 2) structural control on the co-kriging interpolation.

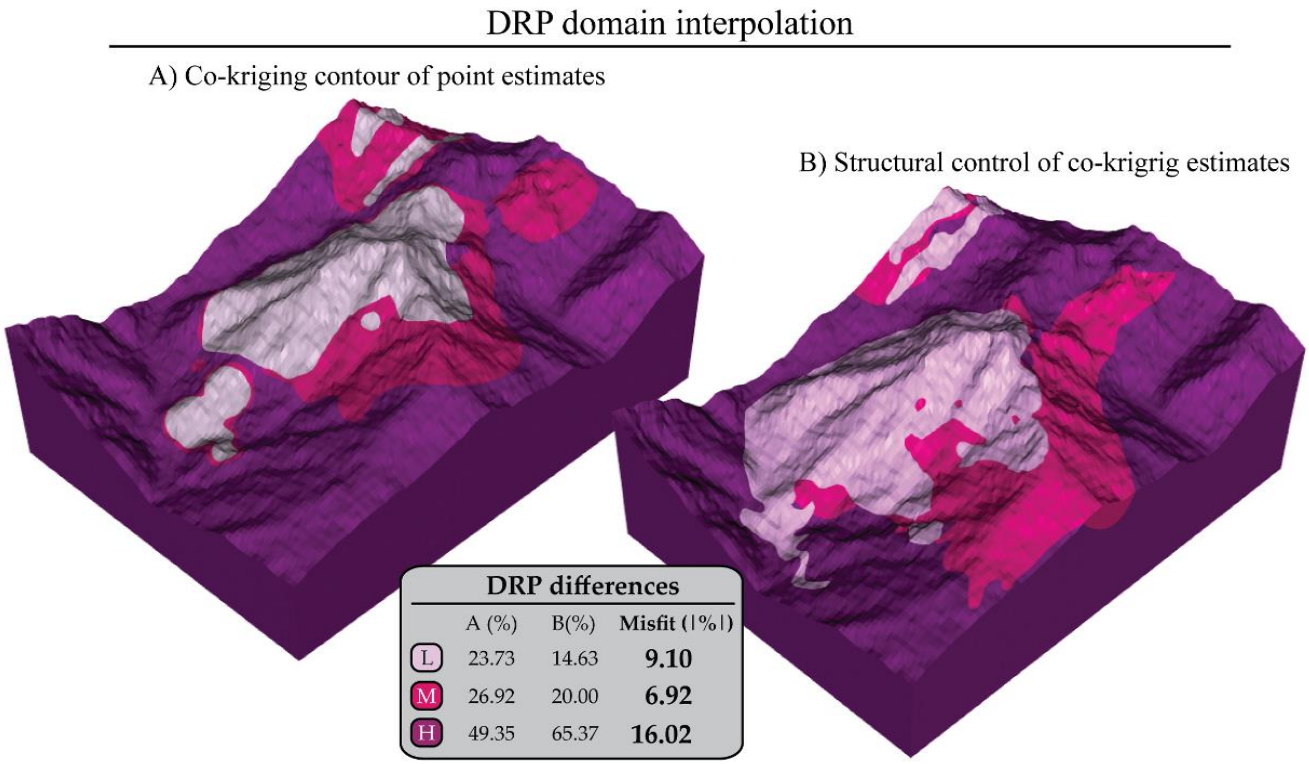

Figure 5.1.9. The two different approaches discussed in the text for the DRP quantification and their shape and volume differences in the Mt. Mucrone area. A) DRP domains contoured using co-kriging algorithm.

To explain these two approaches, we performed a 3D modelling focused exclusively on the Mucrone volume (Fig. 5.1.9) where there is the highest concentration of points of D2-related DRP estimates (63 samples widespread in 28.63 km^2). Regardless the structural pattern, the first approach concerns the contouring interpolation of the DRP point estimates through the co-kriging algorithm (Fig. 5.1.9A). In detail, the geo-refenced DRP values are used as input data for the co-kriging statistical analysis useful for the grid construction in the 3D space. With these points as internal standard Geomodeller® is able to classify all voxels as a function of the value-distances between input data and thus contouring such voxels in the three chosen ranges. Figure 5.1.9B shows the reconstruction of that boundaries using the orientation data, the intersection relationships (Tab. 5.1.1), and the foliation trajectories map (Fig. 5.1.2) as a structural discriminating tool. Integrating the foliation surfaces (iso-potential data) and related structural data orientation (potential gradients) Geomodeller® interpolates the DRP volumes using the co-kriging approach with the structural control. The Figure 5.1.9 shows the volumetric misfit and the different geometries of the DRP domains modelled with the two approaches. Since the multiscale analysis shows that the metamorphism is strictly correlated to the deformation, the structural control on the DRP volume contouring is fundamental for the correct interpolation and evaluation of DRP volume heterogeneities and for the comparison with the corresponding DFE

estimates. In this view, the second approach turns to be more useful for a proper analysis of the DFE-DRP relationships. The 3D reconstruction shows that DFE and DRP are strictly correlated. The localization of the high-strain domains is not controlled by the lithological setting, because high-strain domains of the analysed deformation stages intersect the lithological boundaries. The relationships between DFE and DRP in different rock-types suggest that differences in original mineral assemblages and fabrics (*i.e.* pre-Alpine originally foliated or isotropic) can exert an influence on the mechanical reworking and reaction progress when DFE remains lower than 60%. These results strongly stress the role of strain energy in catalysing metamorphic reactions (Hobbs et al. 2010; Hobbs et al. 2011). At low- and medium- strain conditions, originally isotropic metagranitoids achieved a lower degree of metamorphic reaction progress than the originally foliated metapelites. At a high-strain condition the deformational and metamorphic effects proportionally increase, up to the total replacement of pre-existing minerals, where new fabrics evolved up to the stage of a continuous foliation, in agreement with previous qualitative and quantitative observations (Zucali et al. 2002, Spalla et al. 2005, Roda and Zucali, 2008, Salvi et al. 2010, Delleani et al. 2012, Corti et al. 2017). These differences may be related to strain softening that resulted from strain localization during successive deformation stages, making the originally competent rocks softer by grain-size reduction increasing the amount of reaction surfaces. Below the 60% DFE threshold, the thermal regime can significantly influence the degree of metamorphic transformation: for the same DFE, the metamorphic reaction progress is more evolved during D2 (under eclogite-facies conditions with estimated T= 520 ± 45°C) than during D5 (under greenschist-facies conditions with estimated T= 400 ± 50°C).

5.1.8 Conclusions

Thanks to Geomodeller® software, a quantitative 3D estimation of domains characterized by homogeneous DFE and DRP has been performed for the D2-eclogitic and D5-greenschist stages. Those two are the more pervasive tectono-metamorphic stages at km-scale. The 3D geological model proves to be an excellent tool for the quantitative estimates of rock volumes that recorded different degree of fabric evolution and metamorphic reaction progress during a polyphase tectono-metamorphic evolution, in a portion of continental crust deeply involved in the Alpine subduction system.

The multiscale analysis shows that the metamorphism is strongly correlated to the deformation, therefore the structural control on the DRP reconstruction is fundamental for the correct evaluation of DRP domains and for the comparison with the corresponding DFE volumes.

The analysis shows that the degree of metamorphic reaction progress is controlled by bulk rock, mineral compositions, and that was also strongly influenced by the degree of fabric evolution. In fact, the 15% of rock volume was mechanically and chemically re-equilibrated during D5-greenschist stage. Almost 5% of the volume preserves fabrics and mineral relics of the earlier stages (pre-D1 and D1 events). The eclogitic D2 dominant tectono-metamorphic imprint shows the highest degree of fabric evolution and of metamorphic reaction progress (above the 85% of the modelled volume). The DFE and DRP are strongly correlated, regardless the rock type. The comparison between the models and the geological maps shows that the localization of the high-strain domains is transversal to the lithological boundaries. The relationships between DFE and DRP in different rock-types suggests that differences in original mineral assemblages and fabrics can exert an influence on the mechanical reworking and reaction progress primarily when DFE remains lower than 60%. At low- and medium- strain conditions (coronitic and tectonitic fabrics), metagranitoids achieved a lower degree of metamorphic reaction progress than metapelites. On the contrary, at high-strain conditions the deformation and metamorphic effects developed at the same rate up to the 100% of the considered volume, disregarding the involved rock type.

The thermal regime can exert an additional influence on the degree of metamorphic transformation, if the DFE remains below to the 60% threshold. The metamorphic reaction progress is more evolved during D2, attained at T= 520 ± 45°C than during D5, attained at T= 400 ± 50°C, for the same DFE values.

These results demonstrate that this approach is a powerful tool to unravel the variation in size of rock volumes that sharing a common subduction-collision-exhumation history, developed homogeneous structural and metamorphic records; therefore the results from this 3D approach can be usefully applied to improve the numerical modelling of geodynamic processes. Indeed, the estimation of volumes preserving textural and mineral relicts after phase transitions may shed light on the potential effects of incomplete metamorphic transformations on the rheology of rock volumes during their paths through different lithospheric depth along active margins. Consequently, a main outcome of this work is that phase transitions cannot be properly implemented in numerical modelling of geodynamic processes without evaluating the heterogeneity of reaction progress and fabric evolution.

5.1.9 Acknowledgment

The authors acknowledge funding by University of Milano: Linea 2, Azione A - fondi giovani ricercatori “Analisi strutturale delle catene collisionali” (PSR2018_DZANONI). Results here presented have been developed in the frame of the MIUR Project “Dipartimenti di Eccellenza 2017 - Le Geoscienze per la società: risorse e loro evoluzione (work-package 3, tasks 3.3 and 3.4)”.

References are integrated at the end of the thesis.

5.2 Integrating X-ray computed tomography with chemical imaging to quantify mineral re-crystallization from granulite to eclogite metamorphism in the Western Italian Alps (Sesia-Lanzo Zone)

The following sections refer to the submitted paper: Corti L., Zucali M., Visalli R., Mancini L. and Sayab M.: Integrating X-ray computed tomography with chemical imaging to quantify mineral re-crystallization from granulite to eclogite metamorphism in the Western Alps. Frontiers in Earth Science.

Abstract

Metamorphic transformations and fabric evolution are the consequence of thermo-dynamic processes, lasting from thousands to millions of years. Relative mineral percentages, their grains size distribution, grains orientation, and grain boundary geometries are first-order parameters for dynamic modeling of metamorphic processes. To quantify these parameters, we propose a multidisciplinary approach integrating X-ray computed microtomography (µ-CT) with X-ray chemical mapping obtained from an Electron MicroProbe Analyzer (EMPA). We used a granulite metapelite sample collected from the Alpine H*P*-L*T* metamorphic rocks of the Mt. Mucrone (Eclogitic Micaschists Complex, Sesia-Lanzo Zone, Western Alps, Italy). The heterogeneous Alpine deformation and metamorphism allowed the preservation of pre-Alpine structural and mineralogical features developed under granulite-facies conditions. The inferred granulitic mineral association is Grt + Bt + Sil + Pl + Qtz ± Ilm ± Kfs ± Wm. The subsequent pervasive static eclogite-facies re-equilibration occurred during the Alpine evolution. The inferred alpine mineral association is Wm + Omp ± Ky + Qtz+ Grt though local differences may occur, strongly controlled by the chemistry of the selected microdomains. X-ray µ-CT data extracted from on centimeter-sized samples have been analyzed to quantify the volumetric percentage and shape

preferred orientation for each mineral phase. By combining tomographic phase separation with chemical variation and microstructures (*i.e.*, different grain-size classes for the same phase and morphology of different pre-Alpine microdomains) the pre-Alpine mineralogical phases from the Alpine overprint have been distinguished and quantified. Moreover, the sample preserves 100% of the pre-Alpine granulite fabric, which surprisingly corresponds to less than 22% of the corresponding pre-Alpine metamorphic assemblages, while the Alpine eclogitic static assemblage corresponds to 78% though no new fabric is developed. This contribution demonstrates that the combined use of EMPA X-ray chemical mapping with the X-ray µ-CT shape analysis permits a dynamic approach to constraint the chemistry of the mineral phases linked to the development of metamorphic-related static and dynamic fabrics.

Keywords: X-ray microtomography, X-ray chemical maps, SPO, granulite metamorphism, pre-Alpine fabrics, Sesia-Lanzo Zone.

5.2.1 Introduction

The knowledge of crust and mantle dynamics is mostly based on the study of fabric elements, metamorphic assemblages and their relationships within the rock-volume, now exposed after the subduction- and collision-related processes. The metamorphic basements are usually affected by strong heterogeneities in the degree of fabric and metamorphic evolutions (Salvi et al. 2010; Corti et al. 2017), mainly due to the strain partitioning and consequent heterogeneous distribution of metamorphic assemblages (*e.g.* Myers 1970; Mørk 1985; Spalla et al. 2005; Pearce and Wheeler 2010). Detailed multiscale correlation between deformation and metamorphism has been shown to be of primary importance to constrain the relationships between fabric and metamorphism (*e.g.* Turner and Weiss 1963; Park 1969; Hobbs et al. 1976; Williams 1985; Lardeaux and Spalla 1990; Passchier et al. 1990; Johnson and Vernon 1995; Spalla et al. 1999; Salvi et al. 2010; Hobbs et al. 2011; Gosso et al. 2015; Corti et al. 2017).

Classical structural geology studies have been progressively reinforced by a collection of quantitative data through texture analysis (*e.g.* Frassi et al. 2017; Zucali et al 2014), synchrotron X-ray computed microtomography (*e.g.* Zucali et al 2014b) and chemical mapping of superimposed structures in metamorphic rocks (Lanari et al. 2014; Ortolano et al. 2014a; Visalli, 2017). In this view, the quantitative analysis of the metamorphic textures related to the superimposed fabrics allows the evaluation of the mechanically and chemically reacting volume percentage, during successive tectono-metamorphic stages. In particular, the estimation of relative mineral percentages, their grains size

distribution, grains orientation, and grain boundary geometries for each tectono-metamorphic stage are the first-order parameters for dynamic modeling of metamorphic processes.

To quantitatively investigate the textural and chemical heterogeneities developing during deformation and metamorphism partitioning we propose a novel approach integrating X-ray computed microtomography (μ-CT) with X-ray chemical mapping obtained from an Electron Micro Probe Analyzer (EMPA). This procedure combines (1) the quantitative calibration of the X-ray chemical map for selected microdomains using the Q-XRMA (*i.e.*, Quantitative X-Ray Map Analyzer) statistical approach (Ortolano et al., 2018) to determine different compositional regions within the rock and minerals associated to the superposed metamorphic assemblages; (2) the high-resolution thin section optical scanning to determine the mineral grainsizes distribution and perform the orientation analysis using the Min-GSD (Mineral-Grain Size Distribution) method (Visalli, 2017); and (3) the X-ray μ-CT capability to resolve the three-dimensional (3D) shape and spatial distribution of minerals marking different fabrics in metamorphic rocks (*e.g.*, Denison et al., 1997; Huddlestone-Holmes and Ketcham, 2010; Voltolini et al., 2011; Baker et al., 2012; Sayab et al., 2015; Macente et al., 2017).

We applied this approach to a granulite metapelite sample (*i.e.*, kinzigite gneiss) surfacing within the poly-deformed metamorphic basements of the Mt. Mucrone, Eclogitic Micaschists Complex, Sesia-Lanzo Zone, Western Alps (Hy 1984; Koons et al. 1987; Ridley 1989; Ildefonse et al. 1990; Zucali et al. 2002; Babist et al. 2006; Cenki-Tok et al. 2011; Delleani et al. 2013). The sample pervasively record the pre-Alpine granulite fabric, but the original pre-alpine granulite mineral assemblages were extensively replaced by static eclogite facies minerals, recording the Alpine subduction-related evolution. In this contribution we show how to quantify the modal percentage, the mineral chemical variation, the grain-size distribution, the grains orientation, and the grain boundary geometries of the mineral phases recording the metamorphic evolution from pre-Alpine granulitic- to the eclogitic-facies conditions. This approach allows a detailed and reliable discrimination of these parameters for the pre-alpine and alpine stages.

5.2.2 Material and Methods

5.2.2.1 Geological Outline

The Sesia-Lanzo Zone, in the Western Alps (SLZ, Fig. 5.2.1A and B), is a portion of continental crust, which recorded high pressure (HP) metamorphic conditions during the Alpine subduction (*e.g.* Dal Piaz et al., 1972; Compagnoni et al., 1977; Pognante, 1991; Babist et al., 2006; Meda et al., 2010; Roda et al., 2012; Regis et al. 2014). Its Alpine metamorphic history comprises a prograde blueschist- to eclogite-facies stage followed by blueschist- and greenschist-facies retrograde re-equilibrations (*e.g.* Compagnoni & Maffeo, 1973; Compagnoni, 1977; Gosso, 1977; Lardeaux, 1981; Lardeaux et al., 1982a; Lardeaux et al., 1983; Spalla et al., 1983; Pognante, 1989a; Castelli & Rubatto, 2002; Zucali et al., 2004; Rebay & Messiga, 2007; Zucali & Spalla, 2011; Giuntoli and Engi, 2016; Corti et al., 2018; Giuntoli et al. 2018a; Roda et al. 2018a; Roda et al. 2019). The metamorphic evolution ended at Oligocene with the intrusion of large intrusive bodies which produced contact metamorphic aureole (Zanoni et al. 2008). The Alpine eclogite-facies peak has been dated between 90 and 65 Ma (Rubatto et al., 1999; Cenki-Tok et al., 2011; Regis et al. 2014; Giuntoli et al. 2018b; Halama et al., 2018). The early-Alpine H*P* imprints range between 500–625 °C and 1.3–2.5 GPa (see Roda et al., 2012 for a review of *P-T* estimates). The eclogitized ophiolitic relics of the Liguria-Piedmont Ocean, the Piedmont Zone, bound the external margin of the SLZ, while the SLZ internal margin is a thick mylonitic belt (the Canavese Line) (Fig. 5.2.1); the Canavese Line puts in contact the SLZ from the lower crustal rocks of the Southalpine Ivrea Zone (*e.g.* Bigi et al., 1990; Rebay et al., 2018; Balestro et al., 2019). The SLZ is subdivided into 4 main units (Fig. 5.2.1B): the Eclogitic Micaschist Complex (EMC), the Gneiss Minuti Complex (GMC), the II Dioritic–Kinzigitic Zone (IIDK) and the Rocca Canavese Thrust Sheets (RCT) (*e.g.*: Compagnoni et al., 1977; Pognante, 1989a; Pognante, 1989b; Spalla et al., 1991; Cantù et al. 2016; Roda et al. 2018a; 2019). Eclogitic parageneses are widely described both in EMC and GMC with a strong difference in relative volume affected by the retrograde greenschist re-equilibration. The GMC is widely re-equilibrated under greenschist facies conditions, while the EMC, constituting the internal part of the SLZ, records the greenschist-facies re-equilibration along discrete shear zones (Spalla et al., 1983; Stuenitz, 1989; Spalla et al., 1991; Giuntoli and Engi, 2016). The IIDK consists of kilometric lenses of paragneisses, marbles and metabasites between EMC and GMC. The pre-Alpine high-temperature evolution is well preserved and the Alpine eclogitic assemblages are described only in the Vogna Valley, where the tectonic contact between IIDK and EMC is marked by eclogitic mylonites (Lardeaux, 1981; Lardeaux et al., 1982b).

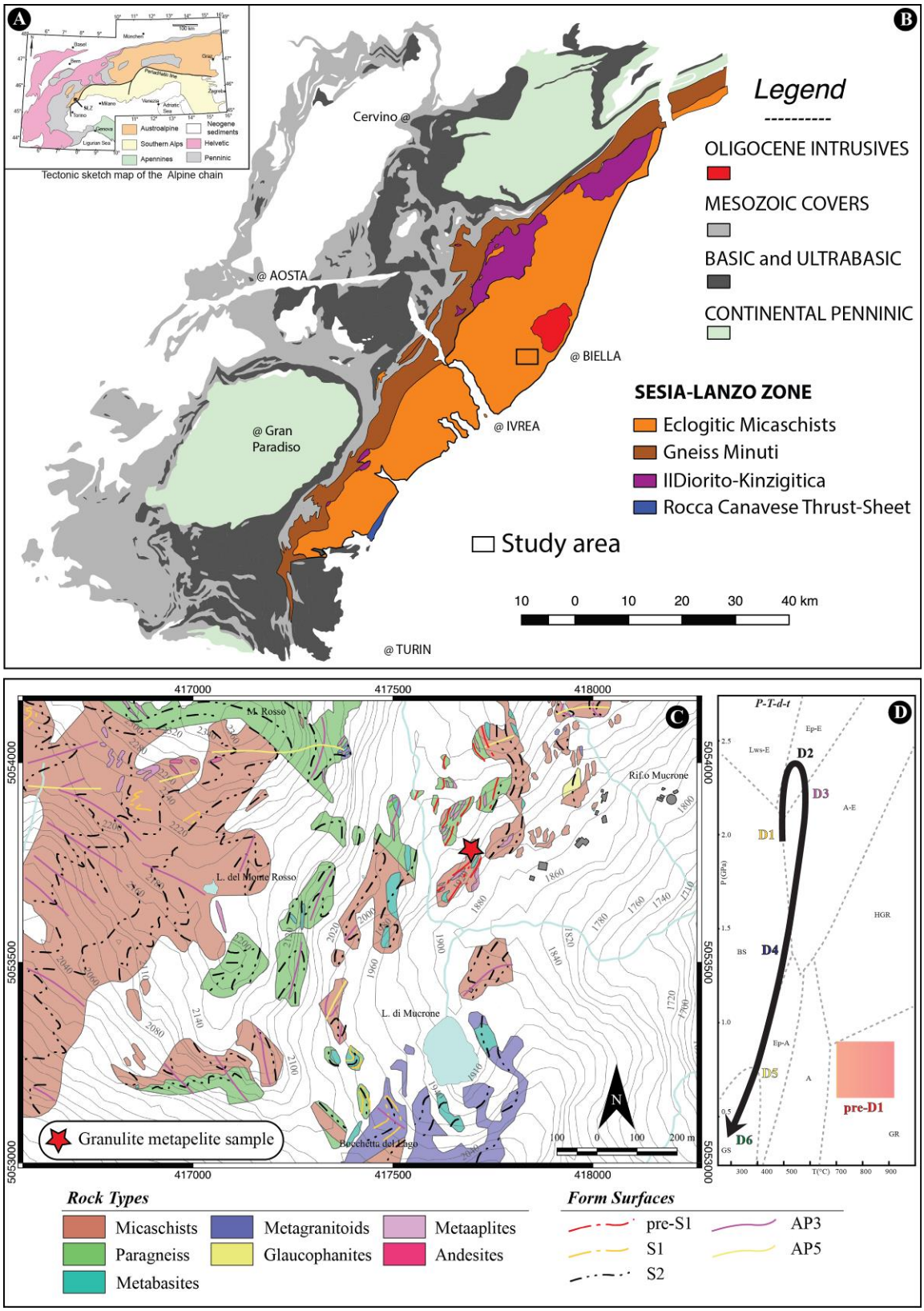

Figure 5.2.1. A) Tectonic outline of the major domain of the Alpine chain. B) Tectonic scheme of the Western Alps with the different metamorphic complexes of the Sesia-Lanzo Zone. The studied area is located. C) Rock-types and foliation trajectories around the Mt. Mucrone. The granulite metapelite sample is located. D) P-T-d-t path modified after Zucali et al. (2002) and Delleani et al. (2013).

The EMC protoliths, composed by high-grade paragneisses, granulites, amphibolites and minor marbles and quartzites, constitute the country rocks of the Permian granitoids and gabbros (Compagnoni & Maffeo, 1973; Callegari et al., 1976; Compagnoni et al., 1977; Lardeaux, 1981; Oberhaensli et al., 1985; Castelli, 1987; Bussy et al., 1998; Cenki-Tok et al., 2011; Zucali, 2011; Corti et al., 2017); the Mt. Mucrone is one of these Permian bodies and the most renown. The deformation history of EMC, in the area of Mt. Mucrone and studied samples, comprises four generations of Alpine folds (Fig. 5.2.1C), two of which are associated with the HP mineral assemblages, and two generations of shear zones synchronous with the blue- and greenschist-facies re-equilibrations, respectively (Hy, 1984; Zucali et al., 2002b; Delleani et al., 2012; 2013).

A pre-Alpine polyphasic metamorphic evolution, from granulite- to amphibolite-facies conditions, has been recognized in marbles, metapelites, metagranitoids and metabasics of the SLZ (Compagnoni et al., 1977; Lardeaux et al., 1982b; Castelli, 1991; Lardeaux & Spalla, 1991; Rebay & Spalla, 2001). This pre-Alpine stage, marked by biotite-, sillimanite-, garnet-rich foliation in paragneiss, is found as relict in paragneiss close to the M.te Mucrone (*i.e.* granulite metapelite sample in Fig. 5.2.1C). The pre-Alpine stage (pre-D1 in Fig. 5.2.1D) has been constrained at T=730–830 °C P=0.7-0.9 GPa (Lardeaux & Spalla, 1991). Pre-D1 has been interpreted as the result of an extension-related uplift of a portion of the Variscan crust; this extensional tectonics is inferred to be of Permian–Triassic time, during the lithospheric thinning leading to the Tethys opening (*e.g.* Lardeaux & Spalla, 1991; Marotta et al., 2009; Roda et al., 2018b).

5.2.2.2 Sample Description

The analyzed samples are pre-Alpine granulite-facies metapelite, characterized by gneissic fabric (*i.e.*, kinzigite). They were collected from the EMC, NW of the Lago del Mucrone (Fig. 5.2.1C, UTM32N – WGS84 417517.69 m E, 5053493.35 m N). They occur as lenses within the eclogitic gneisses and micaschists, country rocks of the Permian Mt. Mucrone metaintrusive body (Eclogitic Micaschists Complex, Sesia-Lanzo Zone, Western Alps). The heterogeneous Alpine deformation and metamorphism allowed the preservation of pre-Alpine granulite-facies relicts in country rocks, preserving a foliation (pre-S1 in Fig. 5.2.1C) at meter-scale, wrapped by the eclogite-facies S1 and S2 foliations (Fig. 5.2.1C). The pre-Alpine fabrics are mostly defined by alternating microfilms and microlithons; microfilms and microlithons are marked, respectively, by red-brown biotite, elongated ex-sillimanite domain, ilmenite, rare white mica and garnet porphyroblasts, K-feldspars, ex-plagioclase domain, quartz and decussate arcs of red-brown biotite (Fig. 5.2.2A).

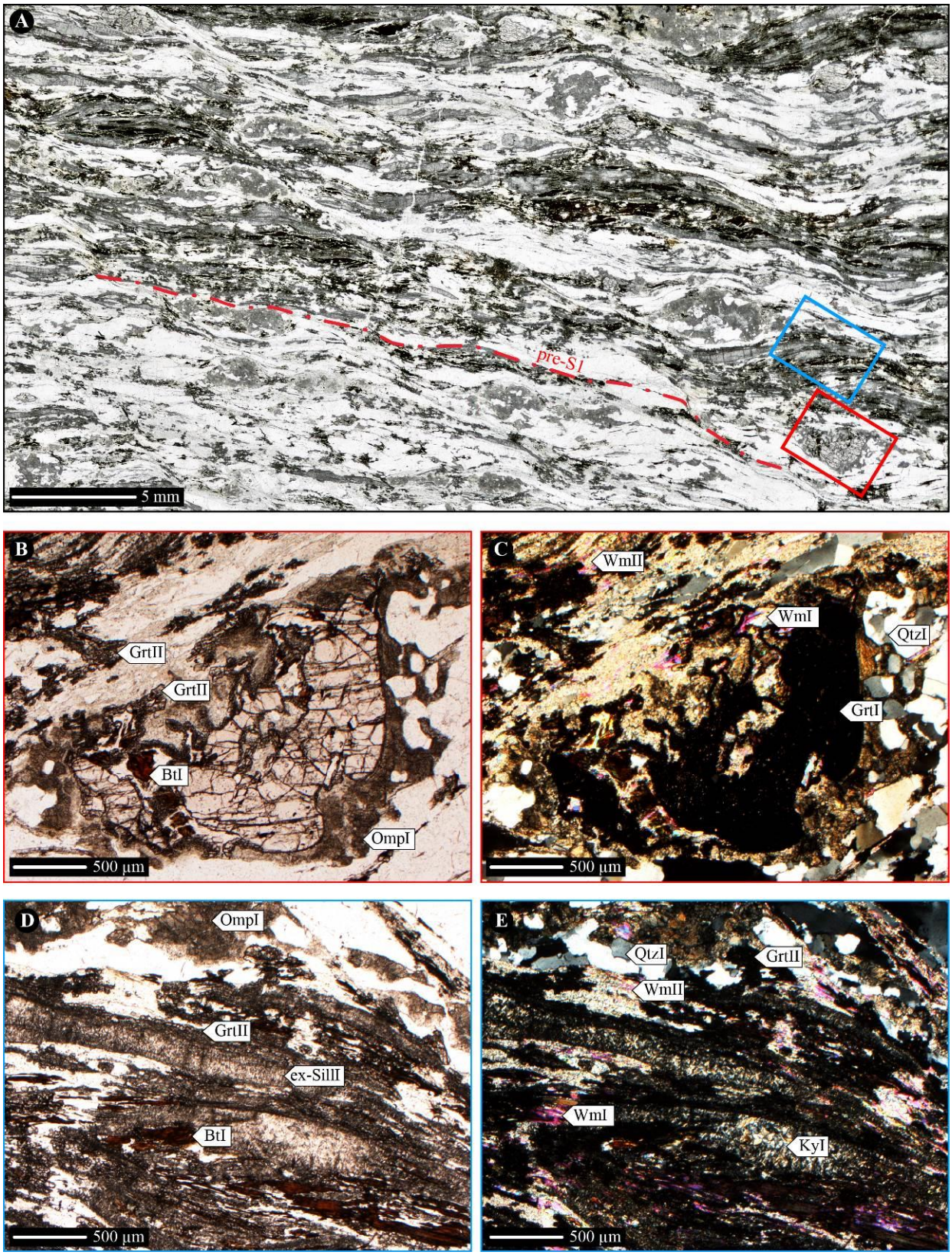

Figure 5.2.2. A) High-resolution optical scan of the entire thin section characterized by well-developed pre-S1 foliation, plane polarized light. B) pre-Alpine Grt microdomains, plane polarized light. C) pre-Alpine Grt microdomains, crossed polars. D) pre-Alpine Sill and Pl microdomains, plane polarized light. E) pre-Alpine Sill and Pl microdomains, crossed polars.

The pre-S1 foliation (Fig. 5.2.2A) is characterized by S-C-like geometry where the C planes, spaced by 2-3 mm, deflect the S planes marked by biotite and ex-sillimanite domains, the latter being characterized by diagnostic columnar shape and transversal fractures (Fig. 5.2.2D). Garnet porphyroclasts are wrapped by the pre-S1 foliation; they are commonly associated with biotite, quartz and white mica (Wm1) inclusions (Figs. 5.2.2B, 5.2.2C). Ex-plagioclase domains are characterized by thin-grained aggregates of white mica and/or a high-relief mineral (omphacite) and may occur as elongated domain, mainly parallel to the S-planes, locally wrapping porphyroblasts, or as coronas of the garnet porphyroblasts (Fig. 5.2.2B). Biotite also marks the pre-S1 foliation; biotite is well preserved in microfilm domains and displays (001) cleavage mainly parallel to the foliation; its red-color at parallel nicols suggests a preserved composition, probably related to the pre-alpine high-temperature conditions (*e.g.*, Hayama, 1958; Wu and Chen, 2015). Locally, isolated grains of white mica co-exist with biotite, suggesting also a pre-alpine age for the white mica (WmI in Fig. 5.2.2E). The pre-S1 pre-alpine fabric is pervasively replaced by static eclogite facies mineral association, namely garnet, white mica, omphacite, kyanite and rutile. Alpine generation of garnet (GrtII in Fig. 5.2.2B) occurs as corona over garnet porphyroblasts (GrtI) or biotite (Fig. 5.2.2B) or as new grains (Fig. 5.2.2). Alpine white mica (WmII, Figs. 5.2.2C, 5.2.2E) defines thin-grained aggregates likely replacing feldspar, biotite or white mica pre-Alpine domains. Omphacite (OmpI) fine-grained aggregates replace pre-alpine plagioclase (Fig. 5.2.2B); large individuals may also occur as in Fig. 5.2.2D. Kyanite occurs as fine-grained aggregates replacing sillimanite in ex-sill domains (Fig. 5.2.2D). The fine grain-size made the recognition of optical characters sometimes hard. The different Alpine metamorphic assemblages or replacements occur strongly controlled by the chemistry of microdomains. Typical examples are kyanite and omphacite that preferentially grow only in specific pre-alpine domains. This is also confirmed by the comparison of the eclogitic assemblages of these rocks with those of eclogitic micaschists where no kyanite occur, likely due to the effect of chemical homogenization of the alpine deformation. The inferred eclogitic mineral association WmII + OmpI ± KyI + Qtz+ GrtII + Rt indicate T = 500–600 °C and $P \geq$ 1.5-2.2 GPa conditions (Zucali et al. 2002) while the pre-alpine granulitic stage, characterized by the mineral assemblage GrtI + BtI + SillI + Pl + Qtz ± Ilm ± Kfs ± WmI and the thermo-barometric estimate indicates metamorphic condition at 0.33-0.45GPa at 580-630°C (see Roda et al., 2018b and reference therein).

5.2.3 Method

5.2.3.1 Chemical imaging and fabric analysis

Three different image processing tools (*i.e.* GSD, Q-XRMA and Min-GSD) developed at the Geoinformatics and Image Analysis Lab of the Biological, Geological and Environmental Sciences Department at the University of Catania, have been applied both at the scale of the entire thin section and of the microdomain one. In this last case, two microdomains (*i.e.* C1, C2) have been selected as the best candidates to execute the tools. These tools are based on various scripts and functions adopted for images analysis, implemented within the most common GIS software, which have been increasingly used in solving various geoscientific issues (*e.g.*, Li et al., 2008; DeVasto et al., 2012; Pradhan, 2013; Ortolano et al., 2014a, 2014b; Belfiore et al., 2016; Fiannacca et al., 2017; Berrezueta et al., 2019). The first tool adopted is the Grain Size Detector (GSD - Visalli, 2017). Such tool permits the users to trace a map of polygonal features representative of the grains composing the rock, by processing high-resolution thin section optical scans. In such a way, a database containing several data of grain sizes and shapes (*e.g.* area, axial ratio, orientation with respect the foliation and others) is obtained. With this aim, a 24 bit-depth optical scan has been acquired with a resolution of 4800 dpi via an Epson V750 dual lens system scanner. According to Visalli (2017), the above scan resolution was selected as the best setting for acquiring an image at high quality, reducing, at the same time, the required hard drive space storage and image processing time. The analytical procedure of the tool is based on the sequential application of four image-processing steps, within the GIS environment: (i) the filtering step, to improve the quality of the input scan, by emphasizing grains boundaries and reducing noise; (ii) the image segmentation step, required to distinguish, select and extract boundaries of different grains; (iii) the vectorization step, needed to create polygon features that trace the original grains of the thin section; and, finally, (iv) the quantification step, useful to calculate grains sizes and shapes parameters. The second tool applied is the Quantitative X-Ray Map Analyzer (Q-XRMA - Ortolano et al., 2018). In this case, users are able to classify rock-forming minerals starting from an array of X-ray maps as well as to calibrate these maps for deriving pixel-based chemical data and end-member fraction maps, by using a sufficient number of spot chemical analyses as internal standards (De Andrade et al., 2006). With this aims, major element X-ray maps (*i.e.*, Al, Ca, Cr, Fe, K, Mg, Mn, Na, Si, Ti) of the entire thin section (ca. 38∗20 mm) have been acquired using a JEOL 8200 electron microprobe equipped with five WDS spectrometers located at the Department of Earth Science, University of Milan. Operating conditions were 160 ms dwell time, 15 kV accelerating voltage and a probe current of 100 nA. A spatial resolution of about 60 µm in both x and y directions was used for acquiring an image with a resolution of 360x610 pixels. X-ray maps of the C1 and C2 microdomains

were acquired with a dwell time of 130 ms and pixel matrices of 650x700 and 600x770, where the pixel size was equaled to 4 μm and 5 μm, respectively. Spot chemical analyses used as internal standards to calibrate X-ray maps were performed using the JEOL 8200 EMPA. Operating conditions were: ~1 μm beam spot, 15 kV accelerating voltage, and 5 nA beam current. Natural minerals and synthetic oxides were used as standards. Adopted mineral abbreviations are from Siivola and Schmid (2007), whereas mineral formulae were calculated according to Deer et al. (1992) by the jPTGUI software (Zucali, 2005). Representative mineral analyses and structural formulae of garnet, biotite, pyroxene and white mica are given as supplementary material (Table 5.2.1).The analytical procedure of the Q-XRMA tool is subdivided into three different cycles: i) the first cycle consists of various stages implying a multivariate statistical data handling of the X-ray maps, based on the sequential application of the Principal Components Analysis (PCA) and the supervised Maximum Likelihood Classification (MLC) (Ortolano et al., 2014b). As a result, users can distinguish mineral phases constituting the analyzed thin section/microdomain as well as extrapolate the associated modal percentages; ii) the second cycle comprises two sub-procedure allowing to perform, on one hand, an in-depth analysis of a selected phase identified during the first cycle for detecting occurrences of sub-phases (*e.g.* mineral zoning) and, on the other hand, to calibrate native X-ray maps through a multiple linear regression algorithm. In this last case, the element concentrations values (expressed as atoms per formula unit, a.p.f.u) can be predicted for each pixel representative of a specific investigated mineral phase; iii) the third cycle permits users to manage the calibrated X-ray maps obtained during the second cycle, for constructing maps of end-member proportions as well as quantifying chemical variations within the investigated phases.

The third tool adopted is the Mineral Grain Size Detector (Min-GSD - Visalli, 2017). This tool allows users to merge together the outputs of the GSD and Q-XRMA in order to label each grain polygon feature with the appropriate mineral name, as the GSD tool alone is not capable to make any division between grains of the same/different minerals, unless the user manually renames each polygon. The analytical procedure requires the sequential application of three different steps: (i) a preliminary manual georeferencing stage, in ArcGIS® environment, between the GSD and Q-XRMA outputs. This is in order to ensure a valid overlap between the two images; (ii) a raster to point conversion of the Q-XRMA output, with the aim to convert each classified pixel in a point feature storing the datum of the mineral name; and finally, (iii) a spatial join operation between the GSD output and the Q-XRMA point converted image in order to attach the correct mineral name to each polygon feature. In this view, the tool calculates the highest frequency of the pixels having the same label enclosed within a polygon.

5.2.3.2 X-ray computed tomography

X-ray computed microtomography (µ-CT) is a nondestructive technique based on the 3D mapping of the X-ray attenuation coefficient across the investigated sample (Baruchel et al., 2000). Using X-ray µ-CT based on a cone-beam geometry it is possible to achieve a maximum spatial resolution close to the focal spot size of the microfocus X-ray source. Moreover, it has been demonstrated (Wilkins et al., 1996) that by using a tomographic instrument based on a microfocus source, it is possible to take advantage of phase-contrast effects at the edges of the different features present within the sample volume (phase objects). This, under given experimental conditions, could allow to improve the contrast and spatial resolution in the images, obtaining sharper borders of the sample features and detecting details smaller than the pixel size of the detector (Mancini, 1998). Phase-contrast X-ray µ-CT measurements based on synchrotron and microfocus X-ray sources applied in the Earth science domain represent a powerful tool for the non-destructive characterization of the internal microstructures and the mineral phases separation thanks to their different density and/or chemical composition (Zandomeneghi et al., 2010; Polacci et al., 2010; Baker et al., 2012; Cnudde and Boone, 2013). Through virtual slicing of the sample volume and applying image processing and analysis 3D tools, it is possible to achieve a quantitative shape preferred orientation (SPO) analysis by means of the geometrical, morphological, and orientation parameters extraction (Voltolini et al., 2011; Zucali et al., 2014). Phase-contrast X-ray µ-CT data have been acquired on centimeter-sized samples at the TomoLab station at the Elettra synchrotron facility in Basovizza (Trieste, Italy) (https://www.elettra.trieste.it/it/lightsources/labs-and-services/tomolab/tomolab.html). This station is equipped with a sealed microfocus source (Hamamatsu, Japan) which guarantees a minimum focal spot size of 5 µm. For each sample, a set of 2400 projections was acquired over a total scan angle of 360°. A water-cooled, 12-bit, 4008 x 2672 pixels CCD camera (Photonic Science, UK) was used as detector applying a 2 x2 binning to the pixels. Scanning acquisition conditions were: Voltage = 130 kV, current = 61 nA, filter = 1.5 mm of Al, exposure time per projection = 6.5 sec, source-to-sample distance = 220 mm and source-to-detector distance = 311 mm. The reconstruction of the tomographic slices was done using the commercial software COBRA (Exxim, USA) with an isotropic voxel size of 17.7 µm. The reconstructed slices were visualized by using the freeware ImageJ (Schneider et al., 2012), while the 3D visualization, through volume rendering procedure, was obtained by the Pergeos software (https://www.thermofisher.com/it/en/home/industrial/electron-microscopy/electron-microscopy-instruments-workflow-solutions/3d-visualization-analysis-software/pergeos-digital-rock-analysis.html).

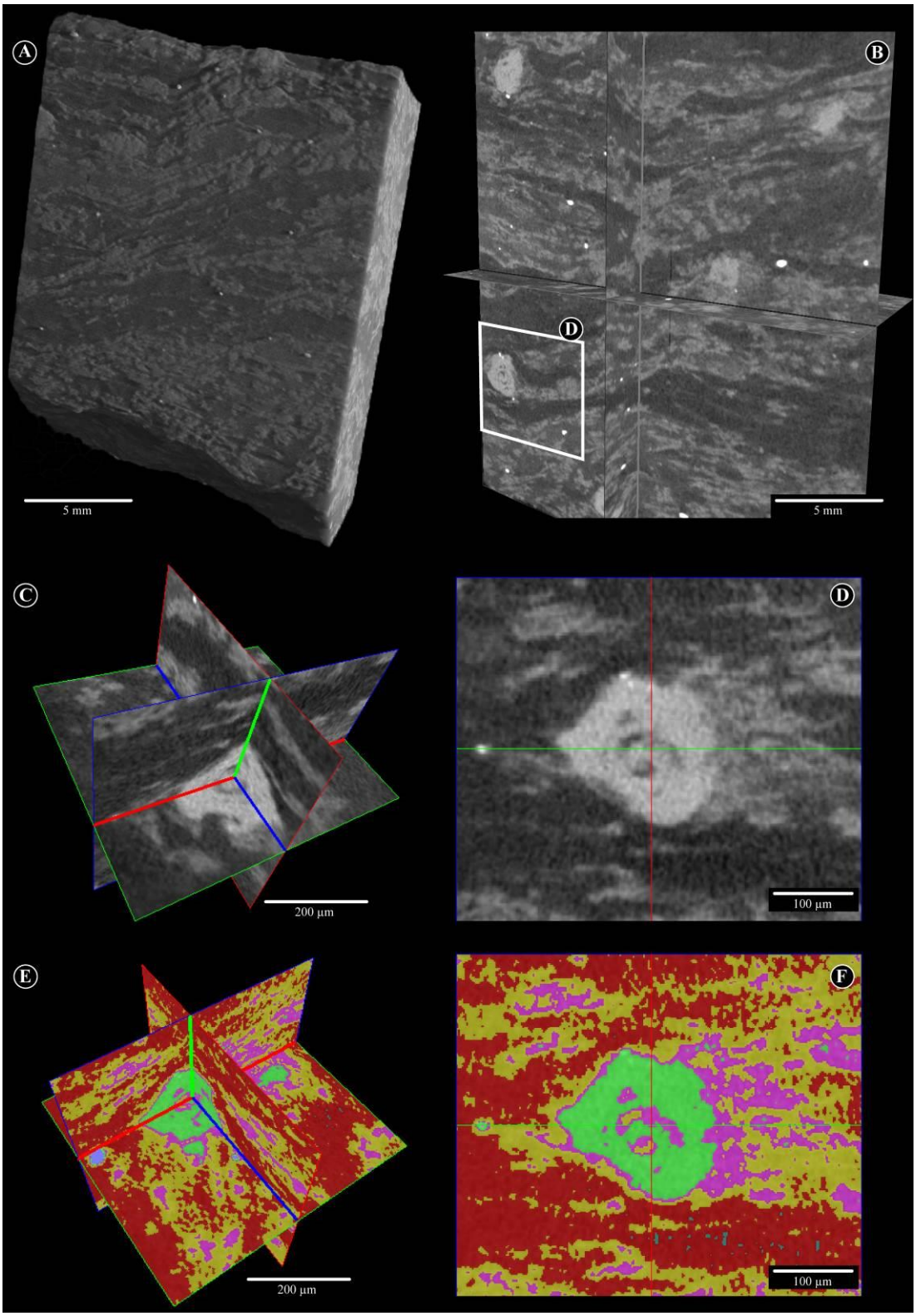

Figure 5.2.3. Segmentation procedure. A) Volume rendering of the original VOI obtained from the X-ray microtomography experiments. B) Visual inspection of the grey levels related to the mineral phases. The sub-volume used as a target for the segmentation is located. Visual inspection of the grey levels related to the mineral phases within the C) sub-volume and along D) XZ plane. 3D Marked-Watershed segmentation procedure for the target E) sub-voume and along D) XZ plane.

PerGeos software allows the mineral quantification through user-friendly 3D visual imaging and mineral phases segmentation by mapping gray value to specific colors. To reduce imaging noise, the reconstructed µ-CT data (Fig. 5.2.3A) was pre-filtered using variance weighted mean filter (Fig. 5.2.3B; noise variance = 400, radius = 2 pixels; Gonzalez & Woods, 2002). Prior to the volume data processing, we crop out a sub-volume (VOI: Volume of Interest) suitable for the analysis avoid the dark background masking the slices with respect to the outer region of the sample. The mineral phases are separated from each other using 3D Marked-Watershed segmentation (MBW; Meyer & Beucher, 1990). The algorithm is based on semi-automatic thresholding, where the boundary between mineral is defined by using the gradient function (*i.e.*, the local deviation) as the grey-values delimiters (Figs. 5.2.3C and 5.2.3D). The material to be segmented is marked using the manual Interactive Overlay Thresholding function seeded with local maxima of distance map. During the procedure it is possible to have areas with multiple adjacent local maxima. This issue can be minimized taking only the largest local maxima (Sayab et al., 2017). The MBW algorithm then expand the seeded markers over the related mineral phases (Figs. 5.2.3E and 5.2.3F) using a landscape function which is defined by the gradient volume (*i.e.*, active contours algorithm). Once the segmentation is achieved post-segmentation filtering was needed to improve the edge preservation and to remove the background voxels. The filtering was retained to a minimum level to preserve the shape of the objects. In this view, we used the closing procedure for avoid dark "unclassified" voxels (Sayab et al., 2014). Thanks to this imaging analysis we separated seven mineral phases: garnet, pyroxene, kyanite, quartz, micas, and opaque minerals. The 3D grain size distribution and the shape preferred orientation (SPO) analysis for each mineral phase have been calculated along with the entire rock volume and for each XY plane thanks to the Separate Object procedure using the Skeleton algorithm. Through the labeling tool it is possible to extract the useful parameters, *i.e.* length, width, volume, orientation angles, eigenvalue, and eigenvector, for each object.

5.2.3 Results

5.2.3.1 2D chemical and fabric results

The first cycle of Q-XRMA allows the modal percentage of the entire thin section (98.41% classified pixels) to be calculated. The identified mineral phases are Qtz (43.04%), Cpx (23.45%), Wm (12.35%), Bt (8.99%), Ky (6.61%), Op (Ilm) (1.64%), Pl (1.38%), and Grt (0.95%) (Fig. 5.2.3), which correspond to the pre-alpine Bt, Qtz, Grt, Op, Pl, and alpine Qtz, Cpx, Wm, Ky, Grt mineral associations.

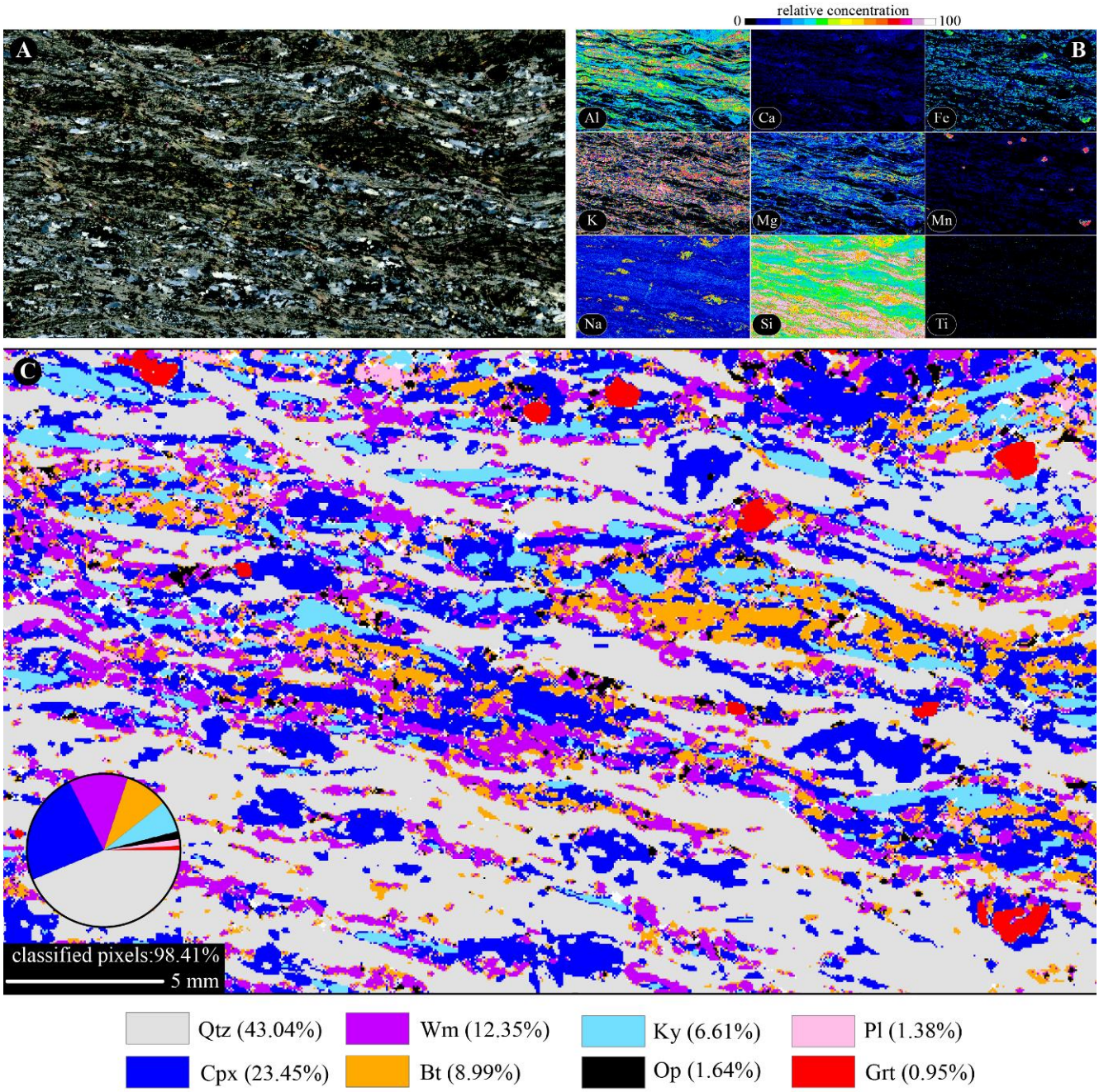

Figure 5.2.4. A) High-resolution optical scan of entire thin section characterized by well-developed pre-S1 foliation, crossed polars. B) X-Ray maps of entire thin section (i.e., Al, Ca, Fe, K, Mg, Mn, Na, Si, and Ti). C) Results of Q-XRMA first cycle classification and mineral modal percentage.

Combining the mineral classification (Fig. 5.2.4) with the grain size distribution (*i.e.* GSD output) using the Min-GSD, all grains were clustered as a function of each rock-forming mineral (Fig. 5.2.4A). The procedure can distinguish 35,138 Qtz-grains, 32,030 Cpx-grains, 11,380 Wm-grains, 8,006 Ky-grains, 6,916 Bt-grains, 1,124 Op-grains, 731 Pl-grains, and 249 Grt-grains. This technique allows the quantitative estimation of the mineral's orientation with respect to the pre-S1 foliation and the calculation of the mineral shape parameters (*e.g.* grain-size, width, length, and aspect-ratio; see Table

5.2.1 in supplemental material for details). The orientation analysis shows as the pre-Alpine fabric (*i.e.* pre-S1 foliation and S-C fabric) is the most preserved. Although the Alpine metamorphic mineral association is the most diffused, the orientation analysis reveals that the forming-minerals are still organized in the pre-Alpine S-C-like geometry (Fig. 5.2.5). In particular, the Bt, Wm, Qtz, Ky, and Cpx grains show two orientation clusters that can be correlated to the S and C structures. The S-related includes 28-35% of grains aligned at 2-13° with respect to the pre-S1. The C-related comprising 20-23% of grains laying at 34-46° from the pre-S1 orientation. The microstructural knowledge about the different microsites and about the variation in size and in shape of every mineral species it is crucial to archive the processed mineral grains to the Alpine or pre-Alpine metamorphic assemblage. For example, Figure 5.2.5B shows the quantification of the Grt generations (*i.e.* GrtI and GrtII) in relation to their grainsize and microstructural positions.

The microstructural analysis allows to assume the 0.1 mm^2 as the area-threshold value between the pre-Alpine and Alpine garnets and to estimate that only the 4.03% of the Grt grains refers to the pre-Alpine metamorphic assemblage. Furthermore, the ArcGis classification functions are useful to obtain 2D maps of the Aspect Ratio (AsR) for the different mineralogical species. The AsR visualization and estimation are shown for the Qtz (Fig. 5.2.5C) and Cpx (Fig. 5.2.5D) grains. The 60.17% of Qtz grains are characterized by the AsR equals to 0.70 ± 0.10 and the 60.80% of Cpx grains have an AsR of 0.70 ± 0.10 denoting a low degree of Alpine fabric evolution at the grain-scale. The mineral chemical variation of the pre-Alpine and Alpine paragenesis are quantitatively explored in the GrtI (C1; Fig. 5.2.6A) and ex-Sill (C2; Fig. 5.2.6D) microdomains using the Q-XRMA software. The C1 forming-minerals and their modal percentage (Fig. 5.2.6B) are Grt (32.50%), Qtz (28.24%), Wm (23.68%), Cpx (12.86%), Bt (2.18%), Ky (0.11%), Ap (0.05%), and Ep (0.02%). The C2 classified minerals and their modal abundance (Fig. 5.2.6E) are Wm (32.31%); Grt (18.69%), Ky (15.66%), Qtz (12.99%), Bt (9.09%), Cpx (8.71%), Pl (1.38%), Ap (0.74%), and Rt (0.05%). Garnet and clinopyroxene were selected due to their chemical composition distributions and as target minerals to highlighting pre-Alpine and Alpine metamorphic evolution, respectively. With the aim of highlighting the maximum range of compositional variability in the selected zoned garnet porphyroblast and the garnet coronae, 35 spot analysis (Table 5.2.2 in supplemental material) were acquired in both the chosen microdomains. For each calculated pixel, the stoichiometry is in agreement with the structural formula of garnet (*i.e.,* $X_3Y_2[ZO_4]_3$). In the same manner, X-Ray maps of clinopyroxene were calibrated using 20 spot analyses (Table 5.2.3 in supplemental material) of different grains to highlight and quantify mineral chemical variations in relation to which pre-Alpine microsite they replaced. The sum of cations is coherent with the structural formula of clinopyroxene (*i.e.,* XYZ_2O_6).

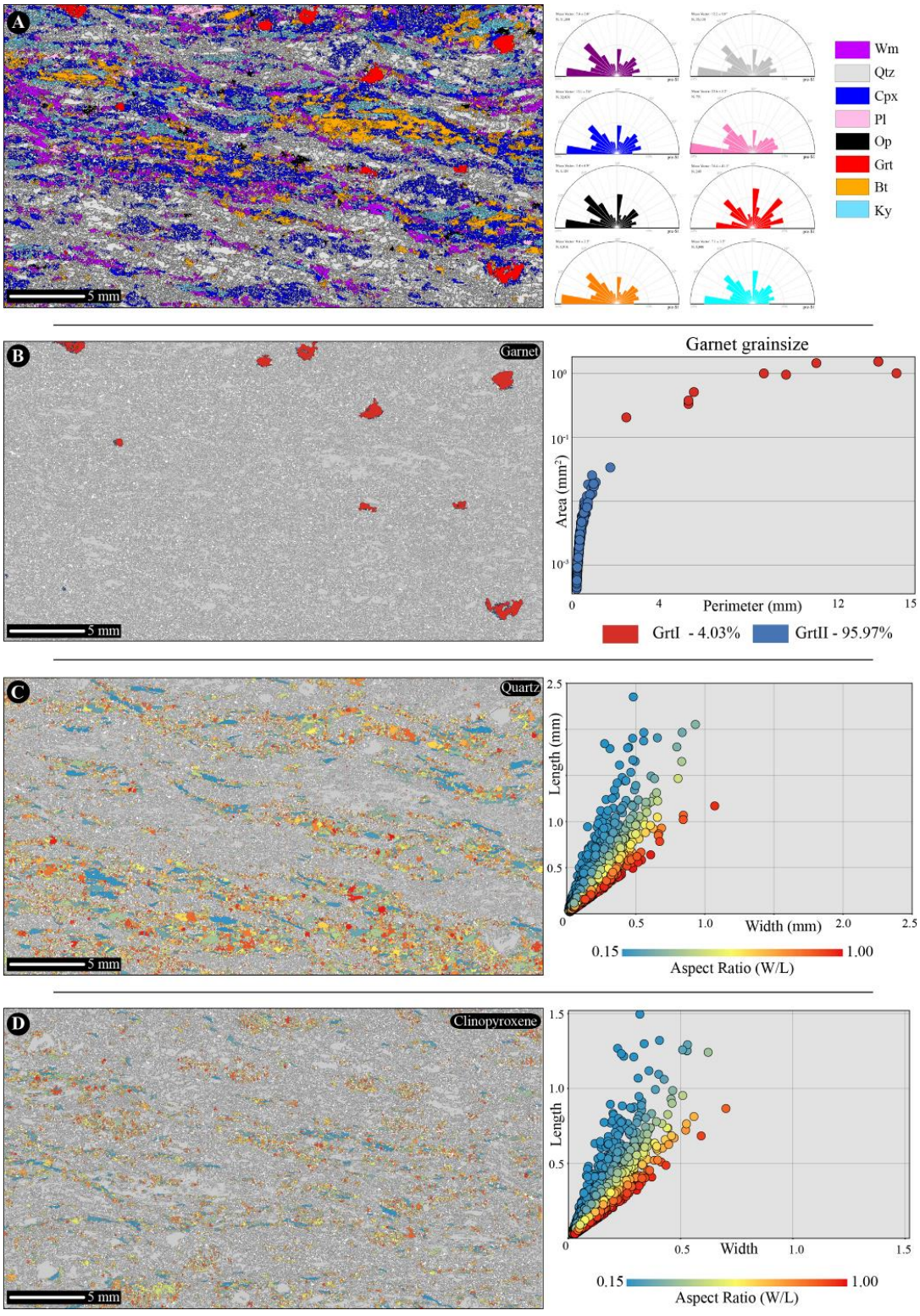

Figure 5.2.5. A) Results of Min-GSD and grains orientation with respect to pre-S1 foliation for each mineral phase. B) Garnet grainsize map and grainsize vs. perimeter plot. C) Aspect Ratio map of Qtz and Length vs Width plot for all Qtz grains. D) Aspect Ratio map of Cpx and Length vs Width plot for all Cpx grains.

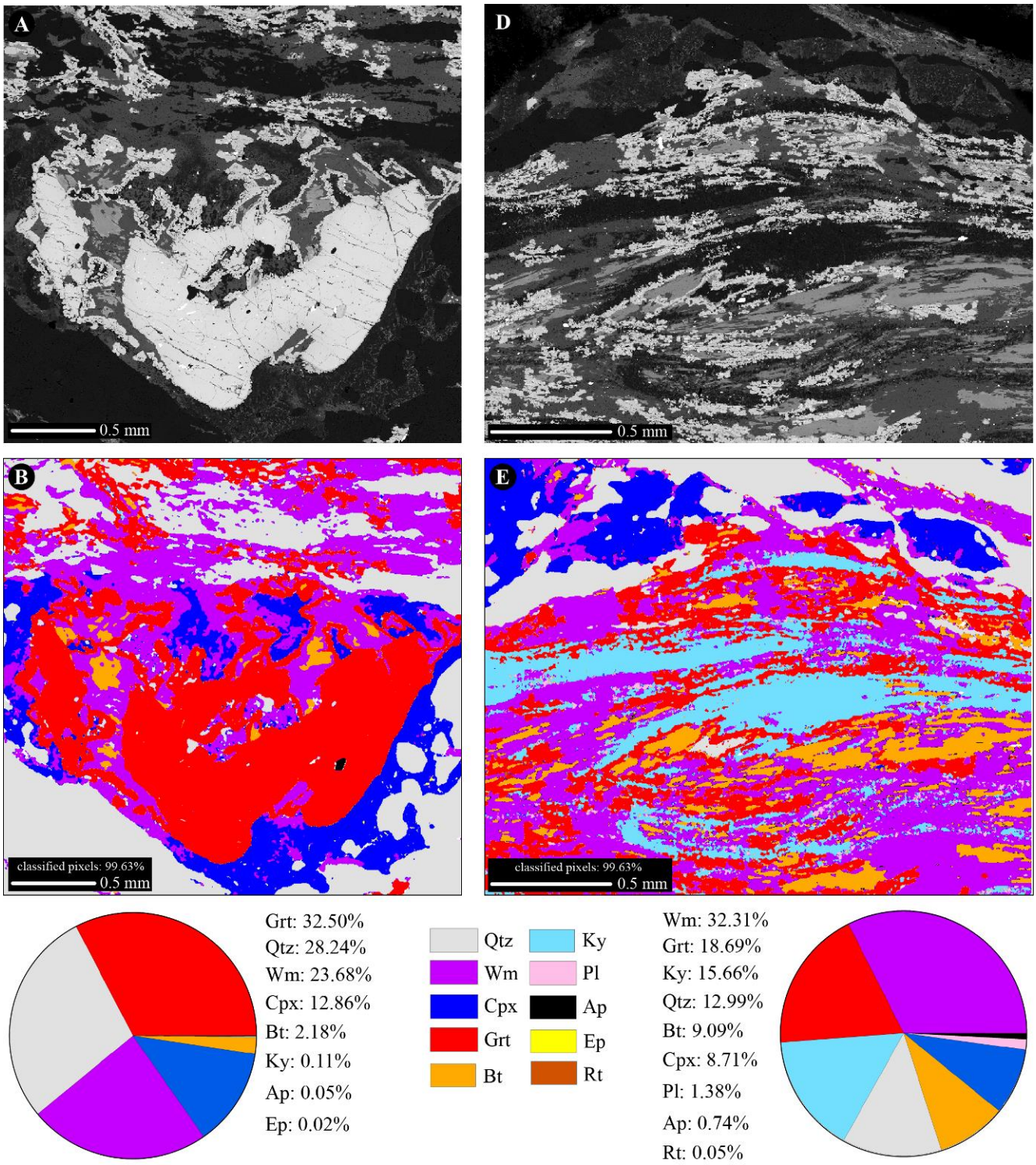

Figure 5.2.6. A) BSE image of pre-Alpine Grt microdomain. B) BSE image of pre-Alpine Sill microdomain. C) Results of Q-XRMA first cycle classification and mineral modal percentage for pre-Alpine Grt microdomain. D) Results of Q-XRMA first cycle classification and mineral modal percentage for pre-Alpine Sill microdomain.

Figure 5.2.7 shows the modal percentage of the Grt and Cpx sub-phase within the C1 microdomain and their calibrated chemical composition. The results of the calibration process for Grt divalent cations (Fig. 5.2.7A; *i.e.*, Ca, Fe, Mg, and Mn) highlight four distinct Grt sub-phases. The pre-Alpine GrtI covers the 51% of the C1-garnets and it is characterized by high Fe content (2.31 ± 0.04 a.p.f.u.), the higher Mn content (0.23 ± 0.03 a.p.f.u.), Mg content of 0.37 ± 0.03 a.p.f.u., and the lowest Ca content (0.10 ± 0.05 a.p.f.u.). The three-type of Alpine Grt show a wider chemical variability in depends on the microstructural location. Higher Ca content (*i.e.* maximum value of 1.23 a.p.f.u.) is observed where GrtII developed in contact with Cpx. Towards the pre-Alpine biotite, GrtII is characterized by a continuous decrease of Mn and Fe contents and a corresponding increase of Mg and Ca contents. The GrtII grown in the pre-Alpine Sill microdomain increase their Mg and Fe contents up to 0.89 a.p.f.u. and 1.91 a.p.f.u., respectively.

This mineral chemical variability was probably caused by differential diffusive exchange of the divalent cations in relation with pre-Alpine microdomains replaced. The clinopyroxene grown in equilibrium with Qtz replacing the pre-Alpine plagioclase and are mostly in contact with Grt porphyroblasts. The calibrated maps of Ca, Fe, Mg, and Na occupying the X and Y site in CpxI are shown in Fig. 5.2.7B, where it is possible to observe a higher Na content (0.89 ± 0.07 a.p.f.u.).

Figure 5.2.8 shows the modal percentage of the Grt and Cpx sub-phase within the C1 microdomain and their calibrated chemical composition. The calibrated elemental maps of the Grt show a continuous Ca content enrichment and Mg and Fe contents depletion from the pre-Alpine Sill and Bt to the Pl microdomains (Fig. 5.2.8A). In details, the Grt IIc is characterized by the highest Mg content (0.61 ± 0.13 a.p.f.u.) and the lowest Ca content (0.05 ± 0.03 a.p.f.u.). The Ca content reaches the maximum values of 0.68 a.p.f.u. and minimum Fe content (*i.e.*, 1.86 a.p.f.u.) at the contact with the ex-Pl microdomains which is replace by the Cpx and Qtz assemblage during the Alpine metamorphic evolution.

The results of the calibration process for Cpx (Fig. 5.2.8B; Ca, Fe, Mg, and Mn) highlight three sub-phases. Cpx Ia are characterized by the higher Na content (0.91 ± 0.07 a.p.f.u.) than the Cpx Ib (0.68 ± 0.05 a.p.f.u.) and the Cpx Ic (0.57 ± 0.04 a.p.f.u.). The Fe content of 0.61 ± 0.02 a.p.f.u., the Ca content of 0.69 ± 0.06 a.p.f.u., and the absence of Mg content distinguish the Cpx Ic, whereas the Mg enrichment up to 0.28 a.p.f.u. discriminate the Cpx Ib. The third analytical cycle of Q-XRMA allow to obtain for C1 microdomain (Fig. 5.2.9A) the end-member maps of Grt (Fig. 5.2.9B; almandine, grossular, pyrope, and spessartine) and the end-member maps of Cpx (Fig. 5.2.9C; diopside, hedenbergite, and jadeite) which were also used to extract chemical profiles (Fig. 5.2.9D) from the calibrated outputs.

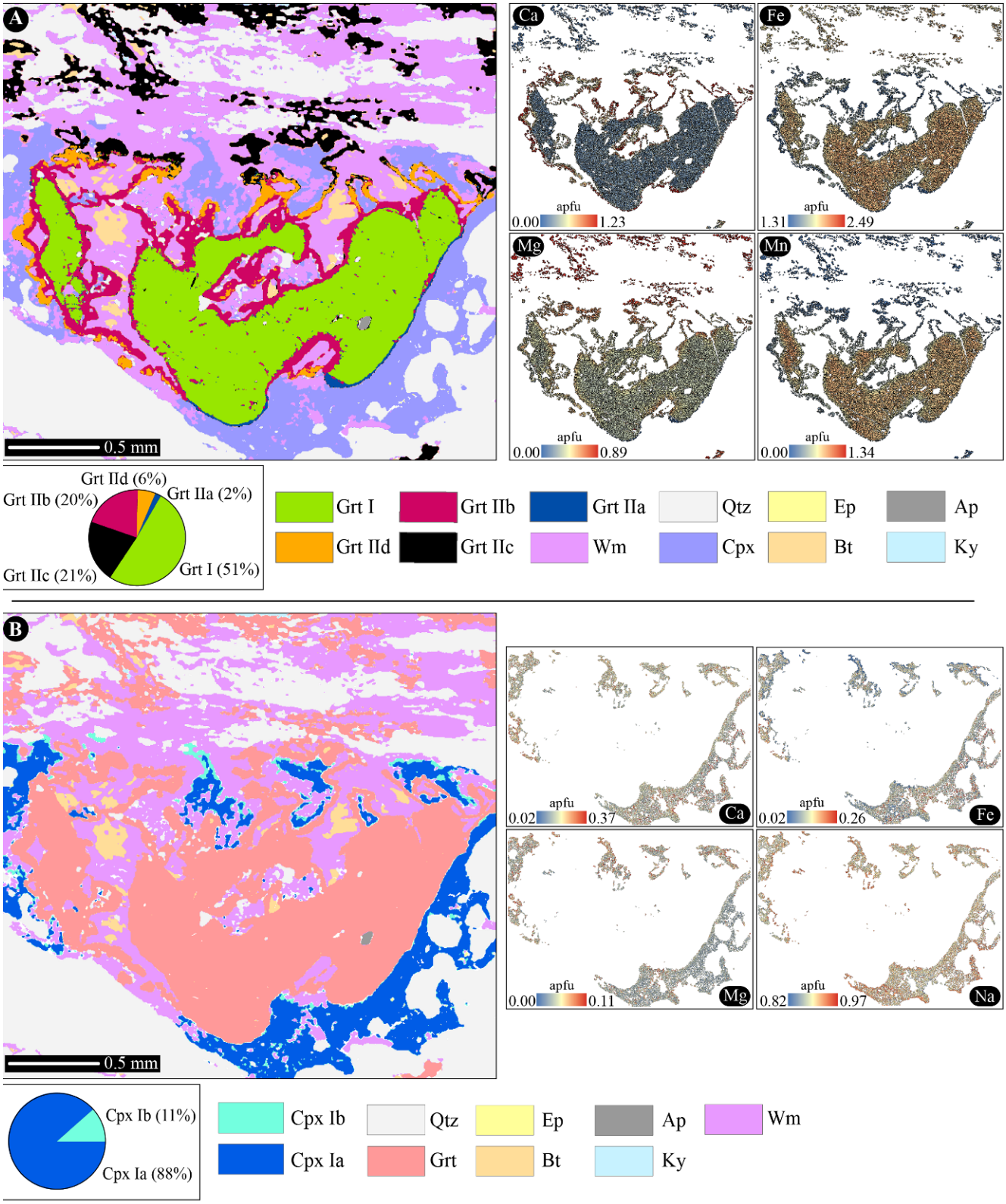

Figure 5.2.7. Results of second cycle of Q-XRMA procedure for pre-Alpine Grt microdomain. A) Grt sub-phases classification and their modal percentage. B) Calibration maps of Ca, Fe, Mg, and Mn contents in Grt. B) Cpx sub-phases classification and their modal percentage. B) Calibration maps of Ca, Fe, Mg, and Na contents in Cpx.

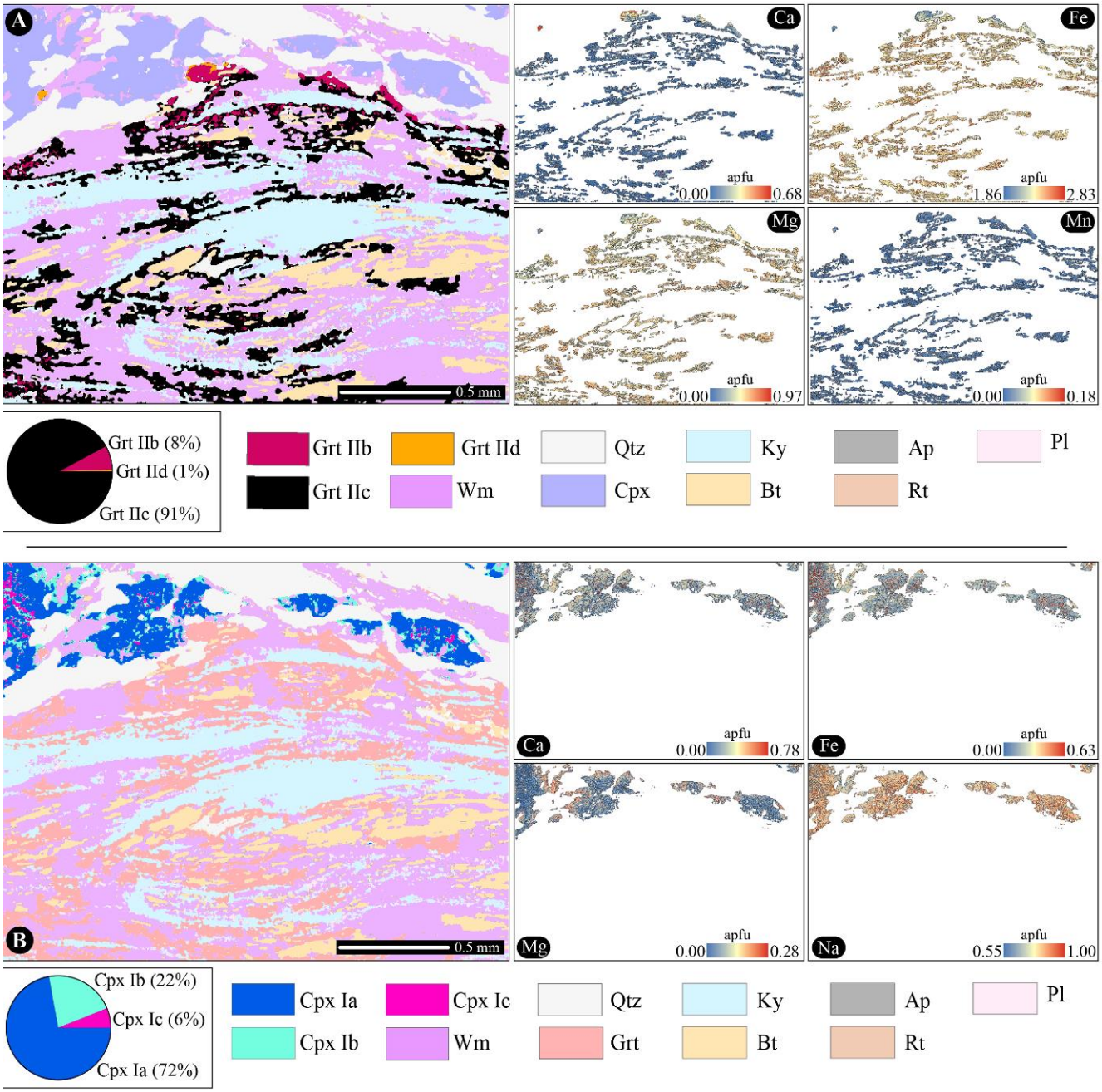

Figure 5.2.8. Results of second cycle of Q-XRMA procedure for pre-Alpine Sill microdomain. A) Grt sub-phases classification and their modal percentage. B) Calibration maps of Ca, Fe, Mg, and Mn contents in Grt. B) Cpx sub-phases classification and their modal percentage. B) Calibration maps of Ca, Fe, Mg, and Na contents in Cpx.

The GrtI is high in almandine content and low in the other three endmembers ranging from Alm83Grs0Prp11Sps6 to Alm73Grs5Prp13Sps9. The Grt IIa is characterized by a sharp discontinuity defined by a steep increase in grossular content and simultaneous depletion in almandine content, clearly visible in the compositional profile of Figure 5.2.9D. Towards the ex-Pl microdomain, the Grt IIa compositions vary from Alm56Grs31Prp11Sps2 to Alm50Grs40Prp4Sps6. The Grt IIb and Grt IId

consist in a continuous corona around Grt I and Bt grains and they are generally characterized by gradual decrease in Alm content and increase in Prp and in Grs contents, respectively. Grt IIb developed towards Grt I and Bt grains exhibiting an average composition of Alm59Grs9Prp24Sps8. Whereas, Grt IId growth between the Grt I and the pre-Alpine Sill microdomains shows an end-member composition of Alm53Grs30Prp11Sps6. The Grt IIc is developed outside of Grt I microdomain showing a gradual reduction of almandine and grossular components and enrichment in Prp and Sps contents towards pre-Alpine Sill microdomain. The composition ranging from Alm47Grs2Prp30Sps21 to Alm46Grs2Prp5Sps47. The clinopyroxene phase mostly consists in jadeite component ranging from 50% to 96%. When Cpx is developed in contact with garnet shows a Jd contents up to 78% with an average value of 93%. Towards pre-Alpine Sill microdomain, the Cpx is characterized by low content in Jd and corresponding enrichment in Hed and Di end-members up to 30% and 12%, respectively.

The end-member components variation for garnet and clinopyroxene within the C2 microdomain (Fig. 5.2.10A) has been explored through the Q-XRMA third cycle. The garnet component maps (Fig. 5.2.10B) and chemical profile (Fig. 5.2.10D) highlight a gradual enrichment in grossular and depletion in almandine and pyrope from Grt IIc (average composition: Alm70Grs0Prp29Sps1) to Grt IIb (average composition: Alm66Grs9Prp23Sps2).

Grt IId developed in contact with clinopyroxene and quartz assemblage and it is characterized by a sharp discontinuity defined by a steep increase in grossular and simultaneous decrease in almandine and pyrope contents. The Grt IId component composition varying from Alm63Grs18Prp18Sps1 to Alm61Grs22Prp15Sps2.

The assemblage consists in clinopyroxene plus quartz developed within the pre-Alpine Pl-microdomains. Although the clinopyroxene is generally high in jadeite composition, the component maps (Fig. 5.2.10C) show a composition variability related to the distance from the pre-Alpine biotite and Alpine garnet. Cpx Ia is charachterized by a gradual increase of Jd content from 82% at the core to 97 % at the rim in contact with Grt IId. Cpx Ib develop in contact with white-mica and it is characterized by a Di content of 33%, whereas Cpx Ic shows a sharp discontinuity defined by a steep increase of Hed up to 73% and simultaneous depletion in Jd content (*i.e.*, minimum value of 27%), clearly visible in the compositional profile of Figure 5.2.10D.

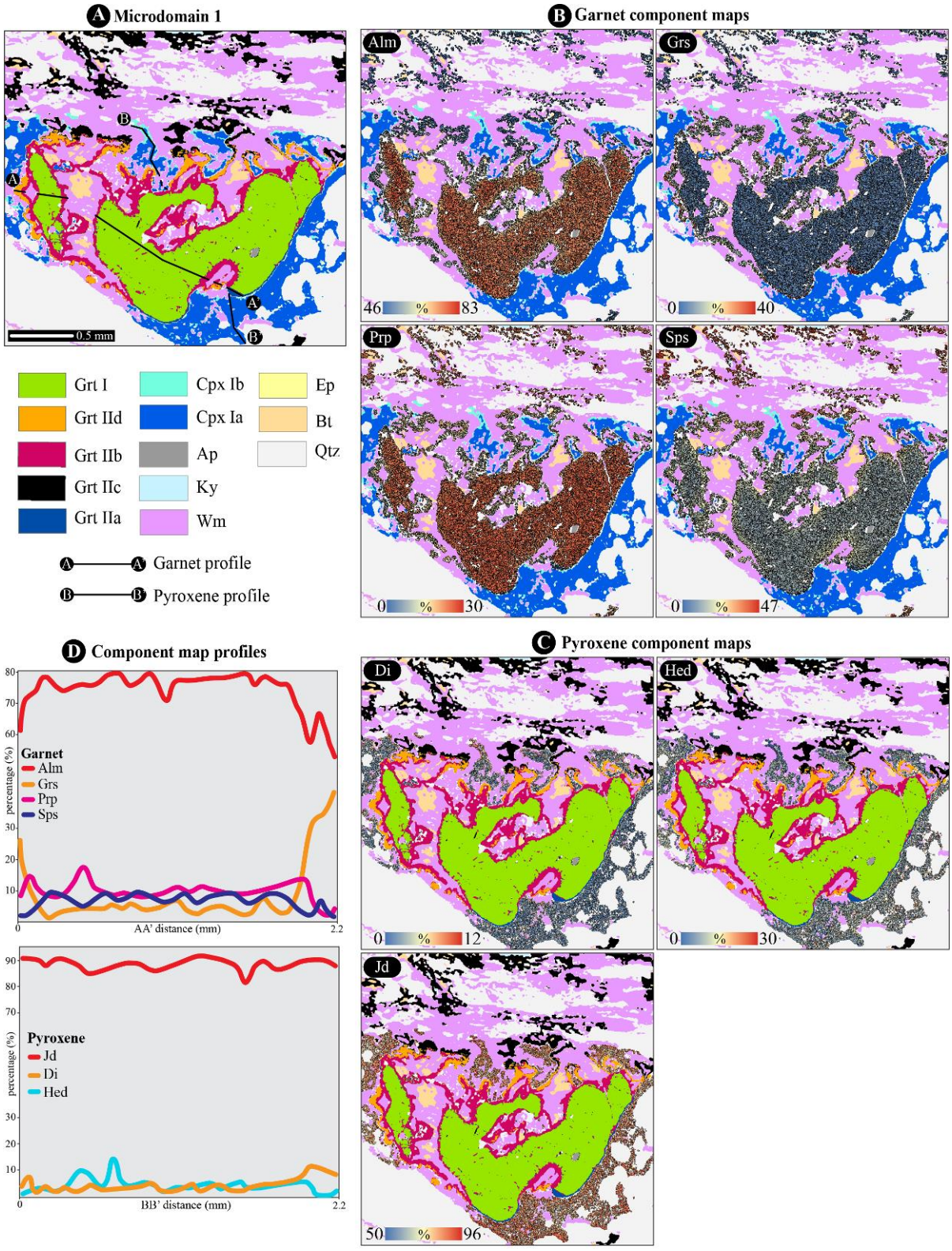

Figure 5.2.9. A) Results of third cycle of Q-XRMA for pre-Alpine Grt microdomain and localization of chemical profiles. B) Component maps for Grt (i.e., Alm: almandine; Grs: grossular; Prp: pyrope; Sps: spessartine). C) Component maps for Cpx (i.e., Di: diopside; Hed: hedenbergite; Jd: jadeite). D) Component profiles for Grt and Cpx.

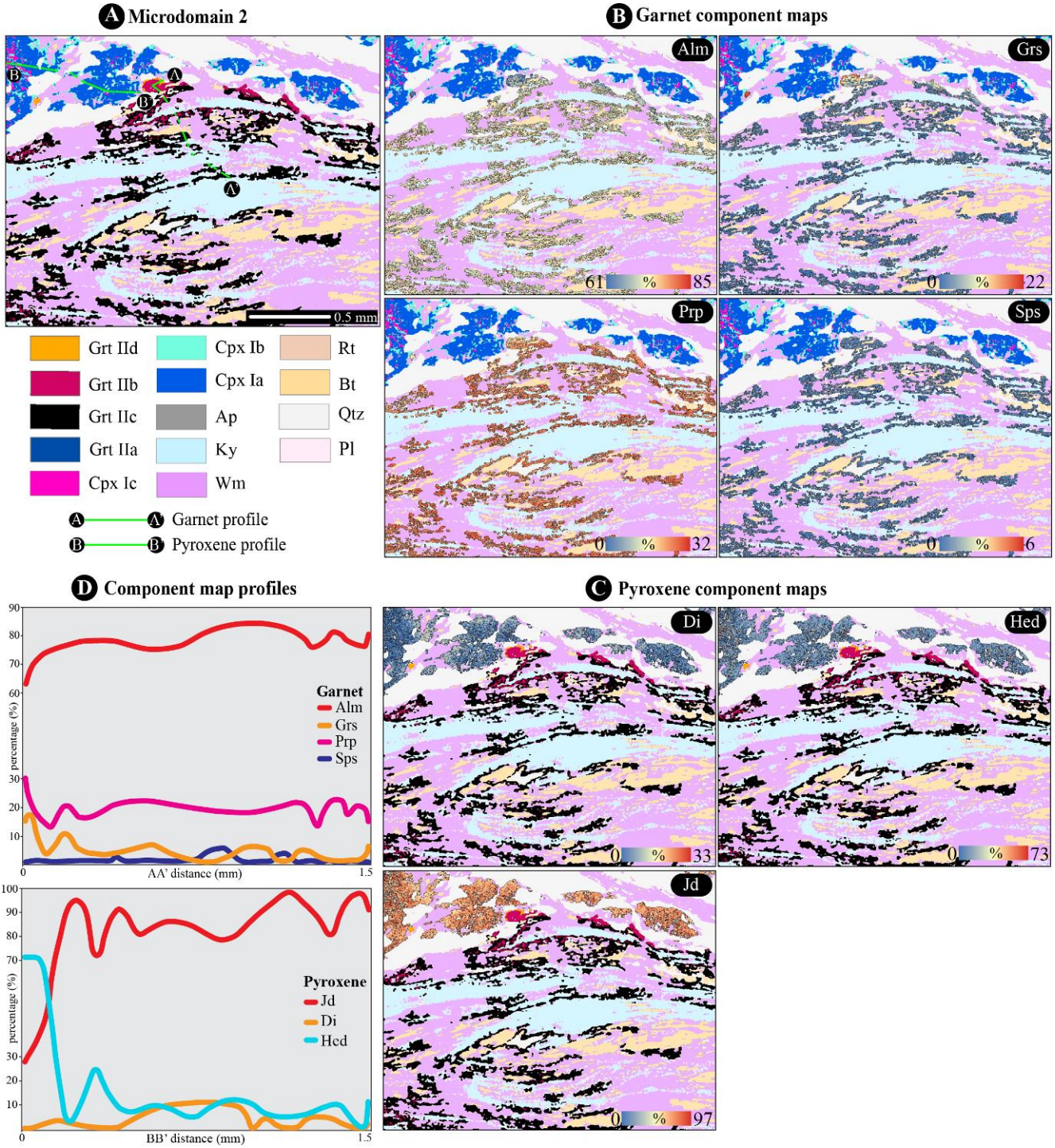

Figure 5.2.10. A) Results of third cycle of Q-XRMA for pre-Alpine Sill microdomain and localization of chemical profiles. B) Component maps for Grt (i.e., Alm: almandine; Grs: grossular; Prp: pyrope; Sps: spessartine). C) Component maps for Cpx (i.e., Di: diopside; Hed: hedenbergite; Jd: jadeite). D) Component profiles for Grt and Cpx.

5.2.3.2 3D fabric and metamorphic results

The X-ray µ-CT data can be segmented into six components. The brightest regions in the images have been attributed to opaque and garnet, followed by the clinopyroxene-kyanite-micas (*i.e.*, biotite and white mica) aggregates, and the darkest layers to quartz. Figure 5.2.11A shows the volume rendering of the segmented phases and the volumetric quantification of each phase processed with the PerGeos software. The segmentation of the Qtz volume (Fig. 5.2.11B) allows to observe how the pre-Alpine S-C-like geometry is well-preserved and the pervasive mylonitic fabric is overprint by static Alpine re-equilibration. By combining mineral phase segmentation based on gray-scale threshold with the characterization of microstructures (*i.e.*, different grain-size classes for the same phase and morphology of different pre-Alpine microdomains) allowed to distinguish the pre-Alpine mineralogical phases from the Alpine overprint and to quantify their ratio (Table 5.2.4 in supplementary material). For instance, the volume rendering of the specimen with 127,073 highlighted garnets (Fig. 5.2.11C) and the garnet grainsize analysis (Fig. 5.2.11D) clearly display two distinct classes (Table 5.2.5 in supplementary material). The Grt I is characterized by a volume of 108 μm^3 and a more marked anhedral morphology than Grt II, as can be visualized by high pseudo-grain surface (Fig. 5.2.11D). Using this approach for each segmented mineralogical phase permits to quantify the volume of pre-Alpine assemblage (Grt I + Wm I + Bt I) and the Alpine overprints. The volumetric analysis shows that the pre-Alpine-related phases represent 21.91% of the volume (Fig. 5.2.11A) and mostly consist in Bt I and Wm I. The Alpine-related phases, comprising the 78.09% of the volume, involve Wm II/Bt II (41.73%), Qtz (30.46%), Cpx (3.86%), Ky (2.04%), and Grt II (0.01%). The distribution patterns, and the shape preferred orientation (SPO) analysis for Qtz and Cpx are shown in Figure 5.2.1, Figure 5.2.12, and Table 5.2.5 in the supplementary material. 3D grain-shape anisotropy and orientation were measured using best-fit ellipsoids to Qtz and Cpx outer surfaces, from which the mean radius was calculated based on a spherical geometry (*i.e.*, X, Y, and Z from longest to shortest axis). A total of 65,5361 quartz and 92,0316 clinopyroxene were measured as enclosed within the sample volume (Figs. 5.2.12A and B) and are both characterized by an aspect ratio (Z/X) ranging from 0.15 to 1.00 (Figs. 5.2.12C and D). The distribution of Cpx and Qtz aspect ratios (Figs. 5.2.13A and B) has an average value of 0.52 ± 0.19 and 0.67 ± 0.26, respectively, persisting among all grainsize classes (Figs. 5.2.12C and D).

Qtz and Cpx shapes can be summarized with a Flinn plot (Figs. 5.2.13C and E) and Zingg shape diagram (Figs. 5.2.13D and F), which suggest a weak planar-type fabric orientation of pseudo-grains roughly distributed among blade-like shapes. Even though the weak shape preferred orientation and the blade-like shape arrangement of Alpine Cpx and Qtz pseudo-grains, the anisotropic aspect ratios

may be the results of pre-Alpine high shape preferred orientation inheritance. The shape preferred orientation and the volumetric measurements verified and quantified the observed weak grain-shape anisotropy and high metamorphic overprint during the Alpine tectono-metamorphic evolution.

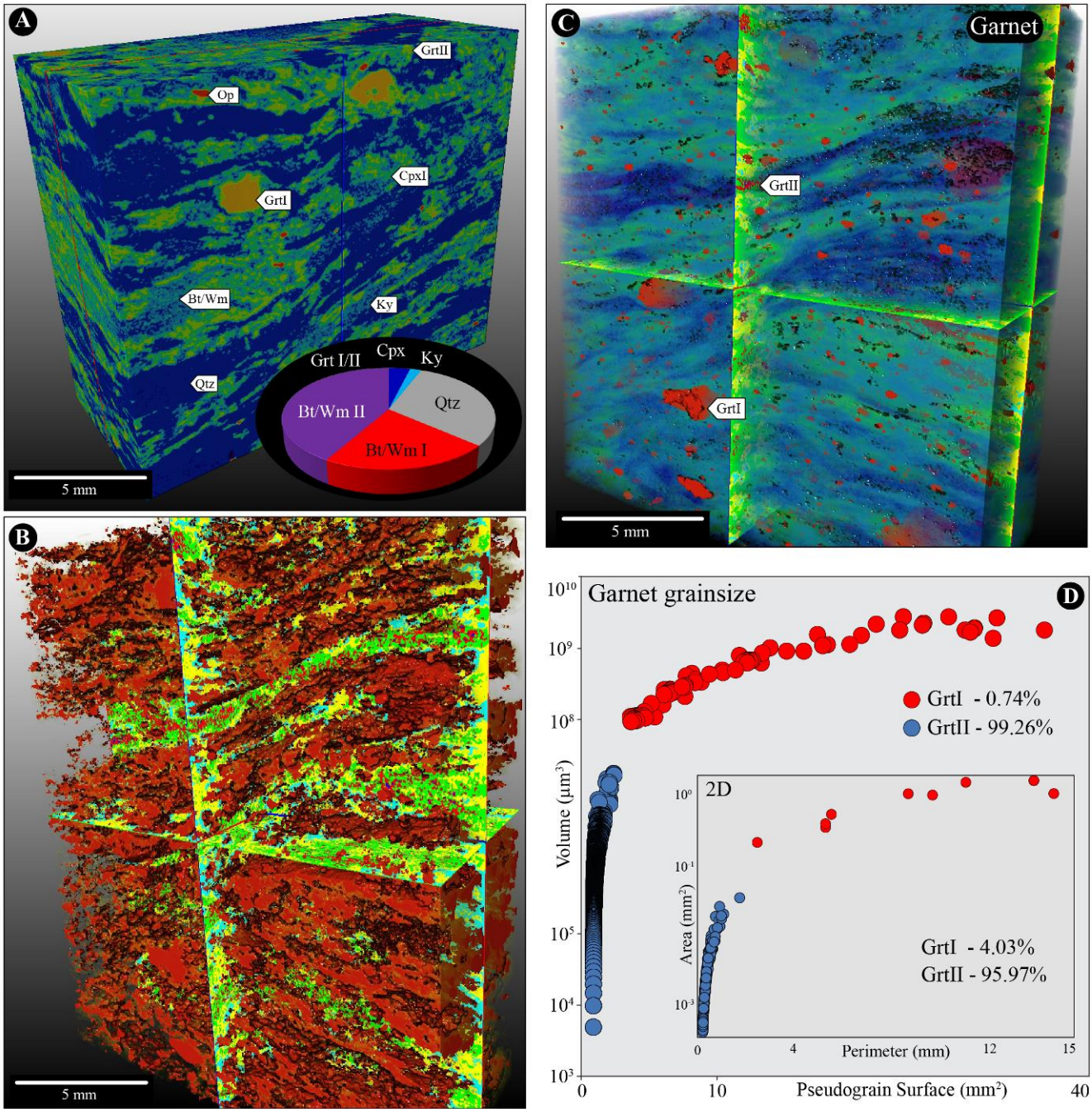

Figure 5.2.11. A) Volume rendering of the segmented phases and the volumetric quantification of each phase. B) Example of mineral segmentation (e.g., Qtz) showing the preservation of pre-S1 fabric. C) Garnet pseudo-grains are highlighted within the entire rock-volume. D) Grainsize vs. surface of Grt pseudo-grains.

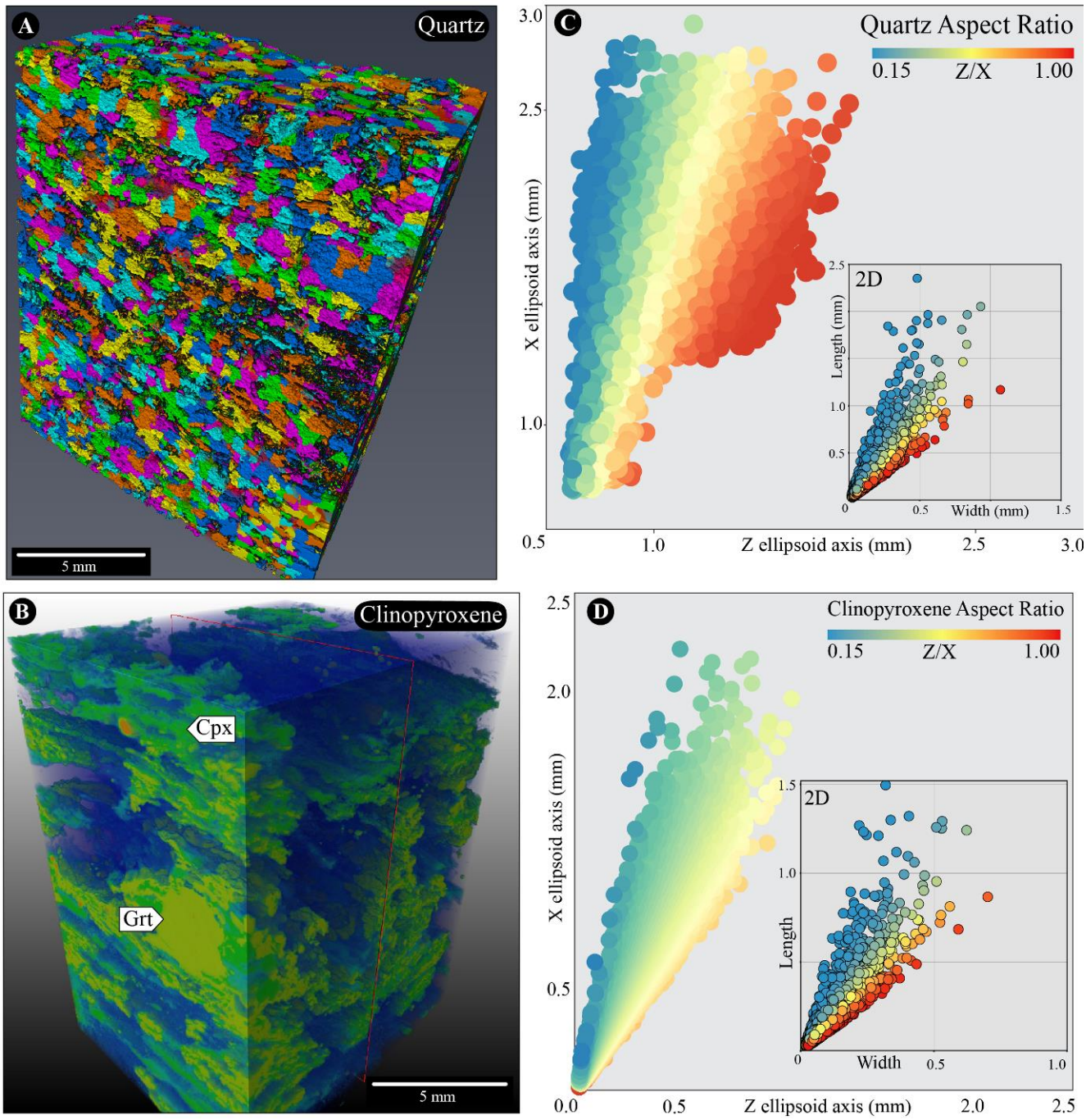

Figure 5.2.12. A) 3D visualization of the Qtz pseudo-grains arrangement. B) Qtz aspect ratio plot defined by the Z ellipsoid axis and X ellipsoid axis ratio. The 2D aspect ratio plot is reported. C) 3D visualization of the Grt (yellow), Qtz (blue), and Cpx (green) relationships. D) Cpx aspect ratio plot defined by the Z ellipsoid axis and X ellipsoid axis ratio. The 2D aspect ratio plot is reported.

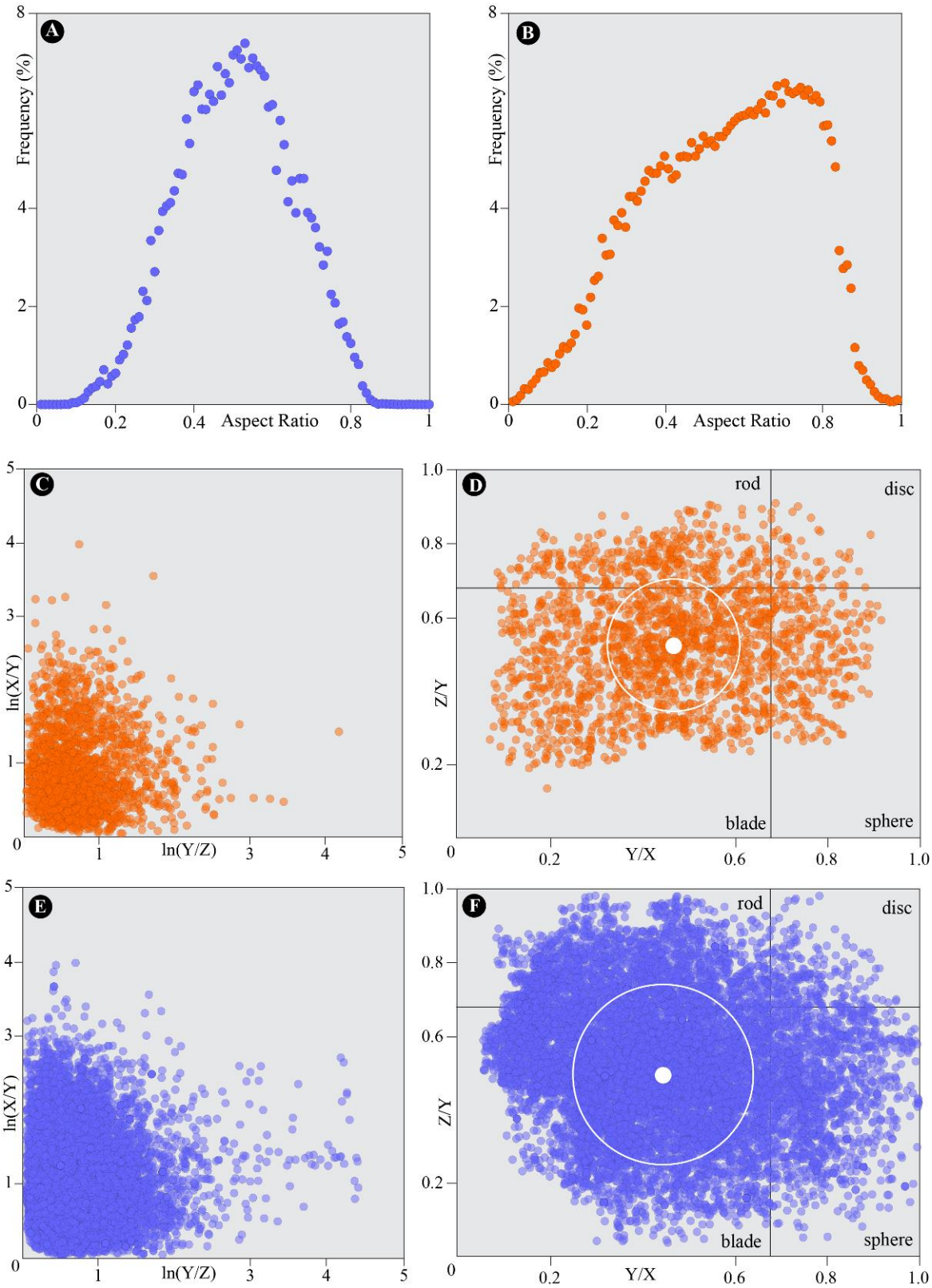

Figure 5.2.13. 3D quantitative fabric analysis. A) Frequency of Cpx aspect ratio. B) Frequency of Grt aspect ratio. C) Flinn diagram of Grt pseudo-grains. D) Zingg diagram of Grt pseudo-grains. The average and the standard deviation are reported. E) Flinn diagram of Cpx pseudo-grains. D) Zingg diagram of Cpx pseudo-grains. The average and the standard deviation are reported.

5.2.4 Discussion and Conclusion

5.2.4.1 Micro-scale and kinetics implications

The 3D visualization and analysis of fabrics and metamorphic minerals achieved by the X-ray µ-CT are well constrained by the 2D micro-structural analysis. In fact, despite the large gap between the two techniques in terms of number of analyzed grains, the results are comparable as shown by 2D vs. 3D description of shape parameters (Figs. 5.2.12 and 5.2.13). The reproducibility shown by the comparison of the shape analysis results allowed us to improve mineral phases identification, during the segmentation procedure, thanks to the knowledge from the 2D analysis, where not only shape parameters were known but also optical properties and mineral chemistry. Consequently, the quantitative chemical information obtained by the Q-XRMA tool were extended to the whole 3D volume.

Figures 5.2.11 and 5.2.12 may also be used to quantitatively support the pervasiveness of the pre-alpine fabrics (100 % of the rock fabric) within the investigated volume. Even though the pre-Alpine fabric is so well preserved the pre-Alpine minerals surprisingly correspond only to less than 22 % (Fig. 5.2.11A).Pre-Alpine minerals mostly consist of GrtI, BtI and WmI and their compositions are known, and the *P-T* estimates might be easily depicted and used as first-order input data for dynamic numerical modelling for geodynamic reconstructions (*e.g.* Roda et al., 2012).

Similar contrasting relations between degree of fabric development and mineral associations have been described for eclogitized rocks in the same area, where Permian intrusive preserve their igneous fabrics, estimated in >90% of the rock fabric (Zucali et al., 2002; Zucali, 2011), but the mineral association related to the magmatic stage is almost totally replaced by eclogite facies minerals, up to 80-90% of the investigated portions (Zucali et al., 2002; Corti et al. 2017; Koons, 1982).

In the investigated case, the Alpine-related mineral phases, comprising the 78.09% of the volume, involve WmII/BtII (41.73%), Qtz (30.46%), Cpx (3.86%), Ky (2.04%), and GrtII (0.01%), and do not mark a new fabric, but statically replace specific pre-Alpine microdomains. The static replacement is also quantitatively shown by the heterogeneous grain-size distribution (Figs. 5.2.11 and 5.2.12), suggesting a dominant control of the growth domain over dynamic recrystallization that would have induced more pronounced shapes preferred orientations (Bell and Hayward, 1991). For example, GrtII grows as corona over GrtI, or Ky grows as aggregates replacing pre-Alpine Sill-microdomains. The volumetric reconstruction of the shape and spatial distribution of Alpine-related phases clearly demonstrate that metamorphic reactions may occur even in absence of deformation, and in the virtual absence of fluid as chemical medium. This was demonstrated by the unchanged bulk chemistry within the selected microsites. As an example, GrtII increases its Fe and Ca content in the ex-sillimanite

domain and ex-plagioclase domains, respectively. Similarly, the Ky phase only occurs as pseudomorphic fine-grained aggregates in ex-sill domains. In the same way, the symplectite textures occurring in the ex-Pl domains are defined by high Jd contents (82-97%) Cpx, Ca-rich Grt (highest Grs component around 22%), and Qtz. All these features suggest that even at low temperature conditions (nominally below 550°C) and in low-strain domains the activation energy of many metamorphic reactions, energetically less favored (*e.g.*, sillimanite to kyanite reaction), may be overstepped.

5.2.4.2 General implications

A relative age of the two generations of minerals (*i.e.* pre-Alpine and Alpine) can be inferred, using their chemistry and microstructural relationships. In fact, GrtII, Cpx and WmII mineral chemistry strongly overlap with those expected for similar phases growth at eclogite-facies conditions (Zucali et al., 2002; Zucali&Spalla, 2011), attributed to an age range of 80-60 Ma (Cenki-Tok et al., 2011; Regis et al. 2014). While the chemistry of GrtI and BtI overlap the compositions known for similar rock sources, as the Ivrea-Zone (*e.g.* Barboza & Berganz, 2000), the Serie di Valpelline (Manzotti and Zucali, 2013), and other Austroalpine or Southalpine slices which they preserve the pre-Alpine (Permian) high-temperature imprint (Roda et al. 2018c).

The investigated 3D microstructures exhibit complex overprinting relationships that are only partially reflected by outcrop-scale structures. In particular, the Bt, Wm, Qtz, Ky, and Cpx grains show two orientation clusters that can be correlated to the S and C mylonitic structures. The S-related structure includes 35% of grains aligned at 2-13° with respect to the pre-S1. The C-related structure comprises 23% of grains laying at 34-46° from the pre-S1 orientation. These S-C fabrics may be compared to pre-Alpine features described by previous authors at the map-scale (Zucali, 2002; Corti et al., 2017) and preserved in similar low-strain volumes of the Sesia-Lanzo Zone. Still remains unclear how those meter-scale domains might preserve such clean fabrics even where no mechanical barriers have been described at the map-scale.

In conclusion, similarly to what described at km-scale by 3D geological modelling (*e.g.*, Salvi et al., 2010), a volumetric quantification is fundamental to improve our knowledge of the tectono-metamorphic evolution of active margins (*e.g.* subduction zone). In particular, the 3D reconstruction of grains shape distribution through X-ray microtomography on centimeters-sized samples allows to improve the knowledge of the metamorphic texture development. Moreover, the combined use of EMPA X-ray chemical mapping with the X-ray µ-CT technique can further permits to dynamically constrain the chemistry of the mineral phases linked to the metamorphic transformation.

5.2.5 Acknowledgments

The authors thank A. Risplendente for assistance during the WDS/EDS-EPMA analysis and Dr. J. Kuva for support during the tomography data analysis with PerGeos in GTK. Funding by PhD School in Earth Sciences from University of Milan; Elettra Proposal (SYRMEP) #20170147, “Towards a geologically meaningful quantification of 3D grains shape distribution in natural rocks” by M. Zucali. Funding by University of Milano: Linea 2, Azione A - fondi giovani ricercatori “Analisi strutturale delle catene collisionali” (PSR2018_DZANONI). Results here presented have been developed in the frame of the MIUR Project “Dipartimenti di Eccellenza 2017 - Le Geoscienze per la società: risorse e loro evoluzione (work-package 3, tasks 3.3 and 3.4)”.

References are integrated at the end of the thesis.

Chapter 6

Third case study – Mt. Frisson area

Tectonometamorphic evolution of Variscan metamorphic basements and pre-Alpine cover rocks

6.1 Introduction

The Argentera Massif, the southernmost of the external crystalline massifs (Helvetic Domain of the Western Alps: e.g. Schmid et al., 2004), is a NW-SE elongated body mainly composed of migmatitic orthogneisses, paragneisses, and amphibolites, together with metavolcanics of Ordovician age (Faure-Muret, 1955; De Pol, 1963; Malaroda et al., 1970; Blasi, 1971; Bortolami et al., 1974; Bogdanoff, 1986; Colombo et al., 1994; Rubatto et al., 2001). It is a portion of European continental crust involved in the late Alpine collision (Polino et al., 1990; Bogdanoff et al., 2000; Schwartz et al., 2007; Schreiber et al., 2010) in which the Variscan tectono-metamorphic evolutions is well-preserved (Von Raumer et al., 1999, 2009, 2013; Guillot et al., 2009; Compagnoni et al., 2010; Spalla et al., 2014; Fréville et al., 2018).

Plates	events (tectonic, geodynamic regime)	age range of geodynamic regime	generation of critical rock types
Plate 1 Continental crust formation during the Variscan orogenic cycle: 400 - 290 Ma (Fig. 6)	1 -- Variscan subduction	Early Devonian (400 - 375 Ma)	Eclogites, serpentinised peridotites, and marbles (Fig. 1)
	2 -- Variscan collision	Late Devonian to early Carboniferous (375 - 320 Ma)	Migmatites and granitoids (Fig. 2, 3, 4)
	3 -- Erosion / dismantling of the Variscan chain	late Carboniferous (320 - 299 Ma)	Sandstones, carbonaceous schists, and conglomerates (Fig. 5)
Plate 2	4 -- Post-Variscan thinning (Fig. 5)	Permian to Triassic (290 - 201 Ma)	Permian clastic sediments and volcanics, Triassic evaporites and clastic and carbonatic sediments (Fig. 1, 2, 3, 4)
Plate 3	5 --Alpine rifting, formation of passive margins, and oceanisation (Fig. 4)	Jurassic to Early Cretaceous (201 - 100 Ma)	Jurassic limestones and dolostones in syn-rift basins and strucutral highs; Early Cretaceous limestones, marls, and sandstones in post-rift pelagic basins (Fig. 1, 2, 3)
Plate 4	6 -- Alpine subduction (Fig. 6)	Late Cretaceous to early Eocene (100 - 45 Ma)	Late Cretaceous turbiditic limestones and marls (Fig. 1, 2) Late Cretaceous Flysch with Helminthoids (Fig. 3, 4, 5) latest Cretaceous to middle Eocene, lacustrine and continental conglomerates, limestones, and red clay with mica
Plate 5	7 -- Alpine collision	late Eocene to Oligocene (45 - 23 Ma)	Flysch and fossiliferous limestones and marls (Fig. 1, 2, 3).
Plate 6	8 -- Apenninic subduction (Fig. 5, 6)	late Oligocene (28 - 23 Ma)	Subduction-related andesitic breccias and tuffs (Fig. 1).
Plate 7	9 -- Opening of the Western Mediterranean (Ligurian-Provençal basin) during the Corsica-Sardinia block rotation (Fig. 2, 3, 4)	late Oligocene to early Miocene (23 - 15 Ma)	Coastal, shelf, slope, and deep sea sedimentary rocks
Plate 8	10 -- Inversion of the Ligurian-Provençal margin (Fig. 3)	late Miocene to Present (from 15 Ma on)	Marine to continental deposits (Fig. 1, 2).

Table 6.1. Geologic history recorded within Argentera Massif integrating the association of tectonic (geodynamic) events, chronology (ages), and rock types related to their genetic environments (Gosso et al., 2019).

The massif consists of migmatites mainly derived from a metasedimentary sequence intruded by lower Paleozoic granitoid bodies, followed by the emplacement of small mafic bodies during the lower Ordovician (Bortolami and Sacchi, 1968; Blasi, 1971; Malaroda, et al., 1970; Bogdanoff and Ploquin, 1980; Bogdanoff et al., 1991; Ferrando et al., 2008; Rubatto et al., 2010; Compagnoni et al., 2010) and the main pre-Alpine fabric is a pervasive steeply dipping regional-scale foliation.

Variscan H*P* and/or H*T* metamorphic and structural features were preserved as centimeter- to meter-thick lenses of mafic rocks, locally in association with ultramafites and calc-silicates (Faure-Muret, 1955; Malaroda et al., 1970; Bogdanoff, 1986; Latouche and Bogdanoff, 1987; Paquette et al., 1989; Ferrando et al., 2008; Compagnoni et al., 2010, Rubatto et al., 2010). High-pressure granulite facies metamorphism has been dated at around 340 Ma with zircon geochronology (Rubatto et al., 2010).

The Argentera massif was involved in the Alpine collision buried at a structural level compatible with greenschist- to epidote-amphibolite-facies conditions (Corsini et al., 2004; Lardeaux, 2014). Alpine fabric consists of ductile shear zones mainly marked by fine grained recrystallized quartz and albite.

Table 6.1. summarize the polycyclic geologic history preserved in the Argentera massif, starting with the Variscan convergence during Devonian, throughout the opening of the Tethys, Alpine convergence, and the Apennine subduction associated with Ligurian-Provençal ocean opening (Gosso et al., 2019).

The study area is a tectonic window within the Permo-Mesozoic sedimentary sequence at the south-eastern end of the massif (Colombo et al., 1994) (Figure 6.1). The area consists of Variscan metamorphic basement and Permo-Mesozoic sedimentary covers, deformed together during the Alpine convergence. The crystalline basement belongs to the Gesso-Stura-Vésubie metamorphic complex, mainly consisting of migmatitic gneiss and granulite, locally containing melanocratic metabasic layers and lenses which pervasively record the Variscan H*P* and H*T* tectonometamorphic evolution. The most common Permian-Mesozoic rock in the area is a metamorphic conglomerate, deformed and re-equilibrated under greenschist facies conditions. Recently, Ferrando et al. (2008) inferred the granulite rocks metamorphic evolutions describing metamorphic peak PT condition of 735 ± 15°C and 1.38 ± 0.05 GPa, followed by decompression down to 709 ± 2°C and 1.10 ± 0.02 GPa, re-equilibration at 665 ± 15°C and 0.85 ± 0.15 GPa, and a latter retrogression occurred at temperatures from 500°C to 625°C and pressures lower than 0.59 GPa. The metamorphic peak of granulites under H*P* granulite-facies conditions is dated by Rubatto et al. (2010) showing Carboniferous ages at ~340 Ma.

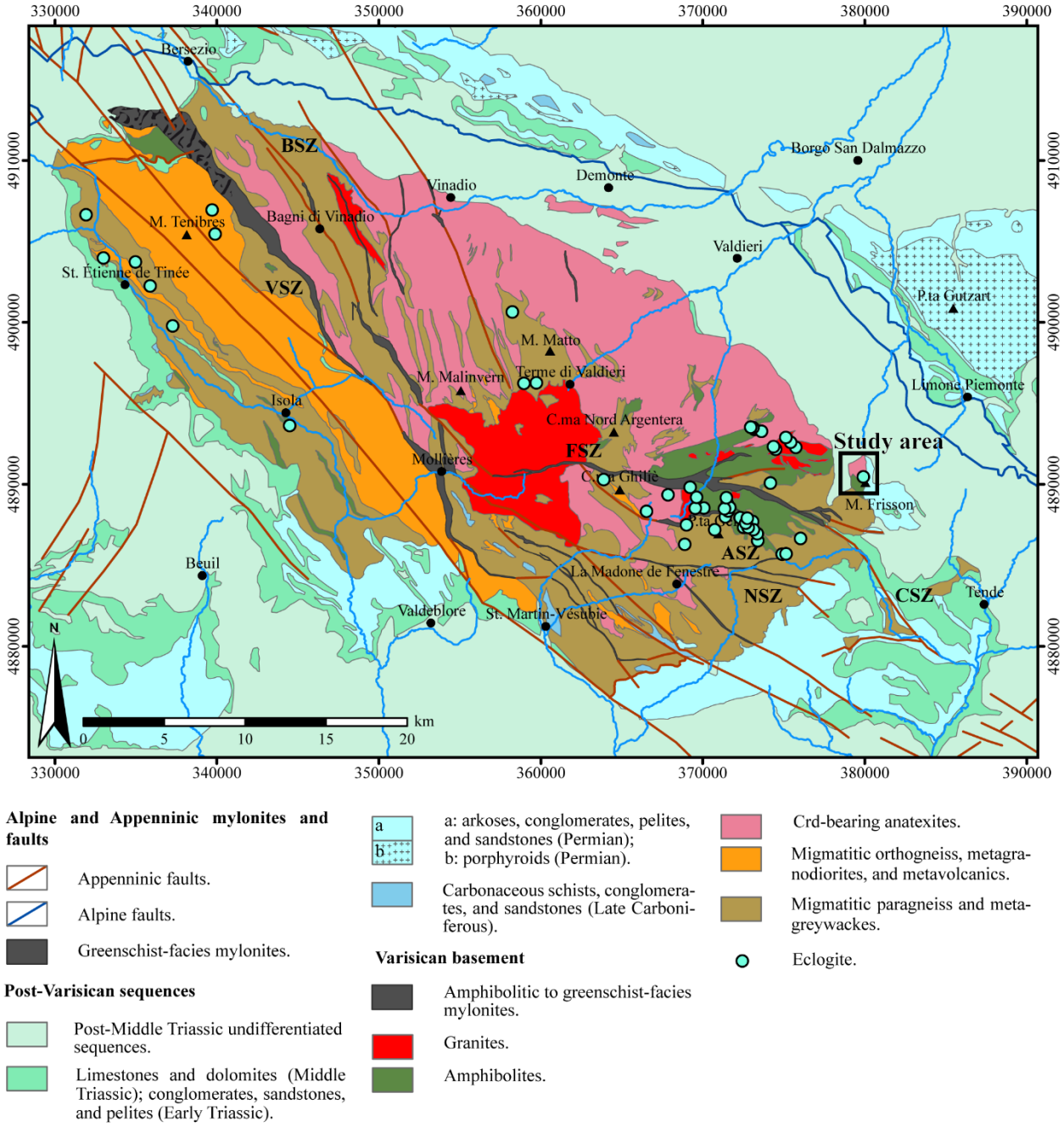

Alpine and Appenninic mylonites and faults

- Appenninic faults.
- Alpine faults.
- Greenschist-facies mylonites.

Post-Varisican sequences

- Post-Middle Triassic undifferentiated sequences.
- Limestones and dolomites (Middle Triassic); conglomerates, sandstones, and pelites (Early Triassic).
- a: arkoses, conglomerates, pelites, and sandstones (Permian); b: porphyroids (Permian).
- Carbonaceous schists, conglomerates, and sandstones (Late Carboniferous).

Varisican basement

- Amphibolitic to greenschist-facies mylonites.
- Granites.
- Amphibolites.
- Crd-bearing anatexites.
- Migmatitic orthogneiss, metagranodiorites, and metavolcanics.
- Migmatitic paragneiss and metagreywackes.
- Eclogite.

Figure 6.1. Geological map of the Argentera-Mercantour 1217 massif (redrawn after Faure- Muret, 1955, Malaroda et al. 1970, Corsini et al., 2004, Carosi et al. 2016, Gosso et al. 2019, Filippi et al., 2019). ASZ - Autier Shear Zone; BSZ - Bersezio Shear Zone; CSZ - Casterino Shear Zone; FMSZ - Ferrere-Mollières Shear Zone; FSZ Fremamorta Shear Zone; NSZ – Neiglier Shear Zone. The study area is located with the black square.

The structural, petrological, geochemical, and chronological analysis of H*P*/UH*P* metamorphic rocks exposed in orogens provide first-order constraints for addressing evolution of convergent margins (*i.e.*, subduction-collision system). In this light, this area is suitable to provide information on pre-continental collision Variscan tectonics framework preserved in the Alpine belt. The detailed structural analysis and petrological investigation on metabasic rock enclosed in the granulites, allowed to infer the metamorphic peak at eclogite-facies conditions. U-Pb dating of rutile grains in textural equilibrium with eclogitic mineral assemblage shows age of 326.1±4.4 Ma. Moreover, this contribution aims to better constrain the structural and metamorphic evolution within the Variscan metamorphic basements and its relationship with the pre-Alpine cover deformed together during the Alpine collision, where only few data are available.

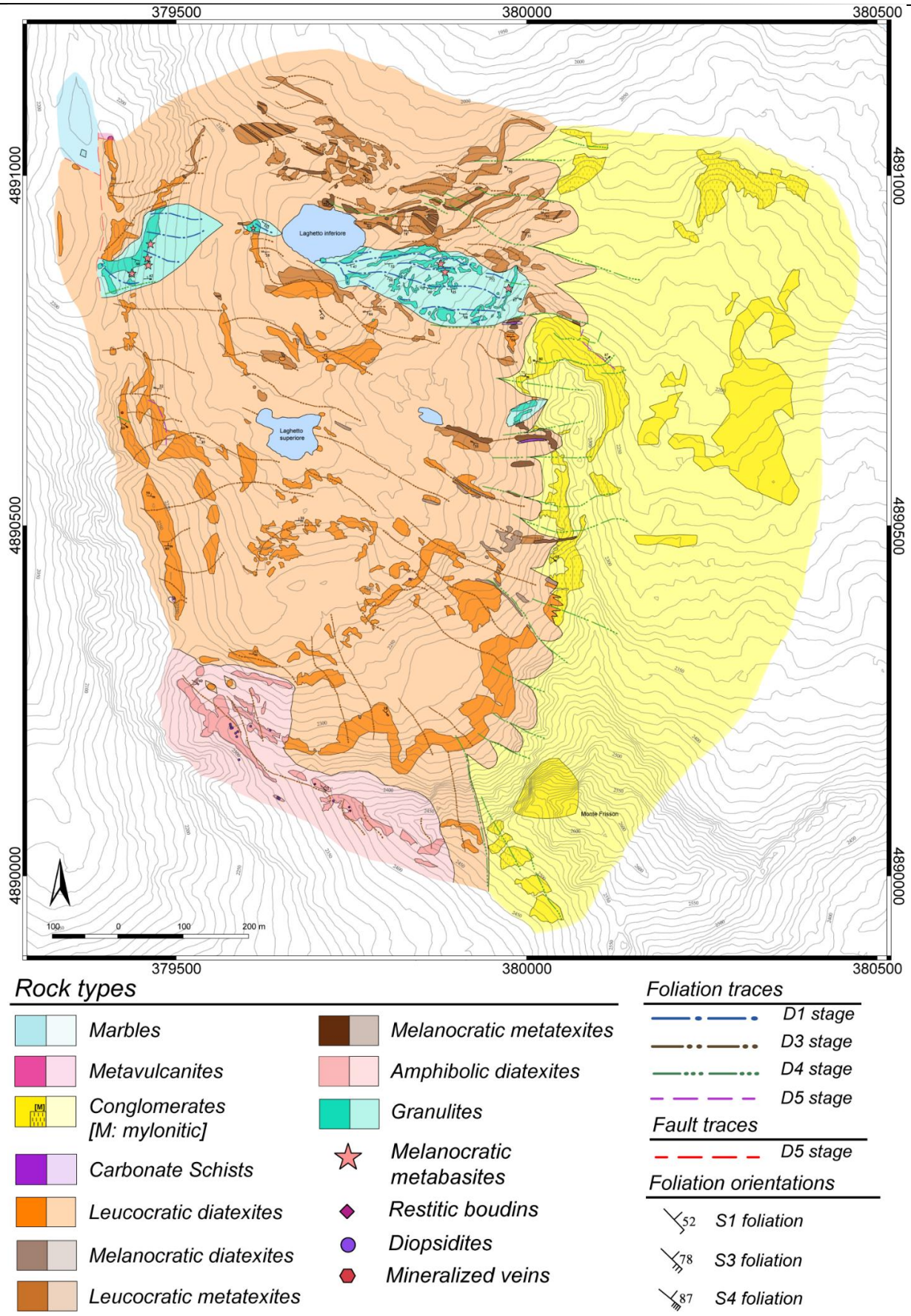

Figure 6.2. Structural map of the Frisson area. The outcrops contours, lithology, superposed structural elements are reported.

6.2 Mesostructural analysis

The structural map presented in Figure 6.2, derived from an original structural mapping at 1:2,000 scale, shows rock types, compositional heterogeneities in the main rock types, superposed foliation trajectories, fold axes, axial plane trajectories and shear zones. The mesoscale structural analysis allowed to detect four ductile deformation phases, followed by one brittle deformation phase. The first three deformation phases (D1 to D3) are recorded only in the Variscan metamorphic basement and the D4-D5 affect in both basement and Permian-Mesozoic cover rocks.

In the migmatites, pre-D3 fabric is observed as structural and mineralogical relict within dominant S3 foliation. Unfortunately, the relative chronology and kinematic compatibility between this pre-D3 stage with the dominant S1 foliation in granulite and melanocratic metabasite is not characterized by reliable structural and metamorphic evidences. This gap in structural and metamorphic correlation is formalized using S1m and S1g acronyms for the relict foliation in migmatites and dominant foliation in granulite and melanocratic metabasite, respectively. The orientation of structural data has been grouped according to their relative chronology and metamorphic assemblage (Fig. 6.3).

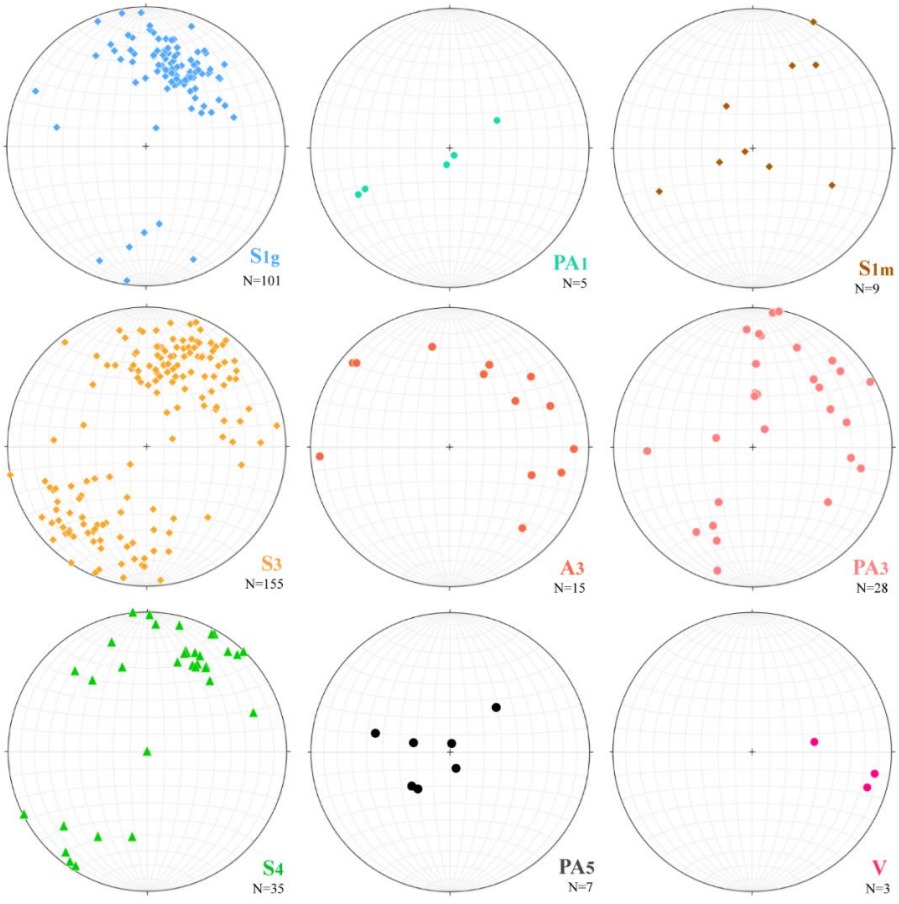

Figure 6.3. Orientation data grouped according to their relative chronology and metamorphic compatibility (Stereonet 9 by Allmendinger, 2016). Equal area Schmidt diagrams (S: foliation; PA: fold axial plane; A: fold axis; V: vein).

6.2.1 Rock types

6.2.1.1 Variscan metamorphic basement

Melanocratic metabasite occurs as meter- to decameter-size boudins and lenses within granulite (Fig. 6.4A) and mostly consists of garnet, clinopyroxene, amphibole, and rutile. These rocks are characterized by a mylonitic fabric, defined by porphyroclasts of garnet, clinopyroxene, amphibole embedded in the S1g foliation; the S1g foliation is chiefly marked by the shape preferred orientation of fine-grained amphibole and clinopyroxene (Fig. 6.4B). Minor plagioclase and biotite occur but do not show any preferred orientations.

Basic Granulite shows a mylonitic foliation (S1g) marked by alternating layers, consisting in millimeter- to centimeter-thick leucocratic and melanocratic levels; these layers generally wrap millimeter- to centimeter-sized garnet porphyroblasts (Fig. 6.4C). Whereas the leucocratic levels mostly consist of fine-grained plagioclase, with minor biotite, amphibole, and garnet, the melanocratic layers are constituted by fine- to medium-grainsize mineral association of amphibole, clinopyroxene and garnet (Fig. 6.4D). In both layers, minor amount of quartz, opaque minerals, white mica, chlorite, and epidote characterize the fine-grained mineral association that mark the coronitic fabrics occurring around garnet and amphibole grains, as well the mylonitic D4 shear zones.

Migmatite is the most widespread rock type in the area. The mesostructural analysis allows to distinguish two main types: metapelitic and amphibolitic migmatites, as it is shown in the Figure 6.2. While the anfibolitic migmatite are mostly diatexites, in the metapelitic migmatite the occurrence of leucosome is highly variable (*i.e.* diatexites and metatexites; Fig. 6.2). The metapelitic migmatites consist of medium- to fine-grained biotite, quartz, feldspar, and minor amphibole, white mica, and chlorite and they show centimeter-thick layering consisting of Bt-rich and Bt-poor levels. In the metatexites, the dominant S3 foliation consists of films marked by biotite and minor white mica and amphibole that bound quartz-feldspar lithons (Fig. 6.4F). The leucosome portion consists of fine-grained quartz and feldspars. The leucosome fraction increases towards the contact with the amphibolitic migmatite. Chlorite, white mica and biotite occur along the D4 shear zones.

The **amphibolitic migmatites** are fine- to medium-grained diatexites, consisting of aligned amphibole with quartz and felspars marking the S3 foliation. Centimeter-sized diopsiditic boudins are widespread.

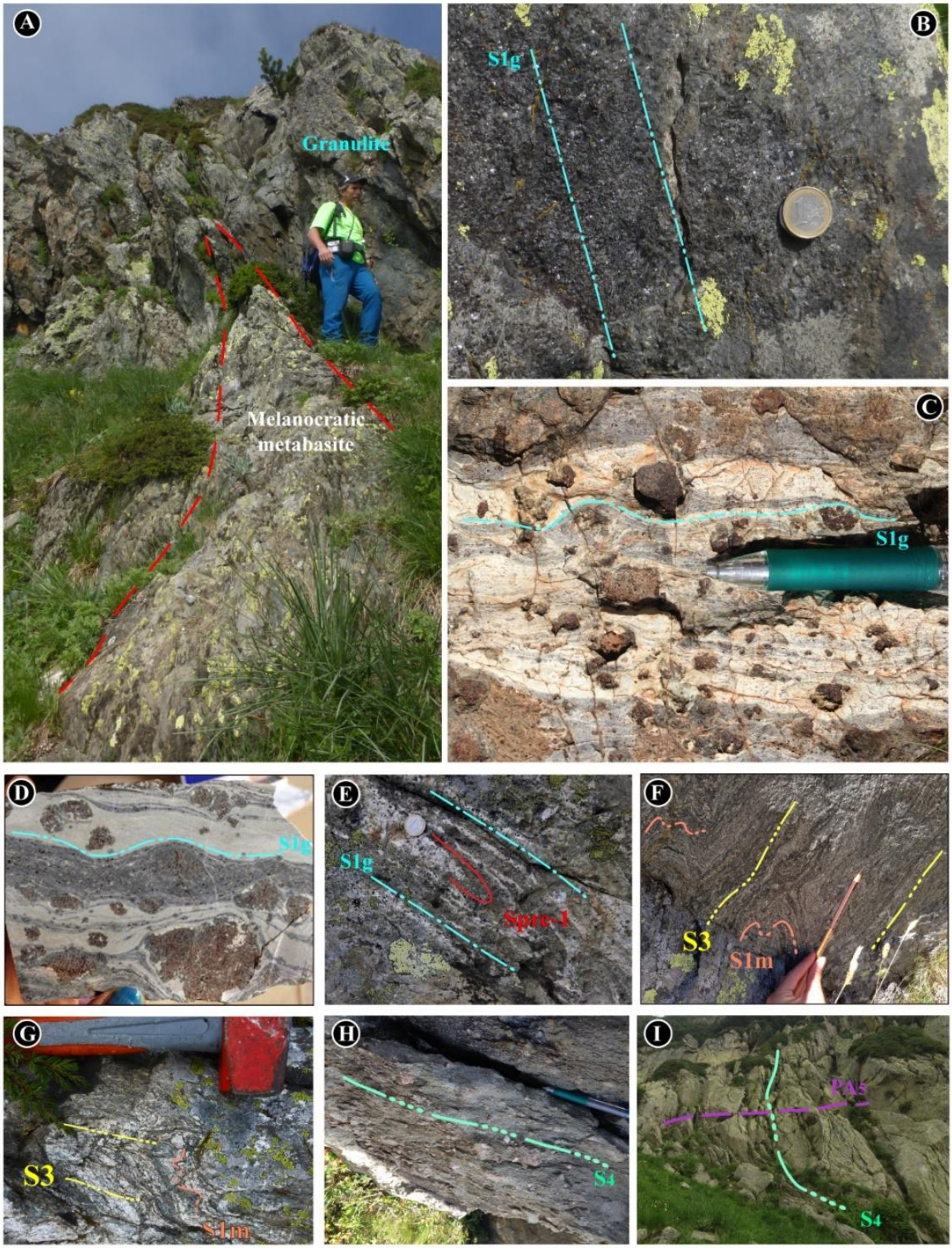

Figure 6.4. Mesostructural analysis. A) Meter-thick and decameter-long melanocratic metabasite lenses within the granulites. B) In the melanocratic metabasites, the S1g foliation is marked by SPO of amphibole and clinopyroxene. C) In the granulites, S1g foliation is marked by compositional layering consisting in millimeter- to centimeter-thick leucocratic and melanocratic levels, wrapping millimeter- to

centimeter-size garnet porphyroblasts. D) Granulites leucocratic levels consist of fine-grained plagioclase with minor biotite, amphibole, and garnet. The melanocratic layers are constituted by fine- to medium-grainsize mineral association of amphibole, clinopyroxene and garnet. E) In the granulites, pre-S1 are folded and transposed along S1g foliation. Pre-S1 are marked by fine-grained clinopyroxene and amphibole. F) and G) In the migmatites, the dominant fabric is the S3 migmatitic foliation that is marked by biotite, amphibole, quartz, and feldspars. S1m foliation is preserved discontinuously within S3 microlithons. H) Metaconglomerates are charaterized by dominant S4 foliation. I) Example of open folds with sub-horizontal axial planes in metaconglomerate.

6.2.1.2 Permian-Triassic metamorphic cover rocks

Metaconglomerates are characterized by angular millimeter- to centimeter-sized clasts mostly consisting of quartz and feldspars. These rocks show fine-grained tectonitic to mylonitic fabrics and the pebbles are elongated parallel to the S4 foliation (Fig. 6.4H). The S4 is defined by chlorite, white mica, biotite, albite, and quartz. Locally fine-grained chlorites mark the foliation, giving a typical greenish color to these rocks. The metaconglomerates are in tectonic contact with the metamorphic basement through ductile to brittle D4 shear zones.

Metavulcanites are medium- to fine-grained foliated rocks and are mostly constituted by quartz and feldspars grains, in an ultra-fine-grained matrix. In the less deformed portions, the original texture is preserved, and they are characterized by a centimetric-thick and fine-grained layering, consisting in reddish and pale levels. Locally, these rocks are characterized by a pervasive S4 foliation, marking the D4 shear zones, underling the tectonic contact with the metamorphic basements.

Carbonatic schists outcrop as decameter-sized elongated bodies in tectonic contact with the migmatites. They are extremely fine-grained and foliated rocks containg calcite, dolomite, opaque minerals and minor phyllosilicates.

Marbles consists in medium- to fine-grained calcite, dolomite, and minor opaque minerals and are characterized by a pervasive S4 foliations. These rocks are in tectonic contact with the migmatites and metavulcanites through steeply dipping brittle faults (Fig. 6.2).

6.2.2 Mesostructural evolution

The relationships between the superposed fabrics and successive mineral assemblages recognized at the mesoscale led to recognize three Variscan (pre-D1, D1, D3) and two Alpine (D4, D5) superposed groups of structures.

6.2.2.1 Variscan

During **D1** the S1 foliation developed. In the melanocratic metabasites, S1g foliation is marked by shape preferred orientation of fine-grained amphibole and clinopyroxene (Fig. 6.4B). S1g in granulites is marked by al millimetre- to centimetre-thick layering consisting of amphibole- and plagioclase-rich levels containing garnet and clinopyroxenes (Figs 6.4C, 6.4D). The S1g foliation in the melanocratic metabasite lens is continuous with the outside foliation in the basic granuiltes. This foliation shows gentle folding in the melanocratic metabasite lens, becaming tighter towards the rim (i.e., clevage refraction mechanism between the two rock types).

Locally, the mylonitic S1g foliation wraps **pre-S1** relicts consisting in aligned fine-grained clinopyroxene and amphibole (Fig. 6.4E). In the metapelitic migmatites, S1m is relict and preserved discontinuously within S3 microlithons (Figs 6.4F, 6.4G). S1m is marked by biotite and amphibole.

D3 stage is characterized by the S3 dominant migmatitic foliation development within the metapelitic and amphibolitic migmatites; S3 is constituted by various amount of biotite, amphibole, quartz, and feldspars (Figs 6.4F, 6.4G). The foliation wraps centimeter- to meter-size diatexite boundis. Figure 5 shows that the contact between granulites and migmatites and S1g foliation are folded, and the associated axial planar foliation is S3.

6.2.2.1 Alpine

D4 is related to the development of ESE-WNW trending shear zones associated with a new S4 foliation marked by Chl+Wm+Bt+Ab, locally overprinted by cataclastic fabric. The D4 developed heterogeneously in the metaconglomerates, ranging from tectonitic to mylonitic fabrics. Increasing the degree of fabric evolution, the millimeter- to centimeter-sized pebbles are flattened, aligned, and boudinaged within the S4 foliation (Fig. 6.4H). The D4 ductile shear zones mark the tectonic contact between metaconglomerate and migmatites. In the metamorphic basement rocks, D4 shear zones mostly reactivate the contacts between granulites and migmatites (Fig. 6.5).

D5 structures consist in N-S and E-W trending brittle faults that mark the tectonic contact between marbles, metavulcanites, and migmatites. In metaconglomerate, open folds with sub-horizontal axial planes occur without formation of new fabrics (Fig. 6.4I).

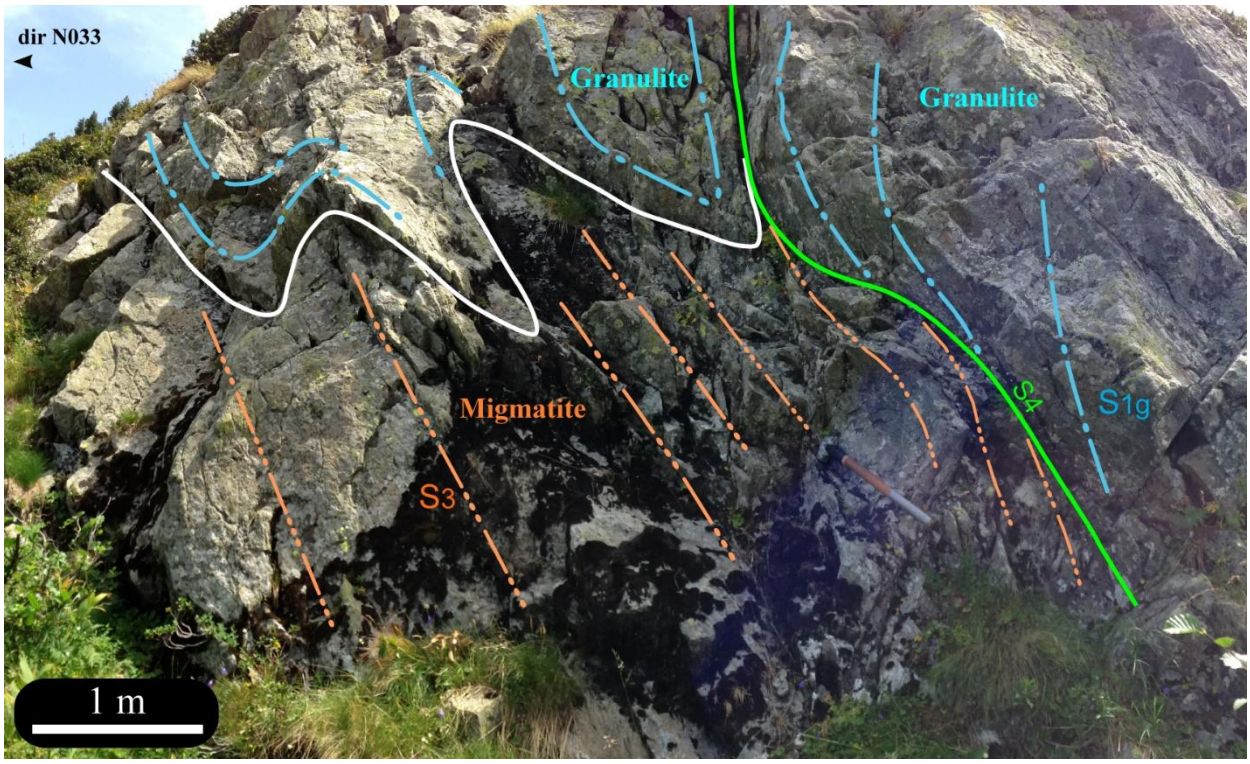

Figure 6.5. Main mesostructural relationships between D1, D3, and D4 structures. The foliation traces and granulite-migmatite contact is shown.

6.3 Microstuctural evolution

6.3.1 Variscan

Pre-D1 mineral relicts are only preserved in melanocratic metabasites and granulites as is shown in Figure 6.6 and 6.7. Millimeter-sized porphyroclast of AmpI, GrtI, and CpxI are observed both in microlithon and cleavage domains showing undolose extinction, exsolution lamellae (Fig. 6.6c, 6.6d), and micro-boudinage (Fig. 6.7c). In the granulites, AmpI and CpxI are observed as inclusion in GrtI porphyroclasts (Fig. 6.7a, 6.7b). In the melanocratic metabasite, 200-300µm sized RtI grains are observed in association with pre-D1 GrtI and CpxI (Fig. 6.6a).

D1 fabric is dominant in melanocratic metabasites and granulites. The melanocratic metabasites show a mylonitic S1 foliation marked by the SPO of AmpII and CpxII in association with GrtII (Fig. 6.6a). This mineral association exhibits a polygonal texture (Fig. 6.6b and 6.6c) which wraps the pre-D1 porphyroclasts and the pre-D1 Cpx-Grt microsites (Fig. 6.6a). TtnI developed a pseudomorphic texture where replacing RtI grains. The granulites show a mylonitic fabric consisting of well-developed millimeter-thick compositional layering (Fig. 6.7a), marked by PlI with polygonal texture (Fig. 6.7e) and by the SPO of AmpII, CpxII, minor PlI and BtI, in Amp-rich and Pl-rich levels, respectively.

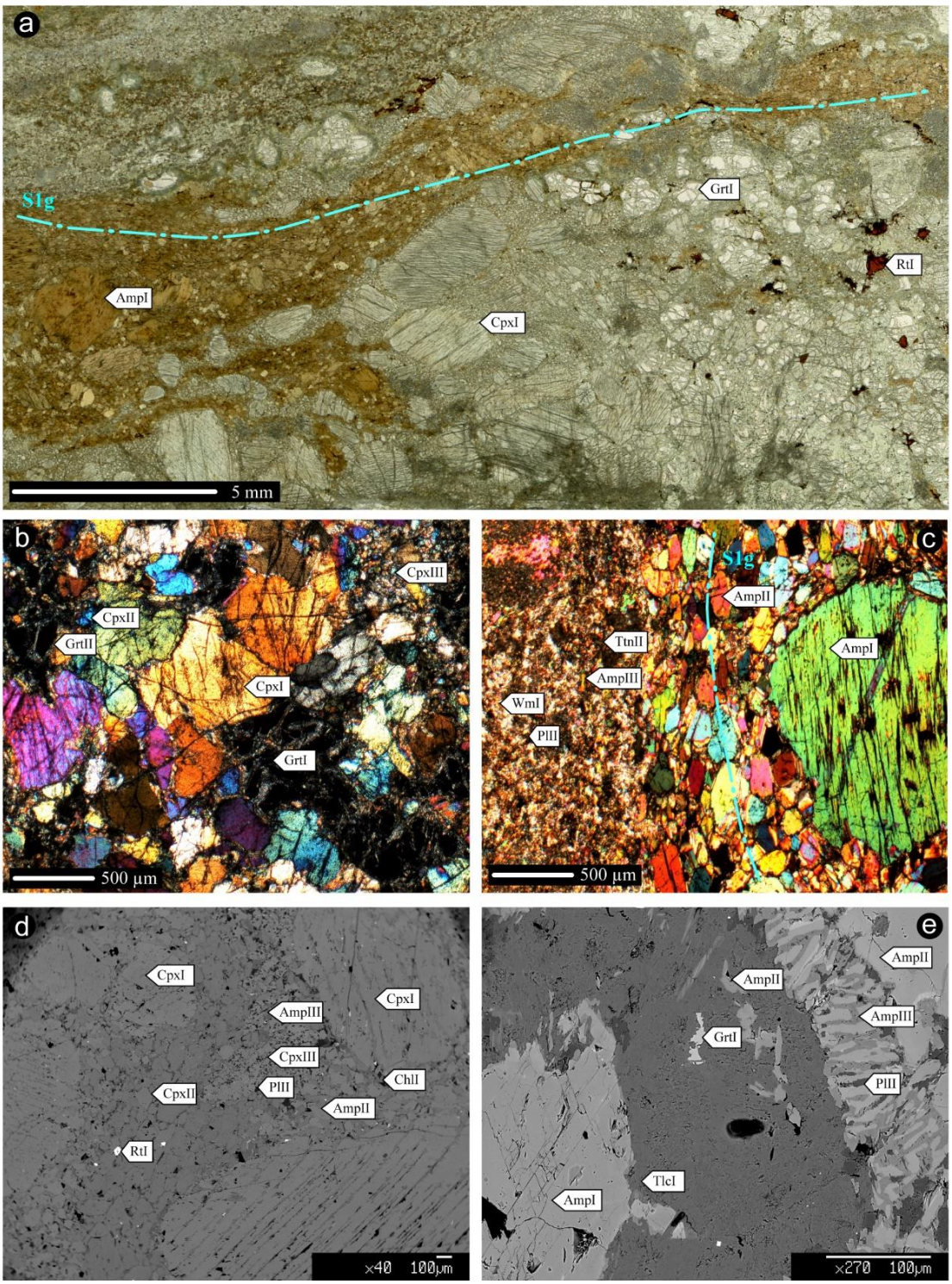

Figure 6.6. Melanocratic metabasites microstructures. a) S1g foliation is marked by SPO of AmpII and wraps AmpI, CpxI, and GrtI porphyroclasts. Millimeter-sized rutile crystals are in contact with CpxI and GrtI. b) Cpx grain-size reduction from pre-D1 to D3 crystals. c) Amp grain-size reduction from pre-D1 to D3 crystals. AmpII, marking the S1g foliation, shows well-definde SPO. d) CpxII and AmpII showing polygonal texture developed between CpxI porphyroclast. Locally, fine-grained mineral association consisting in AmpIII, CpxIII, and PlII developed without preferred orientation. e) D3-related coronae (TlcI + AmpIII + PlII) developed between AmpI and AmpII crystals.

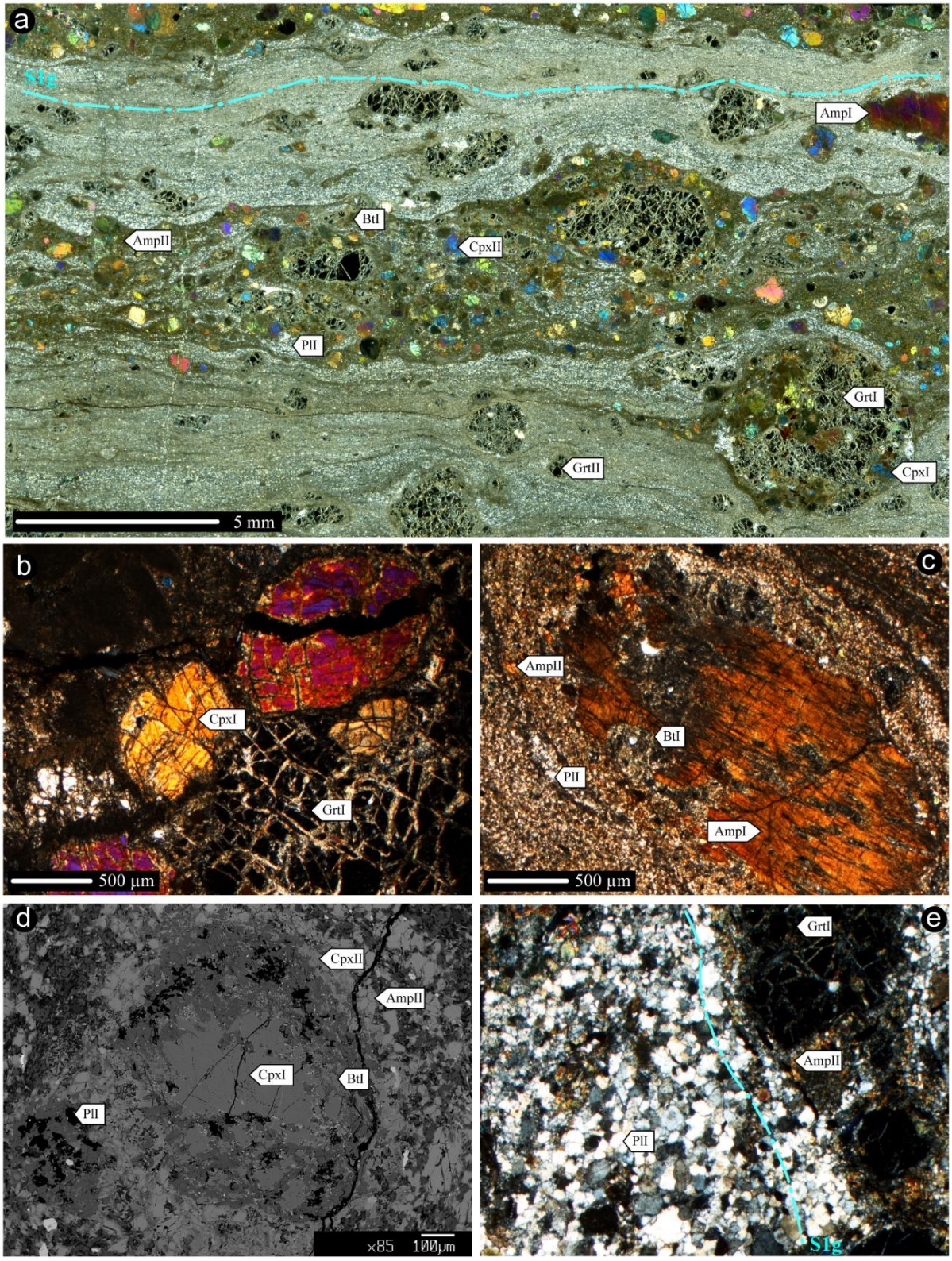

Figure 6.7. Granulites microstructures. a) D1 mylonitic fabric consists of well-developed millimeter-thick compositional layering of Pl-rich and Amp-rich levels. b) The S1g foliation wraps GrtI and CpxI porphyroclasts. c) AmpI porphyroclast is wrapped by S1g foliation consisting in AmpII, and minor PlI and BtI. d) The D1-related corona around CpxI porphyroclast is marked by AmpII, CpxII, BtI, and PlI. e) In the Pl-rich layer, the S1g foliation is marked by polygonal PlI and minor AmpII.

In the melanocratic metabasites and granulites, the **D3**-related metamorphic re-crystallization is poorly developed, and it is mostly defined by coronitic aggregates, that changes as a function of the composition of pre-D3 mineral that replace. In the melanocratic metabasites, AmpIII and CpxIII shows grain-sized reduction and they are in association with PlII and WmI (Fig. 6.6c, 6.6d). Composite corona developed around amphibole porphyroclast, showing TlcI + AmpIII association rimming AmpI porphyroclasts and AmpIII+PlII symplectites rimming AmpII and CpxII grains (Fig. 6.6e). In the granulites, BtII, AmpIII, EpI, and PlII mark coronitic fabric replacing pre-D3 Amp (Fig. 7c), Cpx (Fig. 7d) porphyrpoclasts and Pl-rich domains (Fig. 6.7a).

6.3.2 Alpine

In the granulite the **D4** stage is characterized by the development of coronitic fabrics. Even if the D1 fabrics are still preserved, the D1-related minerals are completely replaced by greenschist-facies mineral assemblages (Fig. 6.8a). The Figure 6.8b shows the pre-D4 garnet that is completely replaced by BtIII, ChlI, TtnII, WmII, EpII, and PlIII. In the metaconglomerate, the matrix consists in QtzI + PlIII (40%), ChlI + WmII +BtIII (40-50%) and minor AmpIV, EpII, and Op. The continuous and 0.5 mm spaced S4 foliation is marked by SPO of BtIII, ChlI and WmII wrapping Qtz-Pl-Kfs pebbles and mineral relict of reddish BtI (Fig. 6.8c, 6.8d). The carbonatic schists consist in 30% of QzI, 30-40% CalI, 10-15% ChlI, 5-10% AmpIV, and minor TtnII and Mag. The S4 foliation is marked by ChlI, AmpIV, TtnII and microlithons consist of QtzI and CalI (Fig. 6.8e). Figure 6.8d shows the preservation of S0 foliation marked by alternating layers of Cal-rich and Dol-rich levels. The axial plane is defined by SPO of recrystallized CalI grains at high angle with respect to the dolomite-rich levels.

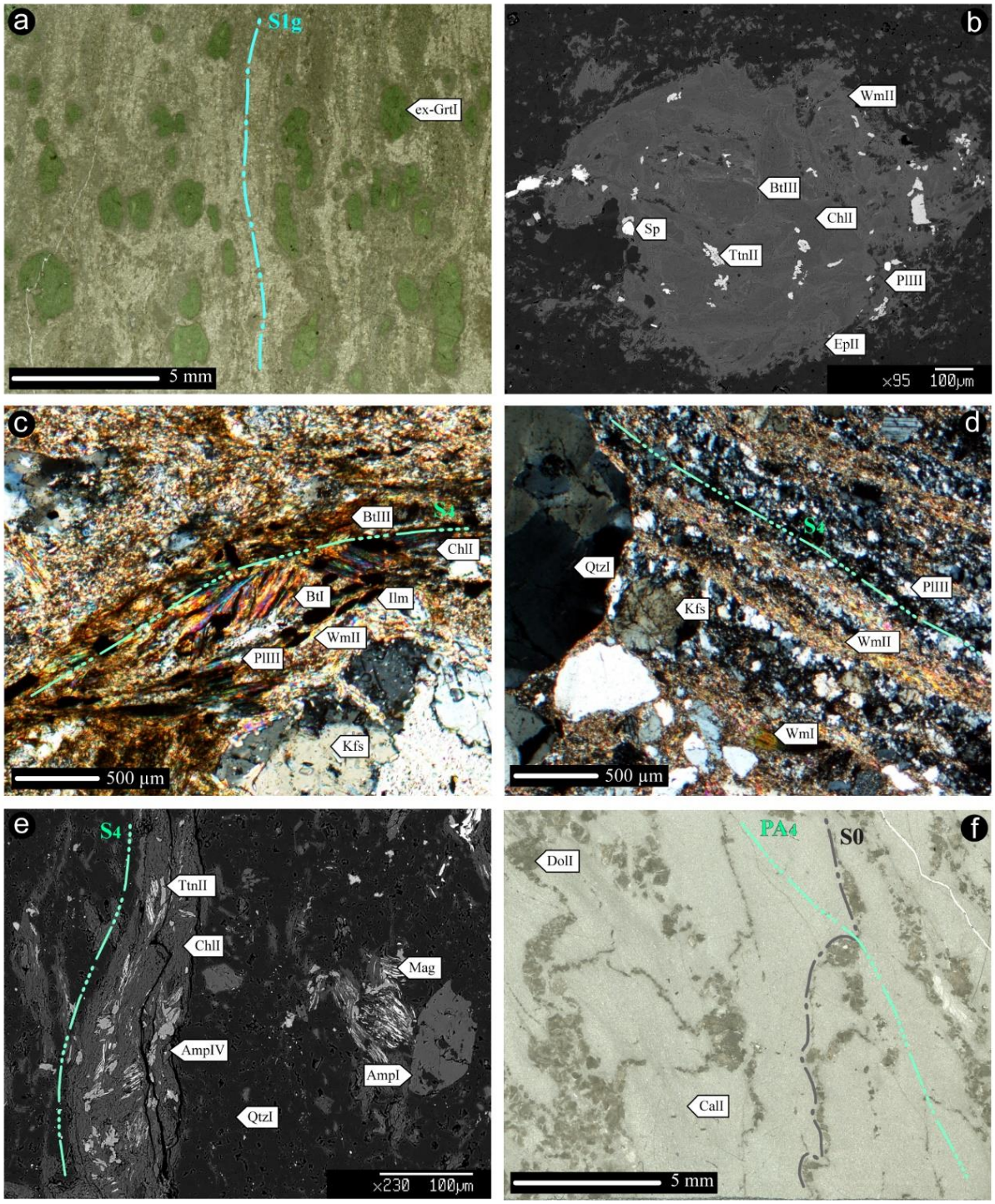

Figure 6.8. Alpine microstructures. a) In granulites, the D1 fabric is preserved but the GrtI are completely replaced by D4-related mineral assemblages. b) Example of granulite GrtI that are replaced by ChlI, BtIII, TtnII, PlIII, EpII, and WmII. c) Metaconglomerates are characterized by S4 foliation marked by BtIII, ChlI, WmII wrapping Qtz-Pl-Kfs pebbles and BtI relict. d) Continuous and spaced S4 foliation in metaconglomerates. e) In carbonatic shists, the S4 foliation is marked by AmpIV, ChlI, and TtnII that isolate QtzI and CalI microlithons. f) In marbles, S0 consisting of Dol-rich and Cal-rich layers is folded during D4 stage.

6.4 Mineral chemistry

WDS mineral chemical analyses were acquired based on the reconstructed mineral-growth sequence for each deformation stage using JEOL 8200 EMPA Super Probe – EMPA with voltage of 20 kV, current of 1.70 Å, and beam sizes of 5µm. Natural silicates were used as standards and matrix corrections were calculated with ZAF (Z=atomic number, A=absorption, F=fluorescence) procedure (Armstrong & Buseck, 1975). Mineral formulae of amphibole and clinopyroxene were calculated following Locock (2014) and Morimoto (1988), respectively. All other mineral formulae were calculated according to Deer et al. (1992) with jPTgui software (Zucali, 2005). The stoichiometric formulae are based on 23 oxygen atoms for Amp, 6 oxygen atoms for Cpx, 12 oxygen atoms for Grt, 22 oxygen atoms for Wm and Bt, 8 oxygen atoms for Fsp, 2 oxygen atoms for Carb, and 14 oxygen atoms for Chl.

6.4.1 Variscan metamorphic basements

Amphibole. In both melanocratic metabasites and granulites, pre-D1 amphibole displays compositions ranging from pargasite to edenite (Fig. 6.9a, 6.9b) with similar XMg. In melanocratic metabasites, AmpI is higher in Na and Ti contents and lower in Al and Si contents than AmpI in granulites (Fig. 6.9c). In the melanocratic metabasite, the D1-related amphiboles show variable compositions between edenite and pargasite endmembers. Within this broad composition, AmpII shows chemical variations depending on the microsites where it developed. AmpII replacing AmpI porphyroclast shows the highest Si, Al, and Na contents with respect to those marking the S1 foliation; the latter characterized by Al and Na depletion and Ti enrichment (Fig. 6. 9). Whereas, the AmpII in granulites shows well-defined pargasite composition characterized by the highest Si content.

In both rock-types, the D3-related amphiboles show large chemical variations, within the edenite composition field. The chemical variations are controlled by the microsite where amphiboles developed. AmpIII coronitic around AmpII is high in Na, Si, and Al contents and lower in Ti content than AmpIII developed in association with CpxIII and/or replacing the D1-related mineral assemblage. The D4-related amphiboles are clustered in the actinolite compositional field (Fig. 6.9).

Clinopyroxene. In the melanocratic metabasites, Cpx are mainly diopside (Fig. 6.9d). Cpx shows enrichment in Mg content and depletion in Na and Fe content from CpxI to CpxIII. Cpx with the highest Fe^{3+} contents developed in the pre-D1garnet-clinopyroxene microsite. In the granulites, pre-D1 Cpx are omphacite displaying Jd content ranging between 25% and 37%, whereas Na contents progressively decrease in CpxII and CpxIII (Fig. 6.9d).

Garnet. In the melanocratic metabasites, the analyzed garnets show a progressively decrease in Mg content (1.32-1.67 a.p.f.u.) and increase in Fe (0.93-1.16 a.p.f.u.) content from GrtI to GrtII suggesting a transition from type A to type B eclogites (Fig. 6.9e; Coleman et al., 1965). The GrtII developed in association with AmpII and CpxII shows enrichment in Ca content. In the granulites, the GrtI are characterized by higher Fe content and lower Mg content than the GrtII showing a transition from type C to type B eclogites (Fig. 6.9e; Coleman et al., 1965).

Biotite. In both rock-types, analyzed biotite shows a similar XMg ranging from 0.5 to 0.7 and are characterized by progressively decrease in Ti content from D1-related (0.48-0.53 a.p.f.u.), D3-related (0.21-0.38 a.p.f.u.) to D4-related (< 0.18 a.p.f.u.) biotites (Fig. 6.9f).

Feldspars. In the basic granulite, the D1-related plagioclase cover the anorthite and bytownite compositional fields. In both rock-types, Na content progressively increase from D3-related to D4-related plagioclase covering oligoclse and albite compositional field, respectively (Fig. 6.9g).

6.4.2 Permian-Triassic metamorphic cover rocks

Biotite. In the mylonitic conglomerates, biotite shows similar XMg (0.37-0.42) and Al^{IV} content enrichment from relict grains (0.5-0.7 a.p.f.u.) to D4-related grains (up to 1.32 a.p.f.u.; Fig. 6.10a). Bt relicts show higher Ti content (0.2-0.4 a.p.f.u.) than BtIII (0.02-0.18 a.p.f.u.) marking the S4 foliation (Fig. 6.10b). In the carbonatic schists, the BtIII are phlogopite in composition with the highest XMg and lowest Al^{IV} content (0.26-0.45 a.p.f.u.).

White mica. In all rock types, Si^{4+} content progressively varies in relation with the microstructural site (Fig. 6.10c). Wm porphyroclasts are characterized by the highest Si^{4+} contents (6.7-6.9 a.p.f.u.) and lowest Al (2.2-4.1 a.p.f.u.). The WmII developed as pseudomorphs on relict WmI grains with Si^{4+} content varying from 6.38 to 6.73 a.p.f.u. and Al content varying from 4.11 to 4.93 a.p.f.u.. WmII along the S4 foliation displays Si^{4+} content varying from 6.11 to 6.32 a.p.f.u. and Al content varying from 4.92 to 5.97 a.p.f.u..

Carbonate. Calcite and dolomite occur in carbonatic schists and marbles. Figure 6.10d shows that the calcite and dolomite are characterized by Ca content enrichment in the carbonatic schists.

Chlorite. In the metaconglomerates, chlorite marking D4 fabrics covers the brunsvigite, ripidolite, and pycnochlorite compositional fields (Fig. 6.10e, 6.10f) and is characterized by Si content varying from 5.6 to 6.1 a.p.f.u. and XFe ≈ 0.58 a.p.f.u. In the other rock-types, chlorites are ripidolite-pycnochlorite in composition and Si content varies from 5.1 to 6.2 a.p.f.u. and XFe between 0.23 and 0.38.

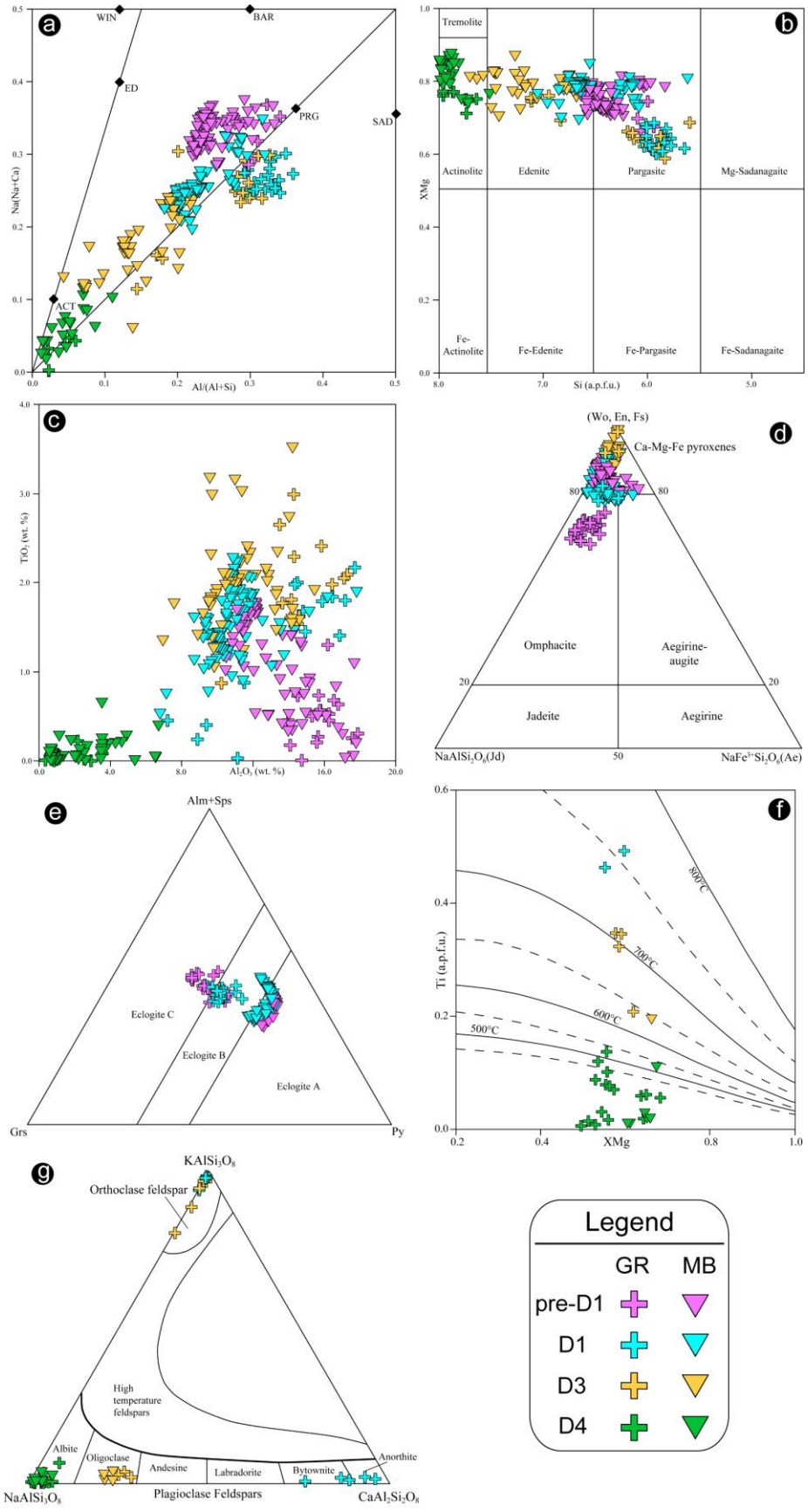

Figure 6.9. Mineral chemistry of Variscan metamorphic rocks (GR: basic granulite; MB: melanocratic metabasite). a) Al/(Si+Al) vs. Na/(Na+Ca) diagram showing the compositional variation of Amp. Diamonds locate end-member compositions (ACT=actinolite; BAR=barroisite; ED=edenite; GL=glaucophane; KTP=katophorite; PRG=pargasite; SAD=sadanagaite; WIN=winchite). Straight lines define high-pressure (HP) and intermediate pressure (IP) amphibole trends from Vermont (after Laird and Albee, 1981). b) Si vs. XMg diagram showing the compositional field of Ca-Na Amp. c) Al_2O_3 and TiO_2 variations in Amp. d) Ternary diagram showing the compositional variation of Cpx in terms of Jd-, Ae-, and Ca-Mg-Fe-endmembers. e) Ternary diagram showing the Grt compositional variations in terms of Grs-, Py-, and Alm+Sps-endmember. Eclogite A-, B-, and C-type field are shown (after Coleman et al., 1965). f) diagram showing the Bt chemical variation in XMg and Ti content; temperature estimation is after Henry et al., (2005). g) Ternary diagram showing the Fds compositional variations in terms of Kfs-, An-, and Ab-endmember.

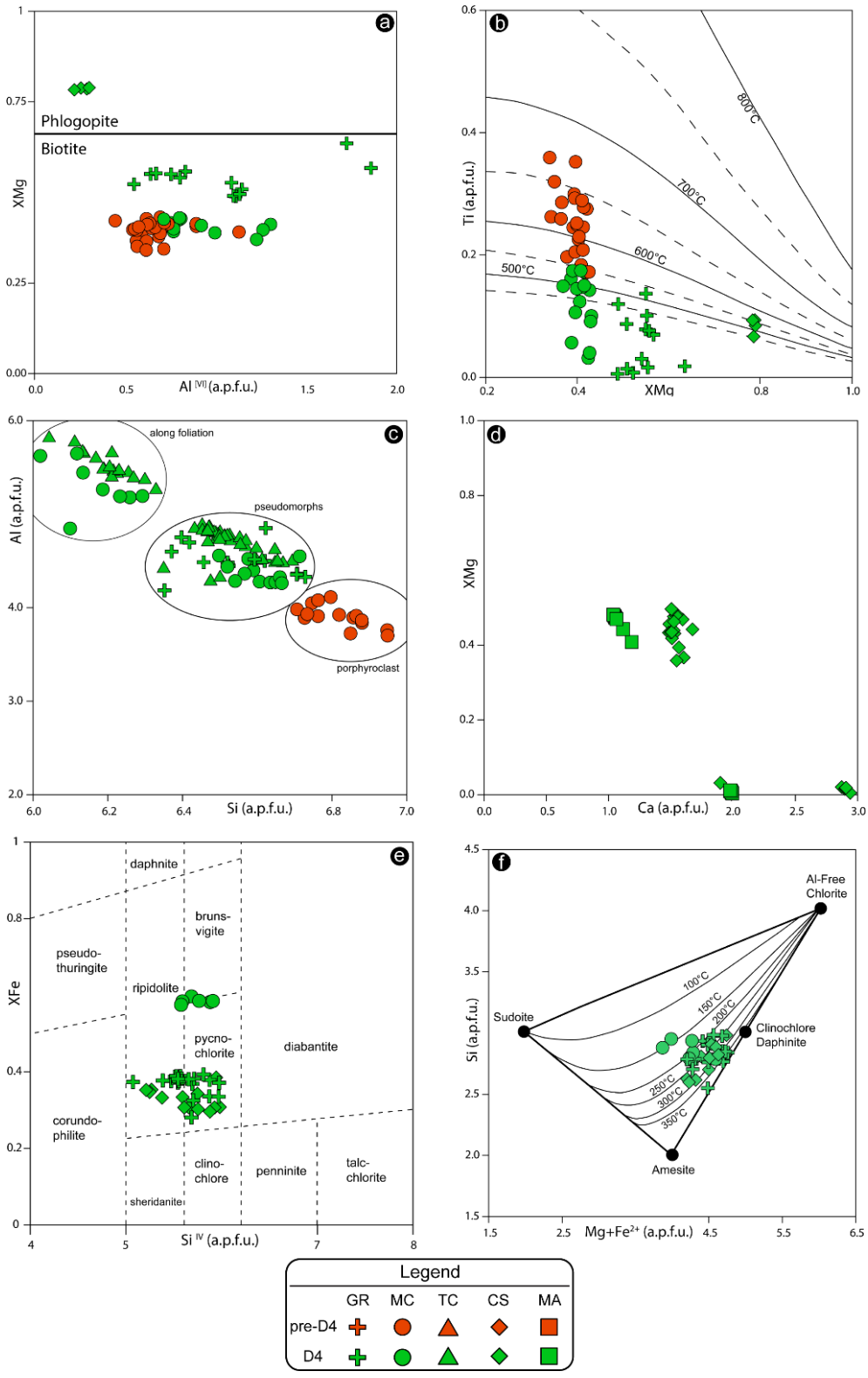

Figure 6.10. Mineral chemistry of metamorphic cover rocks (MC: mylonitic conglomerate; TC: tectonitic conglomerate; CS: carbonatic shist; MA: marble) and retrocessed basic granulite (GR). a) Al^{IV} vs. XMg diagram showing the compositional variation of Bt. b) diagram showing the Bt chemical variation in XMg and Ti content; temperature estimation is after Henry et al., (2005). c) variations of Si and Al contents in Wm. d) XMg and Ca variations in carbonates. e) Si-XFe binary diagram for chlorite (after Hey, 1954). f) variation in $Mg+Fe^{2+}$ and Si in Chl; temperature estimation is after Bourdelle et al. (2013).

6.5 Bulk rock chemical analysis

Three melanocratic metabasites, three granulites, leuco- and mafic-layers of granulites were analyzed for bulk rock chemical composition (Fig. 6.11). Element concentrations were obtained at the "Bureau Veritas Commodities Canada Ltd." at the Bureau Veritas ACME Laboratory (Krakow, Poland). Powders were analyzed and calibrated with international geostandards. Major and trace elements were analyzed using Inductively Coupled Plasma Emission Spectroscopy (ICP-ES) and Inductively Coupled Mass Spectrometry (ICP-MS), respectively. Analytical conditions and results are presented in Appendix G.

Major element chemistry covers gabbro and monzo-gabbro compositional fields for the melanocratic metabasites and granulites, respectively (Fig. 6.11a). SiO_2 content vary from 45 wt.% in the metabasites to 53 wt.% in the leucocratic layers in granulites, according to increasing of plagioclase amount in the granulites samples. Figure 6.11b shows the relationships between MgO and SiO_2 in the analyzed samples and the comparison with the subduction-related ophiolite (Dilek and Funes, 2011; *i.e.*, volcanic arc and Supra Subduction-Zone types). According to Dilek and Funes (2011), the MgO-SiO_2 suggests that all samples could be interpreted as subduction-related ophiolites (Fig. 6.11b). In particular, the granulites could be oceanic back-arc ophiolites (OBA) and the melanocratic metabasites show back-arc to forearc ophiolite (BA-FA) compositions. In the discriminant diagrams (Figs 6.11c and 6.11d) metabasites plot between the field of N-MORB and tholeiitic basalts, whereas the granulites show affinity with calc-alkaline basalts (Fig. 6.11c). The diagrams proposed by Saccani (2015) are useful to decipher the effects of crustal contamination on fractional crystallization and on the MORB-OIB affinity variation. In Figure 6.11d, the melanocratic metabasites plot into MORB compositional field and affinity with back-arc setting. Whereas the granulite samples plot outside the MORB-OIB array suggesting crustal contamination within convergent plate settings.

Figure 6.11e shows MORB-normalized multi-element diagrams. The analyzed sample have similar trend, with melanocratic metabasites being lower in most elements. All the samples cover the subduction-related field proposed by Dilek and Furnes (2011). The granulite samples are comparable with the data presented by Rubatto et al. (2010). Normalized patters show variations of the LREE/HREE ratio, with samples with a ratio >1 and <1, compatible with an E-MORB and N-MORB trends, respectively. A marked positive anomaly for Pb, Rb, and U and trends with Sr, Nb, Ta and Ba depletions are presents. The granulite samples are the richest in incompatible elements, whereas the melanocratic metabasites are enriched in compatible elements such as Cr and Ni. These trends may suggest a crustal contamination (Donnelly et al. 2004) due to partial melting of their country rocks during exhumation re-equilibrations.

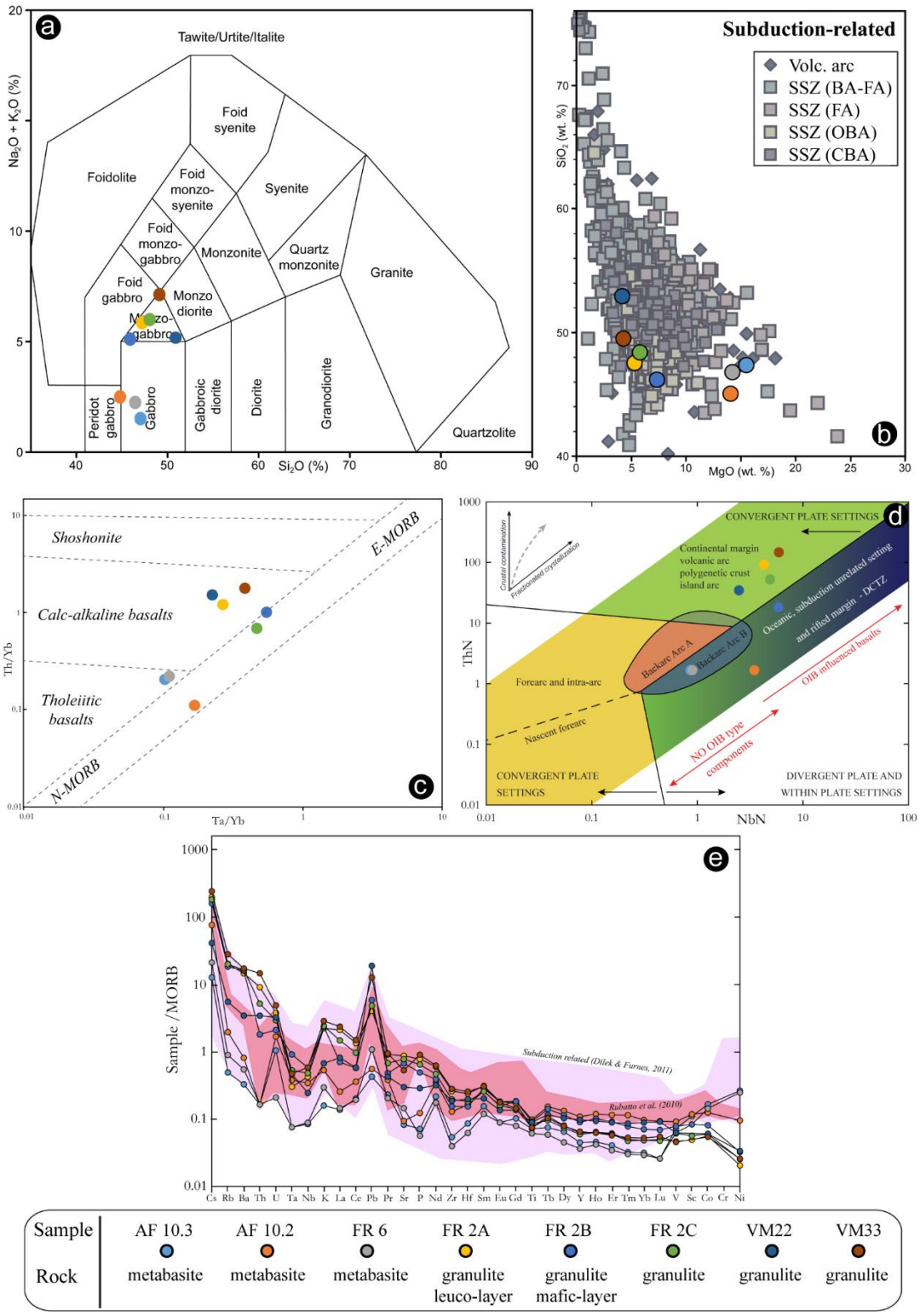

Figure 6.11. Bulk rock chemical analysis. a) Metabasite and granulite samples plotted on TAS diagram (modified after Middlemost, 1985). b) MgO and SiO_2 compositions showing subduction-related ophiolite origins (after Dilek and Funes, 2010). c) Chemical compositions of analyzed samples in the Th/Yb vs. Ta/Yb (after Pierce, 1982). d) Chondrite normalized Th-Nb diagram (after Saccani, 2015). e) Mid-ocean-ridge basalt (MORB)–normalized multi-element diagrams; subduction-related field is shown (violet area; Dilek and Funes, 2010); compositional variation field of Rubatto et al. (2010) is shown (red area).

6.6 Rutile U-Pb geochronology

The melanocratic metabasites contain several rutile crystals with dimension varying from 100 to 800 μm (Fig. 6.12a and 6.12b). Microstructurally, rutile crystals are in association with the pre-D1 mineral phases, such as garnet, pyroxene, and amphibole. Locally, titanite replacement occurs at the rim of rutile crystal which are in contact with D1-related mineral assemblage (Fig. 6.12b). Rutile crystals show no evidence of zonations and they are characterized by U content varying from 7.71 to 12.70 ppm, Pb^{206} content of 1.84-3.39 ppm, and Pb^{207} content ranging from 0.12 to o.25 ppm.

The rutile crystals can be dated using U-Pb method thanks to the uranium ionic radius and charge comparable with Ti^{4+}. However, for consistent results it is advisable to analyze rutile with U content major than 7 ppm. The dating method can be affected by the occurrence of high contents of common Pb (Bracciali et al., 2013). Based on diffusion experiments on natural and synthetic rutile with different trace element pattern, Cherniak (2000) calculated closure temperature of ~650 °C for rutile grains of ~100 μm size. Following the dating procedure proposed by Bracciali et al. (2013), U-Pb LA-ICP-MS analysis, with spot size of 35 μm, are performed to obtain absolute chronological constrain for pre-D1 stage. The 15-analysis returned Carboniferous age defining a Concordia age of 326.1±4.4 Ma (Fig. 6.12c). In the Figure 6.12d, the $^{238}U/^{206}Pb$ vs. $^{207}Pb/^{206}Pb$ diagram is proposed, which shows how the fitting curve of common Pb content intercepts the Concordia age. The analytical data reflect mixing between radiogenic Pb and common Pb and error ellipses for several spots do not overlap the trend and appear older (Figure 6.12d).

A probability density curve (Figure 6.12e), calculated by Isoplot/Ex (Ludwing, 2001), shows a doublet with a main peak at 334±6 Ma and a smaller satellite peak at 310±6 Ma. The curve is obtained by summing the probability distributions of the 15 rutile analyses and is plotted with a histogram of the data. The older peak may be inticate the minimum age of rutile crystallization in equilibrium with the pre-D1mineral assemblage. The shoulder at the younger ages may be the effect of system reopening at temperatures higher than 650°C and therefore indicate the minimum age for thermal rebalancing referred to the successive tectono-metamorphic stages.

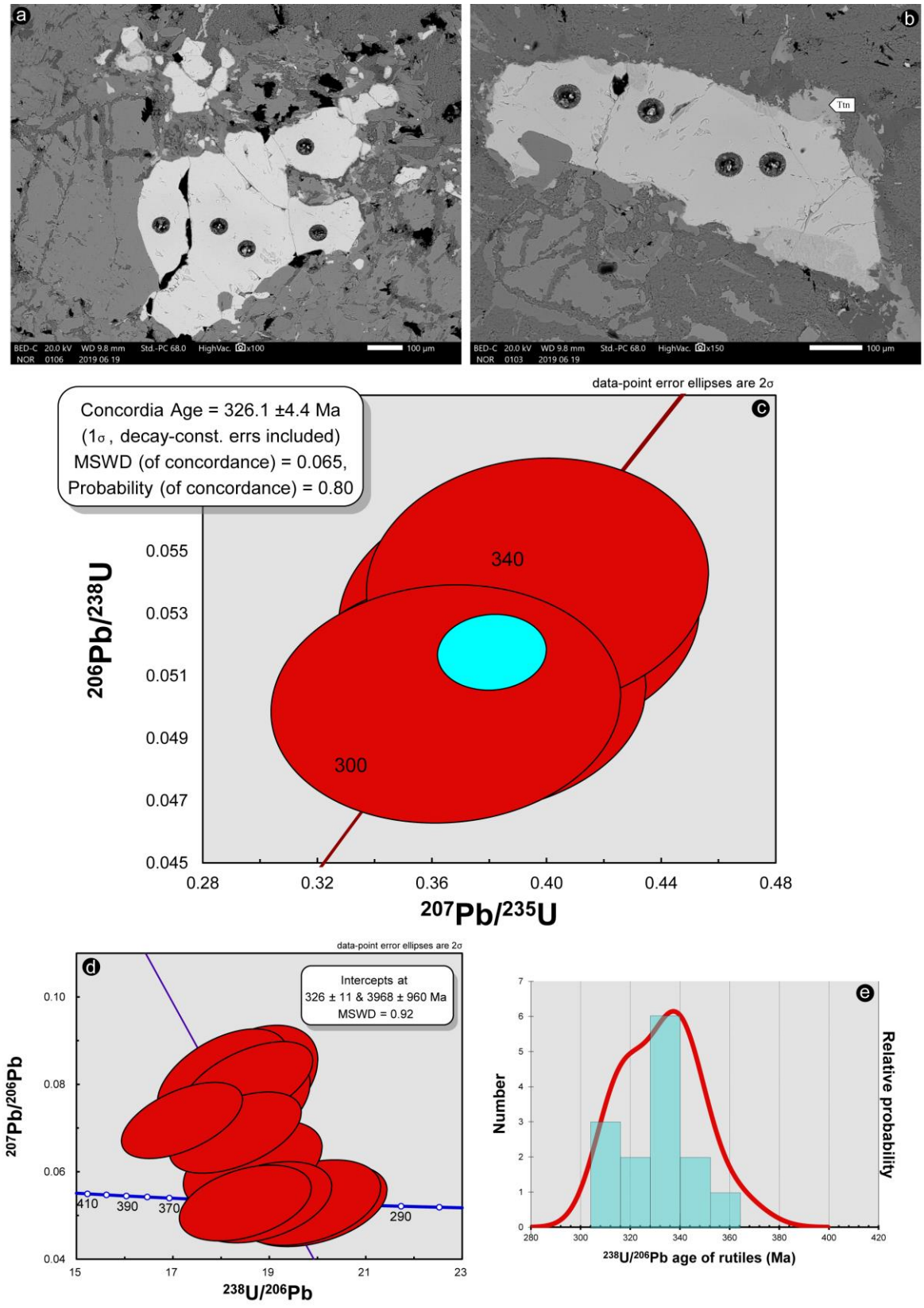

Figure 6.12. BSE image of analyzed rutile (a, b); circles indicate LA-ICP-MS analyses for trace elements. C) U-Pb dating results show concordant data (red filled ellipses) and the Concordia age (light-blue filled ellipse) D) The purple Pb common fitting curve intercept the Concordia age (blue thick-line). E) Relative probability diagram of the analyses.

6.7 Metamorphic conditions

Microstructural analysis shows evidence of superposed structural and metamorphic re-equilibrations allowing the individuation of mineral assemblage sequences. Microstructural analysis also allows to constrain favorable microsites showing grain-scale equilibrium. In this view, thermobarometric estimates have been performed to infer the PT conditions under which the successive tectonometamorphic stages developed. For each paragenesis, physical conditions of metamorphism were performed using: 1) well-constrained geothermobarometers to mineral pairs in mutual contact with rational grain boundaries, indicating textural equilibrium; 2) average PT using the Thermocalc thermodynamic dataset on the basis of the activity of end-members calculated by AX software (Holland and Powell, 1998); 3) calculation of equilibrium fields in pseudosection using Perple_X (Connolly, 2005). The results obtained for each stage are shown in Figures 6.13, 6.14, and 6.15.

Pre-D1 stage. Pseudosection has been used to constrain PT conditions in melanocratic metabasites (Fig. 6.13). Composition was chosen starting from the whole rock analysis (*e.g.*, CNFMASHT compositional systems) and the K_2O amount was not considered, as biotite and K-feldspar occur as interstitial grains suggesting contamination due to successive country rocks partial melting. Perple X software (Connolly, 1990, 2005) was used adopting gridded Gibbs free-energy minimization approach (Connolly, 2005). The thermodynamic database of Holland and Powell (2001) was used. The mineral solution models are garnet, staurolite, cordierite, orthopyroxene, and melt after White et al. (2014); feldspar (Fuhrman & Lindsley, 1988); clinopyroxene after Holland and Powell (1996); Amphibole after Dale et al. (2005).

The mineral assemblage includes Grt, Cpx, Amp, and Rt and is predicted to be sable in PT conditions ranging from 1.56 to 1.94 GPa and 709 to 761°C (Figure 6.13 and Table 6.2). This field is bounded by the appearance of Opx and disappearance of Amp towards higher temperatures, the presence of Ta at higher pressure, the stability of Pl at lower pressure, and the appearance of Ky towards lower temperatures.

D1 stage. In melanocratic metabasites, mylonitic fabric consists of AmpII, CpxII, GrtII, TtnI, and PlI. The Thermocalc average PT calculation suggests a P=1.4 ± 0.2 GPa and a T = 794 ± 25 °C. Pressures of 1.2 ± 0.1 GPa are estimated with the barometer Grt-Amp-Pl (Kohn & Spear, 1990). Temperatures of 781 ± 18 and 775± 25 are suggested by the Grt-Amp (Krogh & Ravna, 2000) and Grt-Cpx (Krogh, 1988) thermometers, respectively. In granutiles, D1 parageneses consists of AmpII, CpxII, PlI, BtI, and TtnI. Pressures of 1.4 ± 0.1 GPa and temperatures of 775 ± 15°C are obtained with Thermocalc average PT calculation. The Grt-Amp-Pl barometer proposed by Kohn & Spear (1990) indicates P =

1.5 ± 0.1. Temperatures of 779 ± 37 and 771 ± 8 are suggested by Grt-Cpx (Krogh, 1988) and Grt-Amp (Krogh & Ravna, 2000) thermometers, respectively.

The inferred metamorphic conditions are synthesized in Figure 6.14 and Table 6.2, with standard deviations obtained from the different thermobarometric calibrations, in melanocratic metabasites and granulites. Figure 6.14 shows D1 cluster ranging from *P*=1.22-1.54 GPa and *T*=762-824°C.

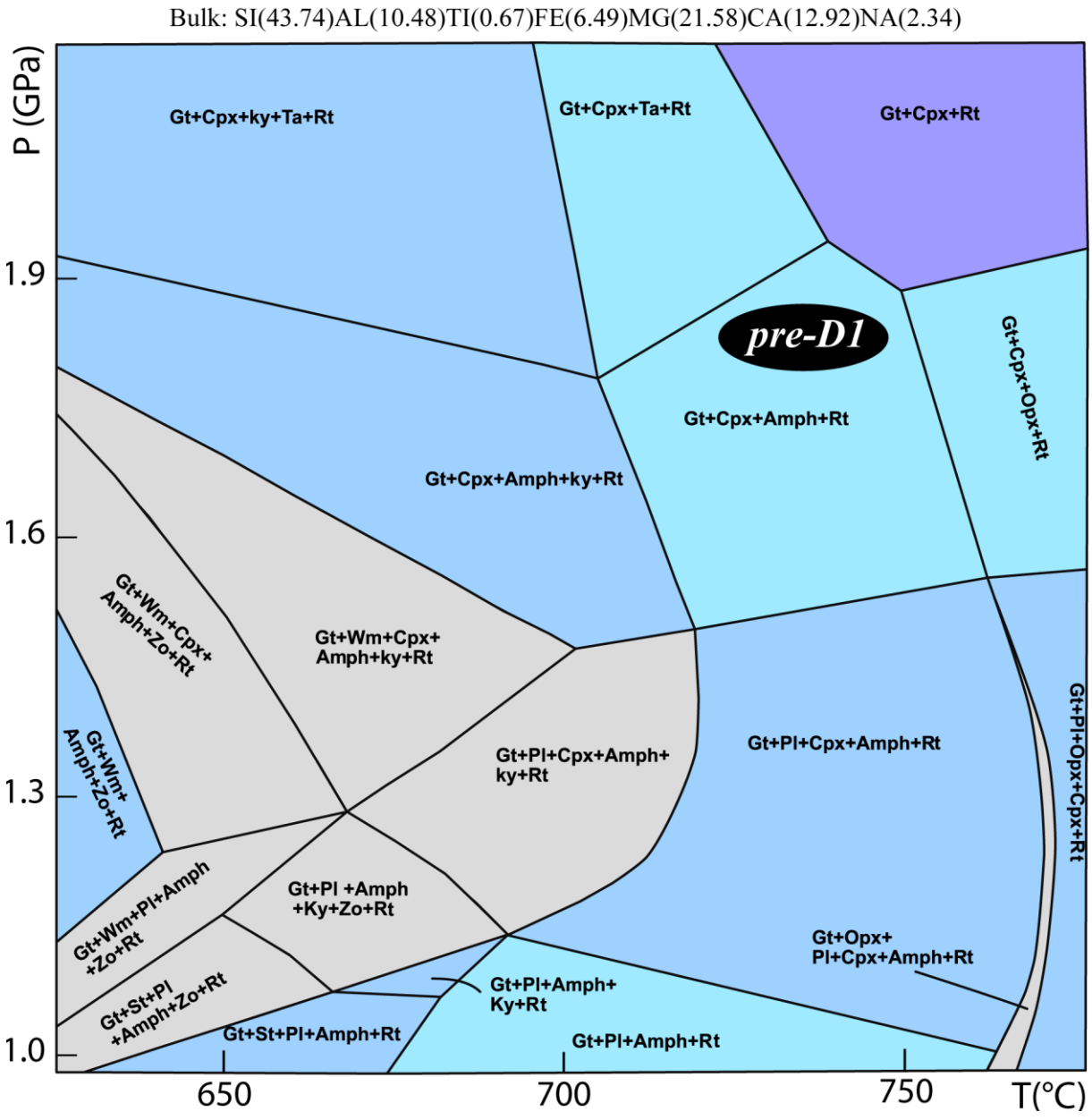

Figure 6.13. Pseudosection performed with Perple_X for melanocratic metabasites. The bulk rock composition (in molar amount) is SiO_2 and H_2O = saturated, Na_2O=2.34, CaO=12.92, FeO=6.39, MgO=21.58, Al_2O_3=10.48, TiO_2=0.67. Variance fields: purple=7; light blue=6; blue=5; grey=4. Pre-D1 metamorphic assemblage stability field is shown.

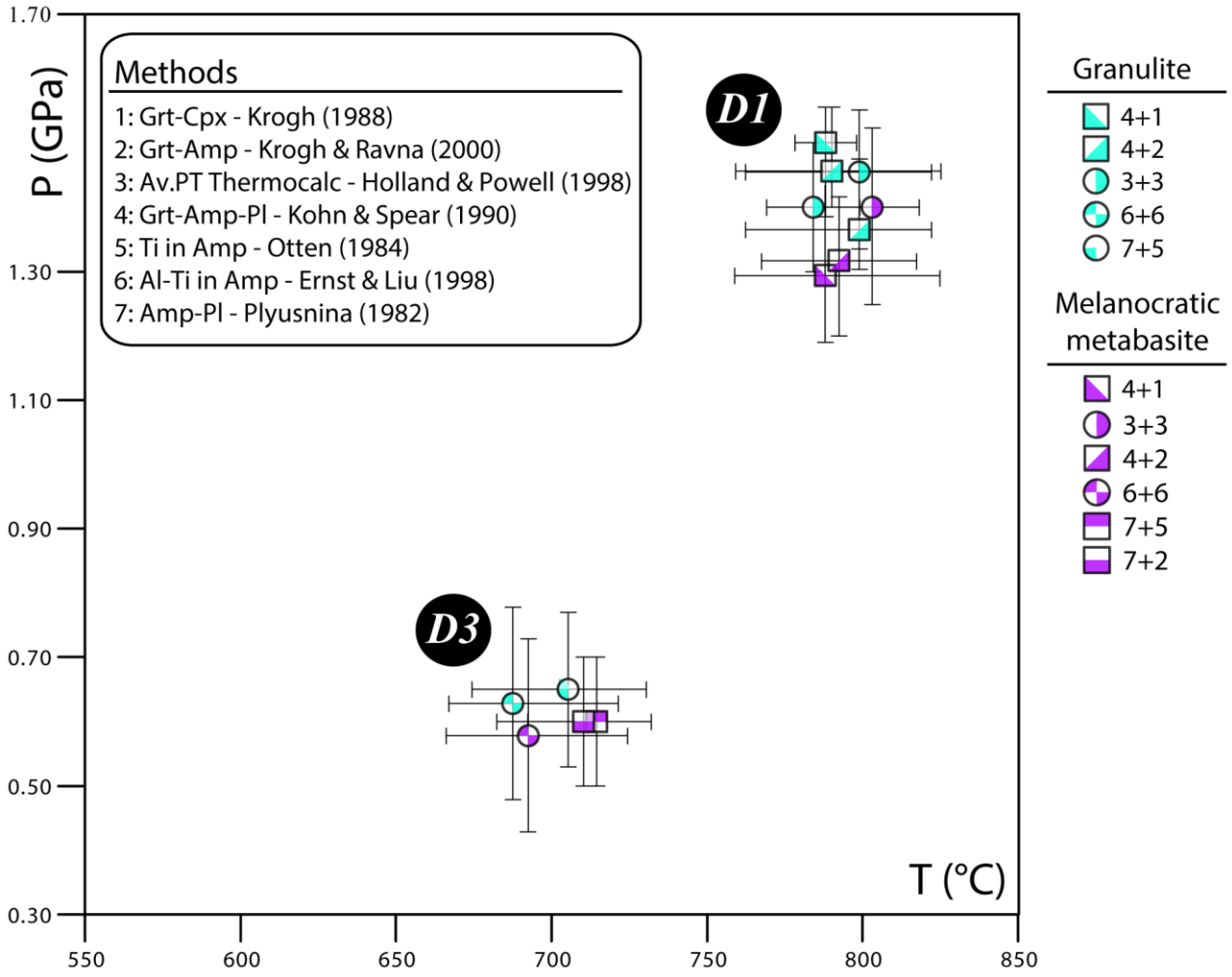

Figure 6.14. D1-D3 P-T estimates of melanocratic metabasites and granulites inferred from relative timing of fabrics and metamorphic assemblage superposition. The geothermobarometers are shown in the legend enclosed.

D3 stage. In the melanocratic metabasites, the D3-related mineral assemblage is AmpIII, CpxIII, PlII, and WmI. Al-Ti contents in amphiboles (Ernst and Liu, 1998) suggest P = 0.55 ± 0.15 GPa and T = 690 ± 32°C. Following Plyusnina (1982) barometer, pressures of 0.55 ± 0.1 GPa are estimated. Temperatures of 709 ± 22°C and 693 ± 28°C are suggested by Ti in Amp (Otten, 1984) and Grt-Amp (Krogh & Ravna, 2000) thermometers, respectively.

D3 in granulites is associated with the mineral assemblage constituted by BtII, AmpIII, EpI, and PlII. Al-Ti contents in amphiboles (Ernst and Liu, 1998) suggest P = 0.65 ± 0.1 GPa and T = 700 ± 31°C. Pressures of 0.6 ± 0.15 are estimated using Amp-Pl barometer (Plyusnina, 1982). Ti in Amp (Otten, 1984) suggests temperatures of 715 ± 20°C.

Figure 6.14 and Table 6.2 show the inferred metamorphic conditions, with standard deviations, for melanocratic metabasites and granulites. The PT conditions vary from *P*=0.45-0.76 GPa and *T*=665-735°C.

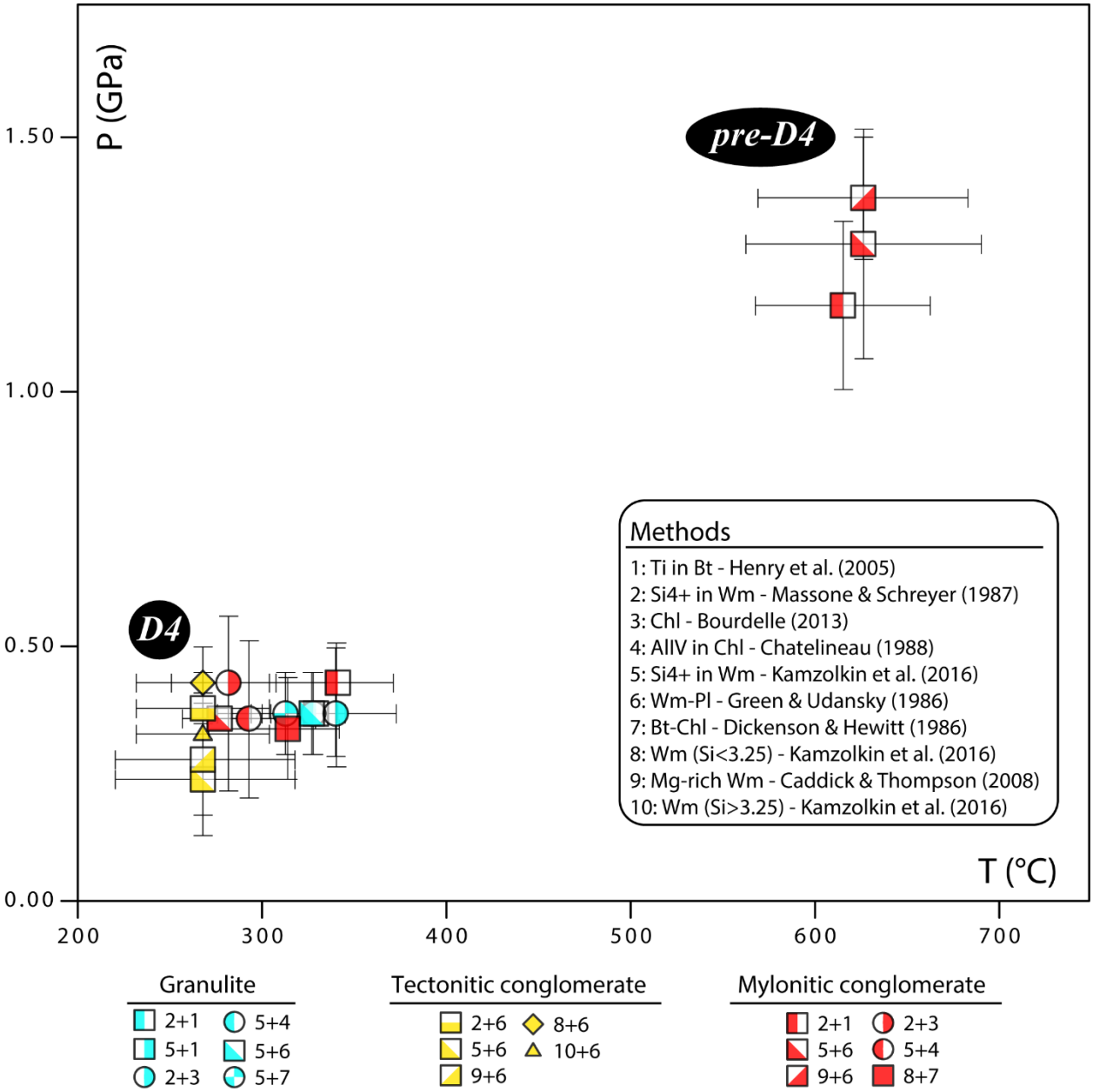

Figure 6.15. pre-D4 (detrital Bt and Wm grains) and D4 P-T estimates of metaconglomerates and pervasively re-equilibrated granulites inferred from relative timing of fabrics and metamorphic assemblage superposition. The geothermobarometers are shown in the legend enclosed.

D4 stage. In the pervasively D4 re-equilibrated granulites, the coronitic fabrics consist of BtIII, ChlI, TtnII, WmII, EpII, and PlIII. The Si4+ content in phengitic mica (Massone and Schreyer, 1987) indicates *P* = 0.3± 0.1 GPa for *T* interval derived by the Ti in Bt (Henry et al., 2005) thermometer that suggests *T*=300±50°C. The Chl thermometer of Bourdelle (2013) suggests temperatures of 290±30°C

and Al^{IV} content in Chl thermometer (Chatelineau, 1988) indicates T = 328±26°C. Pressures of 0.31±0.2 GPa are estimated using Wm barometer (Kamzolkin et al., 2016).

In the metaconglomerates, the D4-related mineral assemblage is marked by QtzI + PlIII + ChlI + WmII + BtIII + AmpIV + EpII + Op. The barometers proposed by Massone and Schreyer (1987), Caddick and Thompson (2008), and Kamzolkin et al. (2016) shows pressures vary from 0.13 to 0.49 GPa. Temperatures are obtained using several thermometers: Wm-Pl (Green and Udansky, 1986) indicates T = 277±35°C, Ti in Bt (Henry et al., 2005) suggests T = 306±30°C, Al^{IV} in Chl (Chatelineau, 1988) suggests T = 293±36°C, and Bt-Chl (Dickenson and Hewitt, 1986) shows T = 314±40°C.

The inferred metamorphic conditions with standard deviations obtained from the different thermobarometric calibrations applied in metaconglomerates and granulites, pervasively re-equilibrated during D4 stage, are synthesized in Figure 6.15 and Table 6.2, which shows D4-related cluster of PT conditions ranging from 0.13 to 0.51 GPa and from 242 to 354°C.

Stage	PT	MB	GR	MC	TC
pre-D1	P (GPa)	1.75 ± 0.19			
	T (°C)	735 ± 26			
D1	P (GPa)	1.32 ± 0.10	1.39 ± 0.15		
	T (°C)	795 ± 29	792 ± 30		
D3	P (GPa)	0.55 ± 0.10	0.61 ± 0.15		
	T (°C)	698 ± 33	705 ± 35		
D4	P (GPa)		0.30 ± 0.15	0.33 ± 0.20	0.28 ± 0.22
	T (°C)		320 ± 36	305 ± 55	270 ± 45

Table 6.2. PT estimates of the superposed deformation stages in melanocratic metabasite (MB), basic granulite (GR), mylonitic (MC) and tectonitic (TC) conglomerate.

6.8 Discussion

6.8.1 Eclogite protoliths

Trace elements and REE patterns indicate that the granulites and metabasites protoliths are MORBs contaminated by continental crust components that can be occurred (1) prior to H*P* metamorphism or (2) during the anatexis of their country rocks during exhumation-related re-equilibrations (D1-D3 stages). Indeed, the Pb, U and Large Ion Lithophile Element (LILE) high values and Nb and Ta low values are compatible with chemical features of supra-subduction zone (Hofmann, 2003; Labanieh et al.,2012) or H*T* hydrothermal environment due to crustal melts formation and migration (Michard and Albarède, 1986; Stipska et al., 2004; Burianek et al., 2017).

6.8.2 Tectonometamorphic evolution and geodynamic implications

The detailed multiscale structural analysis and the inferred PT conditions related to Variscan assemblage (pre-D1, D1, and D3) and Alpine D4 assemblage allow inferring the tectonometamorphic evolution reported in Figure 6.16. To infer the geodynamic implication, the PT estimates are compared with classical metamorphic gradients (Miyashiro, 1961; Ernst,1971, 1973; Spear, 1993) and with geotherms proposed by Cloos (1993) for different geodynamic setting.

The Variscan evolution show a pre-D1 eclogitic metamorphic peak at 1.75±0.19 GPa and 735±26°C compatible with the thermal regime of a warm subduction zone and high *P*/*T* ratio (Fig. 6.16A). The probability density curve (Figure 6.12e) of the U-Pb dating on rutile crystals associated with the pre-D1 metamorphic assemblage can be used to infer a minimum age of 334±6 Ma. Between pre-D1 and D1 stage, a slight temperature increases during exhumation took place at D1 conditions of 1.38±0.16 GPa and 793±31°C and it is closed to the stable geotherm. The D1 stage is characterized by H*P*-granulite facies conditions accompanied by pervasive mylonitic deformation and occurrence of plagioclase in the metamorphic assemblage. Afterwards, the PT estimates show a significant decompression coupled with moderate cooling into L*P*-M*T* amphibolite-facies conditions (D3 stage at P = 0.61±0.15 GPa and T = 698±33°C). D3 coronitic fabrics can be related to the LP anatexis evident in the whole Argentera Massif, which produced migmatites from felsic lithologies melting (Bierbrauer, 1995). Taking into account the closure temperature of U-Pb dating on rutile crystal, the probability density curve (Figure 6.12e) allows to infer a minimum age of 310±6 Ma.

The Alpine evolution characterize both the Variscan metamorphic basement and Permian-Triassic cover rocks at shallow crustal levels with intermediate *P*/*T* ratio. D4 stage developed at greenschist facies conditions (P = 0.32±0.19 GPa and T = 298±56°C). The inferred Variscan *P*-*T*-d-t path (Fig.

6.16B) of granulites and metabasites rocks shows a similar trend with the one proposed by Ferrando et al. (2008) and Rubatto et al. (2010).

In this study, the detailed multiscale structural analysis allows to infer the stable coexistence at metamorphic peak of clinopyroxene, amphibole, garnet, and rutile, and to constrain pre-D1 stage at higher depth and *P*/*T* ratio than in the previous works. Furthermore, the multiscale structural analyisis allowed to infer the Alpine tectonometamorphic stage developed at greenschist-facies condition that affected both the Variscan basement and the Permian-Mesozoic covers. Considering the geochemistry and the inferred tectonometamorphic evolution, the studied mafic rocks can be related to subducted oceanic crust formed in a back-arc basin and thus represent a piece of a paleo-suture dismembered within various migmatite-types. This framework can be the results of the vertical extrusion of partially molten orogenic crust during the continental collision(Stipskà et al., 2004; Schulmann et al., 2014, Gerbault et al., 2018) or can be explained by the hot subduction channel model (Gerya et al., 2008) which shows rapid exhumation of H*P* mafic rocks within molten felsic rocks.

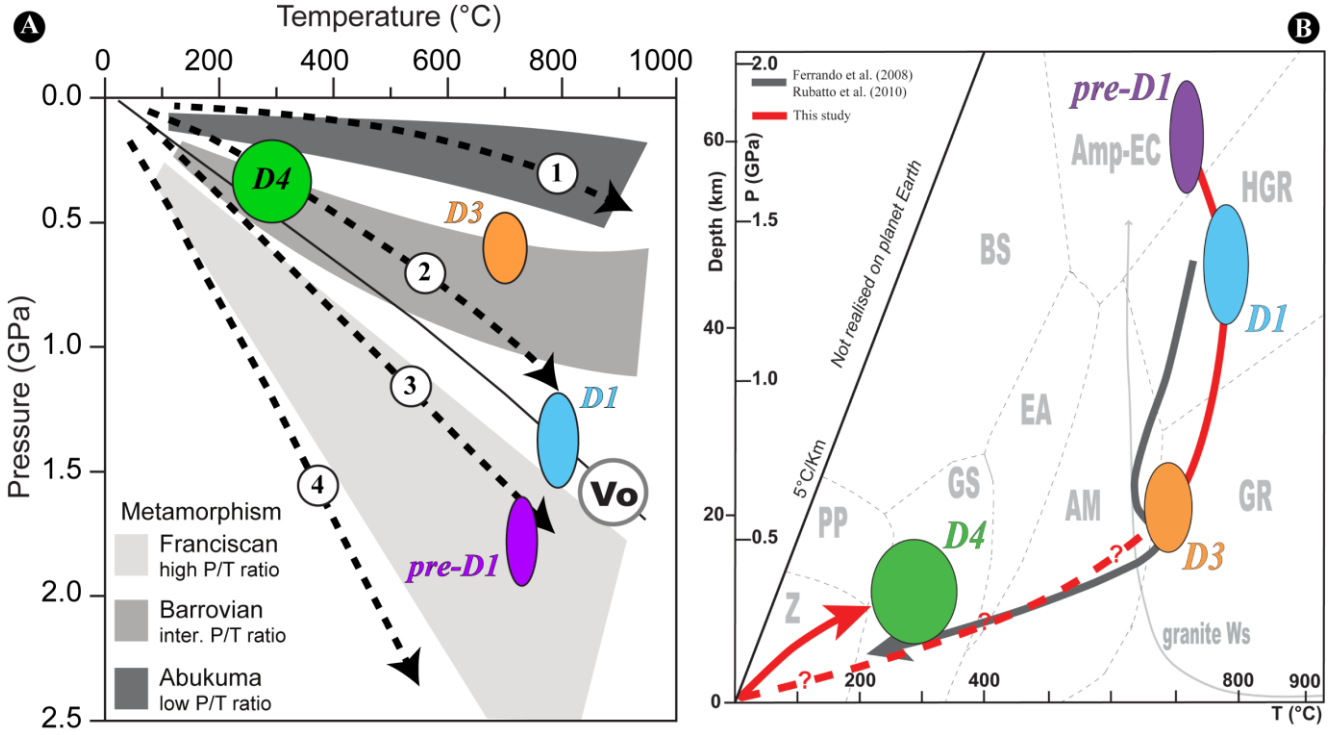

Figure 6.16. PT conditions of the superposed tectono-metamorphic stages (purple: pre-D1; light blue: D1; orange: D3; green: D4). A) The inferred stages compared with metamorphic gradients (after Miyashiro, 1961; Ernst, 1971,1973; Spear, 1993) and geotherms after Cloos (1993): (1) near spreading ridge or volcanic arc, (2) normal gradient of old plate interior, (3) warm subduction zones, and (4) cold subduction zones. Vo: unperturbed geotherm. B) P-T-d-t path of this study compared with those inferred by Ferrando et al., (2008) and Rubatto et al., (2010), The metamorphic facies fields and wet solidus reaction for granite are after Ernst and Liou (2008).

Chapter 7

Discussion

7.1 Pre-Alpine and Alpine geodynamics in paleo-European and African continental crust

African continental crust

Continental crust volumes preserving pre-Alpine metamorphic and structural imprints are widely described within the Western Alps, and consist of rocks that display dominant eclogite, granulite, and amphibolite facies mineral assemblages (Spalla et al. 2014). They were involved in paleo-Tethys oceanic subduction, followed by continental Variscan collision (*e.g.*, Lardeaux & Spalla, 1991; Spalla & Marotta, 2007; Schuster & Stüwe, 2008; von Raumer et al., 2013). Due to the weak Alpine metamorphism and deformation, the Argentera massif (*i.e.*, paleo-European continental crust) preserves large rock volumes characterized by pre-Alpine metamorphic and structural imprints. Relics of the convergent and divergent pre-Alpine evolution are also preserved in the Sesia-Lanzo Zone (*i.e.*, paleo-African continental crust), though the pervasive Alpine structural and metamorphic rework (Roda et al., 2019 and reference within).

The inferred tectonometamorphic evolution and the quantification of the volumes preserving pre-Alpine imprints from the three case studies falls back into this scenario. Indeed, the Frisson rocks (Argentera massif) preserve km-scale volumes of migmatites, basic granulites, and metabasites showing pre-Alpine structural and metamorphic imprints, forged during oceanic lithosphere subduction and continental collisions. The migmatization at 323±12 Ma (*e.g.* Rubatto et al., 2001) is followed by a ca. 295 Ma Central Granite (*e.g.* Corsini et al., 2004). On the contrary, the case studies in the SLZ show grain-scale mineral relicts and meter-scale structural relicts are preserved. In the Lago della Vecchia and Mt. Mucrone area, the pre-Alpine memory includes only meter-scale rock volumes preserving magmatic texture and igneous mineral relicts of the granitoid protolith ascribable to the Permian (291±5 Ma; Cenki-Tok et al., 2011) extensional regime. Thus, acidic igneous magmatism was nearly coeval in SLZ and Argentera. In the Mt. Mucrone area, the combined use of classical multiscale structural analysis and the innovative methodological approach allows to quantify the sizes pf pre-Alpine relicts within meter-scale outcrops of metapelites, showing well-preserved H*T*-L*P* granulite fabric. In that case, the original pre-Alpine granulite mineral assemblages were extensively replaced by static eclogite facies minerals, recording the Alpine subduction-related evolution. This pre-Alpine

imprint can be related to the Permian-Triassic H*T* regime, during long-lasting lithospheric thinning and extensional tectonics leading to the Mesozoic continental rifting.

The Alpine deformation and the associated H*P*-L*T* metamorphism, overprinting pre-Alpine structures and metamorphism, is widespread in the Austroalpine domain of the Western Alps. However, the amount of Alpine reworking is heterogeneous, from almost no signs of strain and metamorphism to strong and pervasive overprinting under eclogite- to greenschist-facies (*e.g.*, Dal Piaz et al. 1972; Compagnoni 1977; Lardeaux et al. 1982; Ballevre and Merle 1993; Gosso et al. 2010; Roda et al., 2012; Butler et al., 2013; Giuntoli and Engi, 2016). In this light, the difference in the dominant tectonometamorphic imprints within the Eclogitic Micaschists Complex (EMC) of the Sesia-Lanzo Zone (*e.g.*, dominant fabric in blueschist-facies for the Lago della Vecchia rocks and dominant fabric in eclogitic-facies for Mt. Mucrone rocks) opens the question about the actual distribution of the eclogitic tectonometamorphic imprint within the EMC. These contrasting dominant fabrics may suggest that the entire EMC could be characterized by kilometer-scale heterogeneities in the tectonometamorphic record and it may consist of several DFE and DRP sub-units formed during Alpine subduction and/or exhumation. These heterogeneities in DFE partitioning are compatible with predictions of numerical modeling of subduction zones (Gerya and Stöckhert, 2006).

On the other hand, the Argentera massif is poorly re-equilibrated during the Alpine collision under greenschist facies conditions. The Alpine deformation caused the reactivation of localized pre-Alpine shear zones promoting the Argentera Massif exhumation through strike-slip dextral faults and thrusting (Corsini et al., 2004; Sanchez et al., 2011 and references therein). In the Frisson area, the Alpine structural and metamorphic overprints are localized in meter- to decameter-thick shear zones, which characterize the coupling between the Variscan metamorphic basement and Permian-Triassic cover rocks at shallow crustal levels.

7.2 Correlation between fabric and metamorphic heterogeneities

In this Thesis a multiscale structural analysis (field- to atomic-scale) approach has been used that combine several techniques (fieldwork, GIS database, optical and electron microscopy, SPO analysis, Quantitative X-Ray Map Analysis, micro-CT, 3D geology modelling, and X-ray single crystal diffraction). The used approach is specifically focused on the investigation of the correlation of metamorphism and deformation. Multiscale analysis shows that there is a strong correlation between DFE (Degree of Fabric Evolution) and DRP (Degree of metamorphic Reaction Progress). As a consequence, the structural control is fundamental for the evaluation of DRP and DFE domain volumes and for the comparison of the corresponding DRP and DFE domain volumes. This is

particularly clear from the 3D modelling of the Mt. Mucrone area (Fig. 5.1.9) that shows that corresponding DRP and DFE domain volumes match by ca. 95%.

The first outcome is that the degree of metamorphic reaction progress is controlled by bulk rock, mineral compositions, and that is also strongly influenced by the degree of fabric evolution. The 2D estimation (CS1 and CS2) and the 3D modelling (CS2) of degree of fabric evolution and degree of reaction progress shows that the dominant metamorphic imprint is characterized by the highest DFE, but there are differences between corresponding DFE and DRP domains in absolute volumetric estimation and spatial distribution. The localization of the high-strain domains is not controlled by the lithological boundaries. Indeed, the comparison between the models and the geological maps for the Mucrone area and Lago della Vecchia area shows that the localization of the high-strain domains is transversal to the lithological boundaries.

These spatial and volumetric differences are also controlled by the rock-type. The micro- to km-scale analysis support that the differences in original mineral assemblages and fabrics can exert an influence on the relationships between DFE and DRP in different rock-types, as the mechanical reworking and reaction progress when DFE remains lower than 60%. Indeed, the 2D and 3D modelling (section 4.1 and section 5.1) demonstrate that metagranitoids achieved a lower degree of metamorphic reaction progress than metapelites at low- and medium- strain conditions (coronitic and tectonitic fabrics). On the contrary, at high-strain conditions the deformation and metamorphic effects developed at the same rate up to the 100% of the considered volume, disregarding the involved rock type. Furthermore, the thermal regime can exert an additional influence on the degree of metamorphic transformation, if the DFE remains below to the 60% threshold. The metamorphic reaction progress is more evolved during eclogitic- and granulitic-facies metamorphic conditions than greenschist-facies conditions, for the same DFE values.

The DFE-DRP relationships constrained at km-scale is used as first-order parameter for deeper analysis of structural heterogeneities at grains- to atomic-scale (section 4.3 and 5.2). The microstructural analysis and X-ray single crystal diffraction demonstrate that the Aln crystals do not show evidence of intra-crystalline plastic deformation from micro- to atomic-scale and along strain gradients. Aln behaves as a rigid object in a weak matrix (metagranitoids with modal amount of Qtz + Wm>60%) and it is characterized by high mechanical strength and it is reluctant to recrystallize during polyphasic tectono-metamorphic history. Even in mylonitic domains, the deformation is accommodated by the recrystallization of Qtz and Pl grains and crystal folding (*e.g.*, Wm). Quantitative mineral chemical analysis and chemical imaging are used to quantify the chemical diffusion of allanite zoning in relation to the rock-matrix strain accumulation. The Aln chemical zoning is mostly defined by the Ca/ and Ce/LREE ratio. The high Ca fraction and lower LREE content

in the Aln3 sample may be due to a more progressed metamorphic transformation, especially in mylonitic domains. Along DFE domains, the LREE released during the exhumation in the subduction mantle wedge for the Aln crystals was estimated through (i) the normalized Ca/LREE ratio and (ii) normalized LREE contents parameters. Therefore, a LREE loss of 1-2%, 5-16%, and 82-84% (Fig. 9b) and increase of Ca/LREE parameter of 18-21%, 29-30%, and 34-38% (Fig. 9a) are estimated for coronitic, tectonitic, and mylonitic domains, respectively. In this view, the chemical zoning of Aln crystal is quantified as a well-defined linear regression ($y = 0.2x + 18.9$, with $R^2 = 0.92$) between the normalised Ca/LREE ratio and the strain accumulation in the rock matrix. The LREE release from the Aln crystals is characterized by an exponential relationship ($y = 0.8e^{0.6}x$, with $R^2 = 0.96$) with the rock-matrix strain accumulation. The high Ca/LREE and LREE loss parameters are corelated to a more progressed metamorphic transformation facilitated by high strain accumulation in mylonitic domains. Thus, this example shows that chemical diffusion may be active in a rigid mineral phase and it is controlled by the total amount of plastic deformation (*i.e.* DFE) and metamorphic transformation (*i.e.* DRP) of the rock matrix.

The innovative approach used in the CS3 (section 5.2) shows how the integrated use of quantitative chemical imaging and 3D microstructures analysis revels complex micro-scale metamorphic and structural overprinting relationships that are only partially reflected by m- to km-scale modelling. The 3D visualization and analysis of fabrics and metamorphic minerals achieved by the X-ray µ-CT are well constrained by the 2D quantitative microstructural analysis. The reproducibility shown by the comparison of the shape analysis results allowed improving mineral phases identification, during the segmentation procedure, thanks to the knowledge from the 2D analysis, where not only shape parameters were known but also optical properties and mineral chemistry. Consequently, the quantitative chemical information obtained by the Q-XRMA tool were extended to the whole 3D volume to quantify the pervasiveness of the pre-Alpine fabrics (100 % of the rock fabric within the investigated volume). Even though the pre-Alpine fabric is so well preserved the pre-Alpine minerals surprisingly correspond only to less than 22 % (Fig. 5.3.11A). The quantitatively shape and orientation analysis on Bt, Wm, Qtz, Ky, and Cpx grains show two orientation clusters that can be correlated to the pre-Alpine S and C mylonitic structures (35% of grains are S-related and 23% of grains are C-related).

The static developed Alpine-related mineral phases, comprising the 78.09% of the volume, involve WmII/BtII (41.73%), Qtz (30.46%), Cpx (3.86%), Ky (2.04%), and GrtII (0.01%) with heterogeneous grain-size distribution (Figs. 5.2.11 and 5.2.12). These features suggest dominant control of the growth domain over dynamic recrystallization (*e.g.*, GrtII grows as corona over GrtI and Ky grows as aggregates replacing pre-Alpine Sill-microdomains). The volumetric reconstruction of the shape and

spatial distribution of Alpine-related phases clearly demonstrate that metamorphic reactions occur in absence of deformation, and in the virtual absence of fluid as chemical medium. This is demonstrated by the unchanged bulk chemistry within the selected microsites. For example, (i) GrtII increases its Fe and Ca content in the ex-sillimanite domain and in the ex-plagioclase domains, respectively; (ii) Ky fine-grained aggregates occurs only in ex-sill domains; (iii) the symplectite textures occurring in the ex-Pl domains are defined by high Jd contents (82-97%) Cpx, Ca-rich Grt (highest Grs component around 22%), and Qtz. All these features suggest that even at low temperature conditions and in low-strain domains the activation energy of many metamorphic reactions energetically less favored may be overstepped.

Chapter 8

Conclusion

- The 2D and 3D models allow the individuation of volumes with homogenous degree of fabric evolution and metamorphic reaction progress. This outcome is used for a proper sampling to quantify parameters that controls fabric and metamorphic heterogeneities. The results of cm- to atomic-scale analysis can be used to refine the previous models and make more constrain km-scale fabric and metamorphism correlation.
- Combining microstructural, mineral chemical, X-ray chemical imaging, and X-ray single crystal diffraction analyses, the physical-chemical behavior of mineral phases along strain gradients can be quantitatively inferred.
- Through the 3D microtomographic analysis the 3D grains shape distribution has been quantified; this allowed to improve the knowledge of the metamorphic texture development in poly-deformed metamorphic rocks, and to quantify the parameters connected to geological processes, in particular to deformation and metamorphic processes.
- To investigate the interactions of mineral chemical and phase changes during strain partitioning, the quantification of the effective rock volumes in which metamorphic transformations progress is fundamental. Petrological results allow more accurate individuation of microdomains in chemical and textural equilibrium for more reliable *PT* estimations and better estimation of degree of metamorphic reaction progress along strain gradients.
- The quantitative individuation of low-strain domains in poly-deformed rocks is fundamental for a reliable petrological modelling of coronitic metamorphic reactions, and to quantify the element diffusion during long-time tectonic processes.
- The multiscale and multidisciplinary approach was demonstrated to be useful to unravel the variation in size of rock volumes that share a common history (*e.g.* subduction-collision-exhumation). The 3D estimation of volumes preserving textural and mineral relicts after phase transitions may shed light on the potential effects of incomplete metamorphic transformations on the rheology of rock volumes during their paths through different lithospheric depth along active margins. Consequently, the phase transitions cannot be properly implemented in numerical modelling of geodynamic processes without evaluating the heterogeneity of reaction progress and fabric evolution.

- The natural data resulting from the proposed approach can be directly compared with outputs from numerical modeling (*i.e.* mechanical behavior, deformation-metamorphism, and geodynamics), as well to improve the numerical modelling of geodynamic processes, by using more constrained input parameters. Indeed, this approach provides physical and chemical constraints from km- to atomic-scale and both the mechanical and chemical evolution of rocks, identifying the size of the active volumes through time.

Chapter 9

References

Aicard P, Autran A, Gérard J, Lougnon J. 1968. Sur l'âge tertiaire syntectonique et synmétamorphique alpin du gisement plombo-zincifère de Valauria (commune de Tende, Alpes Maritimes). Bull BRGM1:5-14.

Allmendinger, R. (2016). Stereonet 9 for Windows [Online]. Available from: http://www.geo.cornell.edu/geology/faculty/RWA/programs/stereonet.html.

Ai Y. (1994) - A revision of the garnet–clinopyroxene Fe^{2+}–Mg Green T. H., Adam J. (1991). Assessment of the garnet– exchange geothermometer. Contributions to Mineralogy and clinopyroxene Fe–Mg exchange using new experimental data. Petrology, 115, 467–473.

Armbruster, T., Bonazzi, P., Akasaka, M., Bermanec, V., Chopin, C., Gieré, R., Heuss-assbichler, S., Liebscher, A., Menchetti, S., et al. (2006) Recommended nomenclature of epidote-group minerals. European Journal of Mineralogy, 18(5), 551–567. doi: 10.1127/0935-1221/2006/0018-0551

Armstrong J.T. & Buseck P.R. (1975) - Quantitative chemical analysis of individual microparticles using the Electron Microprobe: theoretical. Anal. Chem., 47 (13), 2178-2192.

Austrheim, H. (1987). Eclogitization of lower crustal granulites by fluid migration through shear zones. Earth and Planetary Science Letters, 81(2-3), 221-232.

Austrheim, H. (1990). The granulite-eclogite facies transition: A comparison of experimental work and a natural occurrence in the Bergen Arcs, western Norway. Lithos, 25(1-3), 163-169.

Avigad, D., Chopin, C., Goffe, B., & Michard, A. (1993). Tectonic model for the evolution of the western Alps. Geology, 21(7), 659-662

Babist J., Handy M. R., Konrad-Schmolke M., Hammerschmidt K. (2006) - Precollisional, multistage exhumation of subducted continental crust: The Sesia Zone, western Alps. Tectonics, 25, TC6008, doi: 10.1029/2005TC001927.

Balestro G, Festa A, Dilek Y (2019) Structural Architecture of the Western Alpine Ophiolites, and the Jurassic Seafloor Spreading Tectonics of the Alpine Tethys. J Geol Soc. https://doi.org/10.1144/jgs2018-099

Ballèvre, M., Kienast, J. R., & Vuichard, J. P. (1986). La «nappe de la Dent-Blanche» (Alpes occidentales): deux unités austroAlpines indépendantes. Eclogae Geologicae Helvetiae, 79(1), 57-74.

Ballèvre, M., & Merle, O. (1993). The Combin fault: compressional reactivation of a Late Cretaceous-Early Tertiary detachment fault in the Western Alps. Schweizerische Mineralogische und Petrographische Mitteilungen, 73(2), 205-227.

Baker, D. R., Mancini, L., Polacci, M., Higgins, M. D. (2012). An introduction to the application of X-ray microtomography to the three-dimensional study of igneous rocks. Lithos. 148: 262. doi: 10.1016/j.lithos.2012.06.008

Baletti L, Gosso G, Spalla MI, Zanoni D (2012) Structural and petrographic map of the Sassa metaintrusives (Dent Blanche nappe, Austroalpine tectonic system, Western Alps, Italy). J Maps 8(4): 413-430. http://doi.org/10.1080/17445647.2012.745678

Barboza, S. A., Bergantz, G. W. (2000). Metamorphism and Anatexis in the Mafic Complex Contact Aureole, Ivrea Zone, Northern Italy. J. Petrol. 41: 1307. doi: 10.1093/petrology/41.8.1307

Baruchel, J., Buffiere, J. Y., and Maire, E. (2000). X-ray tomography in material science. Paris: Hermes science publications.

Bea, F. (1996) Residence of REE, Y, Th and U in granites and crustal protoliths; implications for the chemistry of crustal melts. Journal of Petrology, 37(3), 521-552. doi: 10.1093/petrology/37.3.521

Belfiore, C. M., Fichera, G. V., Ortolano, G., Pezzino, A., Visalli, R., Zappalà, L. (2016). Image processing of the pozzolanic reactions in Roman mortars via X-Ray Map Analyser. Microchem. J. 125: 242. doi: 10.1016/j.microc.2015.11.022

Bell, T. H., & Rubenach, M. J. (1983). Sequential porphyroblast growth and crenulation cleavage development during progressive deformation. Tectonophysics, 92, 171-194.

Bell TH, Hayward N (1991) Episodic metamorphic reactions during orogenesis: the control of deformation partitioning on reaction sites and reaction duration. J. Metamorp Geol 9:619–640. https://doi.org/10.1111/j.1525-1314.1991.tb00552.x

Berger, A., Thomsen, T. B., Ovtcharova, M., Kapferer, N., & Mercolli, I. (2012). Dating emplacement and evolution of the orogenic magmatism in the internal Western Alps: 1. The Miagliano Pluton. Swiss Journal of Geosciences, 105, 49-65, doi: 10.1007/s00015-012-0091-7.

Berrezueta, E., Domínguez-Cuesta, M. J., Rodríguez-Rey, Á. (2019). Semi-automated procedure of digitalization and study of rock thin section porosity applying optical image analysis tools. Comput. Geosci. 124: 14. doi: 10.1016/j.cageo.2018.12.009

Beltrando, M., Compagnoni, R., & Lombardo, B. (2010). (Ultra-) High-pressure metamorphism and orogenesis: an Alpine perspective. Gondwana Research, 18(1), 147-166.

Beltrando, M., Manatschal, G., Mohn, G., Dal Piaz, G. V., Brovarone, A. V., & Masini, E. (2014). Recognizing remnants of magma-poor rifted margins in high-pressure orogenic belts: The Alpine case study. Earth-Science Reviews, 131, 88-115.

Bearth, P. (1967). Die Ophiolithe der Zone von Zermatt-Saas Fee. Kümmerly & Frey.

Berthelsen, A. (1992). Tectonic evolution of Europe. From Precambrian to Variscan Europe. In A Continent Revealed, the European Geotravers (pp. 153-164).

Bigi G, Castellarin A, Coli M, Dal Piaz GV, Sartori R, Scandone P, Vai GB (1990) Structural Model of Italy, sheets 1-2. In: Progetto Finalizzato Geodinamica del CNR - SELCA, Florence.

Blasi A (1971) Genesi dei noduli a sillimanite nelle anatessiti del Mt. Pélago (Alpi Marittime) in rapporto ai fenomeni di metamorfismo, piegamentoe granitizzazione. Mem Soc Geol It 10(11):167-190.

Blanco-Quintero, I. F., Gerya, T. V., García-Casco, A., & Castro, A. (2011). Subduction of young oceanic plates: A numerical study with application to aborted thermal-chemical plumes. Geochemistry, Geophysics, Geosystems, 12(10).

Blasi A, Schiavinato G (1968) Significato petrologico dei noduli a sillimanite e dei noduli a cordierite diffusi nelle anates-siti biotitiche del M. Pelago (massiccio cristallino dell'Argentera). Boll. Soc. Geol. Ital, 87:253-275.

Bogdanoff S, Ploquin A (1980) Les gneiss et migmatites du massif de l'Argentera (Alpes maritimes); apport de deux coupes geochimiques. Bull Soc géol Fr 7(3): 353-358.

Bogdanoff S (1986) Evolution de la partie occidentale du massif cristallin externe de l'Argentera. Place dans l'arc alpin. Géol France, 4, 433-453.

Bogdanoff S, Ménot RP, Vivier G (1991) Les massifs cristallins externes des alpes occidentales françaises, un fragment de la zone interne varisque. Sci Géol Bull :237-283.

Bogdanoff S, Michard A, Mansour M, Poupeau G (2000) Apatite fission track analysis in the Argentera massif: evidence of contrasting denudation rates in the External Crystalline Massifs of the Western Alps. Terra Nova 12(3):117-125. doi: 10.1046/j.1365-3121.2000.123281.x

Bonazzi, P., Holtstam, D., Bindi, L., Nysten, P. and Capitani, G. (2009) Multi-analytical approach to solve the puzzle of an allanite-subgroup mineral from Kesebol, Västra Götaland, Sweden. American Mineralogist, 94, 121-134. doi: 10.2138/am.2009.2998

Bortolami G, Sacchi R. (1968) Osservazioni geologico-petrografiche sui medi valloni di S.Anna e Rio Freddo (Massiccio Cristallino dell'Argentera). Mem Soc Geol It 7:37-64.

Bortolami G, Callegari E, Gosso, G (1974) Caratteri metamorfici nella copertura permocarbonifera e nel basamento cristalino dell'argentera (Versante meridionale, St. Martin Vésubie, Francia). Società Geologica Italiana.

Boston, K.R., Rubatto, D., Hermann, J., Engi, M. and Amelin, Y. (2017) Geochronology of accessory allanite and monazite in the Barrovian metamorphic sequence of the Central Alps, Switzerland. Lithos. doi: 10.1016/j.lithos.2017.06.025

Boucarut M (1967) Structure du granite de l'Argentera et style tectonique de l'ensemble de ce massif. C R Acad Sci Paris 264:1573-1576.

Bourdelle F, Parra T, Chopin C, Beyssac O (2013) A new chlorite geothermometer for diagenetic to low-grade metamorphic conditions. Contrib Mineral Petrol, 165(4), 723-735.

Bousquet, R., Engi, M., Gosso, G., Berger, A., Spalla, M. I., Zucali, M., & Goffè, B. (2004). Explanatory notes to the map: Metamorphic structure of the Alps. In Central Alps. Mitt. Österr. Miner. Ges.

Bousquet, R., Oberhänsli, R., Goffé, B., Wiederkehr, M., Koller, F., Schmid, S. M., ... & Martinotti, G. (2008). Metamorphism of metasediments at the scale of an orogen: a key to the Tertiary geodynamic evolution of the Alps. Geological Society, London, Special Publications, 298(1), 393-411.

Bracciali L, Parrish RR, Horstwood MS, Condon DJ, Najman Y (2013) UPb LA-(MC)-ICP-MS dating of rutile: New reference materials and applications to sedimentary provenance. Chem Geol, 347, 82-101.

Brooks, C.K., Henderson, P. and Rønsbo, J.G. (1981) Rare-earth partition between allanite and glass in the obsidian of Sandy Braes, Northern Ireland. Mineralogical Magazine, 44, 157-160. doi: 10.1180/minmag.1981.044.334.07

Broska, I. and Siman, P. (1998) The breakdown of monazite in the West-Carpathian Veporic Orthogneisses and Tatric granites. Geologica Carpathica, 49, 161–167.

Broska, I., Petrík, I. and Williams, C.T. (2000) Coexisting monazite and allanite in peraluminous granitoids of the Tribec Mountains, Western Carpathians. American Mineralogist, 85(1), 22-32. doi: 10.2138/am-2000-0104

Bussy F., Venturini G., Hunziker J. C., Martinotti G. (1998) - U-Pb ages of magmatic rocks of the Western Austroalpine Dent-Blanche-Sesia UnItal. Schweiz. Miner. Petrog., 78, 163-168.

Butler, J. P., Beaumont, C., & Jamieson, R. A. (2013). The Alps 1: A working geodynamic model for burial and exhumation of (ultra) high-pressure rocks in Alpine-type orogens. Earth and Planetary Science Letters, 377, 114-131.

Caddick MJ, Thompson AB (2008) Quantifying the tectono-metamorphic evolution of pelitic rocks from a wide range of tectonic settings: mineral compositions in equilibrium. Contrib Mineral Petrol, 156(2), 177-195.

Calcagno P, Chilès JP, Courrioux G, Guillen A (2008) Geological modelling from field data and geological knowledge: Part I. Modelling method coupling 3D potential-field interpolation and geological rules. Phys Earth Planet In 171: 147-157. https://doi.org/10.1016/j.pepi.2008.06.013

Callegari E., Compagnoni R., Dal Piaz G. V., Frisatto V., Gosso G., Lombardo B. (1976) - Nuovi affioramenti di metagranitoidi nella Zona Sesia-Lanzo. Rend. Soc. Ital. Mineral. Petrol., 32, 97-111.

Cantù M., Spaggiari L., Zucali M., Zanoni D., Spalla M. I. (2016) - Structural analysis of a subduction-related contact in southern Sesia-Lanzo Zone (Austroalpine Domain, Italian Western Alps). J. Maps, 12(1), 22-35, doi: 10.1080/17445647.2016.1155925.

Carminati, E., & Vadacca, L. (2010). Two-and three-dimensional numerical simulations of the stress field at the thrust front of the Northern Apennines, Italy. Journal of Geophysical Research: Solid Earth, 115(B12).

Carminati, E., Lustrino, M., Doglioni, C., 2012. Geodynamic evolution of the central and western Mediterranean. Tectonics vs. igneous petrology constraints. Tectonophysics, doi.org/10.1016/j.tecto.2012.01.026.

Carosi R, D'Addario E, Mammoliti E, Montomoli C, Simonetti M (2016) Geology of the northwestern portion of the Ferriere-Mollieres Shear Zone, Argentera Massif, Italy. J Maps sup1:466-475. doi: 698 10.1080/17445647.2016.1243491.

Cassinis, R. (2006). Reviewing pre-TRANSALP DSS models. Tectonophysics, 414(1-4), 79-86.

Castellarin, A., Vai, G. B., & Cantelli, L. (2006). The Alpine evolution of the Southern Alps around the Giudicarie faults: A Late Cretaceous to Early Eocene transfer zone. Tectonophysics, 414(1-4), 203-223.

Carswell, D.A., Wilson, R.N. and Zhai, M. (2000) Metamorphic evolution, mineral chemistry and thermobarometry of schists and orthogneisses hosting ultra-high pressure eclogites in the Dabieshan of central China. Lithos 52, 121-155. doi: 10.1016/S0024-4937(99)00088-2

Casillas, R., Nagy, G., Pantó, G., Brandle, J. and Fórizs, I. (1995) Occurrence of Th, U, Y, Zr and REE-bearing accessory minerals in late-Variscan granitic rocks from the Sierra Guadarrama (Spain). European Journal of Mineralogy, 7, 989-1006.

Catlos, E.J., Sorensen, S.S. and Harrison, T.M. (2000) Th-Pb ion-microprobe dating of allanite. American Mineralogist, 85, 633-648, doi: 10.2138/am-2000-5-601

Cathelineau M. (1988) - Cation site occupancy in chlorites and illites as function of temperature. Clay Miner., 23(4), 471-85.

Castelli D (1987) Il metamorfismo alpino delle rocce carbonatiche della Zona Sesia-Lanzo (Alpi Occidentali). Consorzio Universitario di CA-GE-TO. PhD Thesis.

Castelli D (1991) Eclogitic metamorphism in carbonate rocks: the example of impure marbles from the Sesia-Lanzo Zone, Italian Western Alps. J Metam Geol 9: 61-77. https://doi.org/10.1111/j.1525-1314.1991.tb00504.x

Castelli D, Rubatto D (2002) Stability of Al- and F-rich titanite in metacarbonate: petrologic and isotopic constraints from a polymetamorphic eclogitic marble of the internal Sesia Zone (Western Alps). Contrib Miner Petrol 142: 627–639. https://doi.org/10.1007/s00410-001-0317-6

Cenki-Tok B., Oliot E., Rubatto D., Berger A., Engi M., Janots, E. (2011) - Preservation of Permian allanite within an Alpine eclogite facies shear zone at Mt Mucrone, Italy: Mechanical and chemical behavior of allanite during mylonitization. Lithos, 125, 40-50, doi: 10.1016/j.lithos.2011.01.005.

Cenki-Tok, B., Darling, J.R., Rolland, Y., Dhuime, B. and Storey, C.D. (2014) Direct dating of mid-crustal shear zones with synkinematic allanite: new in situ U-Th-Pb geochronological approaches applied to the Mont Blanc massif. Terra Nova, 26, 29-37. doi: 10.1111/ter.12066

Cherniak DJ (2000) Pb diffusion in rutile. Contrib Mineral Petrol, 139(2), 198-207.

Cliff, R.A., Oberli, F., Meier, M., Droop, G.T R. and Kelly, M. (2015) Syn-metamorphic folding in the Tauern Window, Austria dated by Th–Pb ages from individual allanite porphyroblasts. Journal of metamorphic Geology, 33(4), 427-435. doi: 10.1111/jmg.12127

Cloos M. (1993) - Lithospheric buoyancy and collisional orogenesis: Subduction of oceanic plateaus, continental margins, island arcs, spreading ridges, and seamounts. Geol. Soc. Am. Bull., 10(6), 715-737.

Chapman T, Clarke GL, Piazolo S, Daczko NR (2019) Inefficient high-temperature metamorphism in orthogneiss. Amer Miner 104: 17–30. https://doi.org/10.2138/am-2019-6503

Chilès JP, Aug C, Guillen A, Lees T (2004) Modelling the geometry of geological units and its uncertainty in 3D from structural data: the potential-field method. In Proceedings of international symposium on orebody modelling and strategic mine planning, Perth, Australia 22: 313-320.

Coleman RG, Lee DE, Beatty LB, Brannock WW (1965) Eclogites and eclogites — their differences and similarities. Geol Soc Am Bull 76:483–508.

Colombo F, Compagnoni R, Lombardo B (1994) Le rocce eclogitiche dei Laghi del Frisson (Argentera sud-orientale, Alpi Marittime). Atti Tic. Sci. Terra, serie speciale, 1:75-82.

Compagnoni R. & Maffeo B. (1973) - Jadeite-bearing metagranites l.s. and related rocks in the Mount Mucrone area (Sesia-Lanzo Zone, Western Italian Alps). Schweiz. Miner. Petrog., 53 (3), 355-378.

Compagnoni R., Dal Piaz G.V., Hunziker J.C., Gosso G., Lombardo B., Williams, P.F. (1977) - The Sesia-Lanzo Zone: A slice of continental crust, with alpine HP-LT assemblages in the Western Italian Alps. Rend. Soc. Ital. Mineral. Petrol., 33, 281-334.

Compagnoni R, Ferrando S, Lombardo B, Radulesco N, Rubatto D. (2010) Paleo-European crust of the Italian Western Alps: Geological history of the Argentera Massif and comparison with Mont Blanc-Aiguilles Rouges and Maures-Tanneron Massifs. J. Virt. Explorer, 36: 441-465.

Connolly JA (1990) Multivariable phase diagrams; an algorithm based on generalized thermodynamics. Am J Sci, 290(6), 666-718.

Connolly, JA (2005) Computation of phase equilibria by linear programming: a tool for geodynamic modeling and its application to subduction zone decarbonation. Earth and Planetary Science Letters, 236(1-2), 524-541.

Corsini M, Ruffet G, Caby R (2004) Alpine and late-hercynian geochronological constrains in the Argentera Massif (Western Alps). Eclogae Geol Helv 97:3-15. doi: 10./s00015-004-1107-8.

Corti L., Alberelli G., Zanoni D., Zucali M. (2017) - Analysis of fabric evolution and metamorphic reaction progress at Lago della Vecchia-Valle d'Irogna, Sesia-Lanzo Zone, Western Alps. J. Maps, 13 (2), 521-533, DOI: 10.1080/17445647.2017.1331177.

Corti L, Alberelli G, Zanoni D, Zucali M (2018) Tectonometamorphic evolution of the Lago della Vecchia metaintrusive and its country rocks, Sesia-Lanzo Zone, Western Alps. Ital J Geosci 137(2): 188-207. https://doi.org/10.3301/IJG.2018.08

Cortiana, G., Dal Piaz, G. V., Del Moro, A., Hunziker, J. C., & Martin, S. (1998). ^{40}Ar-^{39}Ar and Rb-Sr dating of the Pillonet klippe and Sesia-Lanzo basal slice in the Ayas valley and evolution of the Austroalpine-Piedmont nappe stack. Memorie di Scienze Geologiche, 50, 177-194.

Cosca, M. A., & O'Nions, R. K. (1994). A re-examination of the influence of composition on argon retentivity in metamorphic calcic amphiboles. Chemical Geology, 112(1-2), 39-56.

Cnudde, V., Boone, M. N. (2013). High-resolution X-ray computed tomography in geosciences: A review of the current technology and applications. Earth-Sci. Rev. 123: 1. doi: 10.1016/j.earscirev.2013.04.003

Cox, R.A., Wilton, D.H.C. and Kosler, J. (2003) Laser-ablation U-Th-Pb in situ dating of Zircon and Allanite: an example from the October Harbour Granite, Central Coastal Labrador, Canada. Canadian Mineralogist, 41, 273-291.

Cuthbert, S. J., Carswell, D. A., Krogh-Ravna, E. J., & Wain, A. (2000). Eclogites and eclogites in the Western Gneiss region, Norwegian Caledonides. Lithos, 52(1-4), 165-195.

Dal Piaz G.V., Hunziker J.C., Martinotti, G. (1972) - La zona Sesia-Lanzo e l'evoluzione tettonico-metamorfica delle Alpi nordoccidentali interne. Mem. Soc. Geol. Ital., 11, 433-466.

Dal Piaz, G. V. (1993). Evolution of Austro-Alpine and Upper Penninic basement in the northwestern Alps from Variscan convergence to post-Variscan extension. In Pre-Mesozoic geology in the Alps (pp. 327-344). Springer, Berlin, Heidelberg.

Dal Piaz, G. V., Bistacchi, A., & Massironi, M. (2003). Geological outline of the Alps. Episodes, 26(3), 175-180.

Dale, J., Powell, R., White, R. W., Elmer, F. L., & Holland, T. J. B. (2005). A thermodynamic model for Ca–Na clinoamphiboles inNa_2O–CaO–FeO–MgO–Al_2O_3–SiO_2–H2O–O for petrological calculations. Journal of Metamorphic Geology,23, 771–791.

De Pol C (1963) Migmatiti e metamorfiti della regione M. Corborant, M. Laroussa (Massiccio dell'Argentera), 1-21.

Deer W.A., Howie R.A., Zussman J. (1992) – An Introduction to the Rock-Forming Minerals. 2nd edition. Longman, London, 549 pp.

Delleani F., Spalla M. I., Castelli D., Gosso G. (2012) - Multiscale structural analysis in the subducted continental crust of the internal Sesia-Lanzo Zone (Monte Mucrone, Western Alps). Journal of the Virtual Explorer, 41(7), 1-35, doi: 10.3809/jvirtex.2011.00287.

Delleani F., Spalla M. I., Castelli D., Gosso G. (2013) - A new petro-structural map of the Monte Mucrone metagranitoids (Sesia-Lanzo Zone, Western Alps). J. Maps, 9(3), 410-424, doi: 10.1080/17445647.2013.800004.

Delleani F., Rebay G., Zucali M., Tiepolo M., Spalla M.I. (2018) - Insights on Variscan geodynamics from the structural and geochemical characterization of a Devonian-Carboniferous gabbro from the Austroalpine domain (Western Alps). Ofioliti, 43, 23-39.

Denison, C., Carlson, W. D., Ketcham, R. A. (1997). Three-dimensional quantitative textural analysis of metamorphic rocks using high-resolution computed X-ray tomography: Part I. Methods and techniques. J. Metamorph. Geol. 15(1): 29. doi: 10.1111/j.1525-1314.1997.00006.x

Delteil J, Stephan JF, Attal M. 2003. Control of Permian and Triassic faults on Alpine basement deformation in the Argentera massif (external southern French Alps). Bull Soc géol Fr174(5):481-496. DOI: 10.2113/174.5.481.

DeVasto, M. A., Czeck, D. M., Bhattacharyya, P. (2012). Using image analysis and ArcGIS® to improve automatic grain boundary detection and quantify geological images. Comp. Geosci. 49: 38. doi: 10.1016/j.cageo.2012.06.005

Dewey, J.F., Pitman, W.C., Ryan, W.B.F., Bonnin, J., 1973. Plate tectonics and the evolution of the Alpine system. Geological Society of America Bulletin 84, 3137–3180, doi.org/10.1130/0016-7606(1973) 84b3137. PTATEO>2.0.CO;2.

Dewey, J. F., Ryan, P. D., & Andersen, T. B. (1993). Orogenic uplift and collapse, crustal thickness, fabrics and metamorphic phase changes: the role of eclogites. Geological Society, London, Special Publications, 76(1), 325-343.

Dickenson MP, Hewitt D (1986) A garnet–chlorite geo-thermometer. Geological Society of America Abstracts with Programs,18, 584.

Dilek Y, Furnes H (2011) Ophiolite genesis and global tectonics: Geochemical and tectonic fingerprinting of ancient oceanic lithosphere. Bulletin, 123(3-4), 387-411.

Dini, A., Rocchi, S. and Westerman, D.S. (2004) Reaction microtextures of REE-Y-Th-U accessory minerals in the Monte Capanne pluton (Elba Island, Italy): A possible indicator of hybridization processes. Lithos, 78, 101-118. doi: 10.1016/j.lithos.2004.04.045.

Doglioni, C. (1991). A proposal for the kinematic modelling of W-dipping subductions-possible applications to the Tyrrhenian-Apennines system. Terra Nova, 3(4), 423-434.

Doglioni, C., Gueguen, E., Sàbat, F., Fernandez, M., 1997. The western Mediterranean extensional basins and the Alpine orogen. Terra Nova 9, 109–112.

Doglioni C., Carminati E., Cuffaro M. & Scrocca D. (2007) - Subduction kinematics and dynamic constraints. Earth Sci. Rev., 83, 125-175.

Dollase, W.A. (1971) Refinement of the crystal structures of epidote, allanite and hancockite. American Mineralogist, 56, 447-464.

Donnelly K E, Goldstein SL, Langmuir CH, Spiegelman M (2004). Origin of enriched ocean ridge basalts and implications for mantle dynamics. Earth and Planetary Sci Lett, 226(3-4), 347-366.

Duchêne S., Blichert-Toft J., Luais B., Télouk P. (1997) - The Lu-Hf dating of garnets and the ages of the Alpine high-pressure metamorphism. Nature, 387(6633), 586.

Duretz, T., & Gerya, T. V. (2013). Slab detachment during continental collision: Influence of crustal rheology and interaction with lithospheric delamination. Tectonophysics, 602, 124-140.

Engi, M., Bousquet, R., & Berger, A. (2004). Explanatory notes to the map: Metamorphic structure of the Alps-Central Alps. Mitteilungen der Österreichischen Mineralogischen Gesellschaft, 149, 157-173.

Engi, M. (2017) Petrochronology Based on REE-Minerals: Monazite, Allanite, Xenotime, Apatite: Review in Mineralogy and Geochemistry, 83, 365-418. doi: 10.2138/rmg.2017.83.12

England, P. C., & Thompson, A. B. (1984). Pressure—temperature—time paths of regional metamorphism I. Heat transfer during the evolution of regions of thickened continental crust. Journal of Petrology, 25(4), 894-928.

Ernst WG (1971) Metamorphic zonations on presumably subducted lithospheric plates from Japan, California, and the Alps. Contrib. Miner. Petrol., 34:43–59.

Ernst WG (1973) Blueschist metamorphism and *P-T* regimes in active subduction zones, Tectonophysics, 17:255–272.

Ernst WG, Liu J (1998) Experimental phase-equilibrium study of Al-and Ti-contents of calcic amphibole in MORB—A semiquantitative thermobarometer. Am mineral, 83(9-10), 952-969.

Ernst W.G. & Liou J.G. (2008) - High- and ultrahigh-pressure metamorphism: Past results and future prospects. Am. Mineral., 93: 1771-1786.

Escuder-Viruete J. & Pérez-Estaún A. (2006) - Subduction-related *P–T* path for eclogites and garnet glaucophanites from the Samaná Peninsula basement complex, northern Hispaniola. Int. J. Earth Sci., 95: 995–1017.

Evans MJ, Elliot *T*. 1999. Evolution of a thrust-sheet-top basin: The Tertiary Barrême Basin, Alpes de Haute Provence, France. Geol Soc Am Bull111:1617-1643. DOI: 10.1130/0016-7606(1999)111<1617:EOATST>2.3.CO;2.

Exley, R.A. (1980) Microprobe studies of REE-rich accessory minerals: implications for Skye granite petrogenesis and REE mobility in hydrothermal systems. Earth and Planetary Science Letters, 48(1), 97-110.

Faure-Muret A (1955) Etudes géologiques sur le Massif de l'Argentera-Mercantour et sur ses enveloppes sédimentaires. Paris: Mém Carte Géol France, pp. 336.

Ferrando S, Lombardo B, Compagnoni R (2008) Metamorphic history of HP mafic granulites from the Gesso-Stura Terrain (Argentera Massif, Western Alps, Italy). Eur J Mineral 20:777-790. doi: 10.1127/0935-1221/2008/0020-1891.

Ferrara G, Malaroda R (1969) Radiometric age of granitic rocks from the Argentera Massif (Maritime Alps). Boll Soc Geol It 88:311-320.

Fiannacca, P., Ortolano, G., Pagano, M., Visalli, R., Cirrincione, R., Zappalà, L. (2017). IG-Mapper: A new ArcGIS® toolbox for the geostatistics-based automated geochemical mapping of igneous rocks. Chem. Geol. 470: 75. doi: 10.1016/j.chemgeo.2017.08.024

Filippi, M., Zanoni, D., Gosso, G., Lardeaux, J. M., Verati, C., and Spalla, M. (2019). Structure of lamprophyres: a discriminant marker for Variscan and Alpine tectonics in the Argentera-Mercantour Massif, Maritime Alps. BSGF - Earth Sciences Bulletin, doi: 10.1051/bsgf/2019014

Finger, F., Broska, I., Roberts, M.P. and Schermaier, A. (1998) Replacement of primary monazite by apatite-allanite-epidote coronas in an amphibolite facies granite gneiss from the eastern Alps. American Mineralogist, 83, 248-258. doi:10.2138/am-1998-3-408.

Fischer, R.X. and Tillmanns, E. (1988) The equivalent isotropic displacement factor. Acta of Crystallography, C44, 775-776.

Fréville K, Trap P, Faure M, Melleton J, Li XH, 840 Lin W, Blein O, Bruguiere O, Poujol M (2018) Structural, metamorphic and geochronological insights on the Variscan evolution of the Alpine basement in the Belledonne Massif (France). Tectonophysics, 726 :14–42.

Franz, G., Thomas, S. and Smith, D.C. (1986) High-pressure phengite decomposition in the Weissenstein eclogite, Münchberger Gneiss Massif, Germany. Contributions to Mineralogy and Petrology, 92(1), 71-85.

Franz, G. and Liebscher, A. (2004) Physical and Chemical Properties of the Epidote Minerals. An Introduction. Reviews in mineralogy and geochemistry, 56(1), 1-81. doi: 10.2138/gsrmg.56.1.1

Frassi, C., Musumeci, G., Zucali, M., Mazzarini, F., Rebay, G., Langone, A. (2017). The Cotoncello Shear Zone (Elba Island, Italy): The deep root of a fossil oceanic detachment fault in the Ligurian ophiolites. Lithos. 278: 445. doi: 10.1016/j.lithos.2017.02.015

Frost B. R., Barnes C. G., Collins W. J., Arculus R. J., Ellis D. J., Frost C. D. (2001) - A geochemical classification for granitic rocks. J. Petrol., 42, 11, 2033–2048.

Ford M., Lickorish W. H. 2004. Foreland basin evolution around the western Alpine Arc. In: Joseph P. Lomas S. A. eds. Deep-Water Sedimentation in the Alpine Basin of SE France: New perspectives on the Grès d'Annot and related systems. Geol Soc London Spec Publ221: 39-63. doi: 10.1144/GSL.SP.2004.221.01.04.

Ford M., Lickorish W. H., Kusznir N. J. 1999. Tertiary foreland sedimentation in the southern Subalpine chains, SE France: a geodynamic analysis. Basin Res11: 315-336. DOI: 10.1046/j.1365-2117.1999.00103.x.Gerya and Stockhert, 2005

Fuhrman M.L., Lindsley D.H. 1988 Ternary-feldspar modeling and thermometry. American Mineralogist, 73, 201-215.

Gatta GD, Rotiroti N, Zucali M (2009) Plastic deformations in kyanites by tectonometamorphic processes: a single-crystal X-ray diffraction study. Min Mag 73(3): 359-371. https://doi.org/10.1180/minmag.2009.073.3.359

Gatta, G.D., Alvaro, M. and Bromiley, G. (2011a) A low temperature X-ray single-crystal diffraction and polarised infra-red study of epidote. Physics and Chemistry of Minerals, 39, 1–15. doi: 10.1007/s00269-011-0455-y

Gatta, G.D., Merlini, M., Lee, Y. and Poli, S. (2011b) Behavior of epidote at high pressure and high temperature: a powder diffraction study up to 10 GPa and 1,200 K. Physics and Chemistry of Minerals, 38, 419-428. doi: 10.1007/s00269-010-0415-y

Gatta, G.D., Milani, S., Corti, L., Comboni, D., Lotti, P., Merlini, M. and Liermann, H.P. (2019) Allanite at high pressure: effect of REE on the elastic behaviour of epidote-group minerals. Physics and Chemistry of Minerals, 46, 783-793. doi: 10.1007/s00269-019-01039-9

Gerya T.V., Stöckhert B., Perchuk A.L. (2002) - Exhumation of high-pressure metamorphic rocks in a subduction channel-a numerical simulation. Tectonics, 21, 6, 1056.

Gerya, T., and Stöckhert, B. (2006). Two-dimensional numerical modeling of tectonic and metamorphic histories at active continental margins. International Journal of Earth Sciences 95.2: 250-274.

Giere, R. and Sorensen, S. (2004) Allanite and Other REE-Rich Epidote-Group Minerals. Review in Mineralogy and Geochemistry, 56, 431-493. doi: 10.2138/gsrmg.56.1.431.

Giuntoli F. & Engi M. (2016) - Internal geometry of the central Sesia Zone (Aosta Valley, Italy): HP tectonic assembly of continental slices. Swiss J. Geosci., 109(3), 445-471, doi: 10.1007/s00015-016-0225-4.

Giuntoli F, Lanari P, Engi M (2018a) Deeply subducted continental fragments – Part 1: Fracturing, dissolution–precipitation, and diffusion processes recorded by garnet textures of the central Sesia Zone (western Italian Alps). Solid Earth 9: 167–189, https://doi.org/10.5194/se-9-167-2018

Giuntoli F, Lanari P, Burn M, Kunz BE, Engi M (2018b) Deeply subducted continental fragments - Part 2: Insight from petrochronology in the central Sesia Zone (western Italian Alps). Solid Earth 9(1): 191–222. https://doi.org/10.5194/se-9-191-2018

Gonzalez, R., Woods, R. (2002). Digital Image Processing. Prentice Hall. doi: 10.1016/0734-189X(90)90171-Q

Gosso G. (1977) - Metamorphic evolution and fold history in the eclogite micaschists of the upper Gressoney valley (Sesia-Lanzo zone, Western Alps). Rend. Soc. Ital. Mineral. Petrol., 33, 389–407.

Gosso G., Kienast J.R., Lardeaux J.M., Lombardo B. (1982) - Replissement intense et transposition (en climat me´tamor- phique de haute pression) fes contacts tectoniques majeurs dans l'edifice supe´ rieur des nappes alpines (zone Sesia-Lanzo). C. R. Acad. Sci. Paris, 294, 343–348.

Gosso G., Messiga B., Rebay G., Spalla M. I. (2010). Interplay between deformation and metamorphism during eclogitization of amphibolites in the Sesia-Lanzo Zone of the Western Alps. Int. Geol. Rev., 52(10), 1193-1219, doi: 10.1080/00206810903529646.

Gosso G., Rebay G., Roda M., Spalla M. I., Tarallo M., Zanoni D., Zucali M. (2015) - Taking advantage of petrostructural heterogeneities in subduction-collisional orogens, and effect on the scale of analysis. Period. Mineral. (2015), 84(3B), 779-825, doi: 10.2451/2015PM0452.

Gosso G, Lardeaux JM, Zanoni D, Volante S, Corsini M, Bersezio R, et al. (2019). Mapping the progressive geologic history at the junction of the Alpine Mountain Belt and the Western Mediterranean Ocean. Ofioliti, 44(2), 97-110.

Graham C.M. & Powell R. (1984) - A garnet-hornblende geothermometer: Calibration, testing, and application to the Pelona Schist, southern California. J. Metamorph. Geol., 2, 13-21.

Green N. & Usdansky S.I. (1986) - Toward a practical plagioclase-muscovite thermometer. Am. Mineral., 71(9-10), 1109-1117.

Gregory, C.J., Rubatto, D., Allen, M.A., Williams, I.S., Hermann, J. and Ireland, T. (2007) Allanite micro-geochronology: A LA-ICP-MS and SHRIMP U–Th–Pb study. Chemical Geology, 245, 162-182. doi: 10.1016/j.chemgeo.2007.07.029

Gregory, C.J., Rubatto, D., Hermann, J., Berger, A. and Engi, M. (2012) Allanite behaviour during incipient melting in the southern Central Alps. Geochimica et Cosmochimica Acta, 84, 433-458. doi: 10.1016/j.gca.2012.01.020

Gromet, L.P. and Silver, L.T. (1983) Rare earth element distributions among minerals in a granodiorite and their petrogenetic implications. Geochimica et Cosmochimica Acta, 47(5), 925-939. doi: 10.1016/0016-7037(83)90158-8

Guillot S, Di Paola S, Ménot RP, Ledru P, Spalla MI, Gosso G, Schwartz S (2009) Suture zones and importance of strike-slip faulting for Variscan geodynamic reconstructions of the External Crystalline Massifs of the western Alps. Bull Soc géol Fr 6: 483-500.

Guillen A, Courrioux G, Bourgine B (2011) 3D kriging using potential fields surfaces. IAMG Conference, Salzburg proceedings 1: 735-741.

Halama R, Glodny J, Konrad-Schmolke M, Sudo M (2018) Rb-Sr and in situ $^{40}Ar/^{39}Ar$ dating of exhumation-related shearing and fluid-induced recrystallization in the Sesia zone (Western Alps, Italy): Geosphere 14 (4): 1425–1450, https://doi.org/10.1130/GES01521.1

Handy, M. R., Babist, J., Wagner, R., Rosenberg, C. L., & Konrad, M. (2005). Decoupling and its relations to strain partitioning in continental lithosphere: Insight from the Periadriatic fault system (European Alps). Special Publications, Geological Society of London, 243(1), 249–276.

Hayama, Y. (1959). Some considerations on the color of biotite and its relation to metamorphism. The Journal of the Geological Society of Japan 65(760): 21. doi: 10.5575/geosoc.65.21

Henry D.J., Guidotti C.V., Thomson J.A. (2005) - The Ti-saturation surface for low-to-medium pressure metapelitic biotites: Implications for geothermometry and Ti-substitution mechanisms. Am. Mineral., 90(2-3), 316-328.

Hermann, J. (2002) Allanite: thorium and light rare earth element carrier in subducted crust. Chemical Geology, 192, 289-306. doi: 10.1016/S0009-2541(02)00222-X

Hermann, J. and Rubatto, D. (2009) Accessory phase control on the trace element signature of sediment melts in subduction zones. Chemical Geology, 265, 512-526. doi: 10.1016/j.chemgeo.2009.05.018

Hey M.H. (1954) - A new review of the chlorites. Mineral. Mag. 80, 277-292.

Hobbs BE, Means WD, Williams PF (1976) An outline of structural geology. Wiley. 571p.

Hobbs BE, Ord A, Spalla MI, Gosso G, Zucali M (2010) The interaction of deformation and metamorphic reactions. Geol Soc London Special Pub 332(1): 189-223. https://doi.org/10.1144/SP332.12

Hobbs BE, Ord A, Regenauer-Lieb K (2011) The thermodynamics of deformed metamorphic rocks: A review. J Struct Geol 33: 758-818. http://doi.org/10.1016/j.jsg.2011.01.013

Hurford AJ, Hunziker JC (1985) Alpine cooling history of the Monte Mucrone eclogites (Sesia-Lanzo zone): fission track evidence. Schweiz Miner Petrogr Mitt 65: 325-334.

Holland T.J.B. (1980) - The reaction albite = jadeite + quartz determined experimentally in the range 600°-1200°C. Am. Mineral., 65, 129–134.

Holland, T., & Powell, R. (1996). Thermodynamics of order-disorder in minerals; II, Symmetric formalism applied to solid solutions. American Mineralogist, 81(11-12), 1425-1437.

Holland T. J. B. & Powell R. (1998) - An internally consistent thermodynamic data set for phases of petrological interest. J. Metamorph. Geol., 16(3), 309-343.

Holland TJB, Powell R (2001) Calculation of phase relations involving haplogranitic melts using an internally consistent thermodynamic dataset. Journal of Petrology, 42(4), 673-683.

Hy C (1984) Métamorphisme polyphasé et evolution tectonique dans la croûte continentale éclogitisée: les series granitiques et pélitiques du Monte Mucrone (zone Sesia-Lanzo, Alpes italiennes). Université Paris VI. PhD thesis, 200 p.

Huddlestone-Holmes, C. R., Ketcham, R. A. (2010). An X-ray computed tomography study of inclusion trail orientations in multiple porphyroblasts from a single sample. Tectonophysics. 480(1-4): 305. doi: 10.1016/j.tecto.2009.10.021

Ildefonse B, Lardeaux JM, Caron JM (1990) The behavior of shape preferred orientations in the metamorphic rocks: amphiboles and jadeites from the Monte Mucrone Area (Sesia-Lanzo Zone, Italian Western Alps). J Struct Geol 12: 1005–1011. https://doi.org/10.1016/0191-8141(90)90096-H

Janák, M., Froitzheim, N., Lupták, B., Vrabec, M., & Ravna, E. J. K. (2004). First evidence for ultrahigh-pressure metamorphism of eclogites in Pohorje, Slovenia: Tracing deep continental subduction in the Eastern Alps. Tectonics, 23(5)

Janots, E., Brunet, F., Goffé, B., Poinssot, C., Burchard, M. and Cemič, L. (2007) Thermochemistry of monazite-(La) and dissakisite-(La): implications for monazite and allanite stability in metapelites: Contribution in Mineralogy and Petrology, 154, 1-14, doi: 10.1007/s00410-006-0176-2

Janots, E., Engi, M., Berger, A., Allaz, J., Schwarz, J.O. and Spandler, C. (2008) Prograde metamorphic sequence of REE minerals in pelitic rocks of the Central Alps: implications for allanite–monazite–xenotime phase relations from 250 to 610°C. Journal of Metamorphic Geology, 26, 509-526. doi: 10.1111/j.1525-1314.2008.00774.x

Johnson, S. E., & Duncan, A. C. (1992). Fault identification in complexly deformed schist terrains: examples from the USA and Australia. Tectonophysics, 216(3-4), 291-308.

Johnson SE, Vernon RH (1995) Inferring the timing of porphyroblast growth in the absence of continuity between inclusion trails and matrix foliations; can it be reliably done? J Struct Geol 17: 1203–1206. https://doi.org/10.1016/0191-8141(95)00021-5

Jowett E.C. (1991) - Fitting iron and magnesium into the hydrothermal chlorite geothermometer: GAC/MAC/SEG. Joint Annual Meeting (Toronto, May 27-29, 1991), Program with Abstracts 16, A62.

Kamzolkin VA, Ivanov SD, Konilov, AN (2016) Empirical phengite geobarometer: Background, calibration, and application. Geology of Ore Deposits, 58(8), 613-622.

Kapferer N., Mercolli I., Berger A., Ovtcharova M., Fügenschuh B. (2012) - Dating emplacement and evolution of the orogenic magmatism in the internal Western Alps: The Biella Volcanic Suite. Swiss J. Geosci., 105, 67-84, doi: 10.1007/s00015-012-0092-6

Ketcham, R.A. (2005) Three-dimensional grain fabric measurements using high-resolution X-ray computed tomography. J Struct Geol, 27, 1217-1228, doi: 10.1016/j.jsg.2005.02.006

Ketcham, R.A. and Carlson, W.D. (2001) Acquisition, optimization and interpretation of X-ray computed tomographic imagery: applications to the geosciences. Comput Geosci, 27, 381-400, doi: 10.1016/S0098-3004(00)00116-3

Kim, Y., Cheong, C.S., Lee, Y. and Williams, I.S. (2009) SHRIMP allanite U-Th-Pb dating of bimodal Triassic metamorphism of Neoarchean tonalitic gneisses, Daeijak Island, central Korea. Geosciences Journal, 13(3), 305-315.

Kerckhove C. 1969. La Zone du flysch dans les nappes de l'Embrunais-Ubaye (Alpes occidentales). Géol Alp 45:5-204.

Kohn MJ, Spear FS (1990) Two new geobarometers for garnet amphibolites, with applications to southeastern Vermont. American Mineralogist, 75(1-2), 89-96.

Koons, P. O. (1982). An investigation of experimental and natural high-pressure assemblages from Sesia Zone, Western Alps, Italy. PhD Thesis. Zürich: ETH Zürich.

Koons PO, Rubie DC, Frueh-Green G (1987) The effects of disequilibrium and deformation on the mineralogical evolution of quartz-diorite during metamorphism in the eclogite facies. J Petrol 28: 679–700. https://doi.org/10.1093/petrology/28.4.679

Kretz, R. (1983). Symbols for rock-forming minerals. American Mineralogist, 68, 277–279.

Krogh-Ravna E. (2000) - The garnet–clinopyroxene Fe^{2+}–Mg geothermometer: an updated calibration. J. Metamorph. Geol.,18, 211–219.

Krogh-Ravna E. & Paquin J. (2003) - Thermobarometric methodologies applicable to eclogites and garnet ultrabasites. EMU notes in mineralogy, 5(8), 229-259.

Kunz B. E., Manzotti P., von Niederhäusern B., Engi M., Darling J. R., Giuntoli F., Lanari, P. (2017) - Permian high-temperature metamorphism in the Western Alps (NW Italy). Int. J. Earth. Sci., 1-27.

Labaume, P., Jolivet, M., Souquière, F., & Chauvet, A. (2008). Tectonic control on diagenesis in a foreland basin: combined petrologic and thermochronologic approaches in the Grès d'Annot basin (Late Eocene–Early Oligocene, French–Italian external Alps). Terra Nova, 20(2), 95-101.

Laird J. & Albee A.L. (1981) - Pressure, temperature, and time indicators in mafic schist; their application to reconstructing the polymetamorphic history of Vermont. Am. J. Sci., 281(2), 127-175.

Lajaunie C, Courrioux G, Manuel L (1997) Foliation fields and 3D cartography in Geology. Math Geol 29(4): 571–584. https://doi.org/10.1007/BF02775087

Lanari, P., Vidal, O., De Andrade, V., Dubacq, B., Lewin, E., Grosch, E. G., Schwartz, S. (2014). XMapTools: A MATLAB©-based program for electron microprobe X-ray image processing and geothermobarometry. Comp. Geosci. 62: 227. doi: 10.1016/j.cageo.2013.08.010

Lardeaux JM, Gosso G, Kienast JR, Lombardo B (1982a) Chemical variations in phengitic micas of successive foliations within the Eclogitic Micaschists complex, Sesia-Lanzo zone (Italy, Western Alps). Bull Minéral 106: 673-689.

Lardeaux J. M., Gosso G., Kiénast J. R., Lombardo B. (1982) - Relations entre le metamorphisme et la déformation dans la zone Sesia-Lanzo (Alpes Occidentales) et le problème de l'eclogitisation de la croute continentale. B. Soc. Geol. Fr., 24(7), 793–800.

Lardeaux JM, Lombardo B, Gosso G & Kienast JR (1983) Découverte de paragenèses à ferro-omphacites dans les orthogneiss de la zone Sesia-Lanzo septentrionale (Alpes Italiennes). C R Acad Sci Paris 296: 453-456.

Lardeaux J. M. & Spalla M. I. (1990) - Tectonic significance of *P*-*T*-t paths in metamorphic rocks: examples from Alpine and Variscan orogenic belts. Mem. Soc. Geol. Ital., 45, 51-69.

Lardeaux J. M. & Spalla M. I. (1991) - From granulites to eclogitesin the Sesia zone (Italian Western Alps): A record of the opening and closure of the Piedmont ocean. J. Metamorph. Geol., 9, 35–59.

Lardeaux J. M. (2014) - Deciphering orogeny: a metamorphic perspective. Examples from European Alpine and Variscan belts Part I: Alpine metamorphism in the western Alps. A review. B. Soc. Geol. Fr., 185(2), 93-114.

Latouche L, Bogdanoff S (1987) Evolution précoce du massif de l'Argentera: apport des eclogites et des granulites. Géol Alp 63:151-164.

Lee, D.E. and Silver, L.T. (1964) Accessory minerals in some granitic rocks in California and Nevada as a function of calcium content. American Mineralogist, 49, 1660-1670.

Lemoine M, Bas T, Arnaud-Vanneau A, Arnaud H, Dumont T, Gidon M, Bourbon M, de Graciansky PC, Rudkiewicz JL, Megard-Galli J, Tricart T. 1986. The continental margin of the Mesozoic Tethys in the Western Alps. Mar Petroleum Geol (3):179-199. DOI: 10.1016/0264-8172(86)90044-9.

Liermann H.P., Isachsen C., Altenberger U., Oberhansli R. (2002) - Behaviour of zircon during high-pressure, low-temperature metamorphism: Case study from the Internal Unit of the Sesia Zone (Western Italian Alps). Eur. J. Mineral., 14, 61–71.

Li, X., Di, L., Han, W., Zhao, P., Dadi, U. (2010). Sharing geoscience algorithms in a Web service-oriented environment (GRASS GIS example). Comp. Geosci. 36(8): 1060. doi: 10.1016/j.cageo.2010.03.004

Liou J.G., Tsujimori T., Zhang R.Y., Katayama I., Maruyama S. (2004) - Global UHP Metamorphism and Continental Subduction/Collision: The Himalayan Model. Int. Geol. Rev., 46, 1-27.

Liu, X., Dong, S., Xue, H. and Zhou, J. (1999) Significance of allanite-(Ce) in granitic gneisses from the ultrahigh-pressure metamorphic terrane, Dabie Shan, central China: Mineralogical Magazine, 63, 579-586. doi: 10.1180/minmag.1999.063.4.10

Liu, X., Shieh, S.R., Fleet, M.E. and Zhang, L. (2009) Compressibility of a natural kyanite to 17.5 GPa. Progress in Natural Science, 19, 1281-1286. doi: 10.1016/j.pnsc.2009.04.001

Locock A.J. (2014) - An Excel spreadsheet to classify chemical analyses of amphiboles following the IMA 2012 recommendations. Computers & Geosciences, 62, 1–11.

Ludwig, K.R., 2001. Users manual for Isoplot/Ex version 2.49. Berkeley Geochronology Center Special Publication, 1a.

Manzotti P., Ballèvre M., Zucali M., Robyr M., Engi M. (2014) - The tectonometamorphic evolution of the Sesia-Dent Blanche nappes (internal Western Alps): review and synthesis. Swiss J. Geosci., 107, 309-336, doi: 10.1007/s00015-014-0172-x.

Macente, A., Fusseis, F., Menegon, L., Xiao, X., John, T. (2017). The strain-dependent spatial evolution of garnet in a high-*P* ductile shear zone from the Western Gneiss Region (Norway): a synchrotron X-ray microtomography study. J. Metamorph. Geol. 36(9): 1287. doi: 10.1111/jmg.12245

Malaroda R, Carraro F, Dal Piaz GV, Franceschetti B, Sturani C, Zanella E (1970) Carta geologica del Massiccio dell' Argentera alla scala 1:50.000 e note illustrative. Mem Soc Geol It 9:557-663.

Malusà, M. G., Faccenna, C., Garzanti, E., & Polino, R. (2011). Divergence in subduction zones and exhumation of high pressure rocks (Eocene Western Alps). Earth and Planetary Science Letters, 310(1-2), 21-32.

Mancel, P., & Merle, O. (1987). Kinematics of the northern part of the Simplon Line (Central Alps). Tectonophysics, 135(4), 265-275.

Marquer, D., Challandes, N., & Baudin, T. (1996). Shear zone patterns and strain distribution at the scale of a Penninic nappe: the Suretta nappe (Eastern Swiss Alps). Journal of structural Geology, 18(6), 753-764.

Manzotti, P., Bosse, V., Pitra, P., Robyr, M., Schiavi, F. and Ballèvre, M. (2018) Exhumation rates in the Gran Paradiso Massif (Western Alps) constrained by in situ U–Th–Pb dating of accessory phases (monazite, allanite and xenotime). Contributions to Mineralogy and Petrology, 173(3), 24. doi: 10.1007/s00410-018-1452-7

Marotta AM, Spalla MI, Gosso G (2009) Upper and lower crustal evolution during lithospheric extension: numerical modelling and natural footprints from the European Alps. Geol Soc London Special Pub 321: 33–72. https://doi.org/10.1144/SP321.3

Massonne H.J. & Schreyer W. (1987) - Phengite geobarometry based on the limiting assemblage with K-feldspar, phlogopite and quartz. Cont. Miner. Petrol., 96, 21-22.

Meda M., Marotta A.M., Spalla M.I. (2010) - The role of mantle hydration into the continental crust recycling in the wedge region. Geological Society, London, Special Publications, 332, 149–172.

Merle O, Brun JP. 1984. The curved translation path of the Parpaillon Nappe (French Alps). J Struct Geol6(6):711-719. DOI: 10.1016/0191-8141(84)90010-5.

Miller, C., Mundil, R., Thöni, M., & Konzett, J. (2005). Refining the timing of eclogite metamorphism: a geochemical, petrological, Sm-Nd and U-Pb case study from the Pohorje Mountains, Slovenia (Eastern Alps). Contributions to Mineralogy and Petrology, 150(1), 70-84.

Miyashiro A (1961) Evolution of metamorphic belts. Journal of petrology, 2(3), 277-311.

Middlemost, E.A., Magmas, K., and Rocks, M. (1985). An Introduction to Igneous Petrology. Magma and magmatic Rocks. Longmans, Ed.

Morimoto N. (1988) - Nomenclature of pyroxenes. Mineral. Mag., 52, 535–550.

Moore, J.M. and McStay, J. H. (1990) The formation of allanite-(Ce) in calcic granofelses, Namaqualand, South Africa. The Canadian Mineralogist, 28(1), 77-86.

Mørk, M. B. (1985). A gabbro eclogite transition of Flemsoy, Suamore, western Norway. Chemical Geology, 50, 283-310, doi:10.1016/0009-2541(85)90125-1.

Meyer, F., Beucher, S. (1990). Morphological segmentation. J. Vis. Commun. Image Represent. 1: 21. doi: 10.1016/1047-3203(90)90014-M

Myers, J. S. (1970). Gneiss types and their significance in the repeatedly deformed and metamorphosed Lewisian complex of Western Harris, Outer Hebrides. Scot. J. Geol. 6: 186. doi: 10.1144/sjg06020186

Musumeci G, Colombo F (2002) Late Visean mylonitic granitoids in the Argentera Massif (Western Alps, Italy): age and kinematic constraints on the Ferriere-Mollières shear zone. C. R. Geosciences 334: 213-220

Oberhänsli R, Hunziker JC, Martinotti G, Stern WB (1985) Geochemistry, geochronology and petrology of Monte Mucrone: an example of Eo-Alpine eclogitization of Permian granitoids in the

Sesia-Lanzo Zone, Western Alps, Italy. Chem Geol 52(2): 165-184. https://doi.org/10.1016/0168-9622(85)90016-8

Ortolano, G., Zappalà, L. and Mazzoleni, P. (2014) X-Ray Map Analyser: A new ArcGIS® based tool for the quantitative statistical data handling of X-ray maps (Geo-and material-science applications). Computer and Geosciences, 72, 49-58. doi: 10.1016/j.cageo.2014.07.006

Ortolano, G., Visalli, R., Cirrincione, R., Rebay, G. (2014b). PT-path reconstruction via unraveling of peculiar zoning pattern in atoll shaped garnets via image assisted analysis: an example from the Santa Lucia del Mela garnet micaschists (northeastern Sicily-Italy). Period. Mineral. 83(2): 257. doi: 10.2451/2013PM0015

Ortolano, G., Visalli, R., Godard, G. and Cirrincione, R. (2018) Quantitative X-ray Map Analyser (Q-XRMA): A new GIS-based statistical approach to Mineral Image Analysis. Computers and Geosciences, 115, 56-65. doi: 10.1016/j.cageo.2018.03.001

Otten M.T. (1984) - The origin of brown hornblende in the Artssjallet gabbros and dolerites. Cont. Mineral. Petrol., 86, 185-199.

Paquette JL, Menot RP, Peucat JJ (1989) REE, SmNd and UPb zircon study of eclogites from the Alpine External Massifs (Western Alps): evidence for crustal contamination. Earth and Planetary Science Letters, 96(1-2), 181-198.

Parrish, R. R. (2001). The response of mineral chronometers to metamorphism and deformation in orogenic belts. Geological Society, London, Special Publications, 184(1), 289-301.

Park RG (1969) Structural correlations in metamorphic belts. Tectonophysics 7: 323–338. https://doi.org/10.1016/0040-1951(69)90077-8

Passchier C. W., Urai J. L., Van Loon J., Williams P. F. (1981) - Structural geology of the central Sesia Lanzo Zone. Geol. Mijnbouw, 60, 497-507.

Passchier, C. W., Myers, J. S., & Kroner, A. (1990). Field Geology of High-Grade Gneiss Terrains. Springer-Verlag Berlin Heidelberg.

Passchier CW, Trouw RA (2005) Microtectonics. Springer Berlin, 366 p.

Pearce JA (1982) Trace element characteristics of lavas from destructive plate boundaries. Andesites, 8, 525-548.

Pearce MA, Wheeler J (2010) Modelling grain-recycling zoning during metamorphism. J Metam Geol 28: 423–437. https://doi.org/10.1111/j.1525-1314.2010.00872.x

Peressini, G., Quick, J. E., Sinigoi, S., Hofmann, A. W., & Fanning, M. (2007). Duration of a large mafic intrusion and heat transfer in the lower crust: a SHRIMP U–Pb zircon study in the Ivrea–Verbano Zone (Western Alps, Italy). Journal of Petrology, 48(6), 1185-1218.

Plyusnina LP (1982) Geothermometry and geobarometry of plagioclase-hornblende bearing assemblages. Contributions to Mineralogy and Petrology, 80(2), 140-146.

Pognante U., Compagnoni R., Gosso G. (1980) - Micro-mesostructural relationships in the continental eclogitic rocks of the Sesia-Lanzo zone: a record of a subduction cycle (Italian Western Alps). Rend. Soc. Ital. Mineral. Petrol., 36, 169–186.

Pognante U., Talarico F., Rastelli N., Ferrati N. (1987) - High pressure metamorphism in the nappes of the Valle dell'Orco traverse (Western Alps collisional belt). J. Metamorph. Geol., 5, 397-414.

Pognante U. (1989) - Lawsonite, blueschist and eclogite formation in the southern Sesia Zone (Western Alps, Italy). Eur. J. Mineral., 1, 89-104.

Pognante U (1989b) Tectonic implications of lawsonite formation in the Sesia zone (Western Alps). Tectonophysics 162(3-4): 219-227. https://doi.org/10.1016/0040-1951(89)90245-X

Pognante U. (1991) - Petrological constraints on the eclogite- and blueschist-facies metamorphism and *P-T*-t paths in the Western Alps. J. Metamorph. Geol., 9(1), 5-17, doi: 10.1111/j.1525-1314.1991.tb00501.x.

Polacci, M., Mancini, L., Baker, D.R. (2010). The contribution of synchrotron X-ray computed microtomography to understanding volcanic processes. J. of Synchrotron Rad. 17: 215. doi: 10.1107/S0909049509048225

Polino R., Dal Piaz G.V., Gosso G. (1990) - Tectonic erosion at the Adria margin and accretionary processes for the Cretaceous orogeny of the Alps. Mem. S. Geo. F., 156, 345-367.

Powell R. (1985) - Regression diagnostics and robust regression in geothermometer/geobarometer calibration: the garnet-clinopyroxene geothermometer revisited. J. Metamorph. Geol., 3(3), 231-243.

Pradhan, B. (2013). A comparative study on the predictive ability of the decision tree, support vector machine and neuro-fuzzy models in landslide susceptibility mapping using GIS. Comp. Geosci. 51: 350. doi: 10.1016/j.cageo.2012.08.023

Qin, F.W., Wang, Y., Fan, D., Qin, S., Yang, K., Townsend, J.P. and Jacobsen, S.D. (2016) High-pressure behavior of natural single-crystal epidote and clinozoisite up to 40 GPa. Physics and Chemistry of Minerals, 43, 649-659. doi: 10.1007/s00269-016-0824-7

Radulescu, I.G., Rubatto, D., Gregory, C. and Compagnoni, R. (2009) The age of HP metamorphism in the Gran Paradiso Massif, Western Alps: a petrological and geochronological study of “silvery micaschists”. Lithos, 110(1-4), 95-108. doi: 10.1016/j.lithos.2008.12.008

Ramsay, J. G., & Huber, M. I. (1983). The techniques of modern structural geology: strain analysis (Vol. 1). Academic press.

Ramsay, J. G., & Lisle, R. J. (2000). Applications of continuum mechanics in structural geology (Techniques of modern structural geology. Vol. 3) (Vol. 3). Academic Press.

Ramsbotham W., Inger S., Cliff B., Rex D., Barnicoat, A. (1994) - Time constraints on the metamorphic and structural evolution of the southern Sesia-lanzo Zone, Western Italian Alps. Mineral. Mag., 58A, 758-759.

Rasmussen, B., Muhling, J.R., Fletcher, I.R. and Wingate, M.T.D. (2006) In situ SHRIMP U-Pb dating of monazite integrated with petrology and textures: Does bulk composition control whether monazite

forms in low-Ca pelitic rocks during amphibolite facies metamorphism? Geochimica et Cosmochimica Acta, 70, 3040-3058. doi: 10.1016/j.gca.2006.03.025

Ratschbacher, L., Frisch, W., Neubauer, F., Schmid, S. M., & Neugebauer, J. (1989). Extension in compressional orogenic belts: the eastern Alps. Geology, 17(5), 404-407.

Rebay G. & Spalla M.I. (2001) - Emplacement at granulite facies conditions of the Sesia–Lanzo metagabbros: an early record of Permian rifting? (Sesia–Lanzo zone, Italy). Lithos, 98(1), 85-104.

Rebay G. & Messiga B. (2007) - Prograde metamorphic evolution and development of chloritoid-bearing eclogitic assemblages in subcontinental metagabbro (Sesia–Lanzo zone, Italy). Lithos, 58, 275-291.

Rebay G, Riccardi MP, Spalla, MI (2015) Fluid rock interactions as recorded by Cl-rich amphiboles from continental and oceanic crust of Italian orogenic belts. Per Miner 84: 751-777. https://doi.org/10.2451/2015PM0453

Rebay G, Zanoni D, Langone A, Luoni P, Tiepolo M, Spalla MI (2018) Dating of ultramafic rocks from the Western Alps ophiolites discloses Late Cretaceous subduction ages in the Zermatt-Saas Zone. Geol Mag 155: 298-315. https://doi.org/10.1017/S0016756817000334

Regis D., Rubatto D., Darling J., Cenki-Tok B., Zucali M., Engi, M. (2014) - Multiple metamorphic stages within an eclogite facies terrane (Sesia Zone, Western Alps) revealed by U/Th-Pb petrochronology. J. Petrol., 55(7), 1429-1456, doi: 10.1093/petrology/egu029.

Reinsch, D. (1979). Glaucophanites and eclogites from Val Chiusella, Sesia-Lanzo zone (Italian Alps). Contrib. Mineral. Petr., 70(3), 257-266.

Ridley J (1989) Structural and metamorphic history of a segment of the Sesia-Lanzo Zone, and its bearing on the kinematics of Alpine deformation in the Western Alps. Geol Soc London Spec Publ 45: 189–201. https://doi.org/10.1144/GSL.SP.1989.045.01.10

Roda, M. & Zucali, M. (2008). Meso and microstructural evolution of the Mont Morion metaintrusive complex (Dent Blanche nappe, Austroalpine Domain, Valpelline, Western Italian Alps). Bollettino della Società Geologica Italiana, 127, 105-123.

Roda M., Marotta A.M., Spalla M.I. (2010) - Numerical simulations of an ocean-continent convergent system: influence of subduction geometry and mantle wedge hydration on crustal recycling. Geochem. Geophy. Geosy., 11(5).

Roda M. & Zucali M. (2011) - Tectono-metamorphic map of the Mont Morion Permian metaintrusives (Mont Morion—Mont Collon—Matterhorn Complex, Dent Blanche Unit), Valpelline—Western Italian Alps. J. Maps, 7(1), 519-535.
Roda M., Spalla M. I., Marotta A. M. (2012) - Integration of natural data within a numerical model of ablative subduction: A possible interpretation for the Alpine dynamics of the Austroalpine crust. J. Metamorph. Geol., 30, 973-996, doi:10.1111/jmg.12000.

Roda M., De Salvo F., Zucali M., Spalla M.I. (2018) – Structural and metamorphic evolution of a tectonic mixing: is Rocca Canavese Thrust Sheet (Italian Western Alps) a subduction-related mélange? Ital. J. Geosci., in this volume.

Roda M, Regorda A, Spalla MI, Marotta AM (2018b) What drives Alpine Tethys opening? clues from the review of geological data and model predictions. Geol J. https://doi.org/10.1002/gj.3316

Roda, M., Zucali, M., Li, Z., Spalla, M. I. (2018c). Pre-Alpine contrasting tectono-metamorphic evolutions within the Southern Steep Belt, Central Alps. Lithos. 310: 31. doi: 10.1016/j.lithos.2018.03.025

Roda, M., Zucali, M., Regorda, A., Spalla, M. I. (2019). Formation and evolution of a subduction-related mélange: The example of the Rocca Canavese Thrust Sheets (Western Alps). Geol. Soc. Am. Bull. in press.

Roda, M., Regorda, A., Spalla, M. I., & Marotta, A. M. (2019b). What drives A lpine Tethys opening? Clues from the review of geological data and model predictions. Geological Journal, 54(4), 2646-2664.

Romain J, Vernet J. 1978. Decouverte d'un volcanisme basique d'age permien dans la vallee de la Gordolasque (Sud-Ouest du massif de l'Argentera-Mercantour, Alpes-Maritimes, France). BullSoc géol FrS7-XX(6):929-933. DOI: 10.2113/gssgfbull.S7-XX.6.929.

Romer, R. L., Schärer, U., & Steck, A. (1996). Alpine and pre-Alpine magmatism in the root-zone of the Western Central Alps. Contributions to Mineralogy and Petrology, 123, 138–158.

Rosenbaum, G., & Lister, G. S. (2004). Neogene and Quaternary rollback evolution of the Tyrrhenian Sea, the Apennines, and the Sicilian Maghrebides. Tectonics, 23(1).

Rosenbaum, G., & Lister, G. S. (2005). The Western Alps from the Jurassic to Oligocene: spatio-temporal constraints and evolutionary reconstructions. Earth-Science Reviews, 69(3-4), 281-306.
Royden, L. (1996). Coupling and decoupling of crust and mantle in convergent orogens: Implications for strain partitioning in the crust. Journal of Geophysical Research: Solid Earth, 101(B8), 17679-17705.

Rubatto D., Gebauer D., Fanning M. (1998) - Jurassic formation and Eocene subduction of the Zermatt–Saas-Fee ophiolites: Implications for the geodynamic evolution of the Central and Western Alps. Contrib. Mineral. Petr., 132, 269–287.

Rubatto D., Gebauer D., Compagnoni R. (1999) - Dating of eclogite facies zircons: The age of Alpine metamorphism in the Sesia-Lanzo Zone (Western Alps). Earth Planet Sc. Lett., 167, 141–158.

Rubatto D, Schaltegger U, Lombardo B, Colombo F, Compagnoni R (2001) Complex Paleozoic magmatic and metamorphic evolution in the Argentera Massif (Western Alps), resolved with U-Pb dating. Schweiz Mineral Petrogr Mitt 81:213-228. doi: 10.5169/seals-61689.

Rubatto D, Ferrando S, Compagnoni R, Lombardo B. 2010. Carboniferous high-pressure metamorphism of Ordovician protoliths in the Argentera Massif (Italy), Southern European Variscan belt. Lithos 116(1-2):65-76. doi: 10.1016/j.lithos.2009.12.013.

Rubatto D., Regis D., Hermann J., Boston K., Engi M., Beltrando M., McAlpine, S. R. B. (2011) - Yo-yo subduction recorded by accessory minerals in the Italian Western Alps. Nat. Geosci., 4, 338-342, doi: 10.1038/NGEO1124.

Ruh, J. B., Le Pourhiet, L., Agard, P., Burov, E., & Gerya, T. (2015). Tectonic slicing of subducting oceanic crust along plate interfaces: Numerical modeling. Geochemistry, Geophysics, Geosystems, 16(10), 3505-3531.

Saccani E (2015) A new method of discriminating different types of post-Archean ophiolitic basalts and their tectonic significance using Th-Nb and Ce-Dy-Yb systematics. Geosc Front 6:481-501.

Salvi F., Spalla M. I., Zucali M., Gosso G. (2010) - Three-dimensional evaluation of fabric evolution and metamorphic reaction progress in polycyclic and polymetamorphic terrains: a case from the Central Italian Alps. Geological Society, London, Special Publications, 332(1), 173-187.

Sanchez G, Rolland Y, Schneider J, Corsini M, Oliot E, Goncalves P, Verati C, Lardeaux JM, Marquer D (2011) Dating low-temperature deformation by $^{40}Ar/^{39}Ar$ on white mica, insights from the Argentera-Mercantour Massif (SW Alps). Lithos 125(1):521-536. doi: 10.1016/j.lithos.2011.03.009.

Sayab, M., Suuronen, J. P., Hölttä, P., Aerden, D., Lahtinen, R., Kallonen, A. P. (2015). High-resolution X-ray computed microtomography: A holistic approach to metamorphic fabric analyses. Geology. 43(1): 55. doi: 10.1130/G36250.1

Sayab, M., Suuronen, J. P., Molnár, F., Villanova, J., Kallonen, A., O'Brien, et al. (2016). Three-dimensional textural and quantitative analyses of orogenic gold at the nanoscale. Geology. 44(9): 739. doi: 10.1130/G38074.1

Sayab, M., Miettinen, A., Aerden, D., Karell, F. (2017). Orthogonal switching of AMS axes during type-2fold interference: Insights from integrated X-ray computed tomography, AMS and 3D petrography. J. Struct. Geol. 103: 1. doi: 10.1016/j.jsg.2017.09.002

Schettino, A., Turco, E., 2006. Plate kinematics of the western Mediterranean region during the Oligocene and early Miocene. Geophysical Journal International 166, 1398–1423, http://dx.doi.org/10.1111/j.1365-246X.2006.02997.x.

Scheuring B., Ahrendt H., Hunziker J. T., Zingg A. (1974) - Palaeobotanical and geochronological evidence for the Alpine age of the metamorphism in the Sesia-Zone. Geol. Rundsch., 63(1), 305-326.

Schmalholz S. M. and Podladchikov Y. (2014) Metamorphism under stress: The problem of relating minerals to depth. Geology (2014) 42 (8): 733-734. https://doi.org/10.1130/focus0822014.1

Schmid, S. M., Aebli, H. R., Heller, F., & Zingg, A. (1989). The role of the Periadriatic Line in the tectonic evolution of the Alps. Geological Society, London, Special Publications, 45(1), 153-171.

Schmid SM, Fügenschuh B, Kissling E, Schuster R (2004) Tectonic map and overall architecture of the Alpine orogen. – Eclog Geol Helv 97:93-117.

Schmidt, M.W. and Thompson, A.B. (1996) Epidote in calcalkaline magmas; an experimental study of stability, phase relationships, and the role of epidote in magmatic evolution. American Mineralogist, 81(3-4), 462-474. doi: 10.2138/am-1996-3-420

Schneider, C.A., Rasband, W.S., Eliceiri, K.W. (2012). NIH Image to ImageJ: 25 years of image analysis. Nature Methods 9: 67. doi: 10.1038/nmeth.2089

Schreiber D, Lardeaux JM, Martelet G, Courrioux G, Guillen A (2010) 3-D modelling of Alpine Mohos in Southwestern Alps. Geophys J Int 180:961-975. doi: 10.1111/j.1365-246X.2009.04486.x.

Schuster, R., & Stüwe, K. (2008). Permian metamorphic event in the Alps. Geology, 36(8), 603-606.

Schwartz S, Lardeaux JM, Tricart P, Guillot S, Labrin E (2007) Diachronous exhumation of HP-LT metamorphic rocks from south-western Alps: evidence from fission track analysis. Terra Nova 19(2):133-140. doi: 1102 10.1111/j.1365-3121.2006.00728.x.

Sengupta P., Dasgupta S., Bhattacharya P.K., Hariya Y. (1989) - Mixing behavior in quaternary garnet solid solution and an extended Ellis and Green garnet–clinopyroxene geothermometer. Contrib. Mineral. Petr. 103 (2), 223–227.

Sheldrick, G.M. (1997) SHELXL-97. Programs for crystal structure determination and refinement. University of Göttingen, Germany.

Simonetti M, Carosi R, Montomoli C, Langone A, D'Addario E, Mammoliti E (2018) Kinematic and geochronological constraints on shear deformation in the Ferriere-Mollières shear zone (Argentera-Mercantour Massif, Western Alps): implications for the evolution of the Southern European Variscan Belt. Int J of Earth Sci 107:2163-2189. doi: 10.1007/s00531-018-1593-y.

Siivola, J., Schmid, R. (2007). Recommendations by the IUGS Subcommission on the Systematics of Metamorphic Rocks: List of mineral abbreviations. Web version 01.02.07. (http://www.bgs.ac.uk/scmr/docs/papers/paper_12.pdf) IUGS Commission on the Systematics in Petrology.

Smith, H.A. and Barreiro, B. (1990) Monazite U-Pb dating of staurolite grade metamorphism in pelitic schists. Contributions to Mineralogy and Petrology, 105(5), 602-615. doi: 10.1007/BF00302498

Sorensen, S.S. (1991) Petrogenetic significance of zoned allanite in garnet amphibolites from a paleo-subduction zone: Catalina Schist, southern California. American Mineralogist, 76(3-4), 589-601.

Spadini, G., Cloetingh, S., & Bertotti, G. (1995). Thermo-mechanical modeling of the Tyrrhenian Sea: Lithospheric necking and kinematics of rifting. Tectonics, 14(3), 629-644.

Spalla M.I., De Maria L., Gosso G., Miletto M. & Pognante, U. (1983) - Deformazione e metamorfismo della Zona Sesia-Lanzo meridionale al contatto con la falda piemontese e con il massiccio di Lanzo, Alpi occidentali. Mem. Soc. Geol. Ital., 26, 499-514.

Spalla M.I., Lardeaux J.M., Dal Piaz G.V. & Gosso G. (1991) - Metamorphisme et tectonique a la marge externe de la Zone Sesia - Lanzo (Alpes Occidentales). Mem. Sci. Geol. Padova, 43, 361-369.

Spalla M. I, Lardeaux J. M., Dal Piaz G. V., Gosso G., Messiga, B. (1996) - Tectonic significance of Alpine eclogites. J. Geodyn., 21, 257–285.

Spalla MI, Carminati E, Ceriani S, Oliva A, Battaglia D (1999) Influence of deformation partitioning and metamorphic re-equilibration on *P-T* path reconstruction in the pre-Alpine basement of central Southern Alps (Northern Italy). J Metam Geol 17 (3): 319-336. https://doi.org/10.1046/j.1525-1314.1999.00199.x

Spalla M. I., Siletto G. B., di Paola S., Gosso, G. (2000) - The role of structural and metamorphic memory in the distinction of tectono-metamorphic units: the basement of the Como Lake in the Southern Alps. J. Geodyn., 30, 191-204.

Spalla M. I., & Zulbati F. (2003) - Structural and petrographic map of the southern Sesia-Lanzo zone (Monte Soglio – Rocca Canavese, western Alps, Italy). Mem. Sci. Geol. Padova, 55, 119 – 127.

Spalla M. I. & Zucali M. (2004) - Deformation vs. metamorphic re-equilibration heterogeneities in polymetamorphic rocks: a key to infer quality PTdt path. Rivista Italiana di Mineralogia e Petrologia, 73, 249.

Spalla M.I., Zucali M., di Paola S., Gosso, G. (2005) - A critical assessment of tectono-thermal memory of rocks and definition of tectonometamorphic units: evidence from fabric and degree of metamorphic transformation. Geological Society of London, Special Publications, 243, 1, 227-247.

Spalla, M. I., Gosso, G., Marotta, A. M., Zucali, M., & Salvi, F. (2010). Analysis of natural tectonic systems coupled with numerical modelling of the polycyclic continental lithosphere of the Alps. International Geology Review, 52(10-12), 1268-1302, doi: 10.1080/00206814.2010.482737.

Spalla M I, Zanoni,D, Marotta A M, Rebay G, Roda M, Zucali M, Gosso G (2014) The transition from Variscan collision to continental break-up in the Alps: insights from the comparison between natural data and numerical model predictions. Geol Soc London Spec Pub 405:363-400.

Spear, F. S., & Peacock, S. M. (1989). Metamorphic pressure-temperature-time paths (Vol. 7). American Geophysical Union.

Spear FS (1993) Metamorphic Phase Equilibria and Pressure-Temperature-Time Paths, pp. 789, Min. Soc. Am. Monograph Series 1.

Spear, F.S. (2010) Monazite–allanite phase relations in metapelites. Chemical Geology, 279, 55-62. doi: 10.1016/j.chemgeo.2010.10.004

Stampfli, G. M., Borel, G. D., Marchant, R., & Mosar, J. (2002). Western Alps geological constraints on western Tethyan reconstructions. Journal of the Virtual Explorer, 8, 77.

Štípská, P., Schulmann, K., & Powell, R. (2008). Contrasting metamorphic histories of lenses of high-pressure rocks and host migmatites with a flat orogenic fabric (Bohemian Massif, Czech Republic): a result of tectonic mixing within horizontal crustal flow?. Journal of Metamorphic Geology, 26(6), 623-646.

Stöckhert B. & Gerya T.V. (2005) - Pre-collisional high pressure metamorphism and nappe tectonics at active continental margins: A numerical simulation. Terra Nova, 17(2), 102-110.

Stünitz H. H. (1989) - Partitioning of metamorphism and deformation in the boundary region of the "seconda Zona Diorito-Kinzigitica", Sesia Zone, Western Alps. Diss. N. 8817, ETH, Zuerich.
Tajcmanova L, Podladchikov Y, Powell R, Moulas E, Vrijmoed JC, Connolly JAD (2014) Grain-scale pressure variations and chemical equilibrium in high-grade metamorphic rocks. J Met Geol 32: 195–207. https://doi.org/10.1111/jmg.12066

Thöni, M., Miller, C., Zanetti, A., Habler, G., & Goessler, W. (2008). Sm–Nd isotope systematics of high-REE accessory minerals and major phases: ID-TIMS, LA-ICP-MS and EPMA data constrain multiple Permian–Triassic pegmatite emplacement in the Koralpe, Eastern Alps. Chemical Geology, 254(3-4), 216-237.

Tomkins, H.S. and Pattison, D.R.M. (2007) Accessory phase petrogenesis in relation to major phase assemblages in pelites from the Nelson contact aureole, southern British Columbia. Journal of Metamorphic Geology, 25(4), 401-421. doi: 10.1111/j.1525-1314.2007.00702.x

Tricart, P., & Schwartz, S. (2006). A north-south section across the Queyras Schistes lustrés (Piedmont zone, western Alps): Syn-collision refolding of a subduction wedge. Eclogae Geologicae Helvetiae, 99(3), 429-442.

Tropper, P., & Essene E. J. (2002). Thermobarometry in eclogites with multiple stages of mineral growth: an example from the Sesia-Lanzo Zone (Western Alps, Italy). Schweizerische Mineralogische und Petrographische Mitteilungen, 82(3), 487-514, doi: 10.5169/seals-62377.

Tribuzio, R., Messiga, B., Vannucci, R. and Bottazzi, P. (1996) Rare earth element redistribution during high-pressure–low-temperature metamorphism in ophiolitic Fe-gabbros (Liguria, northwestern

Italy): implications for light REE mobility in subduction zones. Geology, 24(8), 711-714. doi: 10.1130/0091-7613(1996)024<0711:REERDH>2.3.CO;2

Turco, E., Macchiavelli, C., Mazzoli, S., Schettino, A., & Pierantoni, P. P. (2012). Kinematic evolution of Alpine Corsica in the framework of Mediterranean mountain belts. Tectonophysics, 579, 193-206.

Turner FJ, Weiss LE (1963) Structural analysis of metamorphic tectonites. MacGraw-Hill, 545 p.
Yang X. M. (2017) - Estimation of crystallization pressure of granite intrusions. Lithos, doi: 10.1016/j.lithos.2017.06.018.

Venturini, G., Martinotti, G., Armando, G., Barbero, M., & Hunziker, J. C. (1994). The Central Sesia Lanzo Zone (Western Italian Alps): New field observations and lithostratigraphic subdivisions. Schweizerische Mineralogische und Petrographische Mitteilungen, 74, 115–125.

Visalli, R. (2017). Innovative numerical petrological methods for definition of metamorphic timescale events of southern European Variscan relicts via thermodynamic and diffusion modelling of zoned garnets. PhD Thesis. Catania: University of Catania

Venturini G. (1995) - Geology, geochemistry and geochronology of the inner central Sesia Zone (Western Alps, Italy). Mémoires de Géologie (Lausanne), 25, 1-143.

Voltolini, M., Zandomeneghi, D., Mancini, L., Polacci, M. (2011). Texture analysis of volcanic rock samples: quantitative study of crystals and vesicles shape preferred orientation from X-ray microtomography data. J. Volcanol. Geoth. Res. 202(1-2): 83. doi: 10.1016/j.jvolgeores.2011.02.003

Von Raumer JF, Abrecht J, Bussy F, Lombardo B, Ménot RP, Schaltegger U (1999) The Palaeozoic metamorphic evolution of the Alpine External Massifs. Schweiz Mineral Petrogr Mitt 79:5-22.

Von Raumer, J. F., Stampfli, G. M., & Bussy, F. (2003). Gondwana-derived microcontinents—the constituents of the Variscan and Alpine collisional orogens. Tectonophysics, 365(1-4), 7-22.

Von Raumer JF, Bussy F, Stampfli GM (2009) The Variscan evolution in the External massifs of the Alps and place in their Variscan framework. C. R. Geosciences 341 :239–252.

Von Raumer JF, Bussy F, Schaltegger U, Schulz B, Stampfli GM (2013) Pre Mesozoic-Alpine basements – their place in the European Paleozoic framework. GSA Bulletin, 125(1/2) :89–108.

White R.W., Powell R., Holland T.J.B., Johnson T.E., Green E.C.R. 2014. New mineral activity–composition relations for thermodynamic calculations in metapelitic systems. Journal of Metamorphic Geology. 32(3). pp. 261-286. https://doi.org/10.1111/jmg.12071

Whitney D.L. & Evans B.W. (2010) - Abbreviations for names of rock-forming minerals. Am. Mineral., 95(1), 185-187.

Williams P.F. & Compagnoni R. (1983) - Deformation and metamorphism in the Bard area of the Sesia Lanzo Zone, Western Alps, during subduction and uplift. J. Metamorph. Geol., 1(2), 117-140.

Williams PF (1985) Multiply deformed terrains - problems of correlation. J Struct Geol 7, 269–280. https://doi.org/10.1016/0191-8141(85)90035-5.

Willingshofer, E., & Sokoutis, D. (2009). Decoupling along plate boundaries: Key variable controlling the mode of deformation and the geometry of collisional mountain belts. Geology, 37(1), 39-42.

Willingshofer, E., Sokoutis, D., Luth, S. W., Beekman, F., & Cloetingh, S. (2013). Subduction and deformation of the continental lithosphere in response to plate and crust-mantle coupling. Geology, 41(12), 1239-1242.

Wilkins, S. W., Gureyev, T. E., Gao, D., Pogany, A., Stevenson, A. W. (1996). Phase-contrast imaging using polychromatic hard X-rays. Nature. 384(6607): 335. doi: 10.1038/384335a0

Wing, B.A., Ferry, J.M. and Harrison, T.M. (2003) Prograde destruction and formation of monazite and allanite during contact and regional metamorphism of pelites: petrology and geochronology. Contribution in Mineralogy and Petrology, 145, 228-250. doi: 10.1007/s00410-003-0446-1

Wu C.M., Wang X.S., Yang C.H., Geng Y.S., Liu F.L. (2002) - Empirical garnet–muscovite geothermometry in metapelites. Lithos, 62, 1-13.

Wu, C. M., Chen, H. X. (2015). Revised Ti-in-biotite geothermometer for ilmenite-or rutile-bearing crustal metapelites. Sci. Bull. 60(1): 116. doi: 10.1007/s11434-014-0674-y

Zanchetta, S., Malusà, M. G., & Zanchi, A. (2015). Precollisional development and Cenozoic evolution of the Southalpine retrobelt (European Alps). Lithosphere, 7(6), 662-681.

Zandomeneghi, D., Voltolini, M., Mancini, L., Brun, F., Dreossi, D., Polacci, M. (2010). Quantitative analysis of X-ray microtomography images of geomaterials: Application to volcanic rocks. Geosphere 6(6): 793. doi: 10.1130/GES00561.1

Zanoni, D., Bado, L., Spalla, M. I., Zucali, M., Gosso, G. (2008). Structural analysis of the Northeastern margin of the Tertiary intrusive stock of Biella (Western Alps, Italy). Ital. J. Geosci. 127: 125.

Zanoni D., Bado L., Spalla M. I., Zucali M., Gosso G. (2008) - Structural analysis of the Northeastern margin of the Tertiary intrusive stock of Biella (Western Alps, Italy). B. Soc. Geol. Ital., 127(1), 125.

Zanoni D. (2010) - Structural and petrographic analysis at the north-eastern margin of the Oligocene Traversella pluton (Internal Western Alps, Italy). Ital. J. Geosci., 129(1), 51-68.

Zanoni D., Spalla M.I., Gosso G. (2010) - Structure and PT estimates across late-collisional plutons: constraints on the exhumation of western Alpine continental HP units. Int. Geol. Rev., 52(10-12), 1244-1267.

Zanoni D. (2016) - Structure and petrography of the southwestern margin of the Biella pluton, Western Alps. J. Maps, 12(3), 597-620.

Zhong X, Vrijmoed JC, Tajčmanová L (2017) Effect of grain-scale pressure variations on garnet growth: a numerical approach. J Metam Geol. https://doi.org/10.1111/jmg.12213

Zingg, A., Handy, M. R., Hunziker, J. C., & Schmid, S. M. (1990). Tectonometamorphic history of the Ivrea Zone and its relationship to the crustal evolution of the Southern Alps. Tectonophysics, 182(1-2), 169-192.

Zucali M (2001) La correlazione nei terreni metamorfici, due esempi dall'Austroalpino occidentale (Zona Sesia-Lanzo) e centrale (Falda Languard-Campo/Serie del Tonale). PhD thesis Università degli Studi di Milano, 121 p.

Zucali M (2002) Foliation map of the “Eclogitic Micascists Complex” (Monte Mucrone–Monte Mars–Mombarone, Sesia-Lanzo Zone, Italy). Mem Sci Geol Padova 54: 87-100.

Zucali, M. (2005). JPT-Mineral formula calculation and geo-thermobarometry.

Zucali, M., Spalla, M. I., & Gosso, G. (2002). Strain partitioning and fabric evolution as a correlation tool: The example of the Eclogitic Micaschists Complex in the Sesia-Lanzo Zone (Monte Mucrone-Monte Mars, Western Alps, Italy). Schweizerische Mineralogische und Petrographische Mitteilungen, 82, 429–454.

Zucali, M., Spalla, M. I., Gosso, G., Racchetti, S., & Zulbati, F. (2004). Prograde LWS-KY transition during subduction of the Alpine continental crust of the Sesia-Lanzo Zone: The Ivozio Complex. Journal of Virtual Explorer, 16, 1-21.

Zucali, M. (2011). Coronitic microstructures in patchy eclogitised continental crust: the Lago della Vecchia pre-Alpine metagranite (Sesia-Lanzo Zone, Western Italian Alps). Journal of the Virtual Explorer, Electronic Edition, 38, 3-28, doi: 10.3809/jvirtex.2011.00286

Zucali, M., & Spalla, M. I. (2011). Prograde lawsonite during the flow of continental crust in the Alpine subduction: Strain vs metamorphism partitioning, a field-analysis approach to infer tectono metamorphic evolutions (Sesia-Lanzo Zone, Western Italian Alps). Journal of Structural Geology, 33, 381-398, doi: 10.1016/j.jsg.2010.12.006.

Zucali, M., Voltolini, M., Ouladdiaf, B., Mancini, L., & Chateigner, D. (2014a). The 3D quantitative lattice and shape preferred orientation of a mylonitised metagranite from Monte Rosa (Western Alps): Combining neutron diffraction texture analysis and synchrotron X-ray microtomography. J. Struct. Geol., 63: 91. doi: 10.1016/j.jsg.2014.02.011

Zucali, M., Barberini, V., Voltolini, M., Ouladdiaf, B., Chateigner, D., Mancini, L. (2014b). Quantitative 3D microstructural analysis of naturally deformed amphibolite from the Southern Alps

(Italy): microstructures, CPO and seismic anisotropy from a fossil extensional margin. From: Faulkner, D. R., Mariani, E., and Mecklenburgh, J. (Eds). Rock Deformation from Field, Experiments and Theory: A Volume in Honour of Ernie Rutter. Geological Society, London, Special Publications. 409. doi: 10.1144/SP409.5

Ringraziamenti

A ***Michele***, ***Davide***, ***Iole***, ***Guido*** e ***Gisella***. Mi avete fatto sentire parte di un gruppo, quasi una famiglia, facendomi crescere nella ricerca e, soprattutto, come persona. La ricchezza e la completezza di questa tesi è anche merito vostro. Grazie di questa possibilità!

A ***Manuel***, ***Marco***, ***Zuffa*** e ***Sara***. Nuovi amici del terzo piano, con cui ho condiviso pranzi, cene, sbattimenti di ogni genere, tanti caffè, divertimento, e tanti momenti deliranti e proficui nella stanza 99.

A ***Pietro***, più di un fratello da 5 anni. Nottate a rincorrere le scadenze, giornate splendide tra montagne e nevi perenni. Sei stato testimone della mia crescita e lo sarai ancora per molto tempo.

A ***Roberto***. Ricorderò per sempre i momenti lavorativi e di festa passati con te. Con la tua curiosità, la tua forza e il tuo impegno mi sei stato d'esempio.

Ai miei ***Genitori*** e mia ***Sorella***, Se sono arrivato a questo punto è anche merito vostro. I valori che mi avete trasmesso verso il mondo saranno sempre parte di me.

A ***Fuma*** e ***Chiara***, i megaterrazzi! Momenti di pura gioia e spensieratezza mi hanno sicuramente aiutato nel portare avanti e concludere tanti passi importanti nella mia vita, tra cui questo! Voi ci siete, sempre!

A tutti i miei ***Amici***, siete troppi! Tra ravanate e mazzate tra le montagne, aperitivi e serate, come dimenticarvi!

Infine, a mia moglie, ***Silvia***. Dove tu sei, quella è casa!

…. e alla nuova arrivata, ***Agata***!